Structure and Dynamics of Graphite Intercalation Compounds

by

Graeme Alexander Lindsell

A thesis submitted for the degree of Doctor of Philosophy of The Australian National University

September 1998

Declaration

The research described in this thesis was undertaken at the Australian National University under the supervision of Professor John White.

Except where otherwise stated, all experiments and data analysis described in this work were performed by the candidate. The binary graphite intercalation compounds that serve as the precursors to the ternary compounds studied herein were prepared by Mr Gordon Lockhart with the assistance of the candidate.

None of the work presented in this thesis has been submitted to any other institution for any degree.

G. Lindsell

Graeme Lindsell

22/9/98

Acknowledgments

I owe a great debt to Professor John White for allowing me to work with him as a student, and for his patience, guidance and assistance through all parts of this work. I would also like to thank Dr. Richard Welberry and Dr. Richard Bramley, who with Professor White acted as my supervisors, for their help and advice.

I would particularly like to acknowledge the help of the RSC's technical staff in the construction and design of the experimental equipment used in this work (Chapter 3). The efforts and assistance of Mr Gordon Lockhart in the preparation of the binary GICs and the design of the gas handling line, and of Mr Trevor Dowling in the design and reconstruction of the powder diffractometer and the sample cryostat, were vital to this work, and it could not have been made without their help and friendship. I would also like to thank Mrs Joan Smith, the RSC's librarian, for her particular aid in finding the journals and reference work used herein.

The tutelage, friendship and advice of Dr. Philip Reynolds were essential to the success of this thesis, especially in the fields of crystallography and diffraction theory, and I gratefully thank him for them.

I thank my family and friends for the love and support they have given me over the years this work has taken.

Abstract

The structure of guest compounds in the galleries of graphite intercalation compounds has been the subject of intense study by those interested in the nature of 2-dimensional hindered lattices and incommensurate systems. The in-plane structures of these compounds are often poorly known: it is difficult to prepare single crystals of these compounds, powder diffraction patterns are dominated by the very strong c-axis reflections, and the structures are themselves complex.

In 1971 it was discovered that the alkali-metal graphite intercalation compound KC_{24} would physisorb hydrogen and deuterium at cryogenic temperatures to form a ternary graphite intercalation compound. In the next two years further studies found that a variety of simple gases - argon, methane, nitrogen, hydrogen and deuterium - were absorbed by the related graphite intercalation compounds RbC_{24} and CsC_{24}. Interest in the application of these compounds was also excited by the discovery that KC_{24} absorbed deuterium preferentially over hydrogen.

While these ternary compounds have been known for over 20 years, their *ab*-plane structures are either not known or very poorly understood. The technique of using aligned samples produced from monolithic samples of pyrolytic graphite permits the use of x-ray powder diffraction techniques in probing this in-plane structure, and techniques of full pattern simulation can be used to produce model systems to compare with these diffraction patterns.

This thesis describes three primary fields of study. Firstly, an x-ray powder diffractometer was reconstructed in order that the diffraction studies could take place. Secondly, samples of the parent binary rubidium-graphite and potassium-graphite intercalation compounds were prepared, doped in-situ with stoichiometric quantities of the gases at cryogenic temperatures, and the *ab*-plane and *c*-axis diffraction data acquired. Finally, the diffraction patterns were compared with models produced by the full pattern simulations. These showed that the physisorption of the larger molecules - Ar, CH_4 and N_2 - induce an immediate disproportionation into two ordered phases, while the absorption of H_2 and D_2 produce both an interstitial solid solution and disproportionation at different stoichiometries

Contents

Chapter 1: Graphite Intercalation Compounds

1.1 Graphite Intercalation Compounds - Background and Nomenclature

1.1.1 Structure of Graphite

Graphite has a layered structure, in which sheets of covalently bonded carbon atoms in a hexagonal lattice are held together by weak Van der Waals forces. Figure 1.1 shows two ideal crystalline structures of graphite at room temperature, hexagonal and rhombohedral, which occur due to different stacking orders available to the graphene layers.

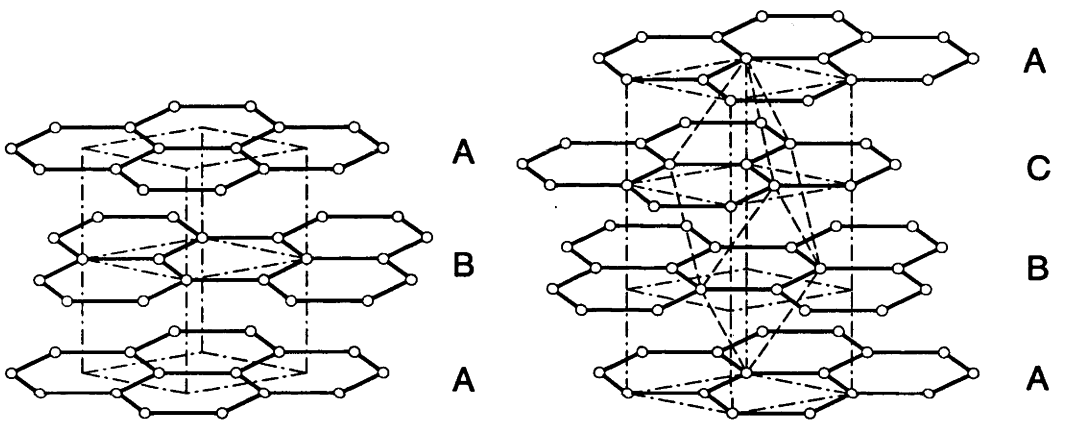

Figure 1.1: *hexagonal and rhombohedral structures of graphite. The unit cells are shown in dotted lines. The hexagonal structure has ABAB stacking, the rhombohedral ABCABC. The hexagonal structure has dimensions a=b=2.465Å, c=6.7Å. The hexagonal supercell of the rhombohedral structure has dimensions a=b=2.46Å, c=10.05 Å*

These ideal structures are usually disordered in a variety of ways, by stacking faults of the graphene layers and by impurity atoms in the layers themselves. Stacking faults may be rotational or translational in the *ab* plane, where the registry of one graphene layer upon another is altered, or along the *c*-axis, where the stacking of one layer upon another is disrupted by an increase in the interplanar layer distance and/or by a tilt angle. Stacking faults may display an ordered sequence superimposed upon the c-axis stacking of the graphite crystallite. In the extreme case of complete turbostratic disorder the *c*-axis identity period is retained but each layer is randomly translated or rotated with respect to the previous one.

Good single crystals of graphite, with a small number of stacking faults, can be found in natural sources, such as coal mines, or are produced as Kish graphite in blast furnaces, but they are rather small for stoichiometric studies. For larger samples one must employ well ordered pyrolytic graphite which is produced by the cracking, under pressure at high temperatures, of large-molecule organic gases such as coronene. Pyrolytic graphite consists of many small crystals deposited with good *c*-axis registry but with random *ab*-plane orientation between the different domains. As a result it is effectively a powder when determining in-plane structure.

1.1.2 Graphite Intercalation Compounds

An intercalation compound is one where a guest atom or molecule is added to a host compound by insertion of the guest into vacancies that are already present in the structure of the host. In a graphite intercalation compound (GIC), these vacancies are the galleries between the graphene layers, available as a result of the weak bonding between the layers. Intercalation forces these layers apart since the compound is of greater thermodynamic stability than the separate components. An intercalation reaction is distinguished from other reactions in that the structure of the host compound is modified but not completely disrupted by the process. In a GIC the carbon layers remain approximately planar and parallel after the reaction[1].

Charge transfer between the guest and host is a stabilising feature of all GICs, which can be divided by this attribute into two types, donor and acceptor[2]. An acceptor GIC is one where there is electron transfer from the graphite host to the guest: acceptor guests include Br_2, HNO_3 and $CoCl_2$. In a donor GIC the guest donates electrons to the host layers; most donors are metal atoms. Commonly used donor guests include the alkali metals, lithium, potassium, rubidium and cesium, as well as the alkaline earth metals and the lanthanides.

	σ_{ab} ($\Omega^{-1}cm^{-1}$)			σ_c ($\Omega^{-1}cm^{-1}$)
	300 K	77 K	4 K	300 K
Graphite	$2.5x10^4$	$3.8x10^4$		~10
KC_8	$1.1x10^5$	$1.0x10^6$	$2.4x10^7$	$3.2x10^3$
KC_{24}	$1.7x10^5$	$1.1x10^6$		
RbC_8	$1.0x10^5$	$8.6x10^5$	$1.2x10^7$	
RbC_{24}	$1.5x10^5$	$5.8x10^5$		

Table 1.1: *The effect of intercalation of rubidium and potassium on conductivity σ in the ab-plane and c-axis directions. After Fischer*[3].

The amount of transferred charge per intercalate atom or molecule, in units of electronic charge, is ~0.2-0.5 for most acceptors, and ~1 for alkali metal donors[2]. This charge transfer increases the conductivity of the bulk GIC compared with that of graphite, as shown in Table 1.1; additionally the difference between the *ab*-plane and the *c*-axis conductivity, which is characteristic of graphite, is reduced in the intercalation compound. The studies described in this work involve the heavy alkali-metal GICs of provisional stoichiometry KC_{24} and RbC_{24}. Thus most of the rest of this introduction will deal with the donor intercalation compounds.

An alkali-metal GIC is usually produced by one of two methods. One can add the correct stoichiometry of a guest in liquid or vapour phase to the graphite sample, seal it under vacuum, and keep the system at the required temperature until the reaction goes to completion. This can often be determined by colour changes in the graphite sample; in the rubidium-graphite intercalates the stage 2 compound is a metallic blue, while the stage 1 compound is orange. Alternatively the "two-zone" method may be employed, where the guest and the host are heated to separate temperatures within a sealed double furnace, and the final composition is determined by the temperature differential between the zones. For the alkali-metal GICs, this reaction can take up to several days at a temperature of 600 K to produce a well equilibrated sample. The process of intercalation will often rearrange or introduce new faults into the crystal structure, as the graphene layers are pushed apart by the guest compound. In the stage 2 alkali-metal GICs the stacking order of the graphene layers is changed from ABAB to BAαABαBA (where α represents a guest layer), so that the carbon hexagons sit above one another when stacked across guest layers. The exact stoichiometry to which a sample is prepared can vary with the methodology of the groups that produced them; in this work, the stoichiometry reported in a given paper will be used when referring to the work in that paper.

In addition to the large number of binary GICs, there also exist ternary graphite intercalation compounds, where two different species are intercalated into the host galleries. They can be produced by the direct absorption of two species into the host compound, or by first making a binary GIC which then absorbs a third compound. Examples of the first are ternaries produced from a solution of two heavy alkali metals, such as the $Cs_{1-x}K_xC_8$ and $K_{1-x}Rb_xC_8$ systems, or alkali-metal-ammonia solutions which then react with graphite. Examples of the second also include the alkali-metal-ammonia GICs where a binary alkali metal GIC is allowed to react with NH_3 gas, and organic-molecule ternaries such as potassium-benzene GIC, $K(Bz)_{1.2}C_{24}$[4].

1.1.3 *c*-axis Structure - Staging

All GICs exhibit the phenomenon of staging, whereby the guest molecules do not occupy all available galleries equally, but instead completely fill some galleries while leaving others empty. As a result each filled layer is separated from the next by the same integer number of empty galleries. The nomenclature used for staged structures is that a "stage N" intercalate has N layers of host material separating two layers of guest: in a stage 1 GIC there is one graphene layer between each layer of guest, and thus all the available galleries have been filled, while in a stage 2 GIC there are two graphene layers intervening, and half the available galleries are filled. Alternatively, the stage number can be considered to be the ratio of total galleries to filled galleries per repeat unit of the GIC[1, 2, 5]. As guest is added to the compound, the structure progresses from higher to lower stage, shown in Figure 1.2.

A considerable number of theoretical and experimental studies have investigated the mechanism behind staging[2], reaching a consensus that the process is driven energetically by the charge transfer to the host layers and the minimisation of crystal strain. This results even from simplest models of charge transfer, which assume that the electrons are transferred to or from the π bands of the graphene sheets immediately adjacent to the guest without changing the electronic structure of these bands; as a result those graphene layers near the guest possess a greater charge than those further away. This creates an effective repulsion between the guest layers, which in turn creates a ordered one dimensional lattice of stages along the c-axis[2].

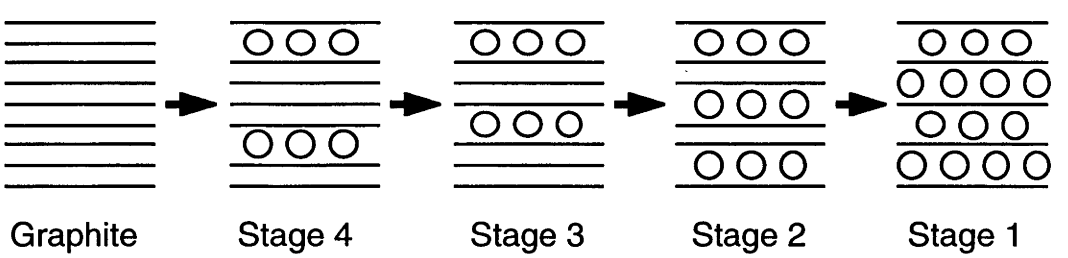

Figure 1.2: *diagram of staging. As the guest is progressively added to the host compound, the structure of a GIC proceeds from a high stage to a lower stage intercalate*[6].

A simple model of intercalate staging, where all galleries are either completely filled with or completely empty of the guest compound, cannot explain certain experimental observations, especially changes of stage number during ternary intercalation reactions or under pressure[2, 7]. Samples seen to evolve from stage N to stage N±1 would in the simple model require the unlikely mechanism that some galleries completely empty

themselves to fill others. The guest would have to migrate out of the host structure in order to do this.

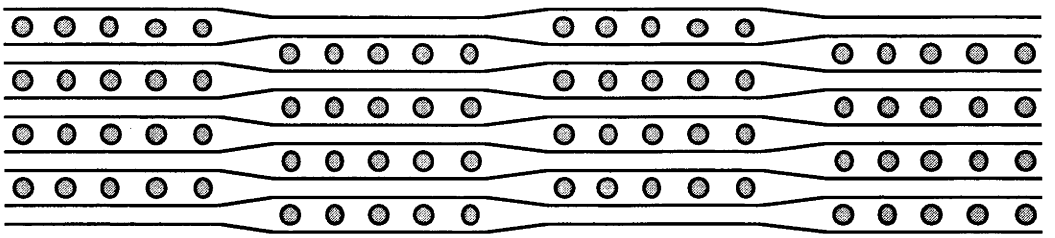

Figure 1.3: *A schematic diagram of the Daumas-Herold "pleated-layer" model of staging, for a stage 2 GIC.*

The Daumas-Herold "pleated-layer" model of GIC staged structures, shown in Figure 1.3, avoids these problems by proposing that each crystallite contains multiple domains, each with the same stage number but with the guest occupying different galleries in each domain[2, 7]. The guest occupies a fraction of the available area of the host galleries equal to (1/stage number); changes of stage by ±1 take place by alteration of this area, as the *ab*-plane structure of the guest expands or contracts[7]. These domains form as a result of elastic strains induced in the graphene layers by the guest atoms or molecules: the deformation of the host is smaller for large, well defined domains than for smaller disordered ones, and while the deformation is obviously nonexistent for the simple model shown in Fig 1.2, simulations have found that not only do the pleated-layer domains bind strongly together but that there is an energy barrier stopping the easy merging of domains in the same gallery[2].

1.1.4 In-Plane Structure of Guests

The *ab*-plane structures of GICs are not as well understood as the *c*-axis structures, for a variety of reasons: firstly in graphite and its intercalation compounds, the *c*-axis structure factor is much greater than the in-plane structure factor; secondly the in-plane structures undergo a variety of temperature dependent phase transitions; thirdly the structures themselves are often more complex than simple registered commensurate superlattices of the graphite structure. Ternary compounds add even more variety to possible in-plane structures.

The variety of possible in-plane structures in a GIC is far greater than those available to the one-dimensional *c*-axis, and the large number of available guests enriches this variety. The 2D array of atoms or molecules in a layer will be influenced by the presence of the graphite host, which presents a hexagonal lattice of potential wells to the guest.

Many guests, both donor and acceptor, exhibit high temperature two-dimensional liquid phases which show no long-range order but exhibit short-range modulations as a result of the graphite lattice[8]. Upon lowering the temperature the liquid phase will crystallise, but the packing density of the guest may not exactly fit the 2.46 Å spacing of the hexagonal graphite lattice - in fact it rarely does - and a wide variety of incommensurate, hindered or domain-walled structures result[7, 8].

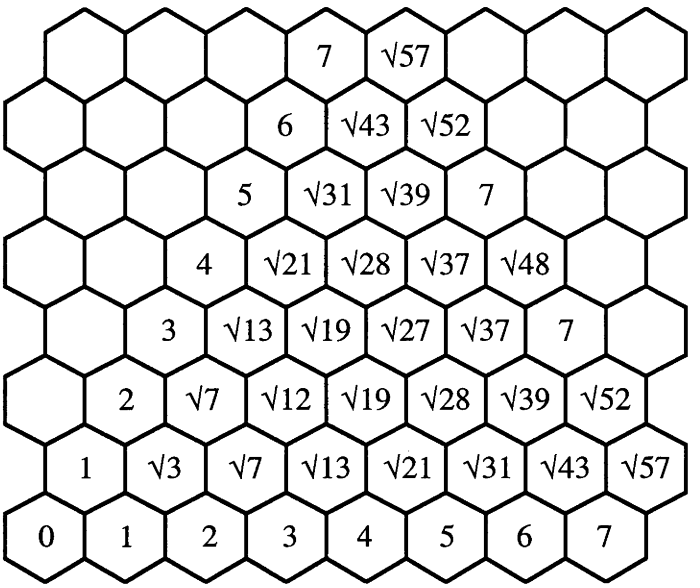

Figure 1.4: *The figure above shows the distances between the marked hexagons, as a multiple of the hexagon centre-to-centre distance. For graphite, this is the in-plane lattice constant of 2.46 Å. In dealing with commensurate guest structures, references will often be made to cells with dimensions that are equal to these distances.*

In such a structure of two layers of different atoms or molecules in close proximity, each species will possess its own plane group; if both of the groups are a rational subset of a larger common cell, the layers are commensurate; if not, the lattices are incommensurate[9]. Incommensurate systems produce diffraction patterns with distinct reflections that can only be indexed using higher dimensional indices[9]. When describing commensurate lattices, the cell is described by reference to the graphite *ab*-plane cell (see Figures 1.1, 1.4 and 1.5). The notation used is AxB R(θ,ϕ), where (A,B) are the lengths of the in-plane axes in units of the graphite in-plane and (θ,ϕ) are the angles between A,B and the graphite cell axes (a,b), though for a hexagonal lattice the angle ϕ can be omitted[10]. Figure 1.5 shows five small commensurate cells, $\sqrt{3}$x$\sqrt{3}$ R30°, 2x2 R0°, 2x$\sqrt{3}$ R(0°,90°), 3x$\sqrt{7}$ R(0°,19.1°) and $\sqrt{7}$x$\sqrt{7}$ R±19.1° - the ±19.1° refers to the two possible $\sqrt{7}$x$\sqrt{7}$ orientations.

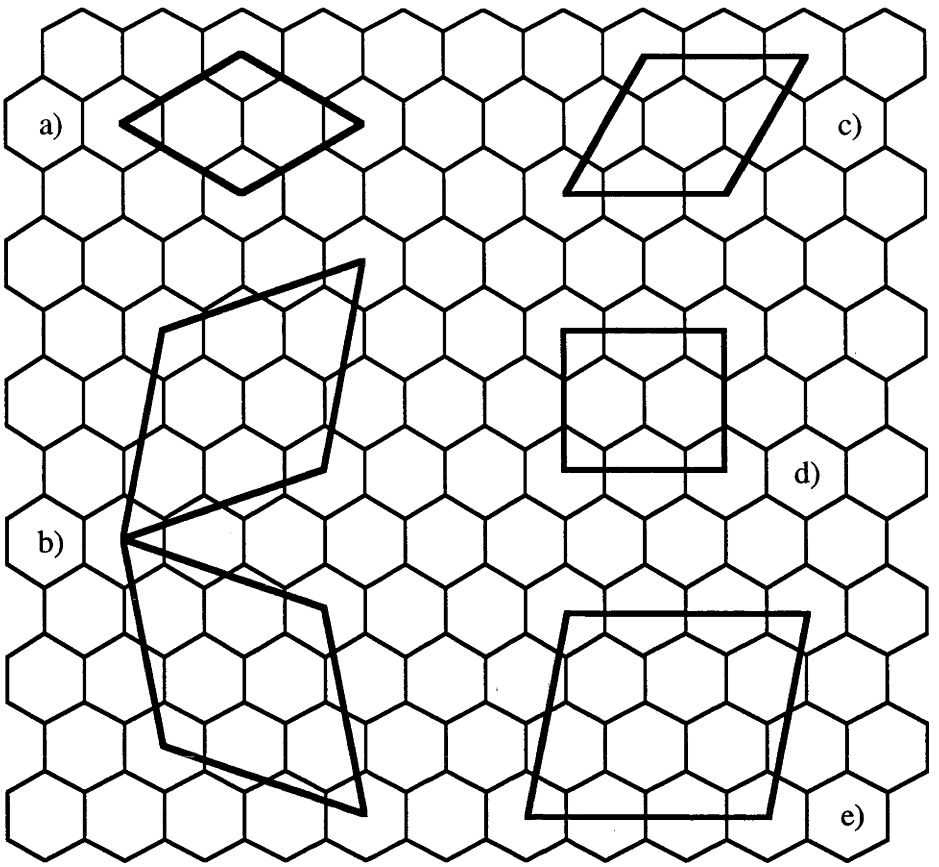

Figure 1.5: *several commensurate cells: a) √3x√3 R30°, b) √7x√7 R±19.1°, c) 2x2 R0°, d) 2x√3 R(0°,30°) and e) 3x√7 R(0°,19.1°).*

Acceptor guests - usually molecular species such as Br_2, $CoCl_2$, $FeCl_3$, $SbCl_5$ and HNO_3 - tend to produce complex in-plane structures which retain features of their pure solid phases, and are often of lower symmetry than the graphite hexagonal structure. They have been more difficult to model than the alkali-metal GICs due to the additional more complex accepter-acceptor molecular interactions, as well as the complex potential for these molecules on the graphite hosts[8]. To take one example, in $SbCl_5$ the guest intercalates at 440 K, and forms a two phase system with the guest disproportionating into $SbCl_6^-$ and $SbCl_3$ via the reaction:

$$3SbCl_5 + 2e^- \longrightarrow 2SbCl_6^- + SbCl_3$$

The $SbCl_6^-$ phase forms a √7x√7 R19.1° commensurate lattice which undergoes a incommensurate transition at ~350 K before melting at around 450 K, while the $SbCl_3$ remains a liquid down to 230 K, where it crystallises into a √39x√39 R16.1° commensurate lattice [11].

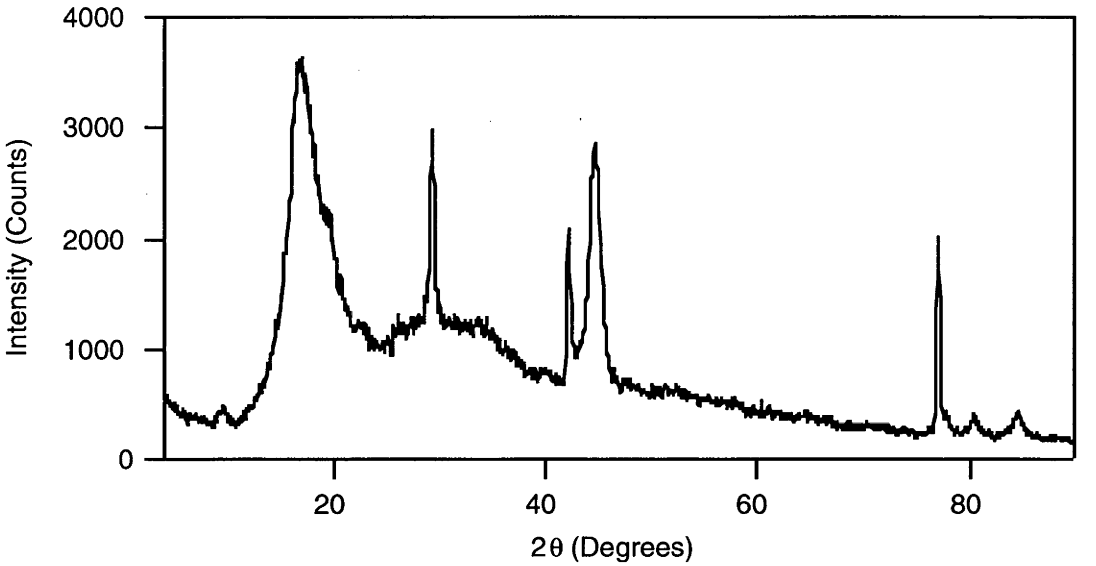

Figure 1.6: *ab-plane oriented powder diffraction pattern of stage 2 Rb-GIC at 300 K, indicative of a liquid structure. Only the wide bands at ~17°and ~30° are produced by the ab-plane structure of the rubidium ions, the other peaks on this pattern are c-axis breakthroughs, caused by mosaic spread of the crystallites, or are reflections of the graphite host. (From the author's experimental studies.)*

With the heavy alkali-metal GICs, the stage 1 compounds possess a different guest *ab*-plane structure than those of the higher stage materials. In the stage 1 compounds the metal ions form a commensurate 2x2 R0° structure which remains stable over the temperature range from 4 K to 700 K, at which temperature the in-plane lattice melts[10], while for GICs of stage 2 and above there is a high temperature liquid phase that at upon cooling to cryogenic temperatures undergoes a phase transition to form various in-plane structures which differ for each of the metals.

At room temperature and above, the stage 2 and higher stage K-, Rb- and Cs-GICs all display simple diffraction patterns (as shown in Figure 1.6) indicating a liquid-like in-plane structure. Single crystal photographs of room temperature alkali-metal GICs display diffuse rings rather than single spots, but also show six-fold intensity maxima, a sign that there is a modulation of the liquid structure by the graphite lattice while powder diffractograms show only the primary liquid-like peak (Figure 1.6). Early attempts to model the graphite peak intensities found that a large percentage of the alkali-metal ions in the liquid-like structure were registered with the hexagons of the graphite lattice.

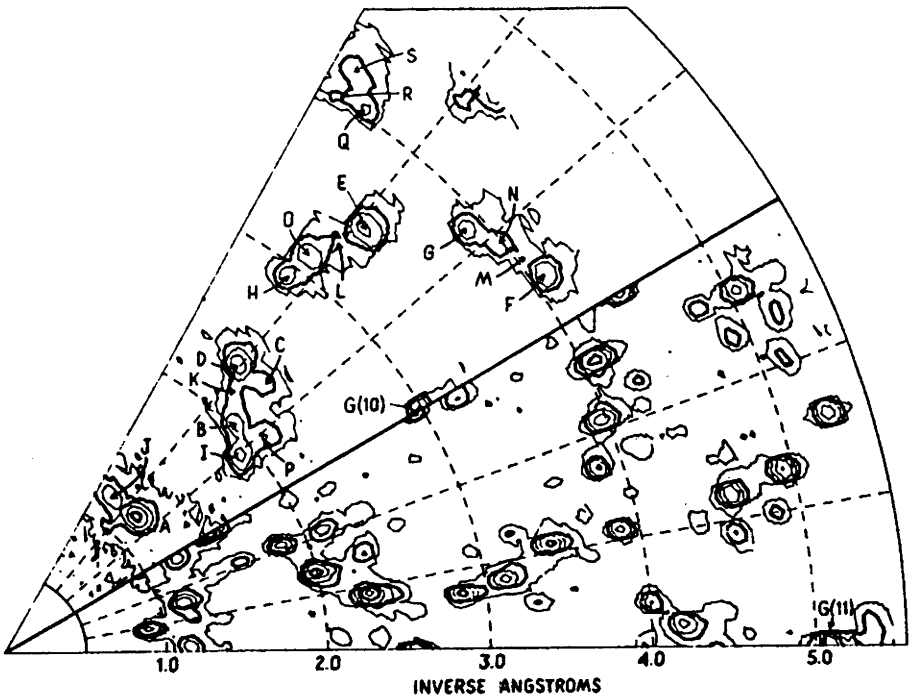

Figure 1.7: *the ab-plane single crystal diffraction patterns for stage 2 (lower segment) and stage 3 (upper segment) cesium-GIC at 10 K. After Winokur and Clarke*[12].

The low temperature phases of the stage 2 heavy-alkali-metal-GICs produce complex *ab*-plane powder and single crystal diffraction patterns. Beneath 228 K the in-plane guest structure of stage 2 cesium-graphite intercalation compound orders to produce the pattern seen in Figure 1.7[12]; a 2-D to 3-D ordering transition is seen at 165 K, together with an increase in in-plane scattering intensity. In stage 2 rubidium-graphite, the in-plane ordering transition occurs at 165 K and the 2-D to 3-D transition at 106 K. The stage 2 potassium-graphite system has an *ab*-plane and 2-D to 3-D ordering transition 125 K, and another structural transition at 95 K.

A schematic interpretation (after Mori et. al.)[13] of the single crystal ab-plane diffraction pattern of KC_{24} is shown in Figure 1.8, where three primary components of the pattern are indicated: the graphite peaks, twelve (10) reflections of the potassium lattice, consisting of two hexagonal structures at an angle $\pm\theta$ to the graphite lattice, and a circle of primary modulation satellite peaks of the alkali-metal lattice surrounding each of the graphite peaks. The entire pattern can be indexed by the linear combination $(\mathbf{q}_G \pm \mathbf{q}_K)$ where $\mathbf{q}_G$ and $\mathbf{q}_K$ are the two-dimensional graphite and potassium wave vectors, each of the form $2\pi(H\mathbf{b}_1+K\mathbf{b}_2)$, where H and K are the peak indices and $\mathbf{b}_1$ and $\mathbf{b}_2$ the unit vectors[8, 12]. Similar diffraction patterns are produced by the rubidium-graphite and cesium-graphite intercalation compounds at temperatures beneath the ordering transitions.

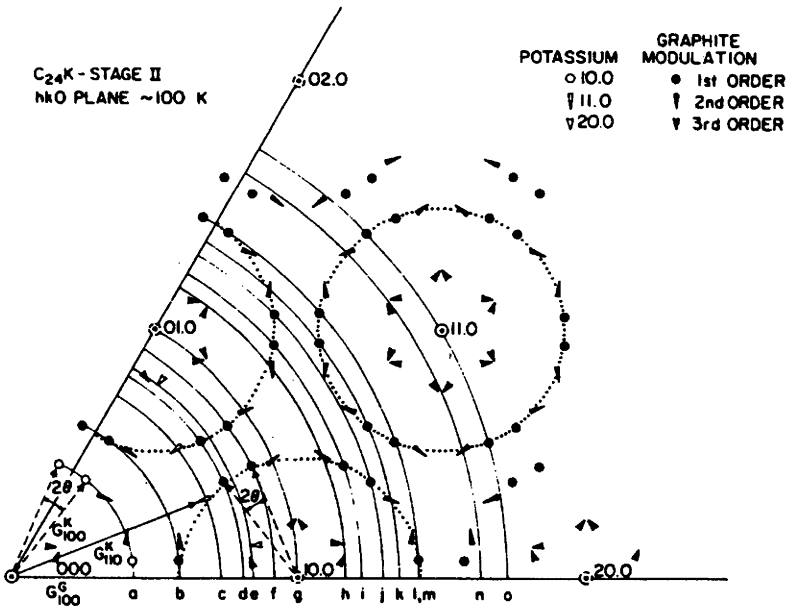

Figure 1.8: *A schematic indexing of the HK.0 reflections of a single-crystal diffraction pattern produced by KC_{24}, showing as the rings a-o the peaks that are seen in a oriented powder diffraction pattern of KC_{24}. Reproduced from Mori et al*[13].

From the same paper[13] a plot of the rotation angle θ - the angle the alkali-metal lattice makes to the graphite lattice - versus the "lattice mismatch" $Z = a_m/a_{gr}$ - the ratio of the length of the alkali metal (10) to the graphite (10) - is shown in Figure 1.9, the points coming from several separate studies. A "universal curve" of the form:

$$\cos(30°-\theta) = \frac{(2z^2+1)}{(2\sqrt{3}z)} \qquad (1)$$

was derived empirically, and found to provide a good fit to the points. At q=0° and z=0.5 is the 2x2 R0° commensurate lattice; the leftmost data point is an RbC_{24} electron diffraction pattern indexed as possessing the $\sqrt{7}x\sqrt{7}$ R 19.1° commensurate lattice.

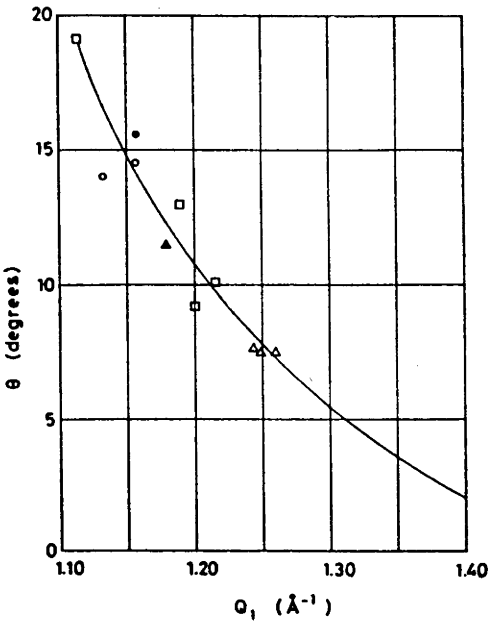

Figure 1.9: *A plot of the rotation angle θ - the angle between the graphite and alkali-metal wave vectors - against the lattice mismatch Z for a number of AM-GIC samples: open circle=CsC_{24}, filled circle=CsC_{36}, open square=RbC_{24}, open triangle=KC_{24}, filled triangle=KC_{36}. Reproduced from Suzuki et al*[14]*. A curve of the form $\cos(30-\theta)=(2z^2+1)/(2\sqrt{3}z)$ is fitted to the data.*

A model originally suggested by Clarke et al[15] has provided the best description available for the stage 2 cesium- and rubidium- GICs. In this model, the alkali metal *ab*-plane lattice is "almost commensurate" with a $\sqrt{7}x\sqrt{7}$ R19.1° superlattice, and the alkali ions form hexagonal domains which internally adopt the $\sqrt{7}x\sqrt{7}$ structure but between which there exist domain walls of higher density. This discommensurate-domain model was expanded by Suzuki et al[14], who show that the domain size L and angle Ω (the angle that the normal to the domain wall makes with the graphite (10) vector) are uniquely determined by the vector **q**, the difference between the $\sqrt{7}x\sqrt{7}$ R19.1° vector and the observed alkali metal wave vector $\mathbf{q}_{AM}$, as follows

$$\frac{L}{a_G} = \frac{1}{\sqrt{7}}\left(\frac{|q_G|}{|q|}\right) \tag{2}$$

$$\Omega = -60° - \theta_C + \arccos\left(\frac{|q|}{|q_G|}\right) \tag{3}$$

where θ_C=19.1°, the rotation angle of a $\sqrt{7}x\sqrt{7}$ commensurate superlattice compared with the graphite hexagonal lattice, and q_G is the primary graphite vector. The "universal curve" of Equation (1) is derived from the same results.

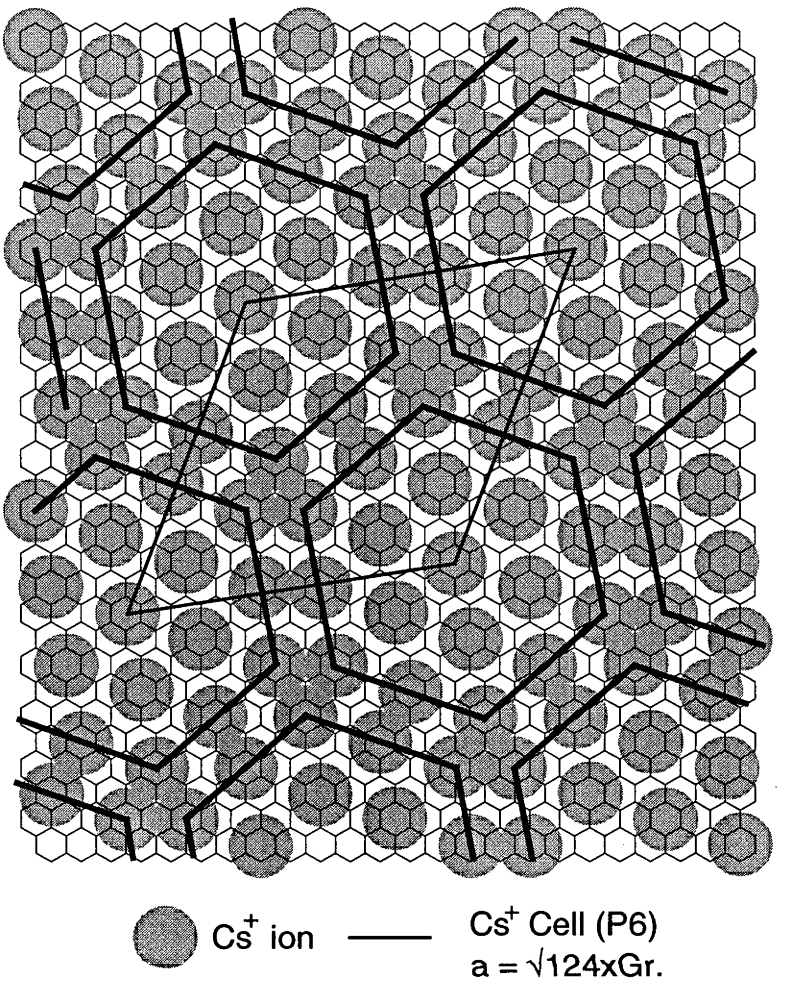

Figure 1.10: *the ab-plane structure of stage 2 cesium GIC beneath the ordering transition, according to the discommensurate domain model. The Van der Waals radius is used for the cesium ions shown.*

This model has been applied successfully to the nominally CsC_{24} and RbC_{24} systems, to suggest the structures shown in Figures 1.10 and 1.11 respectively, which give a $\sqrt{124}x\sqrt{124}$ hexagonal superlattice for the cesium-graphite, and a $\sqrt{43}x\sqrt{43}$ superlattice for the rubidium GIC. These structures suggest that the in-plane stoichiometry of the samples is different from the 1:24 alkali-metal: carbon ratio found from absorption studies: the $\sqrt{124}x\sqrt{124}$ cesium-graphite structure shown has a stoichiometry of $CsC_{26.6}$; the $\sqrt{43}x\sqrt{43}$ rubidium-graphite structure has one of RbC_{25}. The $CsC_{26.6}$ structure shown is an idealised structure of $\sqrt{7}x\sqrt{7}$ domains separated by $2x\sqrt{7}$ domain walls: molecular dynamics simulations[16] have shown the domain walls are of somewhat lower density, with the ions at the domain wall moved away from the graphite hexagon centres; the RbC_{25} structure shows this more realistic position for the ions.

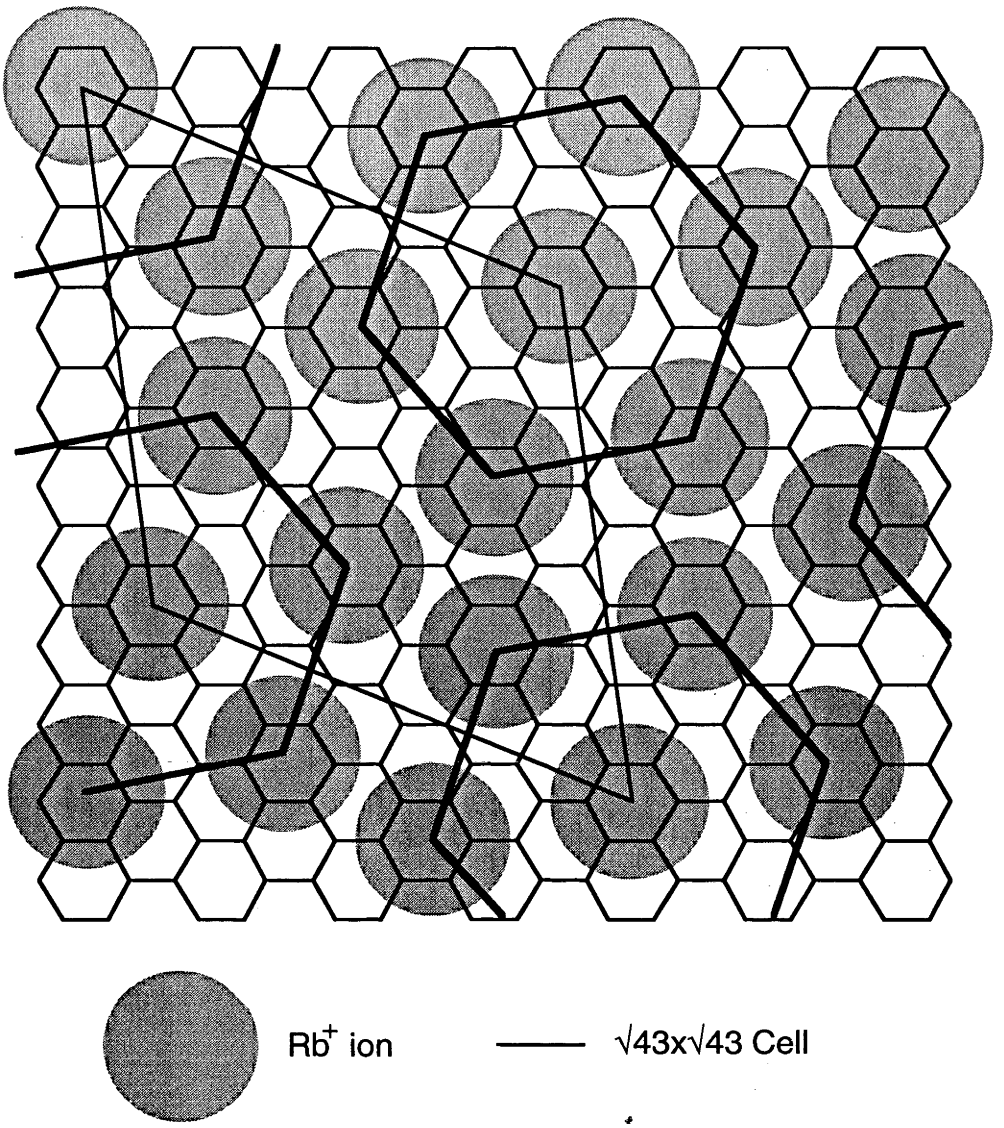

Figure 1.11: *the ab-plane structure of stage 2 rubidium-GIC beneath the ordering transition, according to the discommensurate-domain model. The ions at the domain wall have been moved off the hexagon centres. The Van der Waals radius is used for the rubidium ions shown.*

This model works well for the diffraction patterns observed from the cesium and rubidium GICs, though there are still other competing models[17], but it cannot account for the observed potassium patterns. It predicts a domain size which is too small for a physically possible $\sqrt{7}x\sqrt{7}$ domain to form, even the compressed one seen in the RbC_{25} structure. The structure of the stage 2 potassium-GIC is still uncertain: below the first ordering transition it has been described by a $\sqrt{201}x\sqrt{201}$ hexagonal superlattice containing 2x2 hexagonal clusters of ions separated by $\sqrt{7}x\sqrt{7}$ voids and faulted domain walls; and beneath the second ordering transition at 95 K by a multiphase system of four

commensurate hexagonal superlattices or by a disordered lattice of K^+ ions adopting 2x2 domains with $\sqrt{7}x\sqrt{7}$ borders but with no long range ordering[18, 19].

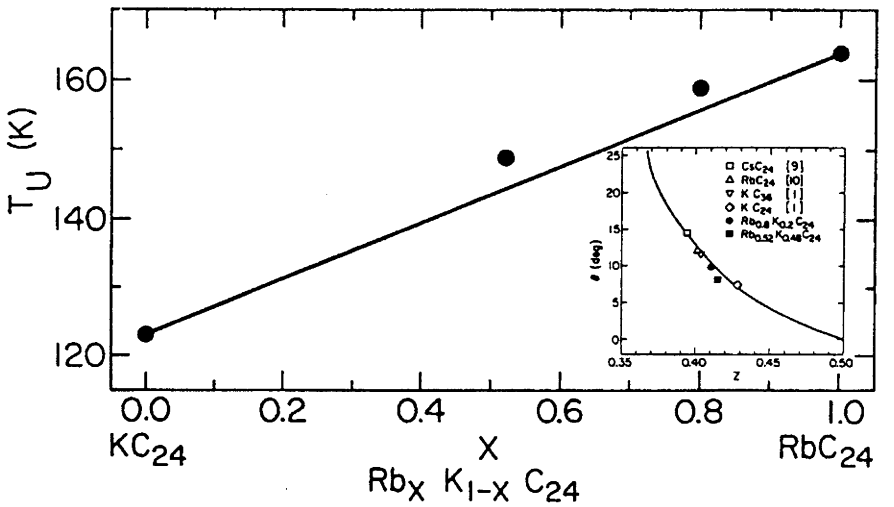

Figure 1.12: *the compositional dependence of the ordering transition in $Rb_xK_{1-x}C_{24}$. The inset shows the position of the ternary phases on the "universal curve" of Moreh. Reproduced from Chow and Zabel*[20].

Stage 1 ternary GICs of the form $A_{1-x}B_xC_8$ have been formed of the heavy alkali-metals potassium, rubidium and cesium, but the only stage 2 substitutional ternary reported is $K_{1-x}Rb_xC_{24}$. The stage 1 ternary compounds have the same 2x2 *ab*-plane superlattice that all the stage 1 binary alkali-metal GICs possess; the two metals make a random occupation of each available site with a probability based purely on stoichiometry. The *c*-axis diffraction data show that these compounds have a significant deviation from the linear expansion expected by Vegard's law. While it was speculated that these deviations are a result of the appearance of an in-plane $\sqrt{12}x\sqrt{12}$ ordered superlattice no such structures have been observed[21]. In the stage 2 compound it was found that the temperature of the ordering transition in the ternary mixture was close to the straight line between the ordering temperatures for the two binary compounds predicted by Vegard's Law, as shown in Figure 1.12[20].

The *ab*-plane structure was described as a discommensuration-domain structure similar to that observed in the rubidium and cesium binary compounds; the observed diffraction patterns fall on the "universal curve" for these compounds, between the positions of RbC_{24} and KC_{24}, which is shown in the inset in Figure 1.12. A second ordering transition at a lower temperature was seen only in the ternary compounds, with the

appearance of new satellite peaks characteristic of an incommensurate modulation. These were explained as a result of a additional compositional modulation of the lattice.

1.2 Gas Physisorption by Alkali-Metal GICs

A new type of ternary GIC was described in 1971 by K. Watanabe et. al.[22], when they reported the absorption of hydrogen and deuterium gas by KC_{25} at temperatures of less than 90 K. This process was determined to be physisorption - where the absorbed molecule remains intact and is released unchanged upon heating - as opposed to chemisorption, where the hydrogen is dissociated and adsorbed as hydride ions.

Later papers in 1972[23] and 1973[24] from the same group described the absorption at cryogenic temperatures of a variety of simple gases - Ar, H_2, D_2, N_2 and CH_4 - by CsC_{24}, RbC_{24} and KC_{24}, and also noted that there was no physisorption of the same gases by the stage 1 GICs (stoichiometry C_8M). These later papers are so important to this work that they will be described here in considerable detail. Table 1.2 is taken directly from the 1973 paper[24]: it shows the maximum amount of gas physisorbed at saturation, the value being the ratio of absorbed molecules to alkali ions.

	He	H_2, D_2	Ne	N_2	Ar	CH_4
$C_{24}K$	no sorption	2.10	no sorption	0.7	no sorption	no sorption
$C_{24}Rb$	no sorption	2.05	no sorption	1.0	1.2	0.9
$C_{24}Cs$	no sorption	2.00	no sorption	1.3	1.4	1.2
C_8M	no sorption	no sorption	no sorption	no sorption	no sorption	no sorption

Table 1.2: *Sorptive capacity of gases physisorbed by the Stage 2 GICs KC_{24}, RbC_{24} and CsC_{24}, after Watanabe et al*[24].

Table 1.2 shows that the absorption behaviour of the gases can be divided into two types: the small molecules, H_2 and D_2, not only have a greater maximum sorption than the larger argon, nitrogen and methane molecules, but additionally the sorptive capacity shows the opposite behaviour with increasing alkali-metal ion size.

The systems showed differing pressure-sorption isotherms for the various gases, again depending on the size of the adsorbed molecules and alkali-metal ions. Figures

1.13-1.15 show these results, and the three types of isotherms reported, while Table 1.3 shows the types of sorption for all systems studied.

	H_2,D_2	N_2	Ar	CH_4
KC_{24}	II	-	-	-
RbC_{24}	I	II	III	III
CsC_{24}	I	I	II	III
Molecular Diameter (Å)	2.40	3.00	3.80	4.00

Table 1.3: *Types of absorption isotherms found in physisorbed alkali-metal-gas-graphite systems. After Watanabe et. al*[24].

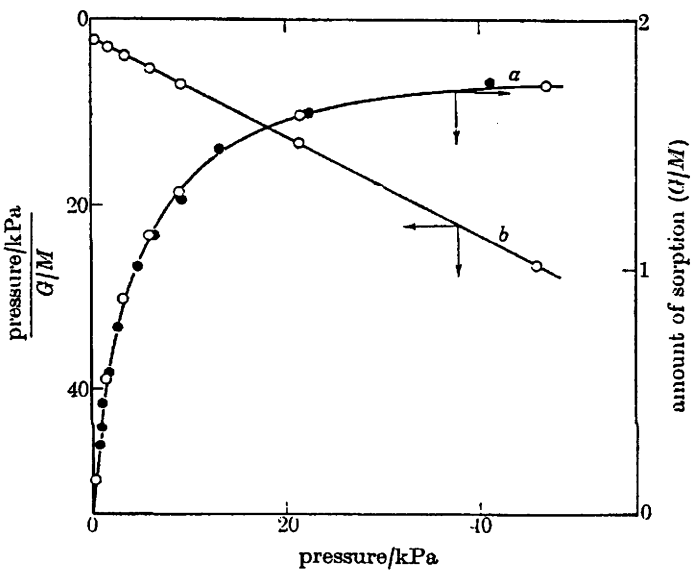

Figure 1.13: *The Type I isotherm, from the $Rb(D_2)_xC_{24}$ system at 113 K, showing a) pressure-sorption plot and b) Langmuir plot. Open circles are sorption, filled desorption. Reproduced from Watanabe et al*[24].

The isotherm denoted Type I (Figure 1.13) is the standard Langmuir isotherm, characteristic of the physisorption of a monolayer of gas on a surface, and is here seen in the Rb-H_2/D_2, Cs-H_2/D_2 and Cs-N_2 ternary GICs: systems where there is a large disparity in the size of the absorbed gas molecules and the larger alkali-metal-ion compounds. The Type II and Type III isotherms (Figures 1.14 and 1.15 respectively), seen in the systems with relatively larger guest molecules compared to the host alkali ions, are both characterised by a critical pressure beneath which there is little or no physisorption, and above which the system moves rapidly to a saturation stoichiometry as

pressure increases - almost immediately reaching saturation in the Type III systems, but less rapidly with the Type II isotherms.

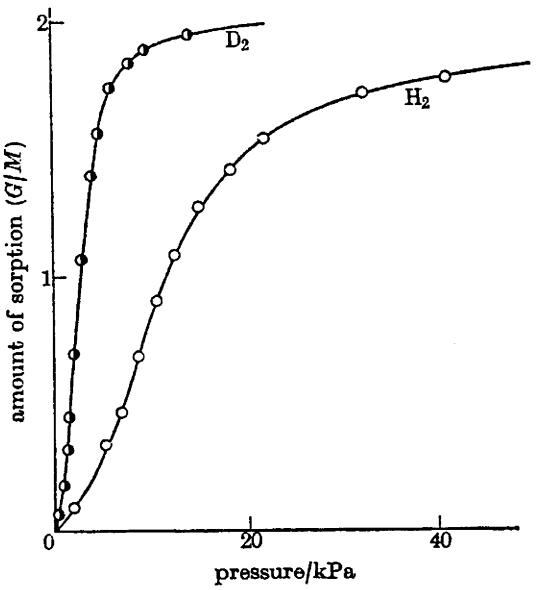

Figure 1.14: *The Type II isotherm, from the $K(D_2)_xC_{24}$ and $K(H_2)_xC_{24}$ systems at 90 K. Note the much more rapid sorption of deuterium. Reproduced from Watanabe et al*[24].

The conclusion was that the Type II and III isotherms were associated with systems where a significant expansion of the interlayer distance between the graphene sheets is required for sorption, while the Type I or Langmuir isotherms were associated with the systems with relatively smaller gas molecules compared to the alkali-metal ions[24].

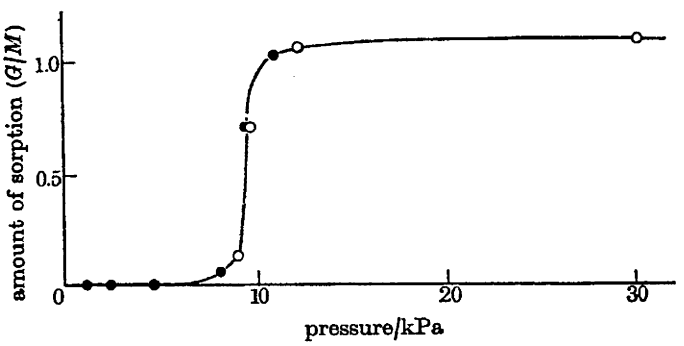

Figure 1.15: *The Type III isotherm, from the $Cs(CH_4)_xC_{24}$ system at 161 K. Reproduced from Watanabe et al*[24].

Tables 1.4 and 1.5 show the equilibrium pressure at half coverage and the isosteric heat of absorption at half coverage respectively, again taken directly from the original paper, where it was noted that the decrease in equilibrium pressure with increasing alkali-

ion size for each gas could be explained by the increase in the heat of sorption for the same sequence.

Further experiments determined that the stage-III GIC KC_{36} possessed sorptive properties and isotherm types for hydrogen and deuterium that were similar to that for KC_{24} except for the maximum amount of gas absorbed. Absorption from binary gas mixtures on KC_{24} and KC_{36} found that the D_2/Ar system absorbed only deuterium, while the D_2/N_2 saw simultaneous absorption of both gases, with greater absorption of N_2 than was found in the $K(N_2)_xC_{24}$ system at the same temperature (77 K); most interestingly, the D_2/H_2 system absorbed the deuterium preferentially over the hydrogen.

	H_2	D_2	N_2	Ar	CH_4
KC_{24}	12.0	2.5	-	-	-
RbC_{24}	$4.9x10^{-1}$	$1.2x10^{-1}$	$(1.0x10^{-5})$	9.7	$3.5x10^{-1}$
CsC_{24}	$1.7x10^{-1}$	$5.5x10^{-2}$	$(1.3x10^{-7})$	$1.0x10^{-2}$	$(7.3x10^{-5})$

Table 1.4: *Equilibrium Pressure in kPa at Half Coverage at 90 K for alkali-metal-gas graphite systems. After Watanabe et. al*[24].

	H_2	D_2	N_2	Ar	CH_4
KC_{24}	9	11	-	-	-
RbC_{24}	11	12	23	11	13
CsC_{24}	12	13	26	15	20

Table 1.5: *Isosteric Heat of Sorption, -Δ@H/kJ mol-1 at Half Coverage for alkali-metal-gas graphite systems. After Watanabe et. al*[24].

In an attempt to determine the *c*-axis structure, neutron diffraction experiments were undertaken on the $K(D_2)_xC_{24}$ system[24]; they found that the c-axis d-spacing expands from 8.67 Å to 8.96 Å at saturation, but were unable to determine the orientation of the deuterium molecules with respect to the graphene layers.

1.3 Further Studies on Physisorbed Ternary GICs

Beyond the original work, published studies of these physisorbed ternaries have tended to be directed specifically to particular compounds. Those studying applications of these compounds have focused upon the hydrogen/deuterium absorption by KC_{25}, which presents useful possibilities in hydrogen storage and isotopic refinement[25-35]. Those interested in observation of molecular tunnelling have concerned themselves with systems containing H_2, D_2 and CH_4, since molecules containing hydrogen atoms have large

incoherent scattering cross-sections, which allow the hydrogen rotors to be easily distinguished from the much more weakly scattering host[36-39]. Those pursuing structural studies have tended to employ the larger absorbed molecules[40-42], such as methane or nitrogen, which have adequate structure factors for X-ray diffraction methods, or have used other molecules that have been found to physisorb at higher temperatures, such as n-hexane[43]. No published work on the alkali-metal-argon GICs could be found apart from the original papers.

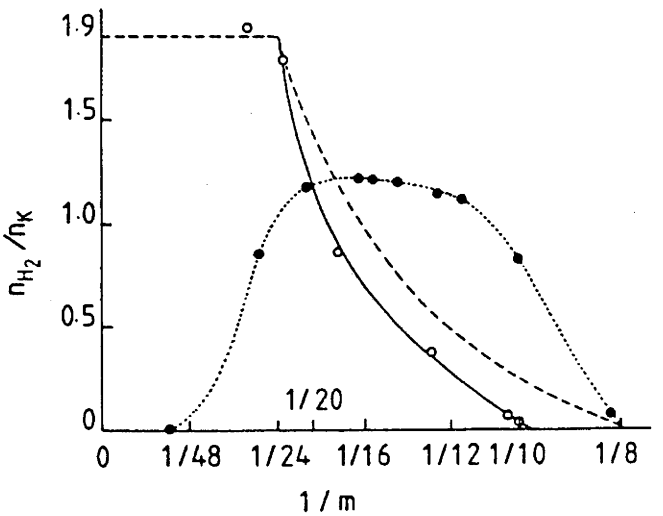

Figure 1.16: *The saturation ratio of physisorbed hydrogen to potassium n_{H_2}/n_K for a series of GICs of stoichiometry KC_m, where m varies between 8 and 48 as shown. The GICs were produced from a) solid circles and dotted lines, coke heat treated at 1250 °C and b) empty circles and solid line, coke heat-treated at 2000 °C. Reproduced from Enoki et al[27] from data originating in Lagrange et al[35].*

Further studies of hydrogen absorption[27, 35] have investigated alkali-metal GICs produced from sources of graphite cheaper than pyrolytic graphite, such as heat treated petroleum cokes. They have found that sorptive properties of a GIC are strongly influenced by the nature of the carbon from which the intercalation compound was produced. Figure 1.15 shows the maximum hydrogen sorption achieved by potassium-GICs of varying K:C stoichiometry, based on cokes produced at 1250 °C and 2000 °C. The sorption of the sample based on the lower-temperature carbon shows a different shape and maximum sorption, having the ability to absorb significant amounts of H_2 at much lower K:C ratios than the higher temperature material. Later studies found that the preferential absorption of deuterium was also a function of graphite origin, concluding that the material with the best potential for isotopic separation was KC_{12} produced from petroleum coke heat-treated at 1500 °C; preferential absorption of tritiated hydrogen (HT)

over H_2 was also found [30]. It was also noted that CsC_{24} would be the best choice as a getter in a cryosorption pump, due to its low equilibrium pressure for hydrogen.

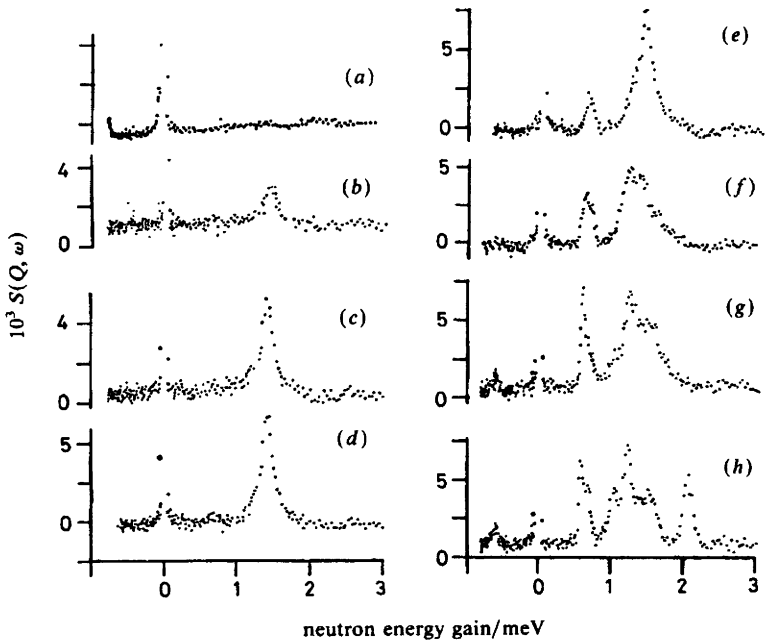

Figure 1.17: *The inelastic neutron scattering spectrum of a $Rb(H_2)_xC_{25}$ sample for a) x=0.0, b) x=0.30, c) x=0.59, d) x=0.89, e) x=1.19, f) x=1.48, g) x=1.78, h) x=2.00. The peak at 0.0 meV is the elastic scattering reflection; the other peaks are produced by the rotational tunnelling of the hindered hydrogen molecules. Reproduced from Stead et al*[39]

Inelastic neutron spectroscopic studies of the $Rb(H_2)_xC_{25}$ system at 5 K [39] found that there was a single tunnelling peak at 1.4 meV which grew steadily in intensity up to x=0.89, that an extra peak at 0.7 meV appeared by x=1.19; at greater fillings the peaks began to broaden, giving the appearance of unresolved structure; at x=2.00 a strong new peak appears at 2.05 meV. These results are shown in Figure 1.16. The peaks at 1.4 meV and 0.7 meV were attributed to the hydrogen molecules preferentially filling two different vacancies in the $\sqrt{43}x\sqrt{43}$ RbC_{25} lattice shown in Figure 1.11; firstly the triangular vacancies in the hexagonal $\sqrt{7}x\sqrt{7}$ domains are filled, secondly the $2x\sqrt{7}$ vacancies in the domain walls. The new and less well-resolved peaks that appear at and above x=1.48 are attributed to a reconstruction of the rubidium in-plane lattice into an unknown structure. Inelastic neutron scattering from $Cs(H_2)C_{27}$ found that a similar two-site model could explain the data at low hydrogen filling, again with the appearance of unexplained new peaks, and thus a possible reconstruction of the *ab*-plane lattice, at higher hydrogen fillings[44, 45].

The only published analysis of the *ab*-plane structure of a hydrogen-alkali-metal-GIC is a neutron diffraction study of the $Rb(D_2)_{0.2}C_{24}$ system. The binary GIC was produced from pyrolytic graphite; the sample was aligned so that the neutron elastic scattering vector was parallel to the *ab*-plane of the sample, with the result that the diffraction pattern would contain only (*hk0*) peaks, rather than the very strong (*00l*) series produced by the *c*-axis structure. The conclusions from the neutron studies were that the deuterium molecules were randomly decorating the triangular interstitial sites of a hexagonal structure of alkali-metal ions[46].

A single study[32] measured the change in resistivity in a $Rb(H_2)_xC_{24}$ sample as hydrogen was absorbed, observing that while the resistance steadily rose there was a minimum at $x \approx 1$. The authors concluded that an ordered superstructure was forming near a stoichiometry of $Rb(H_2)_{1.0}C_{24}$.

A series of experiments on $K(N_2)_xC_{25}$ and $Rb(N_2)_xC_{25}$ were made using the novel technique of nuclear-resonant photon scattering, where by measuring the change in the photon scattering cross section - which is produced by Doppler broadening of the nuclear level in ^{15}N by the molecule's internal zero-point vibrational motion - one can determine the orientation of the molecule with respect to the photon beam. This was used to determine the orientation of the intercalated nitrogen molecules in a sample produced from HOPG; it was found that in both systems the molecules were oriented with the axis parallel to the graphite planes[40, 41, 47].

The $Cs(CH_4)_xC_{27}$ system has been the subject of rotational tunnelling and structural experiments and considerable molecular dynamics modelling. The tunnelling studies found a relatively featureless spectrum, with a broad peak at 25 meV in the librational energy region[36]; this was in agreement with a MD calculation which showed the methane molecule centred in the triangular interstitial sites in the cesium $\sqrt{7}x\sqrt{7}$ domains[48, 49]. Two separate groups[42, 50] have used neutron powder diffraction to study the structure of $Cs(CH_4)_xC_{27}$; because both of these studies used powdered samples rather than oriented HOPG the diffraction patterns, one of which is shown in Figure 1.17, were dominated by the c-axis peaks. Both studies concluded that the low temperature $Cs(CH_4)_xC_{27}$ structure contained at least two phases: in the earlier study[50] a phase was identified as containing methane in the interstitial sites of a $\sqrt{7}x\sqrt{7}$ lattice; the later study[42] found that at and beneath 167 K the sample consisted of a ternary phase containing the methane as well as binary material, while at 187 K the sample was an interstitial solid solution at all fillings.

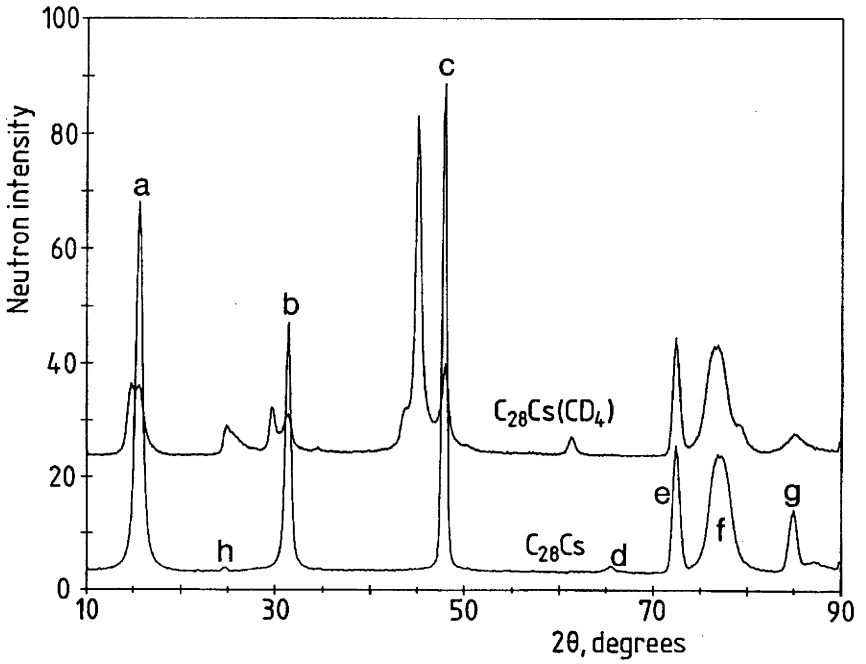

Figure 1.17: *the neutron powder diffraction patterns of CsC_{28} and $Cs(CD_4)_xC_{28}$ at 5 K. The labelled peaks are all part of the CsC_{28} pattern: a) (001), b) (002), c) (003), d) (004), e) the (100) of the graphite lattice, f) The graphite (101), g) (005), h) assigned as stage 1 impurity. Reproduced from Trouw et al*[50].

Similar behaviour to the low temperature phase separation in $Cs(CH_4)_xC_{27}$ has been seen in the physisorption of n-hexane in CsC_{24}, which takes place at 300 K[43]. In this compound there is a phase separation into a stage 2 ternary compound and a stage 1 binary. The $Cs(C_2H_4)_xC_{24}$ system has also been observed through x-ray powder diffraction to phase separate into a stage 1 binary and stage 2 ternary at x=1.1, though by saturation at x=2.1 the compound is a single stage 1 ternary phase[51].

1.4 Directions for this work

While there have been a number of studies of the physisorbed ternaries GICs described by the original workers, structural knowledge of the compounds has been limited to analysis of the *c*-axis structure. This seems to be primarily a result of the problems of powder diffraction: most structural experiments on these compounds appear to have used powdered samples, which are easier to produce than single crystals. While single crystals of GICs can be prepared, there is no reason to expect that the ternary GIC after physisorption will still be a single crystal, especially if a phase transition takes place.

In a pure powder diffraction experiment of graphite or one of its derivative intercalation compounds, the layered *c*-axis structure has such a large structure factor that it will be the dominant feature of the diffraction pattern. Neutron diffraction has the advantage that the adsorbed ternary guest has a scattering factor of similar order as the alkali metal ions, and will thus have a significant contribution to the diffraction pattern, whereas with x-ray diffraction the alkali metal ions will be much stronger scatterers, such that in the hydrogen- or deuterium-based compounds the ternary guests will be effectively masked in an x-ray diffraction pattern.

While the *ab*-plane structure of the guest molecules in a GIC will be very weak in a pure powder diffraction pattern, there is the possibility of using a sample made from a pyrolytic or similar graphite, where the bulk material consists of many platelets with a random *ab*-plane orientation but with a common *c*-axis direction. By aligning the sample so that the momentum transfer of the scattering vector is in the *ab*-plane of the sample, the diffraction pattern observed will primarily consist of the (hk0) reflections, a procedure used in several of the papers described above.

	H_2	D_2	CH_4	N_2	Ar
Mass	2	4	16	28	40
Diameter (Å)	2.4	2.4	4.0	3.0	3.8
Polarizability ($x10^{-24}$ cm^3)	0.8042	0.7954	2.593	1.7403	1.6411
Quadrupole Moment ($x10^{-40}$ Cm^2)	2.17	2.14	0	-4.67	0

Table 1.6: *relevant physical properties of the physisorbed species that will be studied in this thesis*[24, 52, 53].

In this thesis we determine the *ab*-plane structures of many of the stage 2 ternary alkali-metal graphite intercalation compounds found in the early work of Watanabe et. al.[24], via the technique of x-ray powder diffraction of aligned GICs. While x-ray diffraction will emphasise the scattering contributions of the alkali metal ions over that of the physisorbed molecules, it is proposed that the observed modifications of the alkali metal ion lattice should allow us to determine the positions of the ternary guests. The cesium GIC ternaries will not be studied, because the very high x-ray absorption of Cs presents problems in the gathering of experimental data with the experimental

arrangement we employed. Therefore, the compounds investigated will be the hydrogen, deuterium and nitrogen ternaries of K-GIC, and the argon, nitrogen, methane, hydrogen and deuterium ternaries of Rb-GIC.

The second chapter of this work will describe the diffraction theory employed in analysing and modelling the experimental data; the third chapter the preparation of the samples and the design and reconstruction of the x-ray diffractometer used to gather the data. The fourth chapter gives the data analysis and provides structural models to reproduce the diffraction patterns, while the fifth and final chapter will discuss these results and compare them with previous studies.

References

1. H.-P. Boehm, R. Setton, and E. Stumpp, *Nomenclature and Terminology of Graphite Intercalation Compounds (IUPAC Recommendations 1994).* Pure and Applied Chemistry, 1994. **66**: p. 1893-1901.

2. G. Kirczenow, *Staging and Kinetics*, in *Graphite Intercalation Compounds I Structure and Dynamics*, H. Zabel and S.A. Solin, Editors. 1990, Springer-Verlag: Berlin. p. 59-100.

3. J.E. Fischer, *Electronic Properties of Graphite Intercalation Compounds*, in *Intercalated Layered Materials*, F. Levy, Editor. 1979, D. Riedel Publishing Company: Dordrecht. p. 481-532.

4. R. Setton, *Ternary Systems*, in *Graphite Intercalation Compounds I Structure and Dynamics*, H. Zabel and S.A. Solin, Editors. 1990, Springer-Verlag: Berlin. p. 305-345.

5. H. Zabel and S.A. Solin, *Introduction*, in *Graphite Intercalation Compounds I Structure and Dynamics*, H. Zabel and S.A. Solin, Editors. 1990, Springer-Verlag: Berlin. p. 1-3.

6. D.E. Nixon and G.S. Parry, *Formation and Structure of the Potassium Graphites.* Journal of Physics D, 1968. **1**: p. 291-298.

7. A. Herold, *Crystallo-Chemistry of Carbon Intercalation Compounds*, in *Intercalated Layered Materials*, F. Levy, Editor. 1979, D. Riedel Publishing Company: Dordrecht. p. 321-422.

8. S.C. Moss and R. Moret, *Structural Properties and Phase Transitions*, in *Graphite Intercalation Compounds I Structure and Dynamics*, H. Zabel and S.A. Solin, Editors. 1990, Springer-Verlag: Berlin. p. 5-58.

9. T. Janssen, A. Janner, A. Looijenga-Vos, and P.M. de Wolff, *Incommensurate and commensurate modulated structures*, in *International Tables for Crystallography,*

Volume C: Mathematical, Physical and Chemical Tables, A.J.C. Wilson, Editor. 1992, Kluwer Academic Publishers: Dordrecht. p. 797-835.

10. D. Hwang, *Microscopic Properties of Graphite Intercalation Coumponds*, in *Graphite Intercalation Compounds I Structure and Dynamics*, H. Zabel and S.A. Solin, Editors. 1990, Springer-Verlag: Berlin. p. 247-281.

11. H. Homma and R. Clarke, *Structural Phase Transitions in $SbCl_5$-intercalated Graphite.* Physical Review B, 1985. **31**: p. 5865-5877.

12. M.J. Winokur and R. Clarke, *Pinned Incommensurate Structure of Cesium Intercalated Graphite.* Physical Review Letters, 1985. **54**(8): p. 811-814.

13. M. Mori, S.C. Moss, Y.M. Jan, and H. Zabel, *Mass- and charge-density modulation of graphite in potassium-graphite intercalates.* Physical Review B, 1982. **25**(2): p. 1287-1296.

14. M. Suzuki and H. Suematsu, *A Model for In-Plane Structure of High-Stage Alkali-Metal Graphite Intercalation Compounds.* Journal of the Physical Society of Japan, 1983. **52**(8): p. 2761-2768.

15. R. Clarke, J.N. Gray, H. Homma, and M.J. Winokur, *Evidence for Discommensurations in Graphite Intercalation Compounds.* Physical Review Letters, 1981. **47**(19): p. 1407-1410.

16. G.R.S. Naylor and J.W. White, *Structure of Second Stage Graphite-Rubidium, $C_{24}Rb$.* Journal of the Chemical Society, Faraday Transactions, 1987. **83(11)**: p. 3447-3458.

17. L. Duclaux, I. Rannou, S. Delpeux, M. Lelaurain, and F. Beguin, *Determination of the Low Temperature Structures of the Second Stage Cesium Graphitide.* Journal of Physics and Chemistry of Solids, 1996. **57**(6-8): p. 733-740.

18. M.J. Winokur and R. Clarke, *Low-temperature structural transition in KC_{24}.* Phys. Rev. B, 1986. **34**(7): p. 4948-4951.

19. F. Rousseaux, R. Moret, D. Guerard, and P. Langrange, *X-ray study of the liquid and solid phases of the alkali metals in KC_{24}- and RbC_{24}-intercalated graphite single crystals.* Phys. Rev. B., 1990. **42**(1): p. 725-742.

20. P.C. Chow and H. Zabel, *Compositional modulation of K-Rb mixtures in graphite.* Physical Review B, 1987. **35**(7): p. 3663-3666.

21. S.A. Solin and H. Zabel, *The physics of ternary graphite intercalation compounds.* Advances in Physics, 1988. **37**: p. 87-254.

22. K. Watanabe, T. Kondow, T. Onishi, and K. Tamaru, *Sorption of Molecular Hydrogen by Potassium Graphite.* Nature Physical Science, 1971. **233**: p. 160-161.

23. K. Watanabe, T. Kondow, T. Onishi, and K. Tamaru, *Molecular-Sieve Type Sorption on Alkali Graphites.* Chemistry Letters, 1972: p. 477-478.

24. K. Watanabe, T. Kondow, M. Soma, T. Onishi, and K. Tamaru, *Molecular-sieve type sorption on alkali graphite intercalation compounds.* Proceedings of the Royal Society of London A, 1973. **333**: p. 51-67.

25. N. Akuzawa, K. Katano, Y. Ohmura, T. Konishi, T. Amemiya, T. Terai, and Y. Takahashi, *Application of Alkali Metal-Graphite Intercalation Compounds to Cryosorption Material for Hydrogen Isotopes.* Tanso, 1988. **133**: p. 100-104.

26. N. Akuzawa, T. Sakamoto, H. Fujimoto, T. Kasuu, and Y. Takahashi, *Hydrogen physisorption by potassium-graphite intercalation compounds prepared from mesocarbon microbeads.* Synthetic Metals, 1995. **73**: p. 41-44.

27. T. Enoki, S. Miyajima, M. Sano, and H. Inokuchi, *Hydrogen-alkali-metal-graphite ternary intercalation compounds.* Journal of Materials Research, 1990. **5**(2): p. 435-465.

28. K. Ichimura and E. Takamura, *Hydrogen in alkali-metal-graphite intercalation compounds.* Synthetic Metals, 1991. **40**: p. 355-368.

29. T. Terai and Y. Takahashi, *Sorption of hydrogen isotopes on potassium-carbon intercalation compounds at low temperatures.* Synthetic Metals, 1983. **7**: p. 49-55.

30. T. Terai and Y. Takahashi, *Storage and isotope separation of hydrogen by alkali metal-graphite intercalation compounds.* Material Science Forum, 1992. **91-93**: p. 839-848.

31. T. Terai and Y. Takahashi, *Sorption behaviour of hydrogen gas and tritiated hydrogen gas on potassium-carbon intercalation compounds.* Carbon, 1984. **22**(1): p. 91-95.

32. Y. Tomono, S. Sato, T. Kondow, and Y. Tanokura, *Hydrogen absorption process by graphite intercalation compound $C_{24}Rb$ at liquid nitrogen temperature.* Synthetic Metals, 1988. **25**: p. 385-391.

33. P. Lagrange, A. Metrot, and A. Herold, *Physisorption de l'hydrogene sur le compose KC_{24}.* Comptes Rendus de l'Academie des Sciences Paris, Serie C, 1972. **275**: p. 765-767.

34. P. Lagrange and A. Herold, *Physisorption de l'hydrogene par les produits d'insertion du potassium dans les carbones imparfaitement organises.* Comptes Rendus de l'Academie des Sciences Paris, Serie C, 1975. **281**: p. 381-384.

35. P. Lagrange, M.-H. Portmann, and A. Herold, *Physisorption selective du protium et du deuterium par le compose d'insertion KC_{24}.* Comptes Rendus de l'Academie des Sciences Paris, Serie C, 1976. **283**: p. 511-514.

36. F.R. Trouw and J.W. White, *Dynamics of Intercalated Molecules, Part 4- Neutron Inelastic Scattering from Methane in $C_{28}Cs(CH_4)$.* Journal of the Chemical Society, Faraday Transactions 2, 1988. **84**: p. 861-884.

37. J.P. Beaufils, T. Crowley, T. Rayment, R.K. Thomas, and J.W. White, *Tunnelling of hydrogen in alkali metal intercalation compounds I: $C_{25}Rb(H_2)_x$ and $C_{24}Cs(H_2)_x$.* Molecular Physics, 1981. **44**: p. 1257-1269.

38. P.R. Hirst, J.W. White, Z.A. Bowden, L.M. Needham, and A.D. Taylor, *High-energy neutron inelastic scattering from H_2 in $C_{28}Cs(H_2)_{1.52}$.* Chemical Physics Letters, 1988. **147**(2,3): p. 228-230.

39. W.J. Stead, I.P. Jackson, J. McCaffrey, and J.W. White, *Tunnelling of Hydrogen in Alkali-Metal-Graphite Intercalation Compounds - A Systematic Study of $C_{24}Rb(H_2)_x$ and its Structural Consequences.* Journal of the Chemical Society, Faraday Transactions, 1988. **84(10)**: p. 1669-1682.

40. R. Moreh, H. Pinto, Y. Finkelstein, V. Volterra, Y. Birenbaum, and F. Beguin, *Oriented N_2 molecules intercalated in $C_{24}Rb$.* Physical Review B, 1995. **52**(7): p. 5330-5334.

41. R. Moreh, S. Melloul, and H. Zabel, *Orientation of molecularly intercalated N_2 in C_{24} K.* Physical Review B, 1993. **47 (16)**: p. 10754-10759.

42. H. Pilliere, J.L. Soubeyroux, and F. Beguin, *Influence of Critical Temperature on the Phases Formed During the Intercalation of Methane into CsC_{24}.* Phase Transitions, 1993. **46**: p. 27-39.

43. M. Goldmann, H. Pilliere, and F. Beguin, *High Temperature Physintercalation into the 2nd Stage CsC_{24}.* Synthetic Metals, 1989. **34**.

44. I.P. Jackson and J.W. White, *Domain Mobility and Rotational Tunnelling of Hydrogen in Graphite Intercalates.* Chemical Physics Letters, 1987. **134**(5): p. 397-399.

45. W.J. Stead, P. Meechan, and J.W. White, *Librations of Hydrogen in Stage II Caesium Graphite $C_{24}CS$.* Journal of the Chemical Society, Faraday Transactions, 1988. **84**(10): p. 1655-1688.

46. H. Zabel, J.J. Rush, and A. Magerl, *Elastic Neutron Scattering on $C_{24}Rb(D_2)_x$ in the Dilute Concentration Regime.* Synthetic Metals, 1983. **7**: p. 251-255.

47. R. Moreh, H. Pinto, Y. Finkelstein, and F. Beguin, *Tilt of N_2 Molecules Physintercalated into $C_{24}K$ and $C_{24}Rb$.* Journal of Physics and Chemistry of Solids, 1996. **57**(6-8): p. 909-913.

48. F.R. Trouw and J.W. White, *Dynamics of Intercalated Molecules, Part 1- Sorption Potentials and Structure of $CsC_{24}(CH_4)$.* Journal of the Chemical Society, Faraday Transactions 2, 1988. **84**: p. 791-812.

49. F.R. Trouw and J.W. White, *Dynamics of Intercalated Molecules, Part 2- A Molecular Dynamics Simulation of Methane in 'CsC_{24}'(CH_4).* Journal of the Chemical Society, Faraday Transactions 2, 1988. **84**: p. 813-839.

50. F.R. Trouw and J.W. White, *Dynamics of Intercalated Molecules, Part 3.- Structure of $C_{28}Cs(CD_4)$.* Journal of the Chemical Society, Faraday Transactions A, 1988. **84(7)**: p. 841-859.

51. H. Pilliere, Y. Takahashi, T. Yoneoka, T. Otosake, and N. Akuzawa, *Oligomerization process during the intercalation of ethylene in CsC_{24}.* Synthetic Metals, 1993. **59**: p. 191-199.

52. A.D. Buckingham, *Electric Moments of Molecules*, in *Physical Chemistry: An Advanced Treatise*, D. Henderson, Editor. 1970, Academic Press: New York. p. 349-386.

53. D.R. Lide, ed. *CRC Handbook of Chemistry and Physics*. 78 ed. 1997, CRC Press: Boca Raton.

Chapter 2: Diffraction Theory: The Simulation of Powder Diffraction Patterns Produced by Turbostratically Disordered Crystals

2.1 Introduction

Graphite intercalation compounds - the topic of this work - consist of layers of intercalated guest compounds separated by sheets of carbon atoms, as described in the first chapter. The focus of the x-ray diffraction studies here is the structure of the layers of guest compounds. Except in the Stage 1 GICs, these layers have weak interactions with the adjacent guest layers due to the screening effect of the intervening graphene layers. As a result, the intercalation compound does not form a true 3D crystal, but rather consists of relatively uncorrelated layers which may be considered to be separate crystals one or a few layers thick along the c-axis. This is referred to as "turbostratic" disorder, and techniques to simulate the diffraction patterns produced by turbostratically disordered crystals have been the subject of several studies, from Warren to the sophisticated techniques of Drits and Tchoubar[1]. Here, the approach of Reynolds[2, 3] will be used. This is computationally intensive but mathematically straightforward, and this chapter borrows heavily from that work.

2.2 Bragg Diffraction

Consider a plane of point scatterers, such as atoms, of sufficient proximity with respect to the wavelength of incoming monochromatic radiation that they are effectively a uniform plane. If the angle of incidence θ is the same as the angle of reflection the path difference between the waves will be zero, and all wavefronts at this angle will be in phase. If the angle of reflection is not the same as the angle of incidence, then the path difference will be non-zero, and for any scattering center on the plane there will be another which is π out of phase, resulting in destructive interference. Thus reflection from an infinite plane will only occur when the angles of incidence and reflection are identical. Figure 2.1 constructs the reflection condition from a pair of infinite parallel planes of point scatterers, though the derivation is valid for any number of parallel planes. It is assumed that each plane only reflects a small percentage of the incoming wave and that most of the intensity continues to interact with further planes. Reflection can only take place when the angle of incidence equals the angle of reflection; but there is now an extra condition imposed by interference with the wave reflected from the parallel plane.

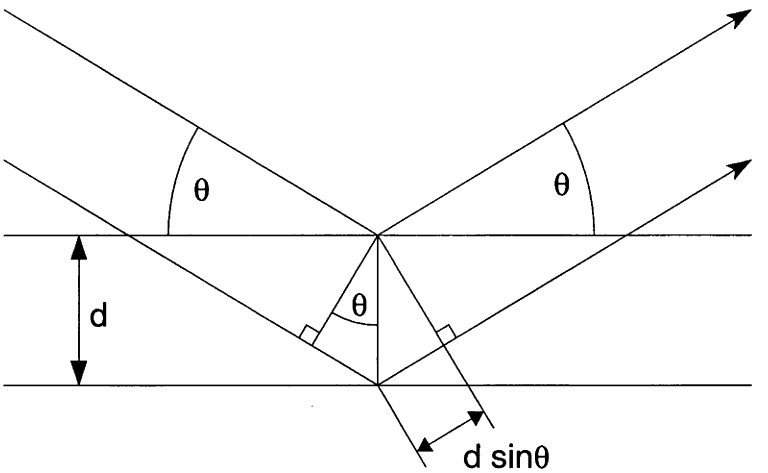

Figure 2.1: *Diagram showing the condition for Bragg diffraction from infinite parallel planes.*

The path difference between the waves reflected from parallel planes is 2dsinθ, where d is the distance between the planes, as shown in Figure 2.1, and this distance must equal an integer number n of wavelengths λ for constructive interference to occur. This results in the Bragg law for diffraction:

$$\frac{2\sin\theta}{\lambda} = \frac{n}{d} \qquad (1)$$

Bragg reflection is only possible for $\lambda \leq 2d$, and thus photons or particles such as x-rays, neutrons and electrons, with a wavelength similar to or less than the distance to be probed, are used for diffraction experiments. From equation (1) one notes the reciprocal relationship between the lattice spacing d and $\sin\theta/\lambda$. This relationship can be understood from the vector condition for diffraction, shown in Figure 2.2[4]. The vectors $\underline{k}_0$ and $\underline{k}$ are the incident and reflected wavevectors respectively. The scattering vector $\underline{Q}=\underline{k}_0-\underline{k}$ is the direction of the normal to the reflecting planes from which the vectors $\underline{k}_0$ and $\underline{k}$ were diffracted. It is clear from Figure 2.2 that $|\underline{Q}| \propto 2\sin\theta$; diffraction will only take place when the path difference is $2\pi/l$, and so $|\underline{Q}| = 4\pi\sin\theta/\lambda$. While the Bragg law presents the necessary conditions to specify the angle of diffraction, to determine the intensity of a reflection requires a description of the unit cell, the atomic positions within the cell and the size of the diffracting crystallite to be included in the analysis. The first two elements are included in the structure factor F, while the size of the diffracting crystallite is incorporated in the interference function Φ.

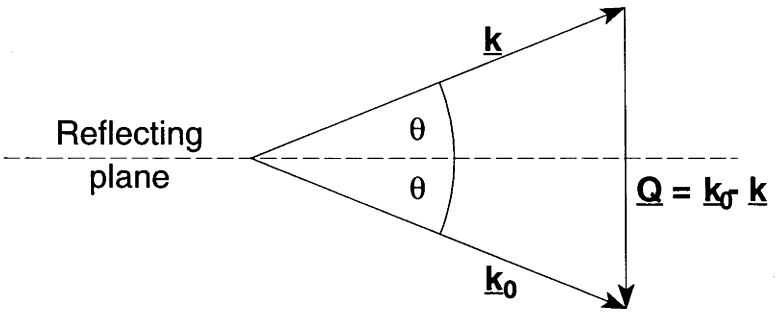

Figure 2.2: *the definition of the vector condition for diffraction, where the scattering vector* $\underline{Q}=\underline{k}_0-\underline{k}$. *After Kittel*[4].

2.3 The Ewald Construction

A reciprocal space description of the condition for Bragg diffraction was proposed by P.P.Ewald, which is shown in Figure 2.3. The reciprocal lattice axes of unit length a*=1/a and b*=1/b are shown, the points in the reciprocal lattice representing diffraction planes hk0. A vector of length 1/λ , joining the points S and T represents the incident beam of radiation.

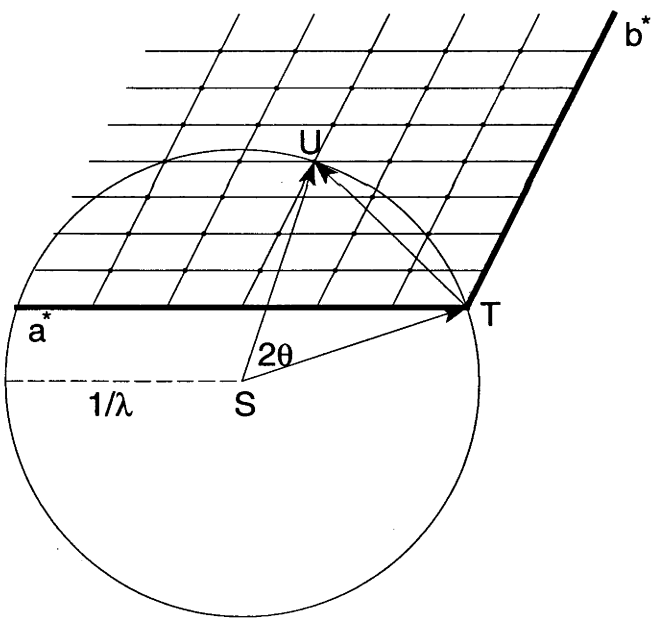

Figure 2.3: *diagram of Ewald's construction of the reciprocal space condition for Bragg diffraction, here showing the condition for the (340) peak of a monoclinic lattice.*

To determine the condition for diffraction, a sphere (a circle in the *hk0* plane) of radius 1/λ is drawn with center S, representing all possible scattering vectors; this sphere is referred to as the sphere of reflection or the Ewald sphere. Diffraction will take place when this sphere intersects a reciprocal lattice point P*(hkl)*, with scattering in the direction

of the vector SU, and the vector TU will be perpendicular to the scattered planes, and of length d* = 1/d*(hkl)*. As the sample rotates with respect to the incident beam, in reciprocal space the vector ST rotates around T, describing a circle. The equivalence of this construction to Bragg diffraction can be shown as follows[5]: given that ST and SU are the incident and reflected waves, the angle TSU must equal 2θ. Therefore the scattering vector

$$TU = 2\ SU\ \sin\theta \tag{2}$$

substituting the lengths of the vectors:

$$d^* = 2(1/\lambda)\sin\theta \tag{3}$$

and as d*=1/d this reduces to the Bragg condition

$$\lambda = 2d\sin\theta \tag{4}$$

Figure 2.3 shows the condition for a single crystal; with a powder sample the reciprocal lattice is rotated around T and the points become circles of radius d*. The reflected radiation is produced in a cone: random orientation of the crystals means that the diffraction condition is satisfied for all azimuthal angles about the incident beam directions ST. The size of the *hkl* domains in reciprocal space is determined by the interference function; with a small or disordered crystal these will be much larger than the point-like domains shown in Figure 2.3. For a turbostratically disordered crystal, which is only one unit cell wide along one cell dimension (usually taken as the *c*-axis) but forms a true crystal along the other two, the reciprocal space hkl domains consist of continuous rods in the *l* direction, with an *h* and *k* size set by the size of the crystallites in the *ab*-plane. As a result of this shape, the interaction of the sphere of reflection with these rods produces an unusual profile shape in powder diffraction patterns. This is characterised by a broad peak with a rapid rise to maximum intensity followed by a much slower drop in intensity as 2θ increases. Simulations of such peaks are shown later in this chapter in Figures 2.11 and 2.12. An explanation of this peak shape, after Brindley (1980)[5], is shown in Figure 2.4 below. In a randomly oriented diffracting powder, the reciprocal lattice must be rotated randomly around T to produce the integrated intensity at 2θ, and a point U (corresponding to a distance 1/d=2sinθ/λ) on this surface describes another sphere as it is rotated around T. The diffracted intensity at 2θ is equivalent to the integrated area of this sphere's intersection with the *hk0* cylinder. This integrated area will increase rapidly as the sphere described by U moves into the *hk* cylinder with the expansion of 2θ, but there

will continue to be a contribution to the scattering even as the point U moves past the Bragg condition for the *hk0* reflection.

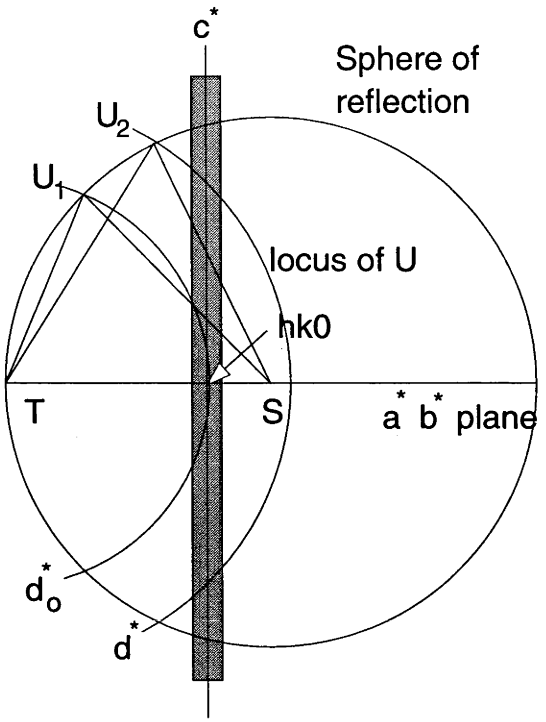

Figure 2.4: *The interaction of the sphere of reflection with the (hk0) cylinder produced by a turbostratically disordered structure. As U moves into the hk0 cylinder at U_1, there is a rapid rise in the diffracted intensity, but a contribution to the intensity continues at U_2, past the 2θ angle of Bragg diffraction for hk0.*

In addition to the (*hk0*) series of rods in (*hk0*) reciprocal space, a turbostratically disordered structure will also produce the (*00l*) series of diffraction peaks arising from planes in reciprocal space, the basal plane c-axis reflections. The reason for this is that while there is no ordering of the ab-plane structure between the different layers of the c-axis stacking, the *c*-axis planes form a well ordered 1-D structure with respect to each other. In the case of graphite intercalation compounds, the peaks of the (*00l*) series are much more intense than those produced by the *ab*-plane structure of the guest compounds, so that in a pure powder sample the diffraction pattern of the basal plane series will dominate the observed pattern.

The GICs used in these studies were produced from a commercial pyrolytic graphite "Papyex", which consists of a sheet aggregate of many small crystalline platelets of graphite, deposited along a common *c*-axis but with random *ab*-plane orientations. This permitted experiments which produced XRD patterns which were dominated by (*hk0*) or (*00l*) reflections, depending on the orientation of the sample. In a powder diffraction

experiment the scattering from the sample is measured in either reflection or transmission mode, as shown in Figure 2.5; in reflection mode the angle θ is measured with respect to the surface of the sample, while in transmission mode θ is taken from the perpendicular to the surface.

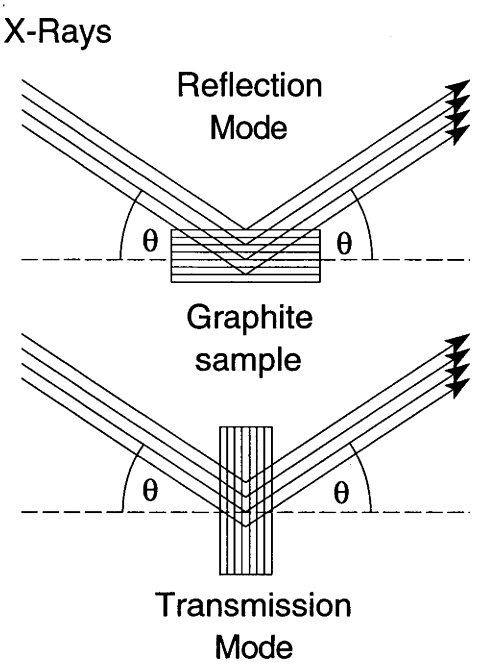

Figure 2.5: *the two sample arrangements used for the GIC samples: in reflection mode the diffraction pattern consists almost entirely of the (00l) series, while in transmission mode the (hk0) peaks dominate the diffraction pattern.*

For a randomly oriented powder sample the choice of reflection or transmission mode makes no difference to the powder diffraction pattern, apart from the absorption corrections. In the case of the highly ordered graphites used in this study, where the c-axis is perpendicular to the surface of the aggregate, the reflection mode will produce a diffraction pattern which is almost entirely (*00l*) c-axis reflections, while in transmission mode the (*hk0*) ab-plane series will dominate. The reason for this is most easily explained in the reciprocal space construction: the scattering vector $\underline{Q}$ connects the ends of the incident and reflected vectors $\underline{k}_0$ and $\underline{k}$. With the highly oriented graphite samples each orientation restricts the planes these vectors can scatter from in the sample - in reflection mode these vectors terminate on (*00l*) points in reciprocal space, while in transmission mode they end in the *ab*-plane, and the scattering vector is limited to the (*hk0*) series. It is only through using such oriented samples that the (*00l*) diffraction pattern is strong enough to permit studies of the *ab*-plane structure.

2.4 The Interference Function

The interference function calculates the scattering effect of the array of unit cells that form a crystal. For example consider a one-dimensional array of cubic unit cells. If there are N such unit cells and the phase difference between the waves diffracted by adjacent cells is F, then the scattered amplitude for entire array of cells is:

$$A = F + Fe^{i\phi} + Fe^{i2\phi} + Fe^{i3\phi} \ldots + Fe^{i(N-1)\phi} \quad (5)$$

reducing this to the geometrical series produces:

$$A = F\,(1 - e^{iN\phi}) / (1 - e^{i\phi}) \quad (6)$$

the actual scattered intensity is $I = A^*A$, where A^* is the complex conjugate of A. The formula for the intensity is thus:

$$I = |F|^2 \frac{(1-e^{iN\phi})(1-e^{-iN\phi})}{(1-e^{i\phi})(1-e^{-i\phi})} \quad (7)$$

replacing this with the equivalent trigonometric terms this reduces to:

$$I = |F|^2 \frac{[1-\cos(N\phi)]}{[1-\cos(\phi)]} \quad (8)$$

and using the relation $2\sin^2 x = 1-\cos(2x)$ this becomes

$$I = |F|^2 \frac{\sin^2(N\phi/2)}{\sin^2(\phi/2)} \quad (9)$$

when ϕ is near a multiple of 2π, which will occur near a Bragg reflection, then $\phi=2\pi(n+l)$ can be substituted:

$$I = |F|^2 \frac{\sin^2(N\pi l)}{N\sin^2(\pi l)} \quad (10)$$

The trigonometric part of equation 10 is the interference function for the (*00l*) series. A factor N has been added to the denominator to normalise the peak area to a constant value.

The complete formula for intensity requires three interference functions, one for h, k and l:

$$I = \frac{Lp(\theta)|F(hkl)|^2}{N_1 N_2 N_3} \frac{\sin^2(N\pi h)}{\sin^2(\pi h)} \frac{\sin^2(N\pi k)}{\sin^2(\pi k)} \frac{\sin^2(N\pi l)}{\sin^2(\pi l)} \qquad (11)$$

This equation contains a new factor: the Lorentz polarization term *Lp*, which includes the polarization effect, a result of the difference in the direction of the electric vector in the incoming x-rays and the direction of scattering, and the Lorentz or angular-velocity factor. Here, the entire *Lp* correction is:

$$Lp = \frac{1+\cos^2 2\theta}{\sin\theta \sin 2\theta} \qquad (12)$$

A post diffraction monochromator, employed in the experimetntal arrangement used, adds another polarization term[6] of the form $p = (1+k\text{Cos}^2 2\theta)/(1+k)$, where $k = \cos^2 2\theta_m$ for a mosaic monochromator with set reflection angle $2\theta_m$.

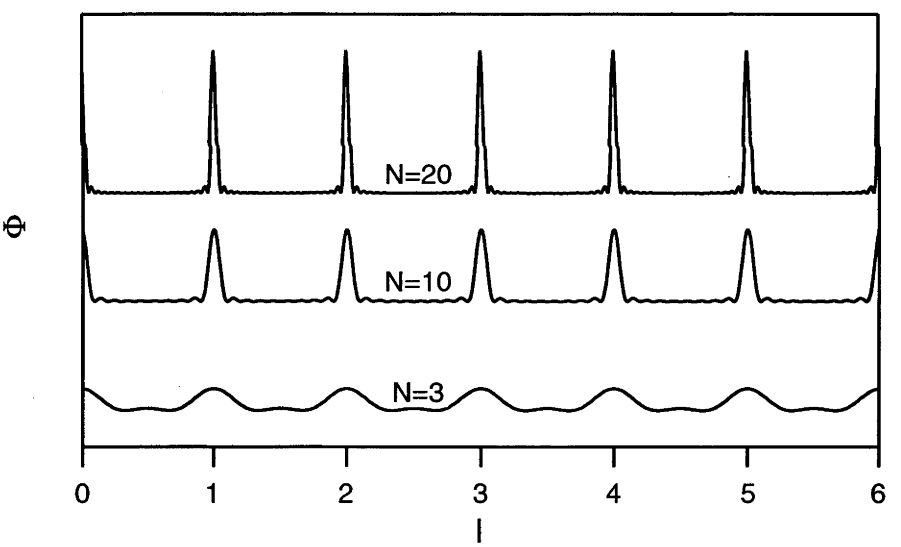

Figure 2.6: *Diagram showing the effect of crystallite size N on the 1-D interference Φ as a function of l. As N increases, the peaks become much higher and narrower. (After Reynolds[2])*

Figure 2.6 plots the 1D interference function Φ from equation (10) as a function of *l*, for N=3, 10 and 20. As N increases, the peaks of the function become narrower and more intense, so that at very high values of N the effect of the interference function on the peak shape is negligible, and the shape of diffracted peaks is dominated by instrumental effects. At low values of N, the function produces broad peaks with significant intensity

at non-integral values of l; at N=1, representing an isolated unit cell, the function $\Phi = 1$ at all values of l, and Bragg diffraction will not take place. As explained above, the *ab*-plane structures studied in this work are either uncorrelated or weakly correlated along the c-axis; effectively these structures are only one layer thick and thus $N_3=1$ for these structures. To simulate the diffraction pattern requires that the calculation of the interference function with non-integral values of h, k and l. The approach used here, taken from Reynolds (1989), uses a reciprocal space computation.

2.5 Diffraction Intensities

The scattering of x-rays by atoms is a function of several processes, primarily coherent (Rayleigh) scattering and incoherent (Compton) scattering as well as thermal, absorption and dispersion effects. Coherent scattering is the result of the interaction of an x-ray with a tightly bound electron, such that the scattering is an elastic process. The intensity of coherent scattering from a single electron of an unpolarized incident beam of photons in a direction θ relative to the incident beam is:

$$I_e = I_o r_e^2 \left[\frac{1+\cos^2 2\theta}{2} \right] \tag{13}$$

where r_e is the classical radius of the electron and I_0 is the intensity of the incident beam[7]. Coherent scattering induces a phase shift of π in the scattered photon. In incoherent scattering the electron is considered to be effectively free, with the result that there is momentum transferred between the photon and the electron, and change in wavelength for the scattered photon, of the form:

$$\Delta\lambda = \frac{2h}{mc}\sin^2\theta \tag{14}$$

The formula for incoherent scattering from a single electron is that same as (13)[7], but with additional correction factor $[\lambda/(\lambda+\Delta\lambda)]^3$ for proportional counters or $[\lambda/(\lambda+\Delta\lambda)]^2$ for scintillation counters[8].

Generalised to the scattering from an atom of atomic number Z, the coherent and incoherent scattering intensities are:

$$I_{coh} = I_e \left(\sum_{j=1}^{Z} f_j \right)^2 \tag{15}$$

$$I_{incoh} = I_e\left(Z - f_j^2 - \sum_{j,k} f_{jk}\right) \tag{16}$$

where $f_j = \int \rho(\mathbf{r}_j) \exp(i\mathbf{Q}\cdot\mathbf{r}_j)\, d\mathbf{r}_j$, $f_{jk} = \int \psi_j^* \psi_k \exp(i\mathbf{Q}\cdot\mathbf{r}_j)\, d\mathbf{r}_j$, $\mathbf{Q} = \underline{k}_0 - \underline{k}$[7].

If all the electrons in an atom were concentrated at a point the scattering factor would be the Fourier transform of a delta function, and would thus be a constant and independent of θ. This is the case for thermal neutron scattering by a nucleus, but the electrons of an atom are distributed over space, and produce a scattering factor which is a function of θ. The scattering intensities of the neutral atoms and the more chemically important ions have been calculated by several techniques and are tabulated in the International Tables for Crystallography[7]. Interpolation to these calculated intensities allows an analytical approximation to be used:

$$f(\sin\theta/\lambda) = \sum_{i=1}^{4} a_i \exp(-b_i \sin^2\theta/\lambda^2) + c \tag{17}$$

where the coefficients a_i, b_i and c are again collected in the International Tables. This analytical approximation was used to calculate the scattering intensities in the simulations that follow. Though they are known to provide a poor fit to the atomic scattering curves outside the range $0 < \sin\theta/\lambda < 2\text{Å}^{-1}$, the diffraction data was taken well within this range.

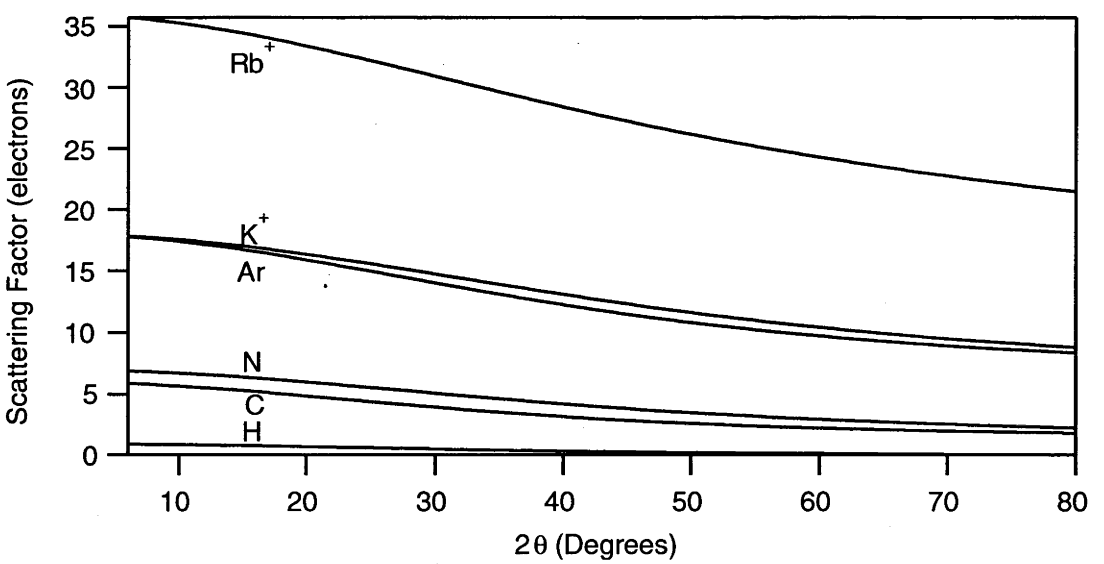

Figure 2.7: *the calculated scattering factors using the analytic approximation[7] for the elements that compose the compounds studied in this work.*

The GICs that were studied in this work are composed of covalently bonded carbon atoms, and rubidium and potassium ions, while the physisorbed ternary species contained argon, nitrogen, carbon and hydrogen atoms. The calculated scattering intensities (in units of the scattering factor of a single electron) of these atoms and ions, over the same range in 2θ that the experimental data covered, is shown in Figure 2.7. These curves are the atomic form factors and reflect not only the number of electrons but the atomic size. The form factors are the Fourier transform of the atomic or ionic electron distribution.

In addition to coherent and incoherent scattering, the scattering intensity of an atom is modified by other terms such as the displacement factor and dispersion correction. While the dispersion correction, which adds an imaginary component to the atomic form factors, is sufficiently small that it can be ignored in these simulations, a displacement or temperature correction must be used. The temperature correction accounts for the vibration of an atom around its mean position; ideally six variables are needed to account for anisotropic harmonic thermal vibrations in three dimensions, but here a simple isotropic Debye-Waller factor of the form:

$$f = f_0 \exp(-B\sin^2\theta / \lambda^2) \tag{18}$$

is included, where B is a single refinable variable of dimensions Å^2. Figure 2.8 shows the effect of a temperature factor B = 2 Å^2 on the scattering factors calculated for Figure 2.7. For a simple Bravais lattice of atoms the diffraction intensities will be proportional to the squares of the scattering factors at the allowed 2θ positions for Bragg diffraction.

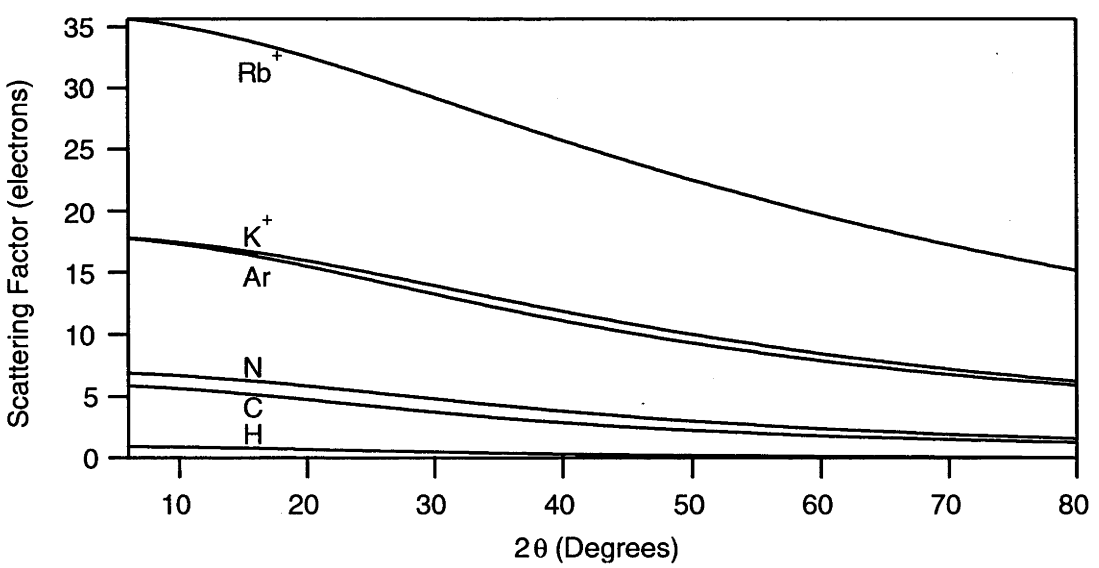

Figure 2.8: *The scattering factors shown in Figure 2.7 with a temperature correction B=2.0 A^2 applied to the calculations. Note the large effect at high 2θ.*

2.6: The Structure Factor

The internal structure of a multi-atom unit cell imposes a further modulation of the scattering intensity at the diffraction angles allowed by the crystalline space group. This modulation is described by the structure factor.

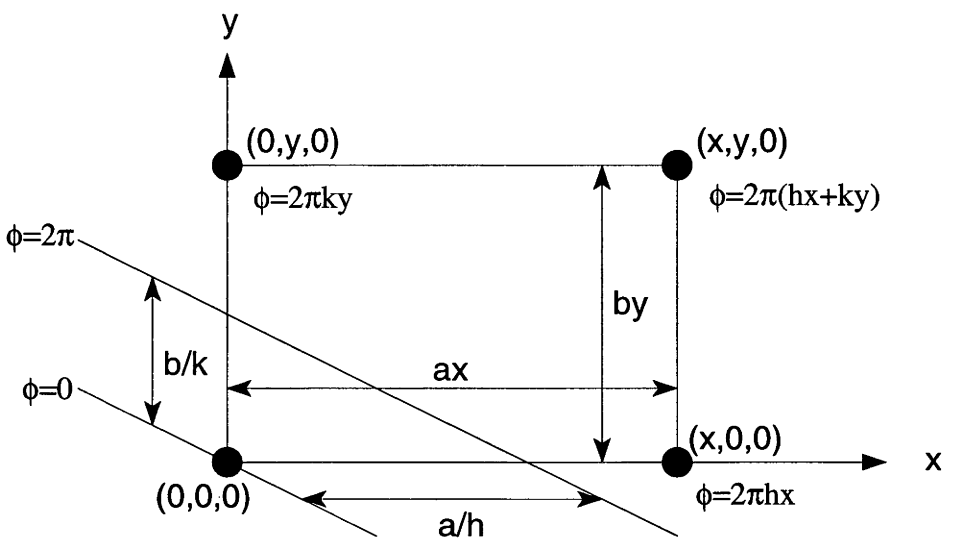

Figure 2.9: *Diagram showing the phase angle ϕ produced by the atoms in the (ab0) plane of a orthorhombic crystal. After McKie&McKie*[9].

To determine the intensity of diffraction peaks, one can begin by considering the interaction of an hkl plane with a simple cell, as shown in Figure 2.8 above. The phase angle ϕ of an hkl plane passing through the origin is set at zero; the next hkl plane from the origin will have ϕ=2π, and will make an intercept on the x-axis at a/h and on the y-axis at b/k. Therefore an atom at a distance *ax* on the x-axis, at a position of (x,0,0) in Figure 2.x, will scatter x-rays with a phase of (2πax)/(a/h)=2πhx into the hkl reflection, and an atom at a distance *by* on the y-axis will scatter x-rays with a phase 2πky[9]. The atom shown at a position (x,y,0) will thus scatter with a phase equal to the addition of the first two: ϕ = 2πhx + 2πky = 2p(hx+ky). For an atom at a position (x,y,z) the phase angle f will thus be:

$$\phi = 2\pi(hx + ky + lz) \tag{19}$$

The scattered wave in the direction hkl will be:

$$\psi(hkl) = f \exp 2\pi\iota(hx + ky + lz) \tag{20}$$

where f is the scattering factor of the atom, which is described below. The total contribution of all the atoms in the unit cell to the hkl reflection is called the structure factor F(*hkl*), and is equal to the sum of waves $\psi(hkl)$ for each atom:

$$F(hkl) = \sum_{n=1}^{N} f_n \exp\left(2\pi i(hx_n + ky_n + lz_n)\right) \tag{21}$$

or alternatively this can be represented by its trigonometric equivalent:

$$F(hkl) = \sum_{n=1}^{N} f_n \cos\left(2\pi(hx_n + ky_n + lz_n)\right) + i\sum_{n=1}^{N} f_n \sin\left(2\pi(hx_n + ky_n + lz_n)\right) \tag{22}$$

This can be simplified where there is a centrosymmetric structure and taking the point of origin as the center of symmetry. In this case every atom at (x,y,z) will have another at (–x,-y,-z), with the result that the imaginary terms of the structure factor are eliminated:

$$F(hkl) = \sum_{n=1}^{N} f_n \cos\left(2\pi(hx_n + ky_n + lz_n)\right) \tag{23}$$

The measured intensity of an *hkl* reflection is proportional to the square of the modulus of the structure amplitude |F(*hkl*)|:

$$I(hkl) \propto |F(hkl)|^2 \tag{24}$$

2.7 Simulation of XRD Patterns from Turbostratically Disordered Structures

The diffraction pattern produced by a turbostratically disordered structure can be divided into two parts, the *ab*-plane (*hk0*) structure and the *c*-axis (*00l*) series. Simulations of these are carried out separately: the (*hk0*) simulations assume a very small crystallite size N_3 (usually 1), while the (*00l*) simulations use a much larger N_3, because the *c*-axis coherence length is the significant factor. The c-axis simulations can be simplified considerably by ignoring the ab-plane structure entirely and only including the interplane spacing in the calculations planes. When dealing with the diffraction data produced by a pure powder sample the two simulated patterns are combined and compared with the data, but given the technique used here produced separate *ab*-plane

and *c*-axis diffractograms the simulations can be compared independently. The method of Reynolds (1989) was used to produce these simulations.

2.7.1 Simulation of the *ab*-plane Pattern

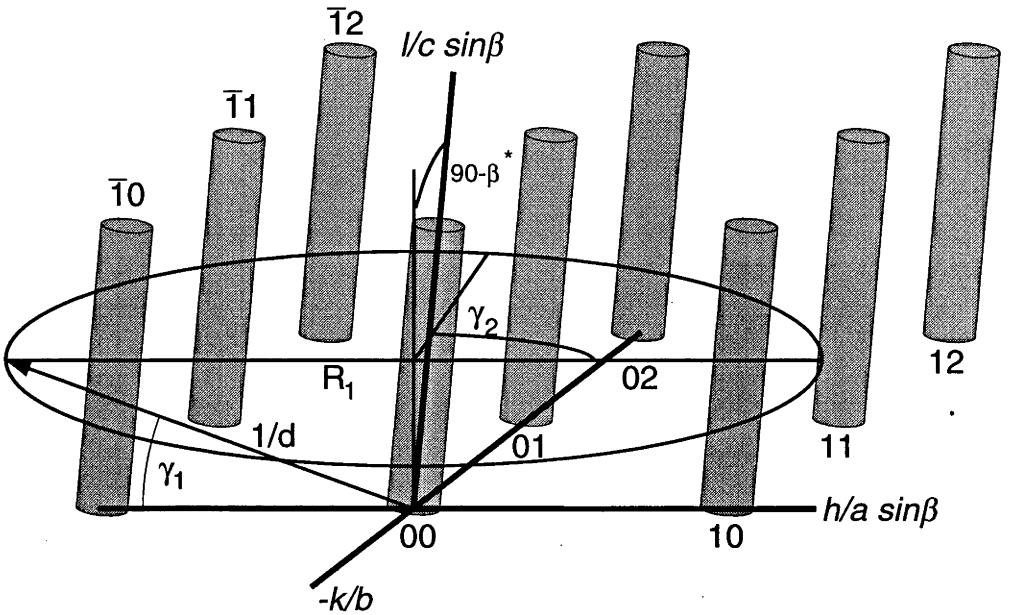

Figure 2.10: *The reciprocal space construction used for Equation 24. The calculated hemisphere of radius 1/d in reciprocal space is shown interacting with the reciprocal space rods produced by a turbostratically disordered compound. After Reynolds*[2].

In producing the simulation of the (*hk0*) diffraction patterns, the technique involves calculating the value of Equation (25) at each increment of 2θ for all values of (*hk0*) that fall on the (hemi-)sphere $1/d=2\sin\theta/\lambda$ in reciprocal space. This summation is shown in Figure 2.10, and proceeds as follows: at an angle 2θ, the reciprocal distance 1/d is calculated; the hemi-sphere is enumerated as a series of circles of radius $R_1=\cos(\gamma_1)/d$, where the angle γ_1 is the angle a radius of the (1/d) sphere makes with the *hk*-plane. At each point of the circle described by γ_2, the values of the continuous functions of h, k and l shown in Equations (27), (28) and (29) are determined, and these values used to calculate the structure factor F(*hk0*) and interference functions Φ_1, Φ_2 and Φ_3 at that point.

$$I = \frac{1+\cos^2 2\theta}{N_1 N_2 N_3 \sin\theta} \sum_{\gamma_1=0}^{\gamma_1=90} 2\pi R_1 \sum_{\gamma_2=0}^{\gamma_2=180} |F(hkl)|^2 \Phi_1 \Phi_2 \Phi_2 \Delta\gamma_1 \Delta\gamma_2 \qquad (25)$$

where

$$\Phi_1 = \frac{\sin^2(\pi h N_1)}{\sin^2(\pi h)}, \quad \Phi_2 = \frac{\sin^2(\pi k N_2)}{\sin^2(\pi k)} \text{ and } \Phi_3 = \frac{\sin^2(\pi l N_3)}{\sin^2(\pi l)} \quad (26)$$

and h, k and l are replaced by the continuous functions:

$$h = a\sin\beta(R_1\cos\gamma_2 - \sin\gamma_1/d\tan\beta^*) \quad (27)$$

$$k = R_1\beta\sin\gamma_2 \quad (28)$$

$$l = (c/d)\sin\gamma_2 \quad (29)$$

where $R_1 = \cos(\gamma_1)/d$, $\beta^* = 180-\beta$, and $d = \lambda/2\sin\theta$.

Figure 2.11 and 2.12 show a number of simulated diffraction patterns. These all use the same crystal structure, a P6 hexagonal lattice of rubidium ions with the ab-plane dimensions a=4.93 Å and the c-axis spacing c=9.0Å between the layers, with the wavelength λ=1.54178 Å. This structure is not chosen at random, it is the structure of a 2x2 hexagonal superlattice of rubidium ions in a stage-II binary GIC, but the diffraction pattern of the graphite is not included in the patterns. The primary difference between the structures used to produce these simulated patterns is the size of the crystallites. In Figure 2.11, the ab-plane crystallite dimensions N_1=N_2=30, while the three patterns are calculated for N_3=1, 5 and 30. At N_3=1, only the *(hk0)* peaks are produced by the simulation, and these now possess the characteristic band shape of a turbostratically disordered structure. In Figure 2.12, N_3=1 for all three simulated patterns, producing the same turbostratic band shapes, while the size of the in-plane crystallite is varied, $N_{1,2}$=10, 20 and 30. This shows the broadening of the peaks as $N_{1,2}$ is decreased, but also that the intensity maximum of the peaks moves to a higher 2θ as $N_{1,2}$ is decreased, a phenomena described by Warren[10], which is a result of the interaction of the sphere of reflection with the broadened *(hk0)* cylinders produced by a small in-plane crystallite.

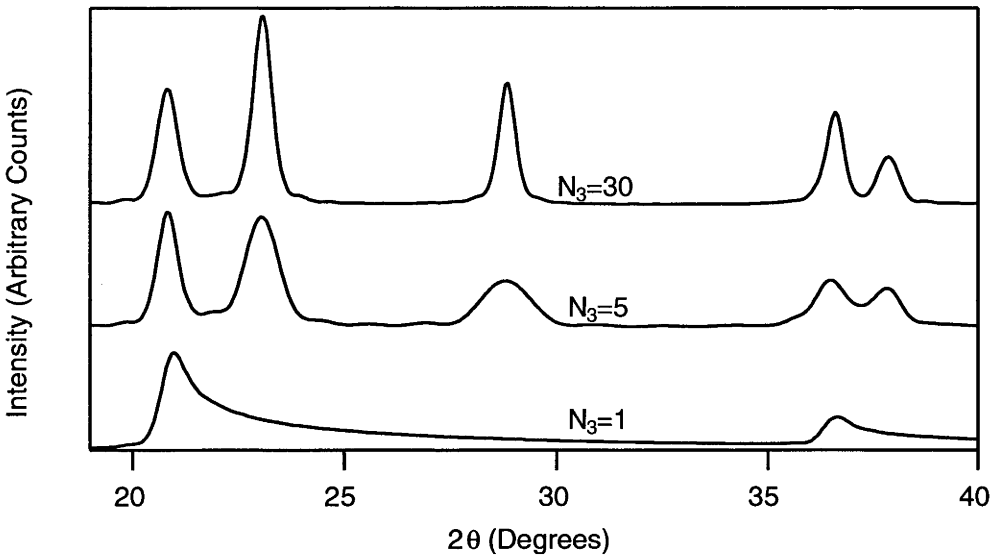

Figure 2.11: *simulated diffraction patterns using crystallites consisting of a hexagonal P6 lattice of rubidium ions, with a=b=4.93Å, c=9.0Å, with a varying c-axis crystallite size N_3, while $N_{1,2}$=30 for all three simulations. The wavelength λ=1.54178Å.*

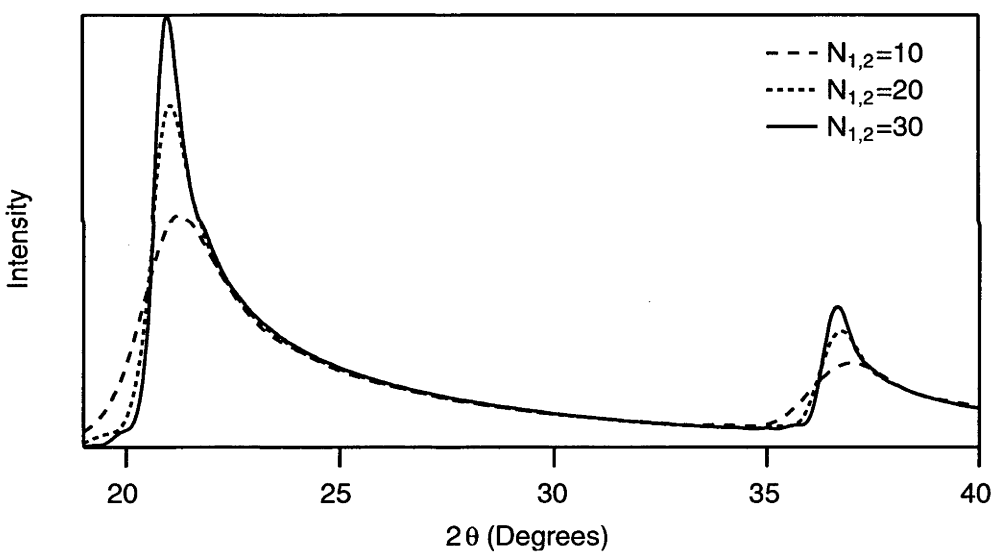

Figure 2.12: *simulated diffraction patterns using crystallites with the same structure as used in Figure 2.11, setting N_3=1 for all three patterns but the in-plane crystallite size $N_{1,2}$ varying as shown. As the size of the in-plane crystallite domain is reduced, the center of the peak shifts away from the true (hk0) position to a higher 2θ.*

While application of the formula for intensity provided by Equation (25) can reproduce the purely turbostratic band shape from an isotropically oriented powder sample, some of the samples studied also included a small degree of interplanar interaction, which caused a significant degree of 3D ordering without producing a fixed c-axis crystallite size N_3.

This was added to the simulation by replacing the interference function Φ_3 with the Fourier series equivalent shown in Equation (30):

$$\Phi_3 = N_3 + 2\sum_{n=1}^{n=N_3-1}(N_3 - n)\cos(2\pi nl) \tag{30}$$

where N_3 is the same crystallite, and n is the number of interfaces separating any two layers in the crystal. Into this equation a negative exponential term is introduced:

$$\Phi_3 = N_3 + 2\sum_{n=1}^{n=N_3-1}(N_3 - n)\exp(-n/\delta)\cos(2\pi nl) \tag{31}$$

where d is the average defect-free distance along the c-axis in each crystallite, in units of number of coherent interfaces[2], and the term exp(-n/δ) is the probability of a defect-free region of n interfaces in the crystallite.

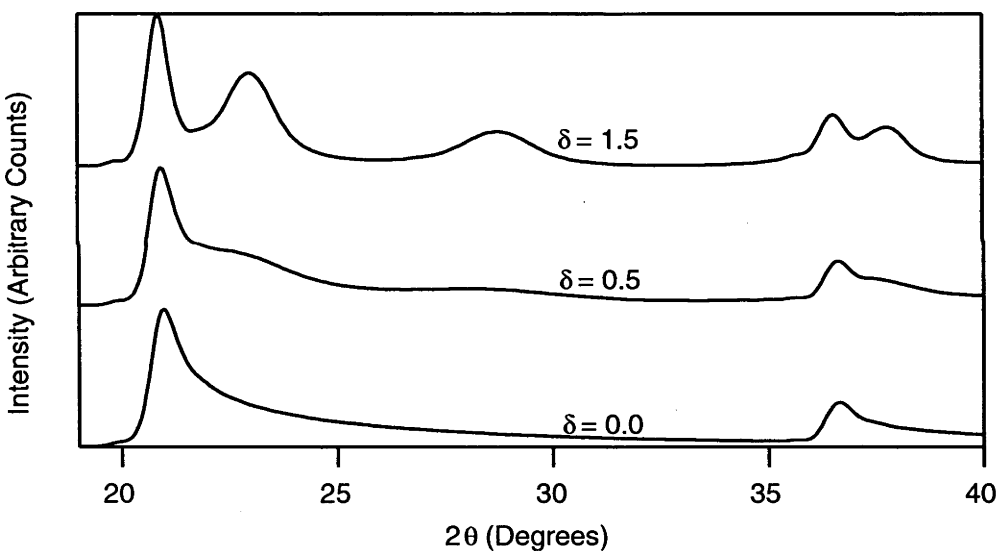

Figure 2.13: *the effect of the ordering parameter δ on the simulated diffraction pattern. Here the same P6 cell as above is used, with $N_{1,2}$=30 and the c-axis crystallite N_3=30, but the alternative interference function Φ_3 in Equation (31) is employed. At δ=0.0 there are no defect-free interfaces along the c-axis, and the pattern is purely turbostratic.*

The effect of this ordering parameter δ on the simulated diffraction pattern is shown in Figure 2.13, where even small values of δ produce considerable changes to the simulated diffraction patterns. At δ=1.5, the probability that any two adjacent layers are 3D ordered is exp(-1/1.5)=0.51, that is, 49% of the layers are not 3D ordered at all and remain in a

purely turbostratic structure, but the diffraction patten has lost many of the characteristic features of the turbostratic pattern produced by δ=0.0.

An additional correction is needed, as Equation (25) assumes a perfect powder distribution, but the diffraction experiments used oriented samples, as described above, to drastically reduce the contribution of the *c*-axis structure to the data. To account for the *ab*-plane oriented samples used in the diffraction experiments, an empirical correction is used to reduce the structure factor F(*hkl*) as l increases, in the same manner as the temperature correction:

$$F(hkl) = F\exp\left(-\mathrm{CD}l^2\right) \tag{32}$$

CD is the c-axis damping factor, which was used as a refinable value in fitting the simulations to the diffraction data. Its effect on the turbostratic peak shape is to suppress the "tail" at high 2θ, as seen in Figure 2.14. It can be thought of as a disorder amplitude in the l direction of the graphene sheet.

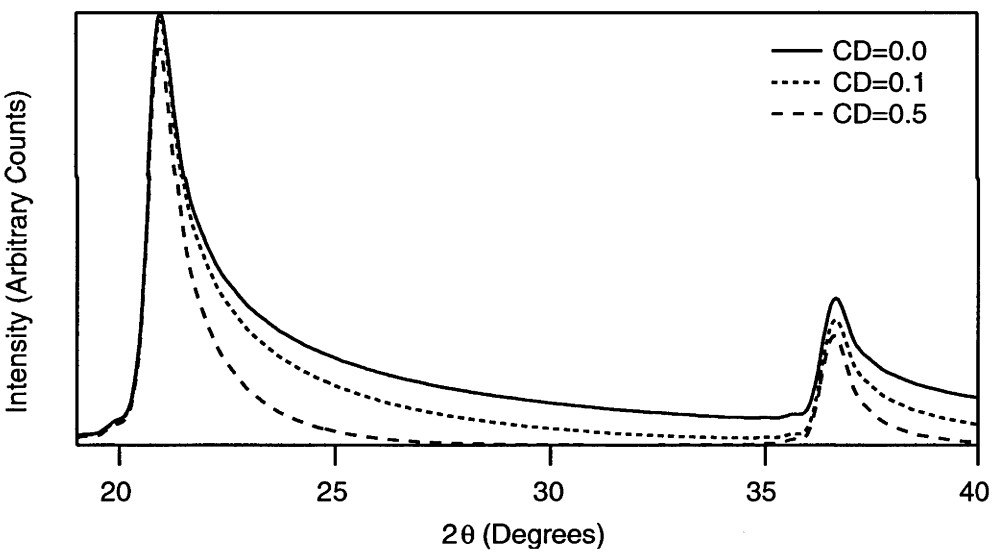

Figure 2.14: *the effect of the c-axis damping factor CD on the turbostratic profile shape. The simulated crystallite has the same P6 unit cell used in the previous simulations, with* $N_{1,2}=30$ *and* $N_3=1$.

2.7.2 Simulation of the *c*-axis Pattern

The c-axis simulations use a similar approach to that taken for the ab-plane pattern, but the simplicity of the (*00l*) series allows a drastic reduction in the complexity of the

mathematics, and the resulting calculations are much faster. The basic form for the intensity function is the same, but is reduced to dependence only on the (*00l*) indices:

$$I(00l) = Lp|F(00l)|^2 F(00l) \tag{33}$$

where Lp is the Lorentz-polarization factor, F(*00l*) is a simplified version of Equation (15),

$$F(00l) = \sum_j n_j f_j \cos\left(2\pi z_j l / D\right) \tag{34}$$

where z_j is expressed in units of Å rather than a fractional and D is the c-axis unit cell dimension, and the interference function Φ(*00l*) uses the Fourier series form of Equation (30)

$$\Phi(00l) = N + 2\sum_{n=1}^{n=N-1}(N-n)\cos(2\pi n l) \tag{35}$$

These can be altered into θ-continuous functions by using the Bragg Law nλ=2dsinθ, letting n=l and substituting l=2dsinθ/λ in both equations:

$$F(\theta) = \sum_j n_j f_j \cos\left(2\pi z_j \sin\theta / \lambda\right) \tag{36}$$

$$\Phi(\theta) = \frac{1}{N}\left(N + 2\sum_{n=1}^{n=N-1}(N-n)\cos\left(2\pi n D \sin\theta / \lambda\right)\right) \tag{37}$$

Simulations using these equations are shown in Figures 2.15 and 2.16, employing a crystallite which only includes *c*-axis positions: a single rubidium ion at z = 0 Å and two layers each of 12.5 carbon atoms at z = 2.825 Å and z = 6.175 Å, which corresponds to a stage 2 rubidium GIC of stoichiometry RbC_{25} and *c*-axis spacing of 9 Å.

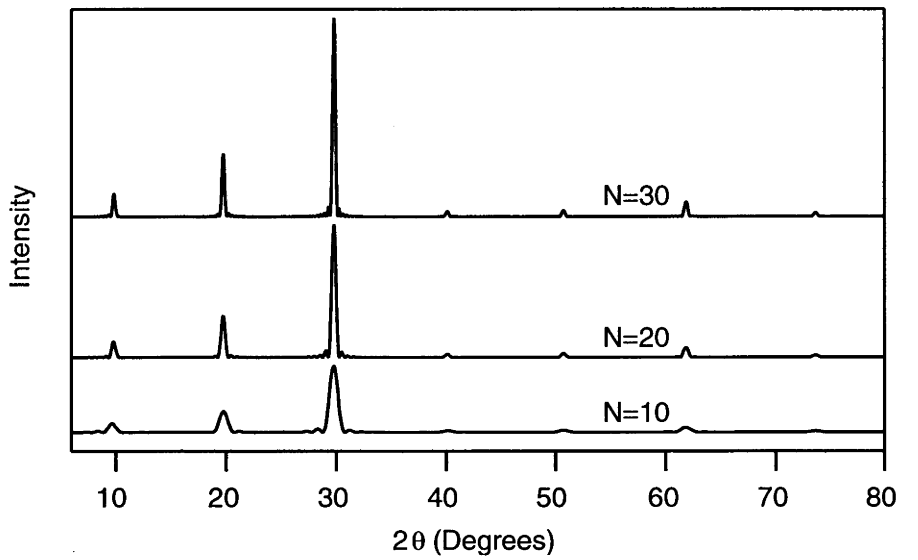

Figure 2.15: *Three simulated c-axis XRD patterns using Equations (36) and (37), for a stage 2 GIC of stoichiometry RbC_{25} and c-axis spacing 9 Å, with the crystallite sizes N = 10, 20 and 30.*

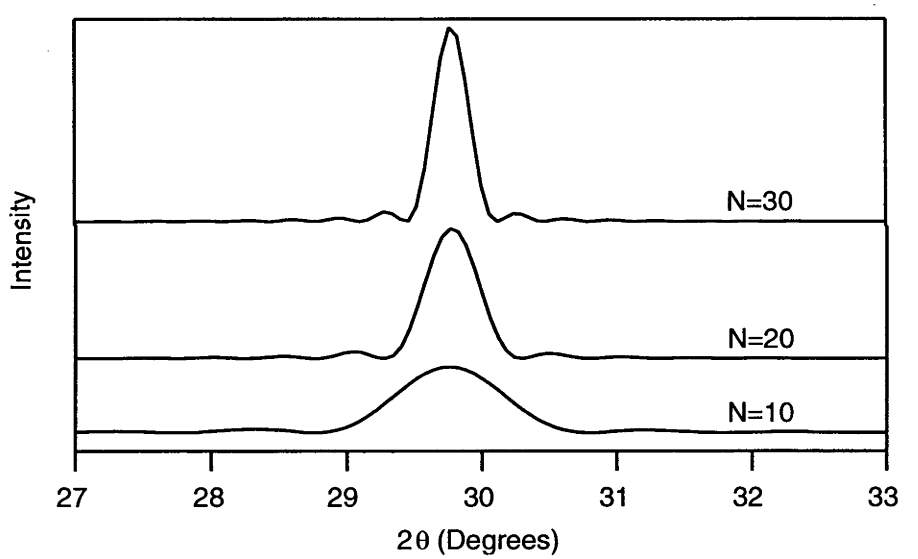

Figure 2.16: *The same three simulated c-axis XRD patterns for a stage 2 GIC of stoichiometry RbC_{25} and c-axis spacing 9 Å shown in Figure 2.15, here showing the region of the (003) diffraction peak.*

The patterns in Figures 2.15 and 2.16 show interference effects bracketing the peaks. That will not be seen in the XRD patterns produced by real crystals of graphite or its intercalation compounds, because they are composed of crystallites of many different sizes, thus smearing the Fourier ringing.

In the same manner as the *ab*-plane simulations, the influence of defects in the *c*-axis stacking can be introduced into the interference function used in Equation (37) by introducing a term of the form exp(-n/δ), producing Equation (38):

$$\Phi(\theta) = \frac{1}{N}\left(N + 2\sum_{n=1}^{n=N-1}(N-n)e^{(-n/\delta)}\cos(2\pi nD\sin\theta/\lambda)\right) \quad (38)$$

The effects of this defect parameter δ, which again is the mean defect-free distance in the stacking, is shown in Figures 2.17 and 2.18. In these simulations, δ is much larger than value used for the equivalent parameter in *ab*-plane simulations, because the (*00l*) diffraction patterns ignore the effects of the rotational and translational defects that characterise the turbostratic (*hk0*) patterns. Here δ represents defects in the stacking of the graphite layers. The effects of a varying d on a crystallite of fixed N=30 are shown in Figure 2.17; as δ reaches the same size as N the peak profile becomes similar to that produced by the pure N=30 pattern in Figure 2.16, though one effect of introducing the defects into the interference function is to smear the function so that the artificial interference effects vanish. Figure 2.18 shows the effect of increasing crystallite size on a crystal with fixed δ: as N becomes much larger than δ, the peak profile becomes dominated by the effects of the distance between defects rather than by the size of the crystallite.

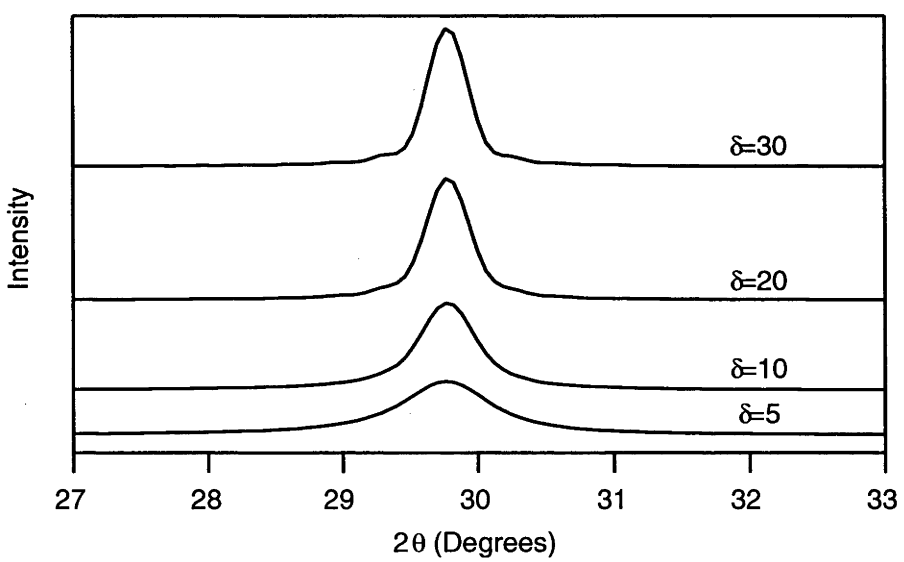

Figure 2.17: *the effect of the defect parameter δ on the simulations produced by the same crystallite used for Figures 2.15 and 2.16 above, with N=30 and δ varying from 5 to 30 as indicated.*

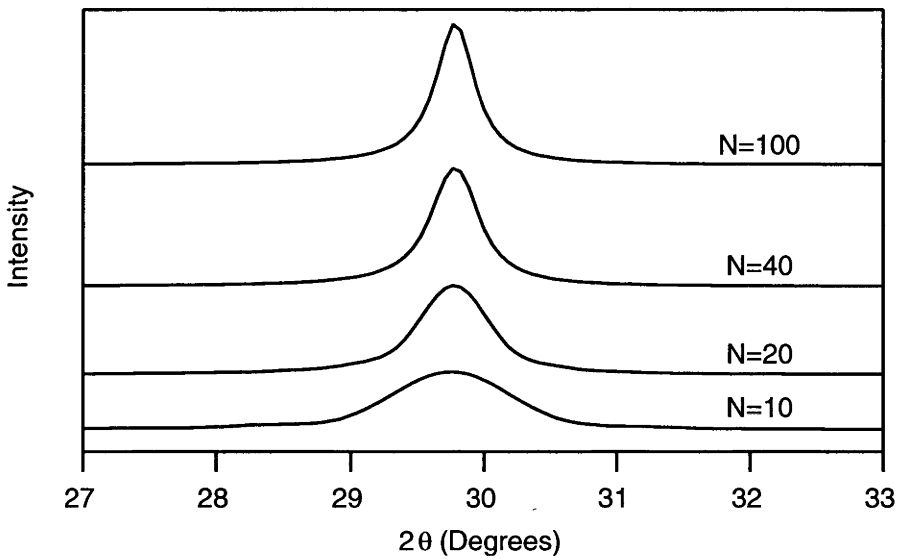

Figure 2.18: *the effect of the crystallite size N on the XRD pattern produced by a simulated crystallite with a fixed defect parameter δ=10 and the other parameter the same as in the simulations above. As N becomes much larger than δ, the diffraction pattern is dominated by the effects of the mean defect free distance δ rather than by the crystallite size: as a result, the peak shapes at N=40 and N=100 are very similar.*

2.7.3: *c*-axis Simulation of Interstratified Crystallites

The *c*-axis simulations above assume that there is only one species with a single *c*-axis spacing in the crystallites. In interstratified systems there co-exist two or more species stacked in the same crystallite, with a probabilistic distribution of finding a particular species occupying a given layer. The effect of this is to cause the reflections to shift to non-integral values of l. Though detailed simulations of interstratified systems are beyond the realm of this work, there is some evidence of interstratification in the (*00l*) series of the precursor RbC_{25} GIC, which is also seen in the ternary compounds derived from it. To attempt some qualitative analysis of this data, the simplified approach of Hendricks and Teller (1942)[11, 12] was used. This calculates the interference function for an interstratified sample of two compounds, each with a fully random occupancy, that is, the type of a particular layer does not influence the types of neighbouring layers. The Hendricks-Teller equation for the interference function Φ is:

$$\Phi = \frac{2P_A P_B \sin^2\left(Q(D_B - D_A)/2\right)}{1 - 2P_A P_B \sin^2\left(Q(D_B - D_A)/2\right) - P_A \cos(QD_A) - P_B \cos(QD_B)} \qquad (39)$$

where P_A and P_B are the fraction of the sample composed of layers A and B of c-axis dimensions D_A and D_B respectively, and $Q=4\pi\sin\theta/\lambda$.

The peak shifts away from the mean lattice spacing in the simulated interference functions produced by Equation (39) are shown in Figures 2.19 to 2.21. The lattice parameters for the two phases in the simulated sample were chosen as 6.0 Å and 9.35 Å, These represent stage 1 and stage 2 of a hypothetical graphite intercalation compound, and thus differ by one graphite layer spacing, equal to 3.35 Å. The (*00l*) peaks are measured over the range 6-80° in 2θ, which is the range used for most of the diffraction experiments used in this study.

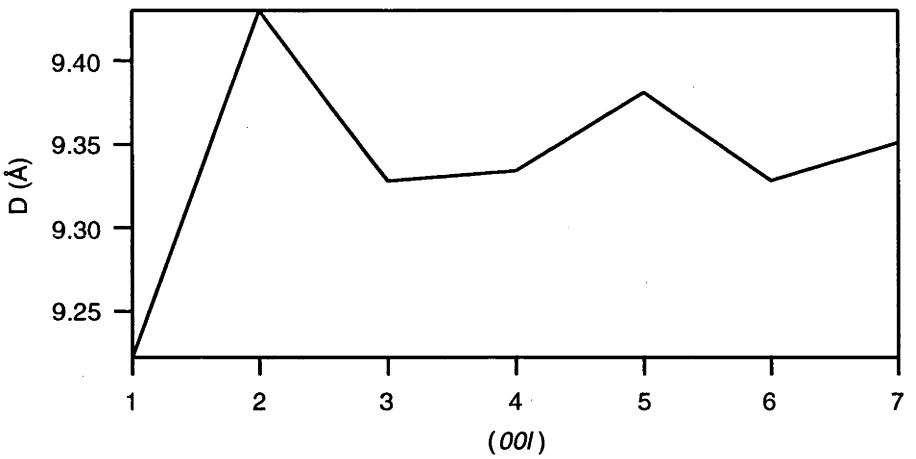

Figure 2.19: *the shift of D-spacing of each (00l) peak away from the average d-spacing, produced by an interstratified system composed of 90% of a 9.35 Å phase and 10% of a 6.0 Å phase. The mean d-spacing of the peaks is 9.34 Å.*

The first simulation, shown in Figure 2.19 uses 90% of the 9.35 Å and 10% 6.00 Å, the second in Figure 2.20 is 50% of each phase; the last in Figure 2.21 is 10 % 9.35 Å and 90% 6.00 Å.

The effect of a small contamination by a second phase is made clear by Figures 2.19 and 2.21: in Figure 2.19 the mean d-spacing of 9.34 Å is very nearly the same as that of majority single phase compound at 9.35 Å, but there is a modulated shift away from this average value. In Figure 4.2.1, the mean d-spacing is 6.00, the same as that of the majorty phase, but again is a modulated shift away from this average. The simulation in Figure 2.20 is a 50:50 mix of the two phases: the average d-spacing of 9.27 Å is very close to that of the larger phase, but the effect has been to greatly increase the size of the peak shifts away from the average value.

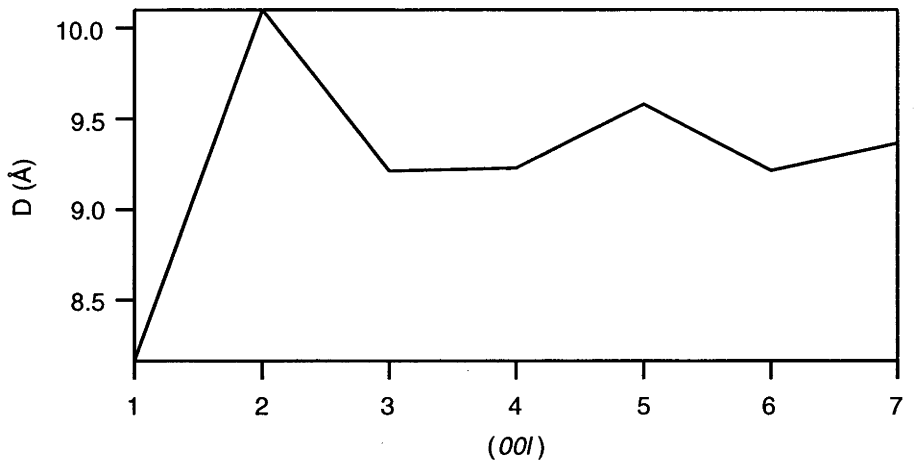

Figure 2.20: *the shift of d-spacing of each (00l) peak away from the average d-spacing, produced by an interstratified system composed of 50% of a 9.35 Å phase and 50% of a 6.0 Å phase. The mean d-spacing of the peaks is 9.27 Å.*

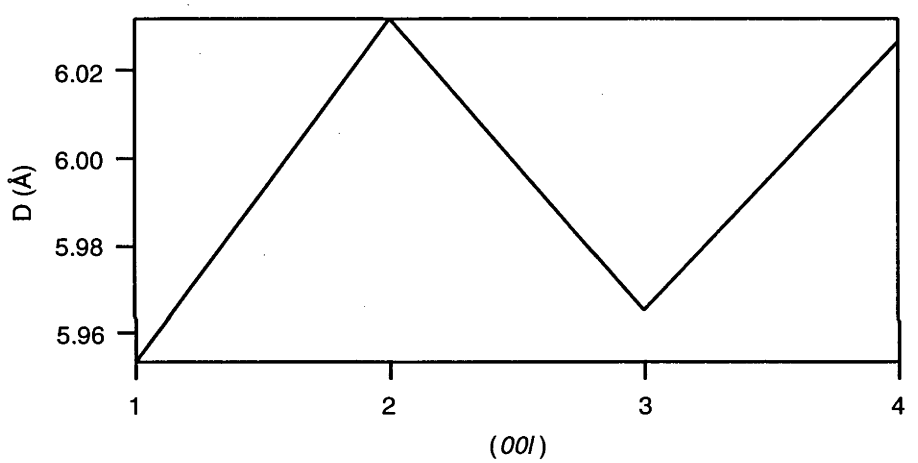

Figure 2.21: *the shift of d-spacing of each (00l) peak away from the average d-spacing, produced by an interstratified system composed of 10% of a 9.35 Å phase and 90% of a 6.0 Å phase. The mean d-spacing of the peaks is 6.00 Å.*

2.8 The Rietveld Refinement Program "GSAS"

While the methods described above can produce an accurate simulation of the *ab*-plane diffraction pattern of a turbostratically disordered structure, they required a considerable amount of computation time to complete. When determining the atomic positions in a structural model, it was much faster to use GSAS[13], a Rietveld refinement program, to reproduce the peak intensities first, and then use the structure found by this method in the full pattern technique described above.

In Rietveld refinement a starting structural model, including the space group and atomic positions, is used to determine the reflection positions and intensities produced by this pattern. At each reflection a profile shape function is used to produce a peak shape in 2θ, and a background function adds intensity at all values of 2θ. The simulated diffraction pattern produced by this structural model is compared with powder diffraction data at all points in 2θ, and the quantity

$$R = \sum_i w_i \left(Y_{io} - Y_{ic}\right)^2 \tag{40}$$

is minimised between cycles of refinement, where Y_{io} is the observed intensity at point i, Y_{ic} is the calculated intensity at i, and w_i is the weighting of that point[14].

In this work only the first stage of the Rietveld process is used, to produce the intensities of a model structure. The primary problem in using a Rietveld refinement program to proceed any further with structural analysis is in the peak profile shapes available, which could not accurately model the turbostratic band shape in any of the public domain Rietveld packages tested.

References

1. V.A. Drits and C. Tchoubar, *X-Ray Diffraction by Disordered Lamellar Structures*. 1990, Berlin: Springer-Verlag. 371 pages.

2. R.C. Reynolds, *Diffraction by Small and Disordered Crystals*, in *Modern Powder Diffraction*, D.L. Bish and J.E. Post, Editors. 1989, The Mineralogical Society of America: Washington. p. 145-181.

3. R.C. Reynolds, *Principles of Powder Diffraction*, in *Modern Powder Diffraction*, D.L. Bish and J.E. Post, Editors. 1989, The Mineralogical Society of America: Washington. p. 1-17.

4. C. Kittel, *Introduction to Solid State Physics*. 6 ed. 1986, New York: John Wiley & Sons, Inc. 646 pages.

5. G.W. Brindley, *Order-Disorder in Clay Mineral Structures*, in *Crystal Structures of Clay Minerals and their X-Ray Identification*, G.W. Brindley and G. Brown, Editors. 1980, Mineralogical Society: London. p. 125-196.

6. W. Parrish, *Powder and related techniques: X-ray techniques*, in *International Tables for Crystallography, Volume C: Mathematical, Physical and Chemical Tables*, A.J.C. Wilson, Editor. 1992, Kluwer Academic Publishers: Dordrecht. p. 42-79.

7. P.J. Brown, A.G. Fox, E.N. Maslen, M.A. O'Keefe, T.M. Sabine, and B.T.M. Willis, *Interpretation of Diffracted Intensities*, in *International Tables for Crystallography, Volume C, Mathematical, Physical and Chemical Tables*, A.J.C. Wilson, Editor. 1992, Kluwer Academic Publishers. p. 476-533.

8. S. Ergun, *X-Ray Studies of Carbon.* Chem. Phys. Carbon, Ser. Advan., 1968. **3**: p. 211-288.

9. D. McKie and C. McKie, *Essentials of Crystallography*. 1986: Blackwell Scientific Publications. 436 pages.

10. B.E. Warren, *X-Ray Diffraction in Random Layer Lattices.* Phys. Rev., 1941. **59**(9): p. 693-699.

11. S. Hendricks and E. Teller, *X-Ray Interference in Partially Ordered Layer Lattices.* Journal of Chemical Physics, 1942. **10**(3): p. 147-167.

12. R.C. Reynolds, *Interstratified Clay Minerals*, in *Crystal Structures of Clay Minerals and their X-Ray Identification*, G.W. Brindley and G. Brown, Editors. 1980, Mineralogical Society: London. p. 249-304.

13. A.C. Larson and R.B. Von Dreele, LANSCE, MS-H805, Los Alamos National Laboratory, NM 87545, USA.

14. J.E. Post and D.L. Bish, *Rietveld Refinement of Crystal Structures Using Powder X-Ray Diffraction Data.*, in *Modern Powder Diffraction*, D.L. Bish and J.E. Post, Editors. 1989, The Mineralogical Society of America: Washington. p. 277-308.

Chapter 3: Experimental Techniques

3.1 Introduction

As described in Chapter 1, the intent of this research was to determine the effect of gas physisorption at cryogenic temperatures on the *ab*-plane and *c*-axis structures of alkali-metal graphite intercalation compounds. The technique used to investigate these structures was x-ray diffraction, the relevant theory of which is in Chapter 2. The four experimental components of this work were: preparation and characterisation of the alkali metal graphite intercalation compounds (GICs); bringing into operation a cryostat that provided a regulated low temperature environment for the samples; construction and calibration of a vacuum line used to measure out doses of gas to the sample; and the redesign and reconstruction of an x-ray diffractometer which produced the primary experimental data.

All of the experiments used the same procedure. Firstly the prepared GIC was weighed, and then transferred inside an argon filled glove box to the sample stick of the cryostat. The stick was transferred to the cryostat, then pumped out and cooled to a temperature where it was known that the GIC would absorb the particular gas used. A small dose of gas was prepared in the vacuum line, and then released to the sample. The drop in pressure due to the GIC absorbing the gas was measured over a period of time, usually until a desired stoichiometry had been reached.

ab-plane and *c*-axis x-ray diffraction scans of the sample (see Chapter 2) were then made to determine if there had been a significant change in the structure of the sample. Once the measurements at a particular stoichiometry had been completed, more gas was added. This procedure was repeated until the gas saturated the sample.

3.2 Preparation and handling of alkali-metal graphite intercalation compounds

The samples used in this study were all prepared using the same method. The host compound was recompressed exfoliated graphite, marketed under the brand name "Papyex" by Le Carbone Lorraine, with a specific surface area of 21 m^2g^{-1} and a mosaic spread of $30°$[1-3]. Rubidium and potassium metal (99.5% pure) were purchased from Johnson Matthey and used without further purification.

The Papyex was purchased in the form of large sheets 1000 x 300 x 0.5 mm. It was decided to prepare all the GIC samples in a shape that would fit into the diffractometer sample holder (see Figure 3.1), and so 65 pieces of Papyex 19 mm by 7.2 mm were cut

from the sheets. The graphite was degassed at 200°C on a vacuum line for several days at a pressure of 10^{-5} τ before being transferred to an argon-filled dry box, a Vacuum Equipment Corporation "Dri Lab" Model DL-002-S-P.

It had been found in previous work[4] that attempts to intercalate large (>1 gram) samples of alkali-metal graphite intercalation compounds (AM GICs) in a single batch often led to poorly equilibrated samples, containing high percentages of stage-1 and stage-3 GICs in addition to the desired stage-2 GIC. In order to avoid this, it was decided to prepare many separate batches each with less than 0.5 grams of the constituents. It was found that using 5 pieces of Papyex per batch would give an appropriate total mass: for example five pieces of 19 x 7.3 x 0.5 mm Papyex weighed 0.321 grams; to make a GIC of the stoichiometry RbC_{25} required 0.091 grams of rubidium for a final mass of 0.412 grams of GIC in the synthesis tube.

The most difficult part of this procedure was accurately measuring quantities of 0.091 grams of Rb inside a glove box. This corresponded to a volume of 0.059 ml of the solid metal. The method used was to liquefy the metal under vacuum, and then use nitrogen to force the metal into previously evacuated glass capillaries with a measured internal diameter of 1.6 mm. After cooling, the Rb-filled capillary was easily cut to a length of 30 mm, equivalent to the correct volume of metal.

The method of preparation of AM GICs used required that the graphite host and the guest metal be sealed in an evacuated container, and then heated to 300° C, exposing the graphite to an atmosphere of the metal[4-8]. To achieve this each batch of material was transferred inside the dry box to a Pyrex tube terminated by a PTFE tap and a fitting for a glass vacuum line. The tubes were sealed with the PTFE tap, then taken out of the dry box and evacuated to 10^{-4} τ on an external vacuum line. The evacuated tube was then cut with a gas torch, resulting in a 10 cm long sealed tube of Pyrex. The tubes were then heated in ovens to 300°C. The stage 2 GIC is a metallic blue colour for both the Rb and K intercalation compounds, and can be easily distinguished from both the black unintercalated graphite and the stage 1 AM GIC, which is an orange-brown, while the stage 3 and stage 4 compounds are dull blue and black, respectively. After 3 weeks at 300°C all the samples were a uniform metallic blue, indicating that no unintercalated graphite or stage 1 GIC was present, and the samples were then allowed to cool to room temperature.

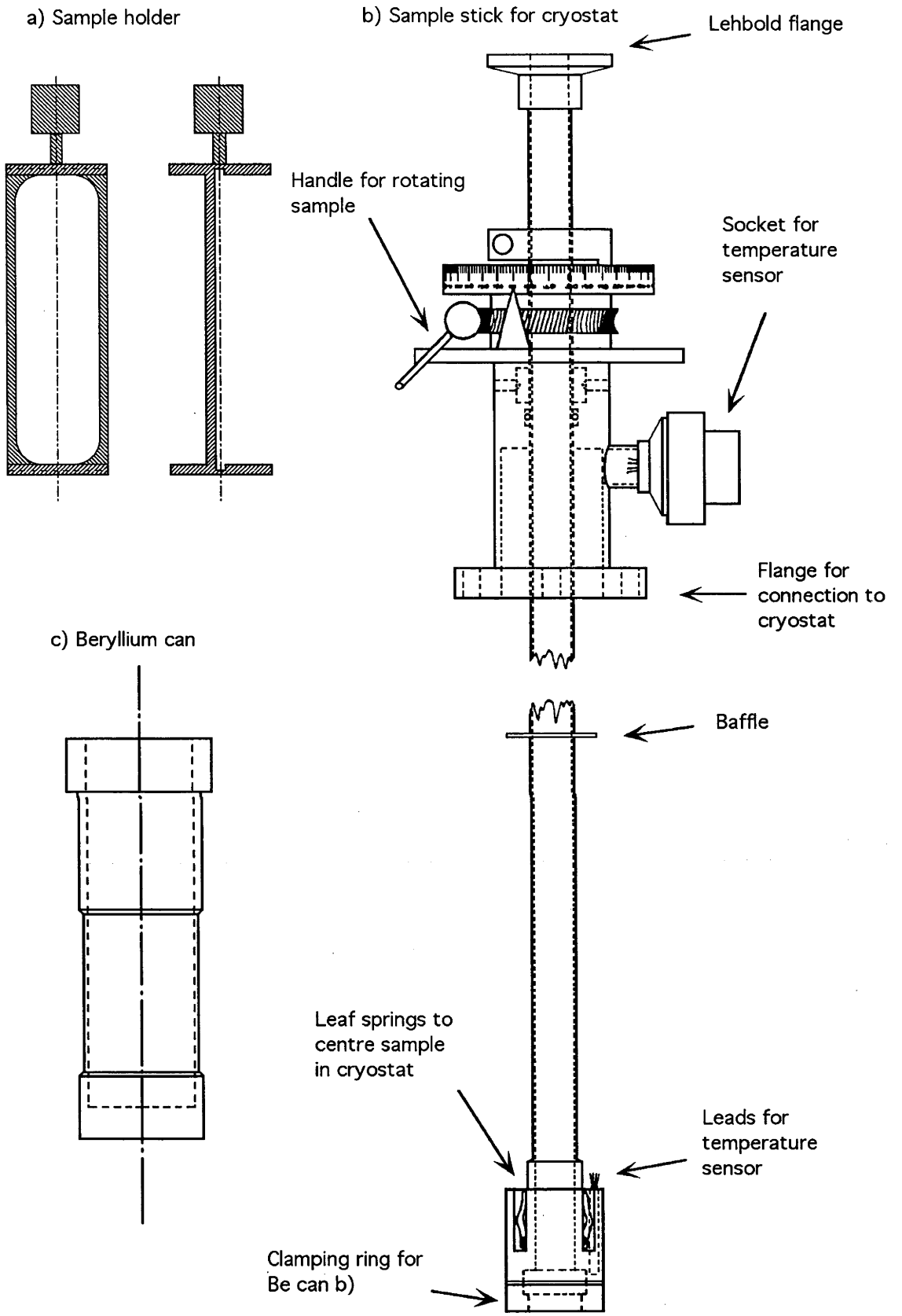

Figure 3.1: *The sample holder, cryostat sample stick and beryllium can that together provide the immediate sample environment inside the cryostat*

The samples were left in the Pyrex tubes for long term storage, and were opened only when a new sample was introduced to the sample stick of the cryostat. One tube, containing 5 pieces of AM GIC, and the sample stick were taken into the Ar dry box where the tube was opened and the sample weighed. One piece of AM GIC was put into the sample holder, shown as a) in Figure 3.1, and the other 4 pieces were inserted into the sample stick above the clamping ring in order to increase the total mass in the system for gas doping measurements. Both sites were equally accessible to the doping gas, ensuring uniform doping. The sample holder was inserted into the beryllium can, shown as c) in Figure 3.1, and the Be can in turn was clamped to the sample stick, using an indium wire seal to ensure vacuum integrity at low temperatures. After the stick had been sealed, it was returned to the cryostat.

3.3 Sample Environment

3.3.1 Cryostat

The sample environment was provided by a cryostat constructed by A&S Scientific Products Ltd, Abingdon, UK. The cryostat, shown in cross-section in Figure 3.2, provides temperature regulation for the sample by taking liquefied gas from a reservoir and then electrically heating it above its boiling point before flowing the gas over the sample. A temperature sensitive resistor mounted near the sample provides feedback for control circuitry, which varies the power to the heater so as to keep the sample at a set temperature. The projected experimental series required that the samples be exposed to stoichiometric doses of gas at low temperatures, so the sample stick, shown in Figure 3.1, was equipped with gas handling fittings for connection to an external vacuum line, shown in Figure 3.3. At the start of this project the cryostat had not been used at cryogenic temperatures for nearly four years, and several problems were discovered and corrected that may have developed during this hiatus or may have been results of the earlier work.

Almost all of the experiments used liquid nitrogen as the cooling gas, though he cryostat was capable of using liquid helium. Early experiments using liquid helium showed little improvement on the diffraction patterns gained at 85 K. Due to the reduced speed of experimentation and much greater cost of operating with helium it was decided to continue the work using liquid nitrogen as the cooling agent.

When working with liquid nitrogen as the cooling fluid it was found necessary to pump the vacuum jacket on at least a daily basis, and preferably continuously, in order to retain cooling fluid on overnight diffraction scans. Filling the upper as well as the lower

reservoir also extended the period where the cryostat could be left unattended, at the cost of increased use of liquid nitrogen.

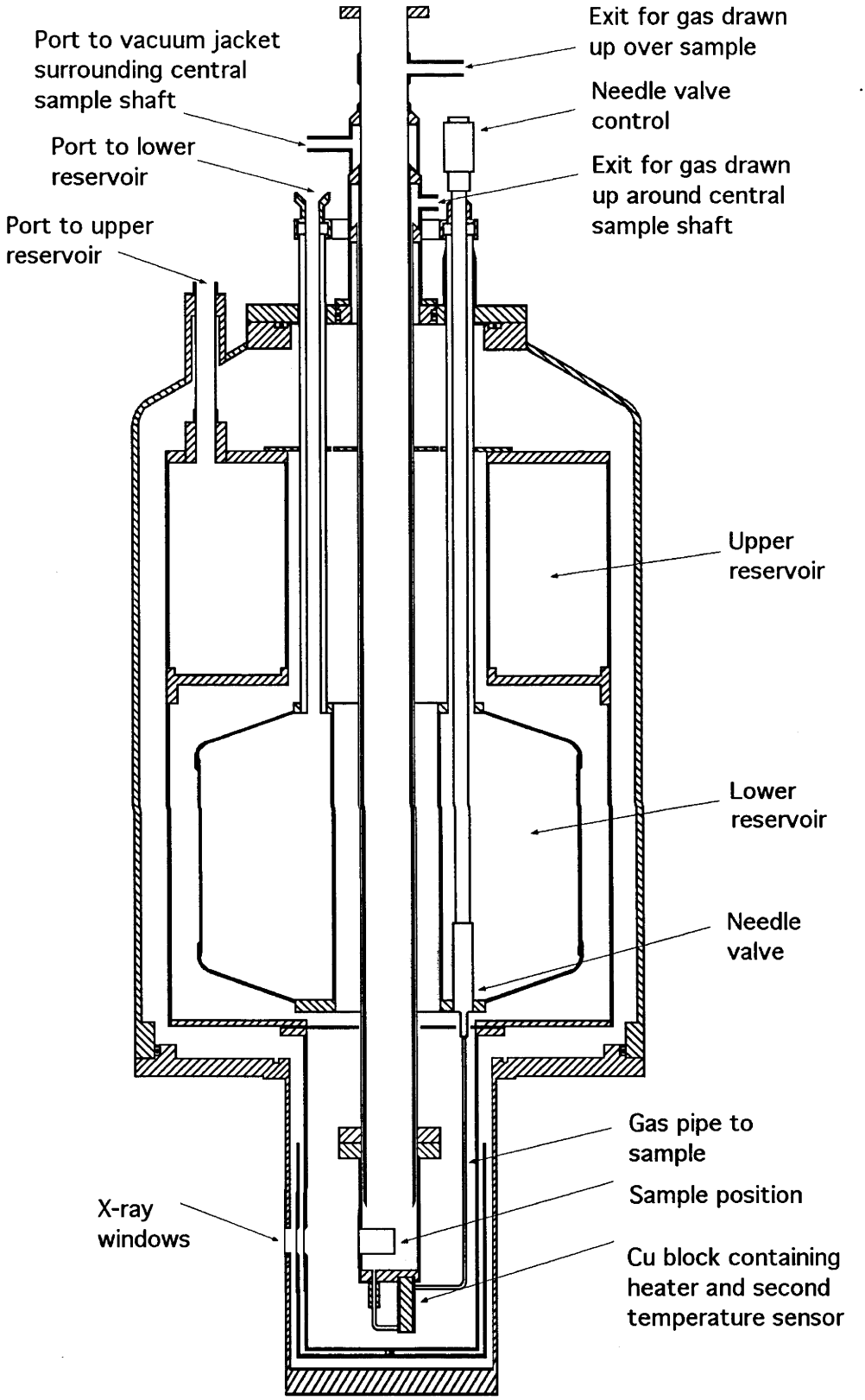

Figure 3.2: *a cross-section of the sample cryostat used for the x-ray diffraction experiments.*

3.3.2 Vacuum and Gas Handling Line

An external glass vacuum line, shown in Figure 3.3, was used for pumping the vacuum jacket of the cryostat as well as for the addition and removal of gases from the sample. The line was evacuated by oil diffusion and rotary pumps with the aid of a cold trap, and used three bulbs, with calibrated volumes of 2214 cm^3, 122.94 cm^3 and 56.41 cm^3 respectively, to hold gas and to measure stoichiometric doses of gas out to the sample held in the cryostat.

Gas uptake by the sample was measured with a Baratron pressure gauge comprising a Type 390 Pressure Sensor, a 270C High Accuracy Signal Conditioner and a 274 Multiplexer 3 Channel Sensor Head Selector, which provided measurement of pressure accurate to 0.06% from 0-1000 τ. A hot filament ionisation gauge was used for determining the ultimate vacuum achievable in the line and thus for tracking leaks in the system.

The connection between the vacuum line and the cryostat had to have a low volume in order to maximise the change in measured pressure when the sample absorbed the gas in the system. It had to be able to connect between a rotating cryostat and a vacuum line that may move relative to one another. Finally it had to be sufficiently gas tight that air wouldn't leak in during the extended periods of gas doping, when the sample stick was opened to the vacuum line, since exposure to even small amounts of oxygen destroys the sample[7].

Three different connection arrangements were tried during this work. The first employed polyethylene tubing terminated at either end with Swagelok connectors using teflon ferrules. This was flexible and cheap, but though it was sufficiently leak tight for doping purposes it was poor enough that we attempted to find a superior system. The second used copper tubing with Swagelok connectors using teflon ferrules. The tubing was not flexible: the teflon ferrules allowed the cryostat to rotate while maintaining a vacuum tight seal. This had the best vacuum, but the rigid tubing was too much of a risk for a system that had to operate unobserved. The third fittings used Tygon tubing with Cajon UltraT O-ring-based seals; it was not far superior to the first arrangement. While all three of these arrangements worked adequately, none of them was ideal.

The volume of the entire doping system was found using expansion of He gas from Bulb 3 (see Figure 3.3) the volume of which had been determined before assembly of the vacuum line. The volume of the lower vacuum line shown in Figure 3.3 was 381.79 cm^3. The volumes of each the three connection arrangements were 58.8 cm^3 for

polyethylene, 106.0 cm^3 for copper, 58.1 cm^3 for Tygon, and of the cryostat sample stick was 103.97 cm^3.

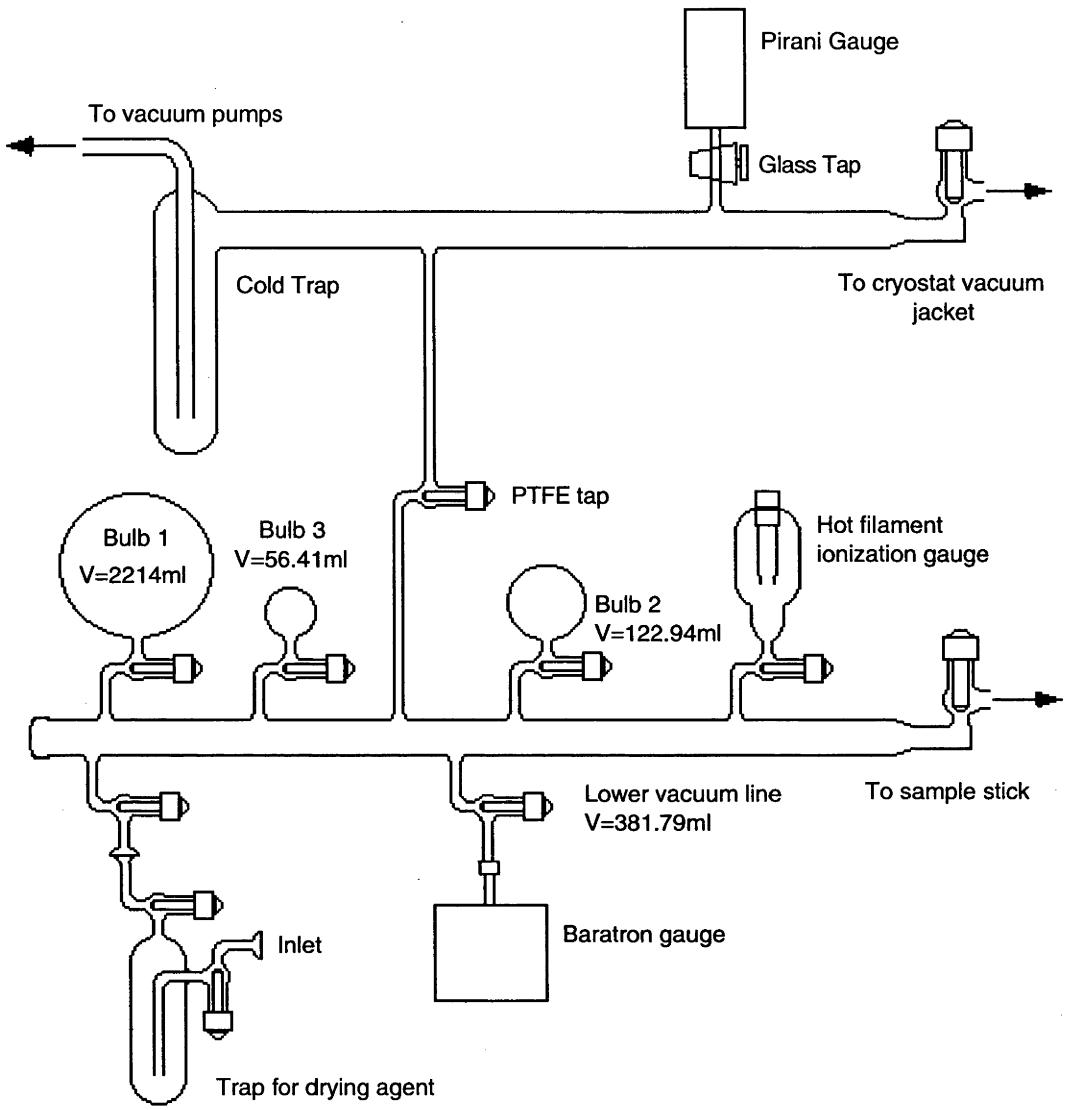

Figure 3.3: *Diagram of the external vacuum line used for gas handling.*

3.3.3 Gas Purification

All of the gases used were purified during introduction into the vacuum line shown in Figure 3.3. The agent used for this was a powdered cesium GIC made to the stoichiometry CsC_{36}, though it may have been a mix of several stages. The gas was introduced though the inlet on the drying agent trap, and allowed to fill the lower vacuum line to a pressure ~770 T, with the taps to the three storage bulbs closed. The drying agent in the trap was then cooled using liquid nitrogen in a separate Dewar, which caused the gas to physisorb onto the GIC, as described in Chapter 1. Once the gas had stopped absorbing, the remainder was pumped away, then the drying agent allowed to heat until

the gas had desorbed. The desorbed gas was then expanded to the various storage bulbs, the remainder in the line and the drying trap removed, and the process repeated until the bulbs were filled with a supply of gas adequate for the experiments planned. This process had been found to be the most effective way of removing H_2O and O_2 from a gas before doping the sample[4].

3.3.4 Sample Doping Procedure

Having determined the weight of the prepared GIC sample (see Section 3.2 above), and the volume of the gas doping system, it was then possible to dope a cooled sample to a given stoichiometry by measuring the change of pressure in the system after the sample was exposed to the gas[5, 9]. Gas was measured from the storage bulbs into the lower vacuum line, expanded to the connection, and then to the sample stick. The pressure in the system was monitored until either a desired stoichiometry was reached or gas uptake by the sample had ceased, after which the sample stick was closed off and the remainder of the gas pumped away. After the diffraction experiments were completed (see below), the gas content of the sample was increased by repeating the above procedure.

One possible problem with this experimental set-up is that gas uptake may continue after the sample stick is closed off. The quantity of gas remaining in the sample stick was low compared to the whole doping volume, but is still significant. This was measured at the start of the next doping cycle by expanding the gas in the stick to the evacuated connection and line, and calculating the remaining pressure in the stick. Usually the gas uptake after closure was negligible.

To give an idea of the quantities involved, the RbC_{25} samples were typically of the order of 1.07×10^{-3} moles. At 293 K, a millimole of an ideal gas is equivalent to 18.834 τ-litres; in the doping volume, which varied with changes to the connection tubing used but was typically 0.544 litres, a pressure change of 37.04 τ would be equivalent to a 1:1 ratio of alkali metal to physisorbed gas in the resultant ternary GIC.

3.4 Huber X-Ray Powder Diffractometer

3.4.1 Introduction

The principal instrument used in this work was a Debye-Scherrer transmission mode x-ray powder diffractometer based on a Huber 422 2-Circle horizontal turntable goniometer[10, 11]. The data needed from the samples required transmission mode diffraction (see Chapter 2), and the samples only physisorbed gases at low

temperatures[12] (see Chapter 1), demanding a cryogenic sample environment. This sample environment was provided by a large (720 mm high by 270 mm diameter) cryostat, described in section 3.3, and the cryostat dictated most of the design decisions made when this instrument was built. A horizontal goniometer is not usually the preferred choice for a powder diffractometer as this requires the sample to be vertical[11, 13], but it was required by the design of the cryostat. Of particular concern in making a useful diffractometer was reconciling the diameter of the focussing circle demanded by the cryostat with optimising the flux at the sample. At the start of this work the diffractometer and cryostat had several design defects and these were corrected as an initial part of this work. Early experiments on the original instrument showed that the primary problem was a lack of x-ray flux, and indicated that the x-ray optics were the cause. To correct this would require that the diffractometer be rebuilt.

3.4.2 Some Relevant Design Considerations for X-Ray Powder Diffractometers

The functions of a powder diffractometer can be separated into three elements: x-ray photons are generated, they interact with the sample and with the optics of the diffractometer, and they are detected[10, 11, 14]. There were no significant problems with the detector system, though a short description of the technique used is included here for completeness; there were problems with the original x-ray source and with the diffractometer optics. Before the corrections made can be described, an explanation of the design considerations that compelled them is in needed.

3.4.2.1 X-Ray Sources

Tabletop x-ray sources produce x-rays by the interaction of energetic electrons with a metal target, most commonly copper or molybdenum[15]. An electron beam is produced by the heating of a tungsten filament and the electrons accelerated by an electric potential to impact the metal target. The focus of the electron beam on the anode is rectangular, with a ratio between the dimensions of between 1:10 to 1:30, depending upon the nature of the source.

In a powder diffractometer scanning in the horizontal plane the vertical divergence of the incident beam can be relaxed to obtain better flux at the sample without significant loss of resolution[11]. As the final collected pattern is a one dimensional function of angle, only the source divergence in one direction is significant. A slit shaped beam at the sample is thus a better choice than a square or spot beam. As x-ray tubes produce line and spot sources[15], the line source is preferred for powder diffractometers. A line source is

produced by viewing the source at a shallow angle to the long axis, as shown in figure 3.4, and an angle of approximately 6° is often preferred[15], as this results in a compression factor of ~10:1.

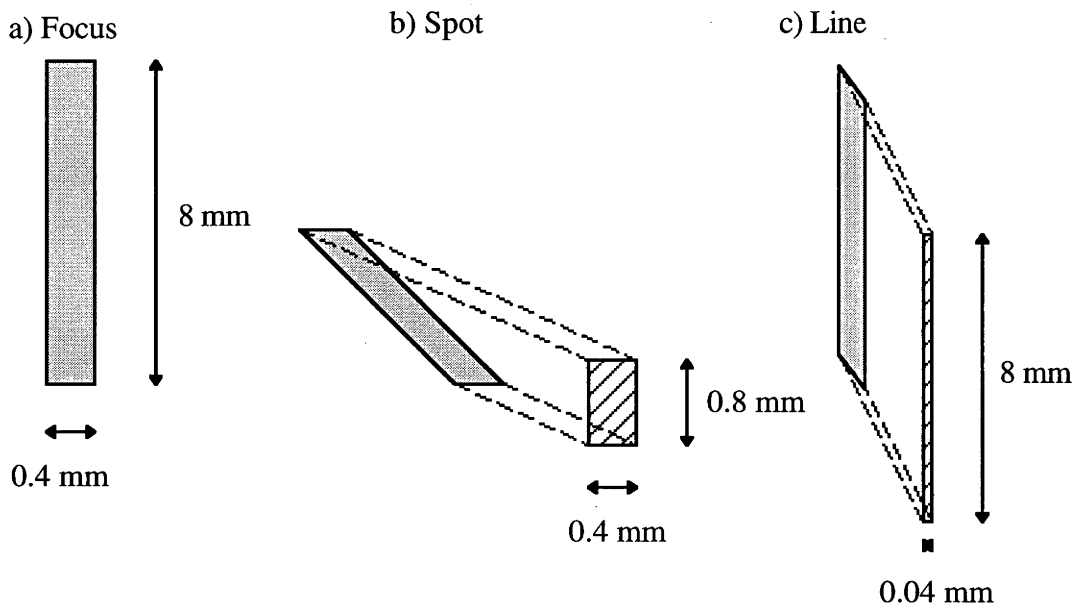

Figure 3.4: *Diagram of an x-ray source in line and spot geometries.*

3.4.2.2 Optics

A powder diffractometer can work in either transmission or reflection mode[10, 11]: the optical system, particularly any focussing elements, must be designed for the mode desired. As can be seen in Figure 3.5, the two focussing conditions are described by the mode of interaction of the x-ray beam with the sample. While in reflection mode (System B) the sample works as a focussing element of the optics, in transmission mode (System A) the beam continues to diverge after passing through the sample. Thus for a transmission mode diffractometer a focussing element is needed to produce an image of the source on the detector. This focussing element is almost always a curved monochromator. As described in Chapter 2, the data required from this investigation would best be gathered using transmission mode diffraction of aligned samples, and so this mode was used in the Huber diffractometer.

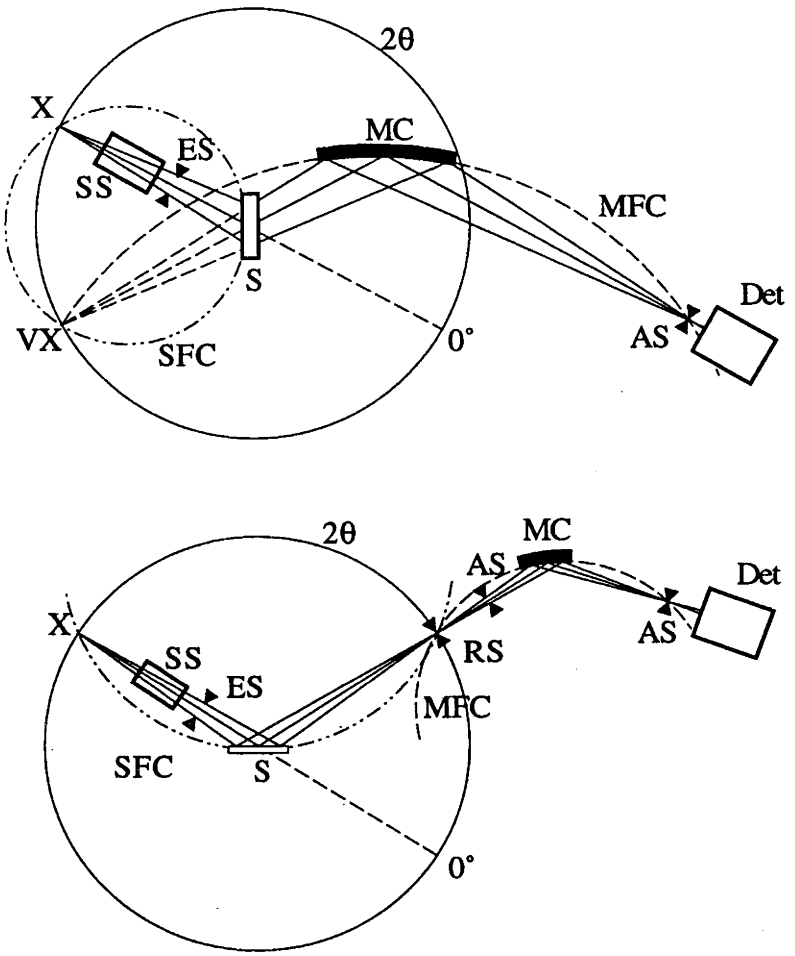

Figure 3.5: *The diffractometer designs for transmission and reflection optics with post diffraction monochromators. X: X-Ray Line Source; S: Sample; ES: Entrance Slit; AS: Acceptance Slit; SS: Soller Slit; RS: Receiver Slit; 2θ: 2-theta circle of goniometer, with 0° position shown; M: Monochromator; Det: Detector; SFC: Sample Focussing Circle; MFC: Monochromator Focussing Circle.*

Though the arrangements shown in Figure 3.5 both employ a post diffraction monochromator, it is possible to construct either type of diffractometer using an incident beam rather than diffracted beam monochromator[11]. A reflection mode diffractometer may dispense with the focussing monochromator entirely, using the sample as the focussing element. In such a system an incident beam filter is commonly used to provide some level of spectral filtering. This filter is composed of an element which has a absorption edge just beyond the Kα lines of the source and for Cu Kα a nickel is used. However, most of the samples studied in this work contained elements such as rubidium that fluoresce when exposed to Cu Kα radiation and as this fluorescence radiates uniformly from the sample a very high background count rate can be produced[11, 15]. Fortunately, this fluorescence will usually be of a different wavelength to the Kα lines of

the tube, and a post-diffraction monochromator will eliminate the fluorescence at the same time as monochromating the tube spectrum.

A monochromator is a common optical component in powder diffractometers, used to remove spectral contamination from a variety of sources[11]. The x-ray line spectrum produced by a Cu source is superimposed upon a continuous background of bremsstrahlung ("braking radiation")[15]. Gradual deposition of tungsten evaporated from the filament onto the Cu target and Be tube windows produces another source of spectral contamination, increasing over the life of the tube. By far the strongest components of the Cu spectrum are the Kα characteristic lines emitted during transitions to K-shell vacancies from L shell orbitals[15], and these lines are usually those selected by the monochromator. The analysis of powder patterns is made much simpler by using monochromatic radiation, and though each of the Kα lines has a finite bandwidth, and the $K\alpha_1$ and $K\alpha_2$ lines differ in wavelength by $\Delta\lambda/\lambda=2.5\times10^{-3}$[11], restricting the spectrum to just this pair of lines is a good trade-off between intensity and bandwidth.

Such monochromators consist of a single crystal oriented so as to reflect the principal incident x-ray wavelengths, such as the Cu Kα doublet, from chosen strongly diffracting planes. Usually a low angle peak is chosen to minimise polarisation effects. A monochromator has an angular acceptance for incoming radiation determined by the perfection of the crystal, and flat single crystals have such a small acceptance angle that the monochromated flux is usually too low for powder diffraction techniques using desktop sources. Curving the crystal allows the crystal to accept a greater divergence in the incident beam and thus increases the reflected flux. Bending the crystal to the surface of a cylinder focuses the diffracted beam to a line[11]. Some monochromator geometries are shown in Figure 3.6.

The focussing length FL of a curved monochromator is [11]

$$FL = 2R\sin(\theta) \qquad (1)$$

where θ is half the angle of diffraction. Unlike a curved mirror a focussing crystal will only reflect at those values of θ that correspond to Bragg angles of the crystal for the incident radiation. For an asymmetric cut crystal there are two focussing distances FL_1 and FL_2 determined by the angle γ the reflecting planes make with the surface of the crystal, these distances are:

$$FL_1 = 2R\sin(\theta-\gamma) \qquad (2)$$

and

$$FL_2 = 2R\sin(\theta+\gamma) \quad (3)$$

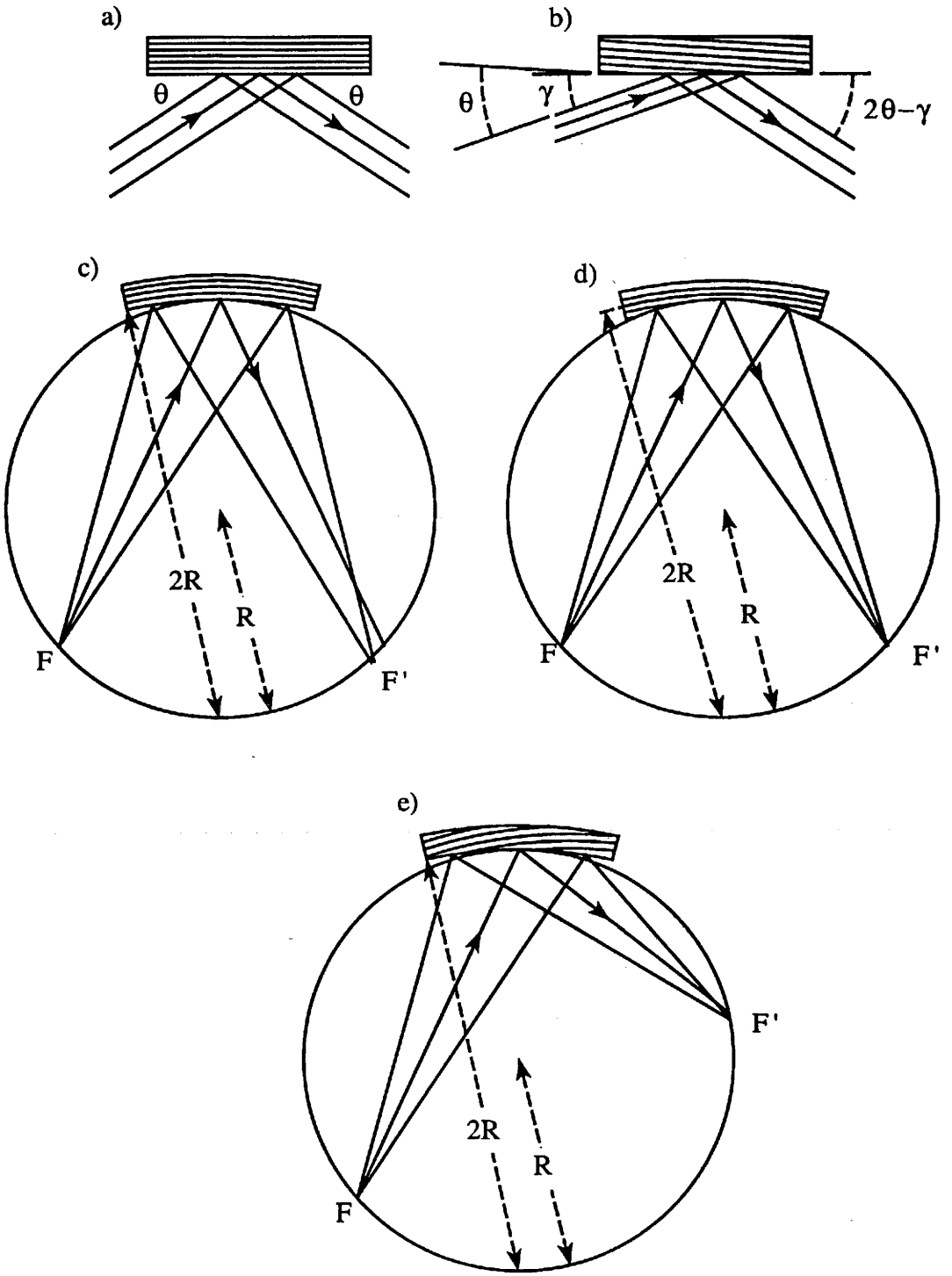

Figure 3.6: *Some common monochromator geometries: a) Flat crystal monochromator; b) Flat crystal with asymmetric cut producing beam expansion; c) Crystal curved to cylindrical radius 2R for focussing; d) Crystal curved to cylindrical surface 2R and ground to radius R to improve focussing; e) Crystal curved to*

cylindrical radius 2R and with asymmetric cut to reduce focussing length. After Parrish[11].

Another method for increasing the flux is to reduce the perfection of the crystal, at the cost of increasing the bandpass of the monochromator[11]. Pyrolytic graphite consists of many small crystallites of graphite produced by the thermal decomposition of a simple organic molecule onto a substrate[16]. In highly oriented pyrolytic graphite (HOPG) the crystallites are deposited with their c-axes well aligned parallel to the substrate, with a mosaic spread of ~0.5°, though the *ab*-plane orientations of the crystals are randomly distributed[17]. The graphite (002) reflection is one of the most efficient known: the reflectivity of HOPG monochromators may reach 50% for CuKα radiation[11].

3.4.2.3 Detectors

There are many methods used for detecting x-ray photons, all of which have to deal with the problem of amplifying a quantum event to a detectable signal. This is either done chemically, through photographic film or the more recent imaging plate, or electronically, as in a variety of counter techniques. While imaging techniques such as photography and position sensitive proportional counters have the ability to record the whole of a diffraction pattern at once these cannot be used with a post-diffraction monochromator. The most common non-imaging detectors are gas proportional and scintillation counters, both of which amplify the initial photon absorption event using an applied high electric potential to create an electron shower. In scintillation counters -the only type used in this study - this amplification occurs indirectly, as the x-ray quanta are absorbed in a scintillating crystal, commonly thallium doped NaI. The crystal fluoresces, producing UV and visible photons that are detected by a photomultiplier tube, which amplifies the signal using a series of induced electron showers[14].

3.4.3 Initial State of Instrument

The original optics were the greatest problem with the diffractometer. The post diffraction monochromator in use at the start of the project was a Union Carbide ZYB grade curved pyrolytic graphite monochromator with a radius of curvature of 155 mm. This is the most commonly used radius for reflection mode diffractometers, as the optics for such an instrument require only a small monochromator focussing circle (see Fig 3.5).

Initially the diffractometer was attached to an Elliott GX-13 Rotating Anode X-ray Generator as the X-ray source, but this was not the ideal configuration because the

geometry of the GX-13 console meant that the Huber goniometer had to be displaced off the console table, leading to a very long source-to-sample flight path of 700 mm.

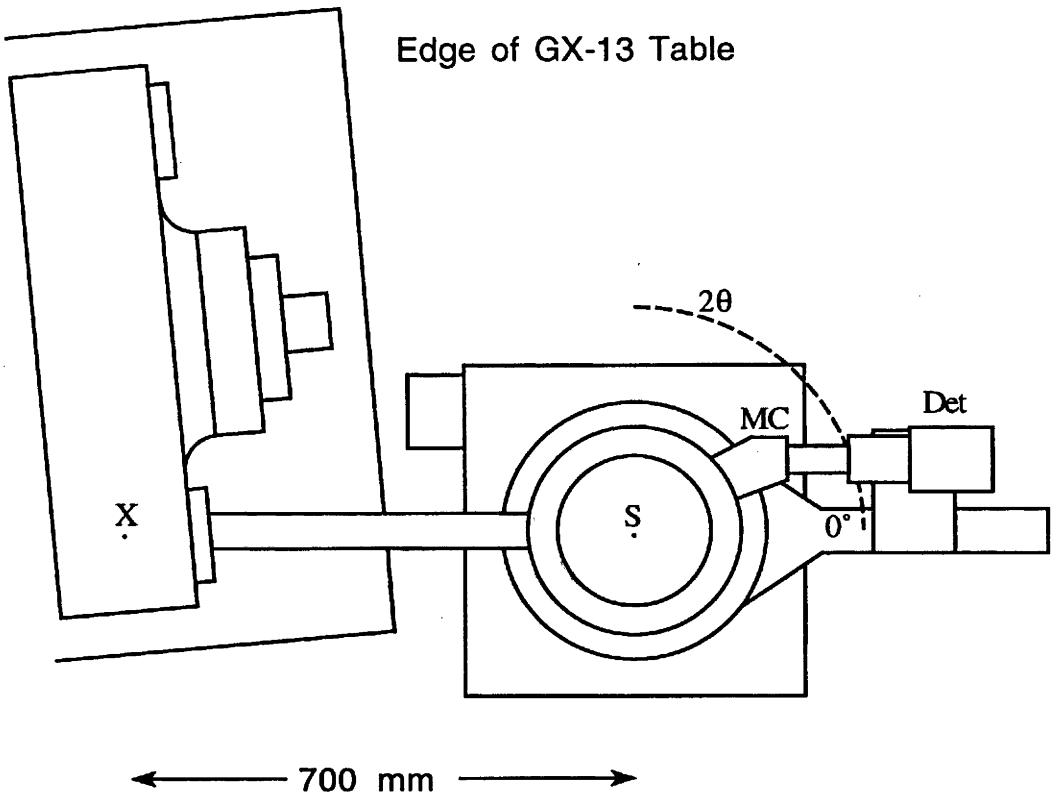

Figure 3.7: *Original experimental arrangement with diffractometer attached to Elliott GX-13 rotating anode x-ray source. X is the source position, S the sample, MC and Det to monochromator and detector respectively. This diagram does not show the flux monitor.*

Both of the GX-13 electron guns use fine-focus filaments, which produce a source spot of 1.0 mm x 0.1 mm on the anode, foreshortened by a viewing angle of 6 degrees to an effective size of 0.1 mm x 0.1 mm, and so a very fine spot source. As described above, this did not optimise the x-ray flux at the sample.

When the instrument was using the GX-13 as the source, the monochromator radius was incorrect for either transmission or reflection optics. The original instrument used a monitor arrangement to determine counting times (not shown in the figures): a second detector views an object illuminated by the direct beam from the source. At each point of the 2θ scan the control software waits until a certain number of counts have been registered on the monitor detector before moving to the next point. Most x-ray diffractometers use a timed step instead; the advantage of the monitor is that it corrects for

variations in source intensity and atmospheric absorption when the length of the monitor arm equals the air length in the diffractometer to the detector.

The x-ray quanta were detected using Philips PW 1964/60 scintillation counters. The EG&G Ortec high voltage supplies and pulse analysis electronics were all mounted in an EG&G Ortec rack. The signals from the two detectors were first fed through a locally made signal conditioner, which employed a DC clamp to eliminate negative going spikes, and then to two Ortec model 550 single channel analysers - one for each detector - for pulse height discrimination. The outputs from the SCAs were sent to a Data Translation DT2806/DTX350 data acquisition board in computer, controlled by locally written software.

The last problem was the control of the diffractometer: the goniometer was controlled, and the data collected, on an Olivetti XT (8086 based) computer. While this was a fast and capable machine when the diffractometer was commissioned, by the beginning of this project it was incapable of running more recent software that we wished to run, especially the networking software available to the R.S.C, which would allow for much more efficient data transfer to other computers.

3.4.4 Modifications

To improve the original design we have attempted to eliminate the problems described above. This involved four separate steps:

i) Changing the source from a spot focus to a line focus, at the same time reducing source-to-sample distances much as possible.

ii) Replacing the monochromator with a more appropriately curved one.

iii) Reconstruction of the diffractometer optics for the new focus and monochromator.

iv) Upgrading the computer.

3.4.4.1 Fixed Focus X-ray Source

With the availability of a Philips PW 1120/90 generator it was decided to move the Huber to this new source. The generator powered Philips PW 2213/20 fixed focus X-ray tube, with a maximum rating of 1500 W, and line source dimensions of 8mm x 0.04mm.

The 1120/90 generator and the diffractometer each required some modifications in order to be successfully adapted to one another. The Philips PW 1316/90 tube tower on the generator was vertical - the most common configuration - which produces a horizontal

line source which is ideal for the most common two circle powder diffractometers made by Philips. Because the Huber goniometer and cryostat require a vertical line source a support was built to hold the Philips tube tower horizontally. This was based on a support designed to hold a Huber tube tower horizontally provided with the purchase of the goniometer.

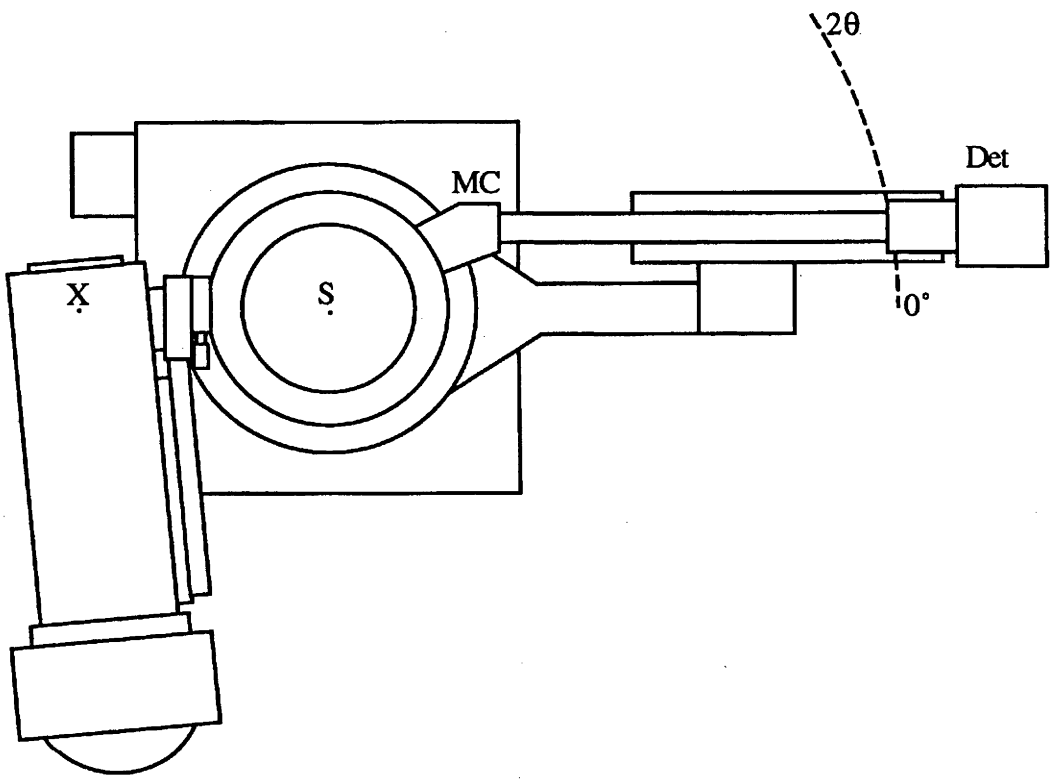

Figure 3.8: *Final experimental arrangement with diffractometer attached to Philips PW 1120/90 x-ray source. X is the source position, S the sample, MC and Det to monochromator and detector respectively. The flux monitor is omitted for clarity.*

As with the GX-13, the table-to-x-ray-source height of Philips x-ray generators is the industry standard of 272 mm, while the height of the Huber from feet to sample is 552 mm. To accommodate the height difference the tube tower was moved and another optical table constructed to support the Huber. The tube tower was held over the edge of the Philips console by a stout aluminium beam (see Figs 3.7 and 3.8).

Finally, an adaptor from the PW 1316/90 tower to the Huber was built, incorporating a Soller slit for vertical collimation and a Sieslit for variable horizontal collimation. The attachment of the Huber to the GX-13 had been insufficiently rigid, allowing the goniometer assembly to move over time as a result of normal laboratory use; for the

Philips generator an 238 cm by 50 cm aluminium bar was attached to the slit assembly at an angle of 6° and then bolted to the tube tower to provide excellent stability.

With the new line source the monochromator had to be a minimum of 300 mm from the x-ray source. From Eqn 3.1 it was clear that using a graphite monochromator this would require a monochromator with 2R = 1308 mm, and so a monochromator to detector flight path of 300 mm also, because graphite cannot be cut asymmetrically. Another advantage of an asymmetrical single crystal is its superior focussing due to the lower mosaic spread[11]. Though these are significant advantages, it was decided to use a graphite crystal for three reasons. Firstly because the monochromator holder was designed for graphite and had no bending capability; secondly because the samples described in Chapters 4 and 5 already had a much higher mosaic spread than HOPG graphite, as well as being turbostratically disordered, and so would not produce sufficiently sharp peaks that a single crystal was warranted; and thirdly because the samples would have also a high attenuation which would be difficult to reduce, and so the monochromator reflectivity would have to be the highest available to maximise flux. An unused port on the PW 1316/90 tube tower was used to allow the monitor to view one of the spot sources.

Attention was given to matching the impedances of cables so as to avoid pulse ringing and an unexplained correlation between peak intensity and monitor counts which was found during the commissioning of the instrument. The optimum settings of the detector windows of the discriminators as well as the operating voltage on the two detectors were redetermined at the same time. The detector voltage was found by measuring the intensity vs photomultiplier potential over the range 700-1300 volts while the goniometer was measuring the attenuated direct beam, with the discriminator windows set wide. It was found that both detectors had the same ideal operating voltage of 1.050 kV. The discriminator windows were set by running repeated scans over the (111) peak of a silicon standard while narrowing the window settings, and then determining the settings with the optimum peak signal to noise ratio. The discriminator windows for both detectors were also set to identical values, 0.3 V for the lower window threshold and 0.7 V for the upper.

The Olivetti XT-based computer was replaced by an Auspac 80486 IBM clone, with the data collection card and control software being moved to the new machine. An ethernet card and networking software were also installed, allowing the collected data to be transferred to other computers more easily.

3.4.5 Comparison between the GX-13 and the Philips Versions of the Diffractometer

The flux at the sample provided by both experimental arrangements can be estimated using available formulae[15]:

$$N_K/4\pi = 10^{10}(E_o\text{-}8.9)^{1.63} \quad (4)$$

where $N_K/4\pi$ is the number of Cu Kα photons per steradian per second per milliampere of tube current, and E_o is the electron energy in keV. Table 3.1 shows the calculated flux at the sample for both experimental arrangements. One known factor is missing: the number of photons emitted from a source at a particular angle is a function of the voltage, because higher energy electrons penetrate deeper into the target[15]. This was ignored because the take-off angle was the same in both cases and the voltage difference was minimal. As can be seen from the table the modified diffractometer was more than an order of magnitude improvement on the original.

X-Ray Source Parameters	GX-13	PW 1120/90
Voltage (kV)	37	40
Current (mA)	37	30
Power (W)	1369	1200
Cu Kα Photons per mA Nk/4π/mA/s	2.3×10^{12}	2.7×10^{12}
Total Cu Kα Photons Nk/4π/s	8.5×10^{13}	8.1×10^{13}
Source-Sample Distance	700	170
Sample Area	$8mm^2$	$8mm^2$
Flux at Sample Nk/s	1.1×10^{8}	1.8×10^{9}

Table 3.1: *Calculated flux at the sample for the Huber diffractometer on the GX-13 and Philips x-ray sources.*

3.4.6 Diffractometer alignment

Commercial diffractometers when purchased include a set of step-by-step instructions on how to properly align them, usually involving specialised tools. In order to align the locally built Huber-Philips diffractometer these procedures had to be determined by

experiment. There were 8 separate variable settings on the diffractometer that an experimenter could adjust: the position of the Huber base with respect to the Philips tube shield (and thus the source); two independently variable edges for each of the two slit assemblies, entrance and acceptance; the setting angle of the HOPG monochromator; the 2θ zero position; and the eccentricity of the sample holder with respect to the θ circle. It was found that varying the eccentricity only caused a deterioration in accuracy, leaving seven variables to be dealt with.

The alignment of the diffractometer needed these 5 tools: a fluorescent screen attached to a plastic paddle that could allow the experimenter to view the x-ray beam; a sample holder for Lindemann glass capillary tubes, which included a small goniometer; a stainless steel spike that would fit in the sample holder; extra sheets of nickel to attenuate the x-ray beam; and a silicon standard available from the US Bureau of Standards which was used to check the final alignment and determine the software 2θ offset.

The procedure used to align the diffractometer was as follows:

a) The entrance slits were set to 1 mm wide, each edge 0.5 mm from the central setting of 5.00 mm. The entrance slits are half the source to sample distance: a 1 mm wide entrance slit will result in a 2mm wide x-ray beam at the sample.

b) The tube sample holder was placed in the sample position, with the stainless steel spike as the sample. The bolts holding the Huber goniometer to the Philips tube tower were loosened, to allow the entire goniometer to be moved parallel to the tube tower. The fluorescent screen was used to view the image of the spike obscuring the beam. The goniometer was moved until the image was centrally placed in the beam; the entrance slits were narrowed to 0.5 mm wide (each 0.25 mm from the central position), and the procedure repeated until the spike image was again centrally placed. If necessary, photographs were taken of the beam rather than using the fluorescent image. The sample holder and the spike were removed, and the bolts tightened again.

c) The nickel attenuator was taped in front of the graphite monochromator, and the 2θ arm driven by the panel controls of the Huber until the monochromator viewed the direct beam. The acceptance slits were set as wide as possible. The setting angle for the monochromator was adjusted for maximum flux, and the 2θ arm driven back to the zero position, and the attenuator removed.

d) The silicon standard (in a 1.00 mm Lindemann glass capillary tube) in the sample holder was replaced in the Huber. The 2θ arm was driven to the silicon (111) peak

position for CuKa at 28.44°. The setting angle was readjusted for maximum flux, and the acceptance slits narrowed until a loss in the flux was seen.

e) A series of scans of the 2θ range near the Si (111) peak were made, and the software 2θ offset adjusted to give the Si (111) peak maximum the correct angle Cu Ka. The acceptance slits were narrowed until an adequate signal-to-noise ratio for the (111) peak maximum to its nearby background was achieved. After this a longer scan from 20-90° in 2θ was done to check the first 6 Si reflections, the intensities and 2θ positions of these peaks compared with published values, and the 2θ software offset and acceptance slit positions adjusted to correct for any remaining errors.

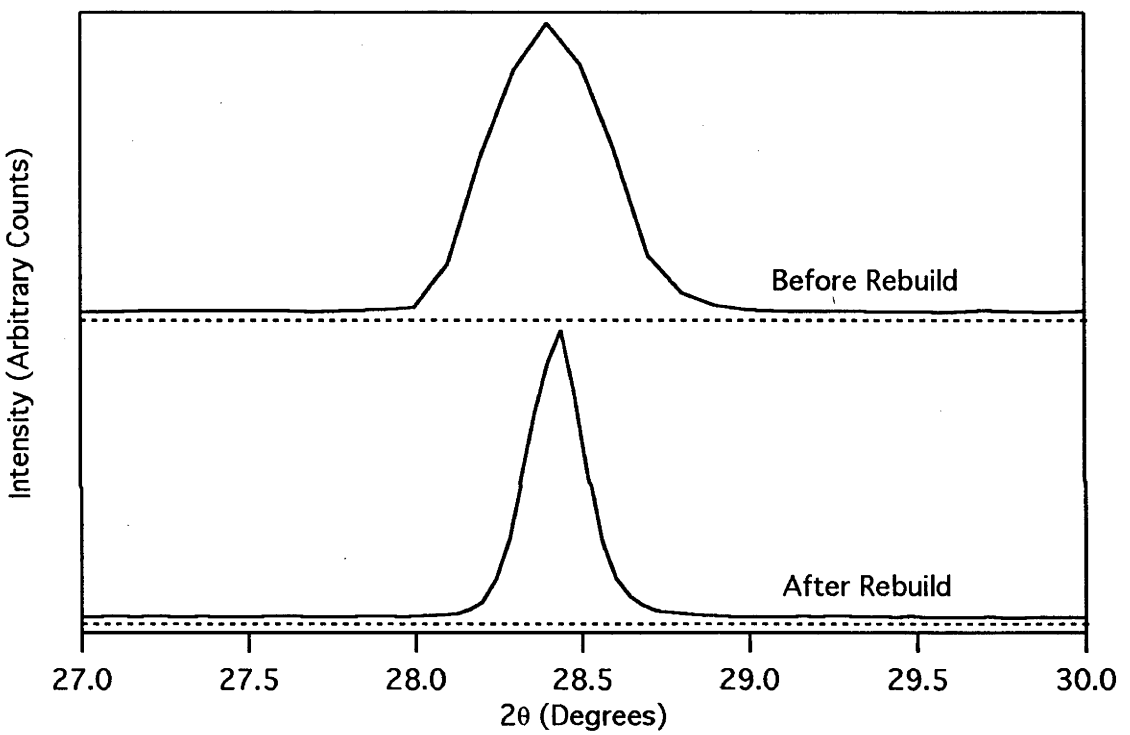

Figure 3.9: *the (003) reflection from the same silicon standard sample before and after the rebuild of the diffractometer described above. The dashed lines indicate the zero intensity level for each scan. The peaks have been normalised to the same maximum intensity, the upper scan having a step size of 0.10° and the lower 0.06°.*

A comparison between the x-ray diffractograms of the silicon (111) peak made before and after the rebuild shown in Figure 3.9 and Table 3.2 demonstrates a considerable improvement in the peak profile and statistics; the same improvement is seen in the statistics for the (220) and (311) reflections, displayed in Table 3.2. Figure 3.10 plots the resolution function of the rebuilt diffractometer, showing a steady drop with angle; the minimum useful diffraction angle that could be measured with the rebuilt instrument was ~4.0° 2θ.

	Before Rebuild			After Rebuild		
Index	FWHM	S/N	a	FWHM	S/N	a
(111)	0.412	34.34	5.439	0.198	50.13	5.431
(220)	0.427	34.49	5.431	0.222	59.24	5.429
(311)	0.427	20.77	5.433	0.241	38.99	5.431

Table 3.2: *the full width at half maximum (FWHM), signal to noise (S/N) and cubic cell dimension derived from diffractograms of the same silicon standard taken before and after the rebuild. At 298 K the standard value for a=5.4309 Å*[18]*. There is a great improvement in the full width and signal to noise values.*

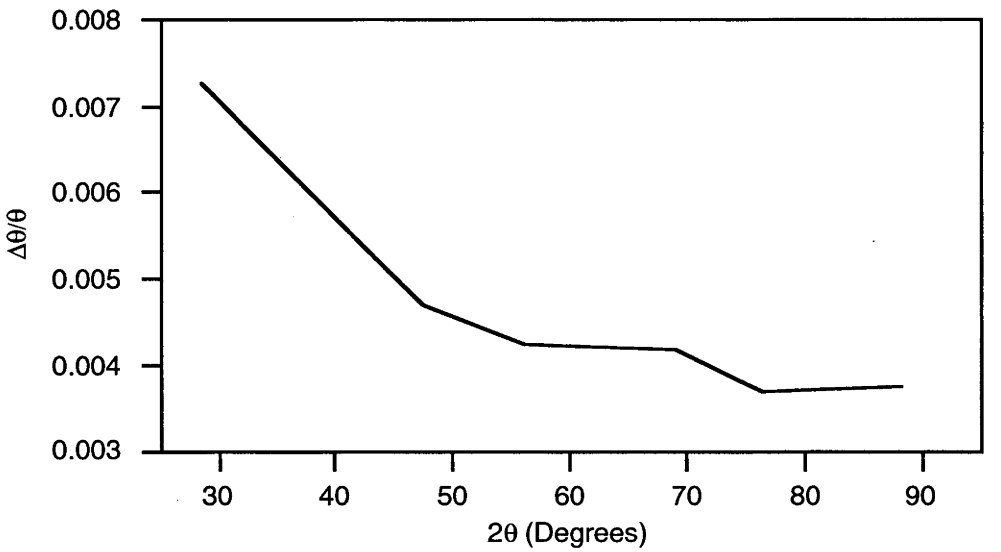

Figure 3.10: *Resolution of the rebuilt diffractometer from silicon standard, showing Δθ/θ (in degrees) versus the reflection angle of the main silicon peaks.*

3.4.7 XRD experimental procedure

The first step after loading a new sample was to determine its alignment with respect to the beam. The attachment between the cryostat and the centre stick allowed the stick, and thus the sample, to be rotated independently of the cryostat, this rotation being equivalent to the θ rotation of the diffractometer. In order to find the sample's alignment the detector arm was driven to the 2θ position of a strong reflection of the sample; initially the graphite (1,0) peak was used, since this would be present with only a minor distortion in any graphite intercalation compound (see Chapter 1). The sample was rotated until a maximum in the x-ray flux at the detector was seen; since graphite (1,0) is an *ab*-plane peak, this corresponds to the sample being in correct alignment for transmission mode. Later the very strong (003) reflection was used instead after it had been determined for Rb- and K-GICs by early experiments; the flux maximum for this peak corresponds to

the correct alignment for reflection mode. A 360° scale on the stick allowed the operator to rotate the orientation of the sample between reflection and transmission modes once the alignment of the sample is determined.

The experimental scans to get the *ab*-plane data on the samples were quite slow, usually taking 15 hours. This was a result of several factors: the samples were highly absorbing, with only ~8% transmission for the Rb-GICs, and were not easily made thinner after preparation; the polymer windows and beryllium can in the cryostat absorbed another 50% of the flux; the optical arrangement needed accommodate the cryostat made the beam flight path very long; and finally the a-b plane structures were often poorly ordered resulting in weak scattering intensities.

c-axis scans were much more rapid, with the most common scan time around 2 hours, as a result of the very strong c-axis peaks.

After data was collected it was uploaded using file transfer protocol (ftp) to one of the RSC's Hewlett-Packard Unix servers and from there transferred to other computers for reduction and analysis.

References

1. A. Inaba, J. Skarbek, J.R. Lu, R.K. Thomas, C.J. Carlile, and D.S. Sivia, *The librational ground state of monodeuterated methane adsorbed on graphite.* Journal of Chemical Physics, 1995. **103**: p. 1627-1624.

2. C. Morphett, PhD Thesis, 1986, Oxford.

3. E.P. Gilbert, P.W. Reynolds, and J.W. White, *Characterisation of a Basal Plane Oriented Graphite.* Journal of the Chemical Society, Faraday Transactions, 1998. **94**(13): p. 1861-1868.

4. G. Lockhart, Personal communication, 1992.

5. J.P. Beaufils, T. Crowley, T. Rayment, R.K. Thomas, and J.W. White, *Tunnelling of hydrogen in alkali metal intercalation compounds I: $C_{25}Rb(H_2)_x$ and $C_{24}Cs(H_2)_x$.* Molecular Physics, 1981. **44**: p. 1257-1269.

6. A. Herold, *Recerches sur les composes d'insertion du graphite.* Bull. Soc. Chim. Fr., 1955. **187**: p. 999.

7. A. Herold, *Crystallo-Chemistry of Carbon Intercalation Compounds*, in *Intercalated Layered Materials*, F. Levy, Editor. 1979, D. Riedel Publishing Company: Dordrecht. p. 321-422.

8. F.R. Trouw and J.W. White, *Dynamics of Intercalated Molecules, Part 3.- Structure of $C_{28}Cs(CD_4)$.* Journal of the Chemical Society, Faraday Transactions A, 1988. **84(7)**: p. 841-859.

9. W.J. Stead, I.P. Jackson, J. McCaffrey, and J.W. White, *Tunnelling of Hydrogen in Alkali-metal-Graphite Intercalation Compounds - A systematic study of $C_{24}Rb(H_2)_x$ and its Structural Consequences.* Journal of the Chemical Society, Faraday Transactions, 1988. **84(10)**: p. 1669-1682.

10. R. Jenkins, *Instrumentation*, in *Modern Powder Diffraction*, D.L. Bish and J.E. Post, Editors. 1989, Mineralogical Society of America: New York. p. 19-43.

11. W. Parrish, *Powder and related techniques: X-ray techniques*, in *International Tables for Crystallography, Volume C: Mathematical, Physical and Chemical Tables*, A.J.C. Wilson, Editor. 1992, Kluwer Academic Publishers: Dordrecht. p. 42-79.

12. K. Watanabe, T. Kondow, M. Soma, T. Onishi, and K. Tamaru, *Molecular-sieve type sorption on alkali graphite intercalation compounds.* Proceedings of the Royal Society of London A, 1973. **333**: p. 51-67.

13. R. Jenkins, *Experimental Procedures*, in *Modern Powder Diffraction*, D.L. Bish and J.E. Post, Editors. 1989, Mineralogical Society of America: New York. p. 47-69.

14. W. Parrish, *Detectors for X-rays: Scintillation and solid state detectors*, in *International Tables for Crystallography*
Volume C: Mathematical, Physical and Chemical Tables, A.J.C. Wilson, Editor. 1992, Kluwer Academic Publishers: Dordrecht. p. 539-542.

15. U.W. Arndt, *Generation of X-rays*, in *International Tables for Crystallography*
Volume C: Mathematical, Physical and Chemical Tables, A.J.C. Wilson, Editor. 1992, Kluwer Academic Publishers: Dordrecht. p. 167-172.

16. A.R. Ubbelolde and F.A. Lewis, *Graphite and its Crystal Compounds*. 1960, London: Oxford University Press. 217.

17. S.C. Moss and R. Moret, *Chapter 2. Structural Properties and Phase Transitions*, in *Graphite Intercalation Compounds I Structure and Dynamics*, H. Zabel and S.A. Solin, Editors. 1990, Springer-Verlag: Berlin. p. 5-58.

18. E. Galdecka, A.W.S. Johnson, O. Olsen, W. Parrish, B.T.M. Willis, and A.J.C. Wilson, *Determination of Lattice Parameters*, in *International Tables for Crystallography, Volume C, Mathematical, Physical and Chemical Tables*, A.J.C. Wilson, Editor. 1992, Kluwer Academic Publishers: Dordrecht. p. 420-466.

Chapter 4: Results

4.1: The Stage 2 Binary Graphite Intercalation Compounds RbC_{25} and KC_{25}

4.1.1: RbC_{25}

The structure of the binary GIC RbC_{25} has been described in several previous works[1, 2]; it is included here to validate on the parent binary GIC the modelling technique which we will later employ on its ternary derivatives. At 90 K it has been found to possess an *ab*-plane unit cell which is a commensurate $\sqrt{43}x\sqrt{43}$ hexagonal superlattice of the hexagonal graphite *ab*-plane structure.

4.1.1.1: Data

Figure 4.1.1 shows the *ab*-plane x-ray powder diffraction pattern produced by an oriented sample of RbC_{25} at 90 K, while Figures 4.1.2 and 4.1.3 show the *c*-axis oriented XRD powder patterns of the same sample. This sample was prepared to a stoichiometry of Rb: 25C in the manner described in Chapter 3, and weighed 0.409 g, equivalent to $1.06x10^{-3}$ moles of RbC_{25}.

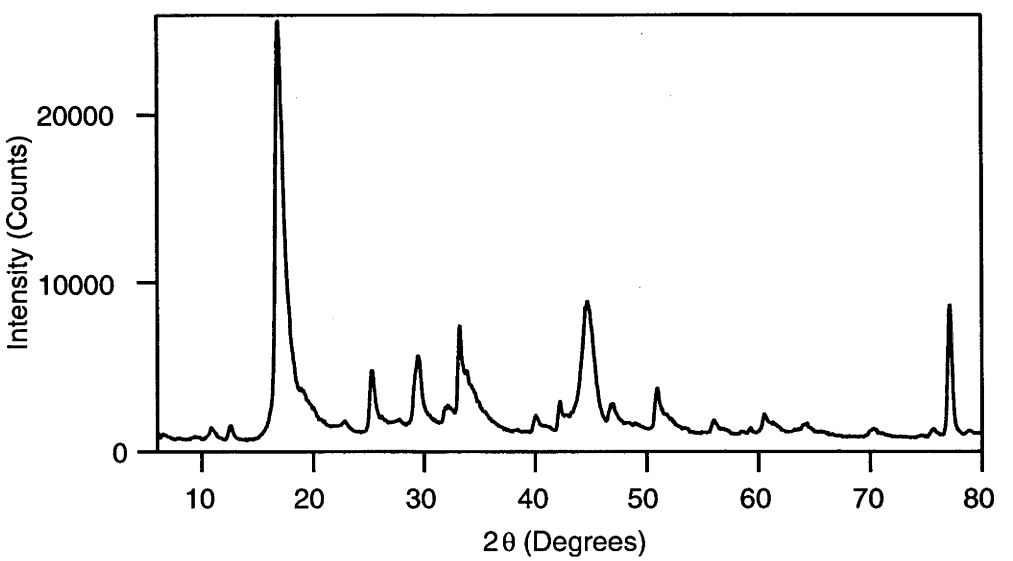

Figure 4.1.1: *x-ray powder diffraction pattern of an ab-plane oriented sample of RbC_{25} at 90 K.*

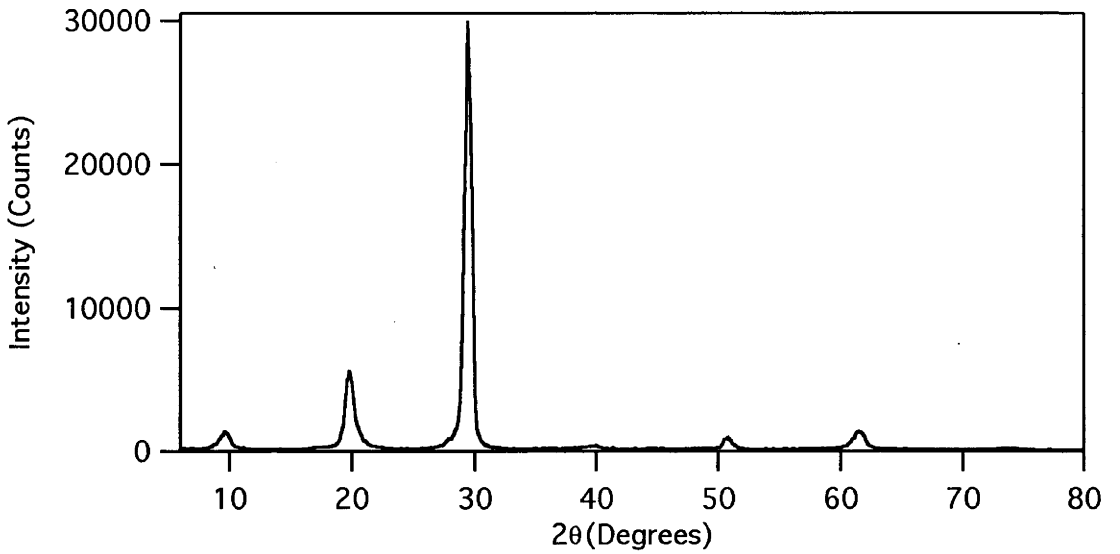

Figure 4.1.2: *x-ray powder diffraction pattern of a c-axis oriented sample of* RbC_{25} *at 90 K.*

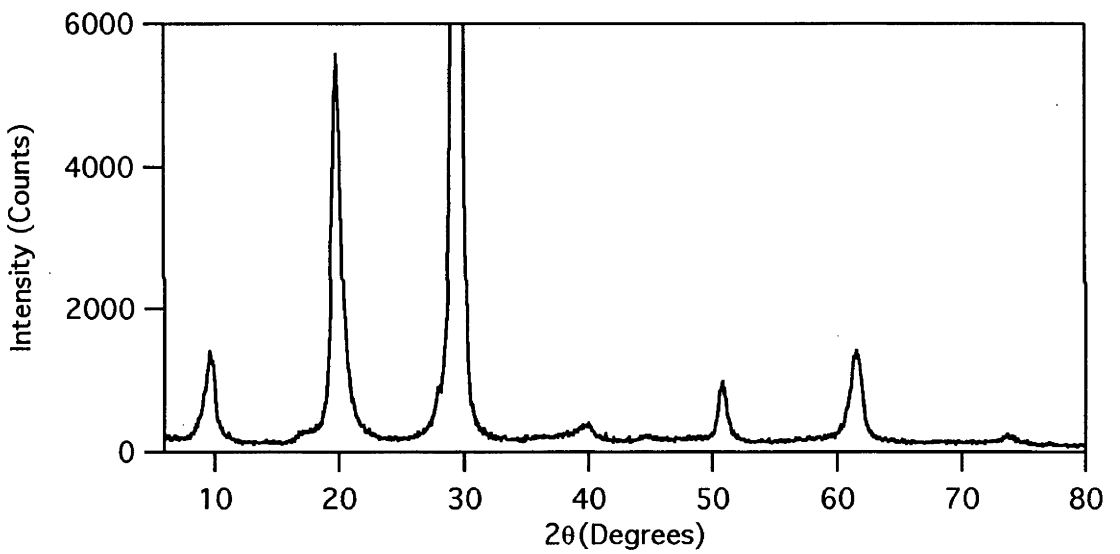

Figure 4.1.3: *x-ray powder diffraction pattern of a c-axis oriented sample of* RbC_{25} *at 90 K, expanded to show the smaller peaks.*

4.1.1.2 Symmetry and Unit Cell

The *ab*-plane and *c*-axis diffraction patterns are indexed from d-spacings derived from peak maxima in Tables 4.1.1 and 4.1.2 respectively. The *ab*-plane indexing in Table 4.1.1 shows a good fit to the $\sqrt{43}$x$\sqrt{43}$ unit cell: if the outlier at 6.6° is removed the average *ab*-plane cell dimension is 6.54 Å - equivalent to a multiple of $\sqrt{42.77}$ of the graphite in-plane dimension of 2.472 Å which was derived from the graphite (10) and (11) peaks in the same pattern - with a standard deviation of 0.03 Å. This value of a_{gr} is

in accordance with the expected expansion of the carbon-carbon bond length in a stage 2 rubidium graphite intercalation compound[3].

Data			√43x√43 Cell			
2θ (Degrees)	Intensity (Counts)	D (Å)	h	k	*a* (Å)	$(a/a_{gr})^2$
6.6	947	13.39	1	0	15.464	39.125
10.86	1431	8.146	1	1	16.293	43.433
12.6	1564	7.025	2	0	16.224	43.066
16.86	25671	5.258	2	1	16.065	42.226
22.86	1820	3.890	3	1	16.195	42.916
25.32	4805	3.517	4	0	16.246	43.185
27.78	1926	3.211	3	2	16.163	42.744
29.52	5659	3.026	4	1	16.011	41.945
32.16	2748	2.783	5	0	16.069	42.248
33.24	7492	2.695	3	3	16.171	42.788
40.02	2194	2.253	5	2	16.246	43.182
42.24	3005	2.139	1	0	2.470	0.999
44.7	8942	2.027	-	-	-	-
46.98	2854	1.934	6	2	16.104	42.433
50.94	3734	1.793	5	4	16.167	42.763
56.04	1834	1.641	8	1	16.189	42.884
58.5	1200	1.578	7	3	16.192	42.898
59.22	1292	1.560	9	0	16.214	43.015
60.54	2084	1.529	8	2	16.185	42.859
64.32	1712	1.448	7	4	16.127	42.555
70.26	1337	1.340	7	5	16.150	42.677
75.6	1359	1.258	10	2	16.173	42.795
77.1	8725	1.237	1	1	2.474	1.001
78.9	1246	1.213	9	4	16.156	42.708

Table 4.1.1: *ab-plane x-ray diffraction pattern shown in Figure 4.1.1 indexed as a single phase commensurate hexagonal superlattice with unit cell dimension equal to* $\sqrt{43} \times a_{gr}$*, the graphite ab-plane dimension. The peaks at 42.24° and 77.1° type are indexed as the (10) and (11) peaks of graphite, from which* a_{gr} *is determined to be 2.472 Å.*

The *c*-axis indexing in Table 4.1.2 indicates that, while the c-axis structure has an average spacing of 9.059 Å, the d-spacings of individual peaks vary widely away from

this average position, with a standard deviation of 0.09 Å. This variation is a characteristic sign of an interstratified system, as described in Chapter 1, and will be analysed later in this section.

Data				Indexing	
2θ (Degrees)	Intensity (Counts)	I/I_{max} x100	D (Å)	l_a	D x l_a (Å)
9.6	1401	4.69	9.213	1	9.213
19.8	5577	18.66	4.484	2	8.968
29.4	29882	100.0	3.038	3	9.114
39.4	380	1.27	2.287	4	9.147
50.82	982	3.29	1.797	5	8.983
61.56	1306	4.37	1.506	6	9.038
73.68	201	0.67	1.286	7	9.000

Table 4.1.2: *The c-axis data shown in Figures 4.1.2 and 4.1.3 indexed as a single phase system. There is a considerable variation of peak positions away from the average d-spacing - an indication that there may be more than one interstratified phase.*

4.1.1.3 *ab*-plane Rietveld simulations of RbC_{25}

As the $\sqrt{43}x\sqrt{43}$ indexing fits the observed Bragg peak positions, the Rietveld package "GSAS"[4] was used next to attempt to locate the rubidium ions inside the unit cell. Previous workers had proposed that the *ab*-plane structure consists of $\sqrt{7}x\sqrt{7}$ domains of rubidium ions separated by $2x\sqrt{7}$ domain walls, which produced a correct $\sqrt{43}x\sqrt{43}$ unit cell and RbC_{25} stoichiometry, with a density between that of the 2x2 superlattice of the stage 1 GICs and the $\sqrt{7}x\sqrt{7}$ superlattice.

The two Rietveld fits shown in Figure 4.1.4 employ firstly an ideal version of this structure, where the rubidium ions are located in the center of the graphite hexagons, and secondly a model where the rubidium ions have been allowed to relax away from the hexagon centres in order to improve the simulated intensities. The second refinement is clearly superior in reproducing the observed peak intensities, and this *ab*-plane structure is shown in Figure 4.1.5, a P6 hexagonal $\sqrt{43}x\sqrt{43}$ superlattice with rubidium ions at the position of (0,0) and (0.442, 0.198).

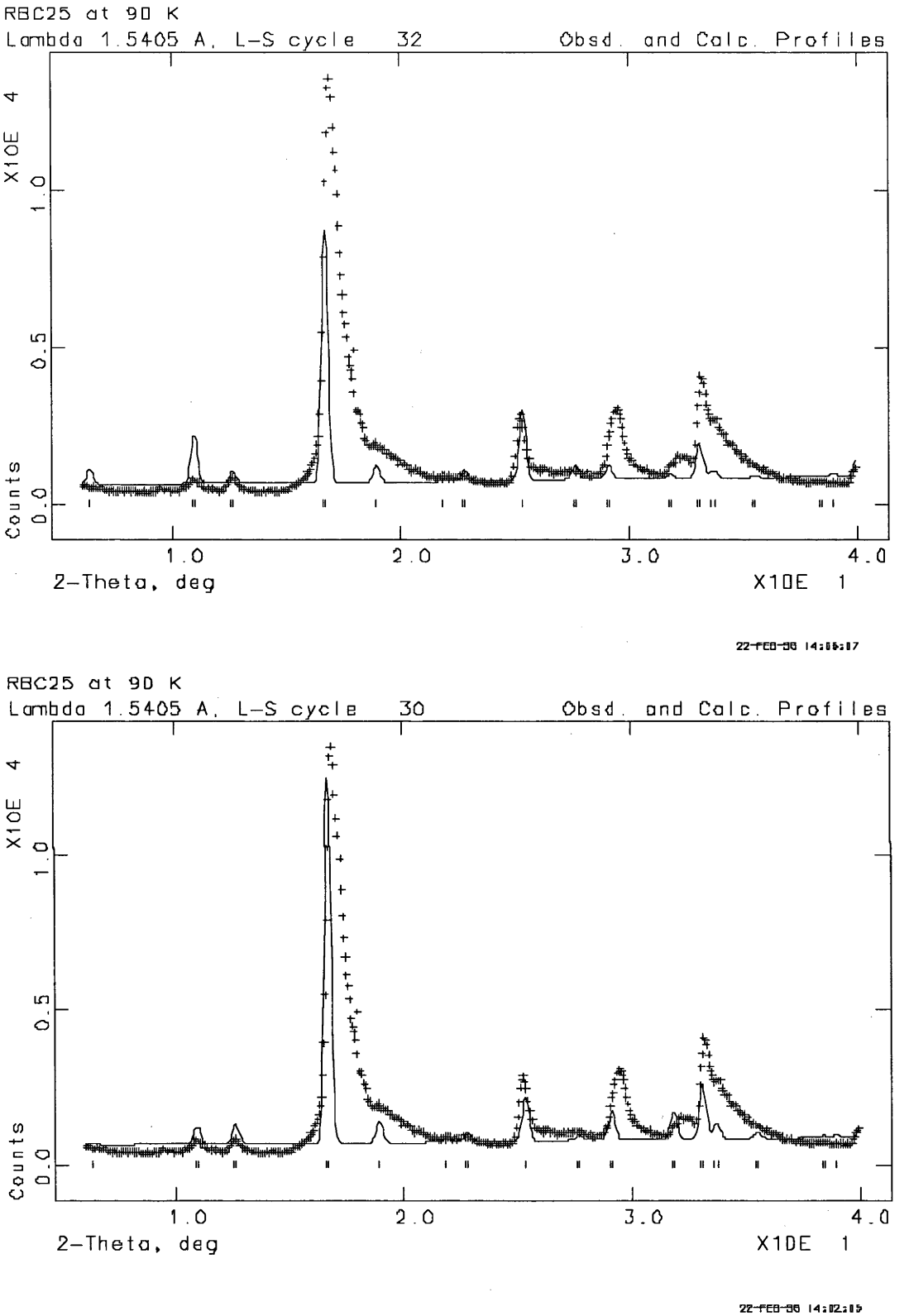

Figure 4.1.4: *Two Rietveld fits to the ab-plane-oriented 90K RbC_{25} pattern, employing a commensurate $\sqrt{43}x\sqrt{43}$ P6 unit cell with seven rubidium atoms. The upper fit has ions located at (0,0) and (0.465,0.209), the lower at (0,0) and (0.442,0.198). These correspond to the ideal and refined models of the structure.*

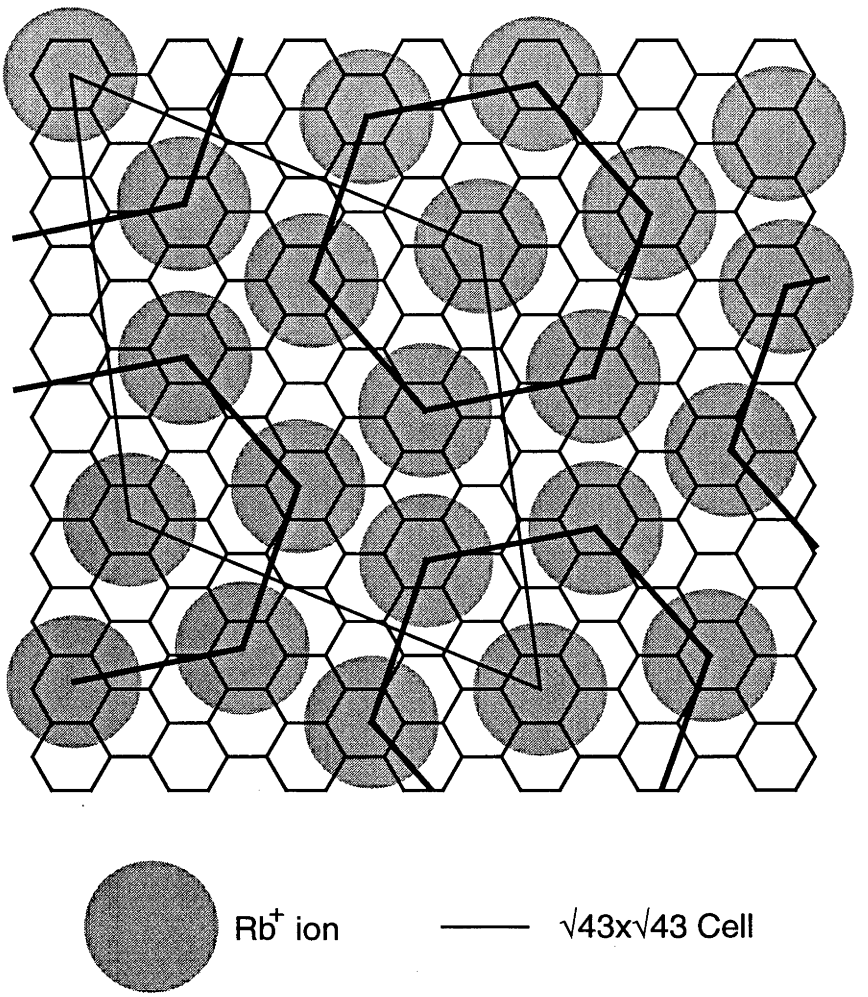

Figure 4.1.5: *The ab-plane structure of RbC_{25} used in the Rietveld simulation shown in Figure 4.1.4 above and in the full-pattern simulations that follow. The unit cell has P6 plane symmetry, with the rubidium ions in two positions, at (0, 0) and (0.442, 0.198).*

4.1.1.4 *ab*-plane full pattern simulations of RbC_{25}

After determining the structure and unit cell composition, further simulations were undertaken using the full pattern method described in Chapter 2. A first step is shown in Figure 4.1.6, where the strongest peak in the observed pattern - the (21) of the √43x√43 structure - is compared with three simulated peaks which vary only in the size of the in-plane crystallite domain size N_1.

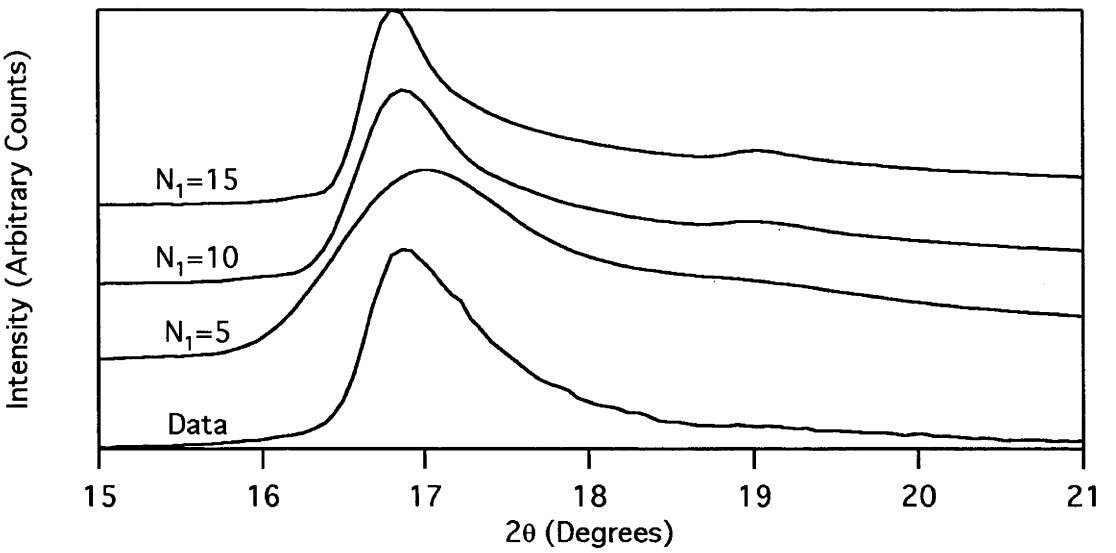

Figure 4.1.6: *The (2,1) peak of the √43x√43 superlattice from the ab-plane oriented experimental data, taken at 90 K, is compared with three simulations of the same peak where the in-plane crystallite size N_1 is varied. The other constants used in the calculations were a_{gr} = 2.472 Å; c = 9.08 Å; λ = 1.54178 Å. The ab-plane crystal structure used for the simulations is shown in Figure 4.1.5.*

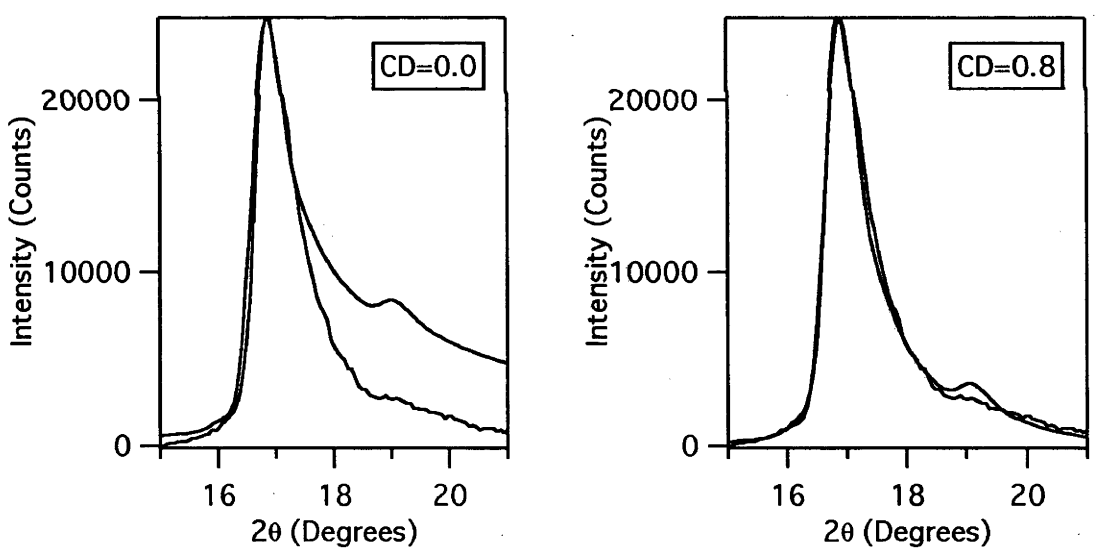

Figure 4.1.7: *The effect of the c-axis damping factor CD on the simulated turbostratic band shape of the (2,1) √43x√43 peak, compared with the data taken at 90K. The pattern simulations all use N_1=10; a_{gr} = 2.472 Å; c = 9.08 Å; λ = 1.54178 Å.*

The second step is to determine the value of the c-axis dampening parameter CD, described in Chapter 2. This is shown in Figure 4.1.7 above.

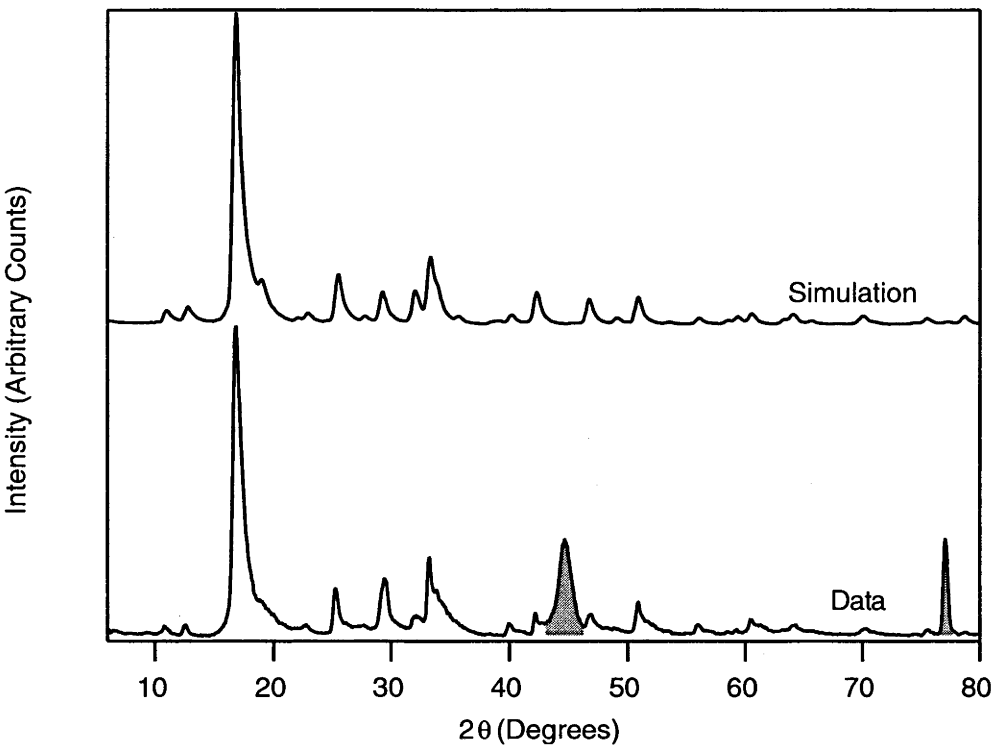

Figure 4.1.8: *ab-plane simulations of the √43x√43 structure of RbC_{25}, compared with the data taken at 90K. There are two Rb^+ ions, at (0, 0) and (0.489, 0.198) respectively, and uses the parameters N_1=10; a_{gr} = 2.472 Å; c=9.08 Å; λ = 1.54178 Å. The shaded peaks are the graphite (101) and (11); the graphite structure is not simulated and thus these peaks do not appear in the simulated pattern.*

Symmetry	P6
a	6.557 (√43)
a_{gr}	2.472 Å
c	9.08 Å
$N_1=N_2$	10
N_3	1
δ	0
CD	0.8
Thermal factors	Rb=0.0

Table 4.1.3: *the parameters used for the ab-plane simulation shown in Figure 4.1.8. These parameters are explained in detail in Chapter 2.*

The final simulation of the whole pattern is shown in Figure 4.1.8, and as with the rest of the *ab*-plane simulations in this thesis does not simulate the graphite structure that produce strong peaks at 44.7° and 77.1°. The parameters are shown in Table 4.1.3. The complete simulation produces a good overall fit, but has several problems in producing exact intensity matches. While the observed peak at 29.5° is much stronger than the simulated one, the c-axis (003) breakthrough is expected to produce a peak at this position; the combined (33) and (42) peaks at 33.2° is a more significant mismatch. No significant thermal factors could be included without eliminating observed high order peaks from the simulated patterns.

4.1.1.5 c-axis simulations of RbC_{25}

The *c*-axis pattern simulations include no *ab*-plane structure at all, and thus were fast enough that no Rietveld modelling was needed. Figure 4.1.9 shows two comparison plots (at different scales) of the c-axis data taken at 90 K and a simulated pattern.

While there is a generally good overall positional and intensity fit, there are two primary problems with the c-axis simulation shown - firstly, the intensity of the (001) and (002) peaks is too high, and secondly the variation of the d-spacing away from the average is not reproduced by the simulation.

These errors may both result because these simulations do not include the effects of interstratification, which is known to produce such variations and is seen in the c-axis indexing in Table 4.1.2. The variation away from the average d-spacing found in the c-axis indexing is plotted in Figure 4.1.10. It is noticeable in this figure that there are minima at l=2 and l=5, and that the maxima appear to be near l=1 and 4. As a first order analysis this implies that there is a modulation by a second structure differing in D from the first by a value approximately 1/3 the average d-spacing, which is equal to 3.02 Å. This permits an educated guess as to the nature of the second interstratified compound - it is probably a GIC of Stage 1 or Stage 3, either of which would differ in d-spacing from the stage 2 compound by 3.35 Å. This possibility can be investigated using the Hendricks-Teller equation for the interference function of a randomly interstratified compound described in Chapter 2. Figure 4.11 plots the shift in peak position for two model interstratified systems: both systems consists of 90% stage 2 GIC of D=9.06 Å, but in first model the remaining 10% is stage 1 (D=5.71 Å), while in the second it is 10% stage 3 (D=12.41 Å). Clearly the second model produces similar peak shifts to those observed, while the stage 1 intercalate does not. We can conclude from this that a significant fraction of the sample is a stage 3 contaminant.

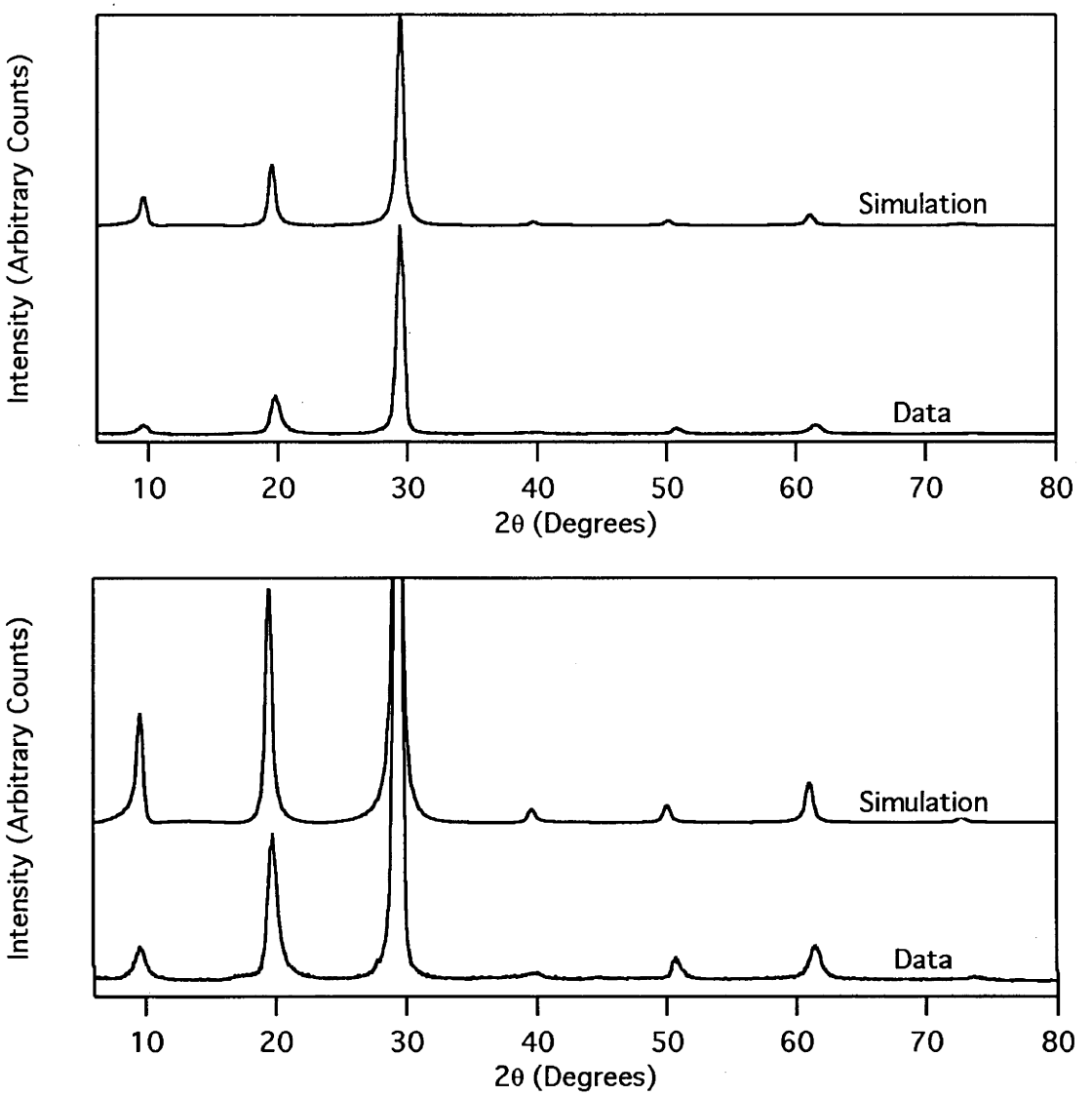

Figure 4.1.9: *c-axis oriented RbC_{25} data taken at 90 K compared with a simulated diffraction pattern calculated with these parameters: c = 9.10, N_3 = 20, δ = 10, λ = 1.54178 Å, and an overall temperature factor of 0.4.*

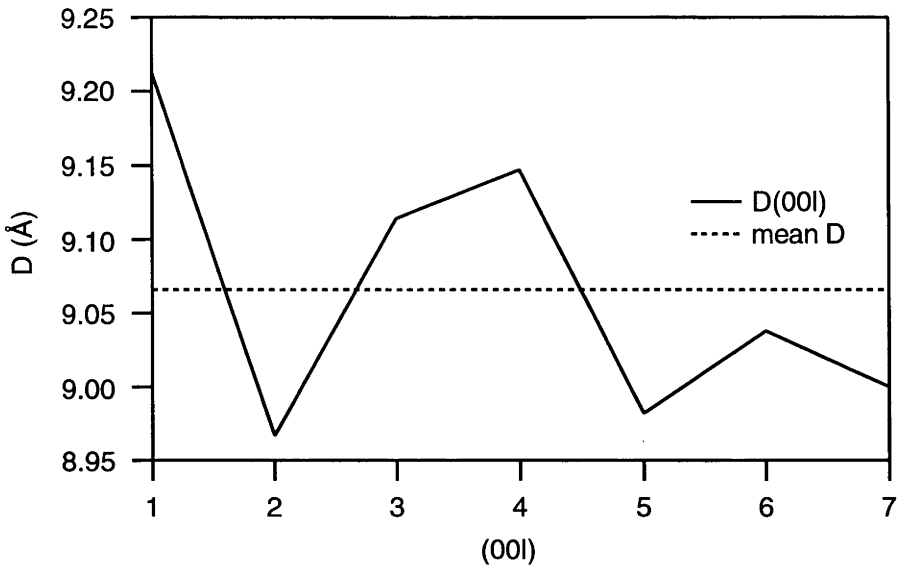

Figure 4.1.10: *d-spacing determined from each (00l) value of the RbC_{25} c-axis pattern, plotted against the (00l) index. The mean d-spacing of 9.066 Å is shown as a dashed line.*

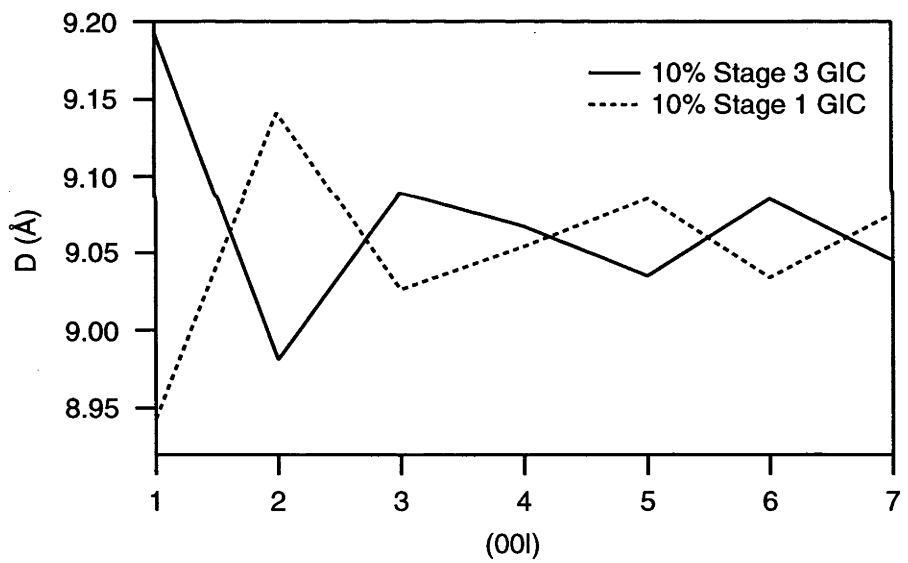

Figure 4.1.11: *the peak shifts produced by two simulated interstratified systems. Both compounds are 90% stage-2 GIC with d=9.06Å, but the remnant 10% is either stage 1 with d=5.71 Å, or stage 3 with d=12.41 Å.*

4.1.2: KC_{25}

The stage 2 graphite intercalation compound KC_{25} has been the subject of considerable previous work[2, 5] which has not produced a universally accepted low temperature in-plane structure, though it is thought to be incommensurate. As attempting to determine the unknown crystal structure of this binary compound outside the subject of this work, no attempt to analyse the *ab*-plane data will be made, especially as the binary *ab*-plane structure is expected to be destroyed by the process of physisorption. Appropriate simulations of the *c*-axis data will be attempted.

4.1.2.1 Data

The sample of KC_{25} was produced using the same method (described in Chapter 3) employed for the RbC_{25} samples, to a stoichiometry of K:25C, and weighed 0.480 grams. The *ab*-plane oriented diffraction pattern taken at 90 K is shown in Figure 4.1.12, and the *c*-axis oriented in Figure 4.1.12.

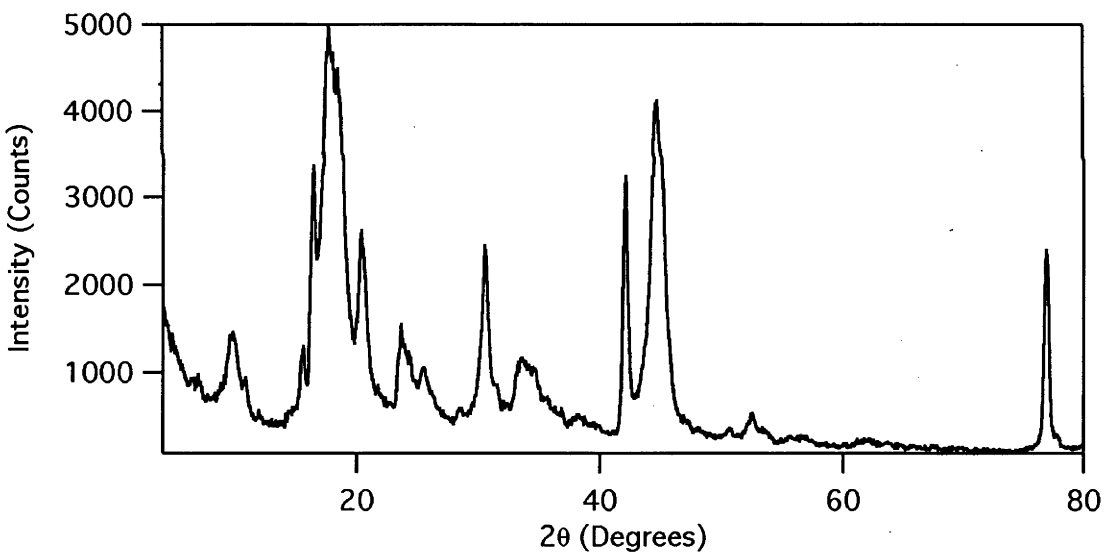

Figure 4.1.12: *XRD pattern taken from an ab-plane oriented sample of KC_{25} at 90 K.*

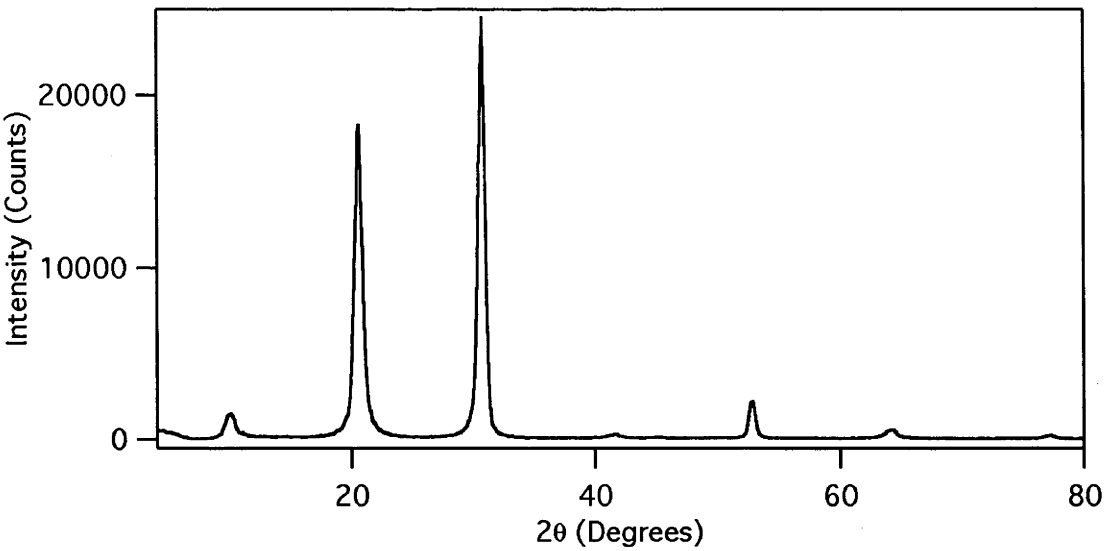

Figure 4.1.13: *XRD pattern taken from an c-axis oriented sample of KC_{25} at 90 K.*

4.1.2.2 *c*-axis Symmetry and Simulations

The *c*-axis diffraction patterns is indexed in Table 4.1.4 below: the c-axis structure has an average spacing of 8.693 Å, but as with the RbC_{25} c-axis patterns, the d-spacings of individual peaks are displaced away from the average position, though with a smaller standard deviation of 0.056 Å.

Data				Indexing	
2θ (Degrees)	Intensity (Counts)	I/Imax x100	D (Å)	l_a	D x l_a (Å)
10.06	1511	6.15	8.792	1	8.792
20.62	18275	74.4	4.307	2	8.614
30.76	24551	100.0	2.907	3	8.720
41.62	327	1.33	2.170	4	8.679
52.78	2032	8.28	1.734	5	8.672
64.12	552	2.25	1.452	6	8.714
77.08	252	1.03	1.237	7	8.661

Table 4.1.4: *The KC_{25} c-axis data shown in Figures 4.1.13 indexed as a single phase system. As with the RbC_{25} system, there is a variation of peak positions away from the average d-spacing of 8.693 Å, an indication that the system may be interstratified.*

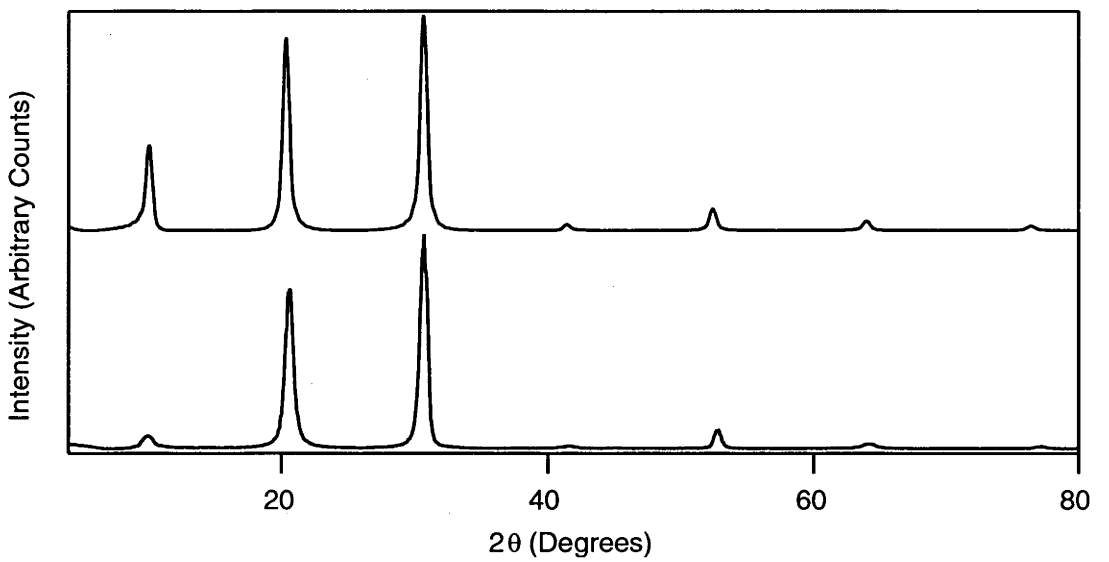

Figure 4.1.14: *c-axis oriented KC_{25} data taken at 90 K compared with a simulated diffraction pattern calculated with these parameters: c = 8.73 Å, N_3 = 20, δ = 10, λ = 1.54178 Å. There is a severe intensity misfit with the (001) reflection.*

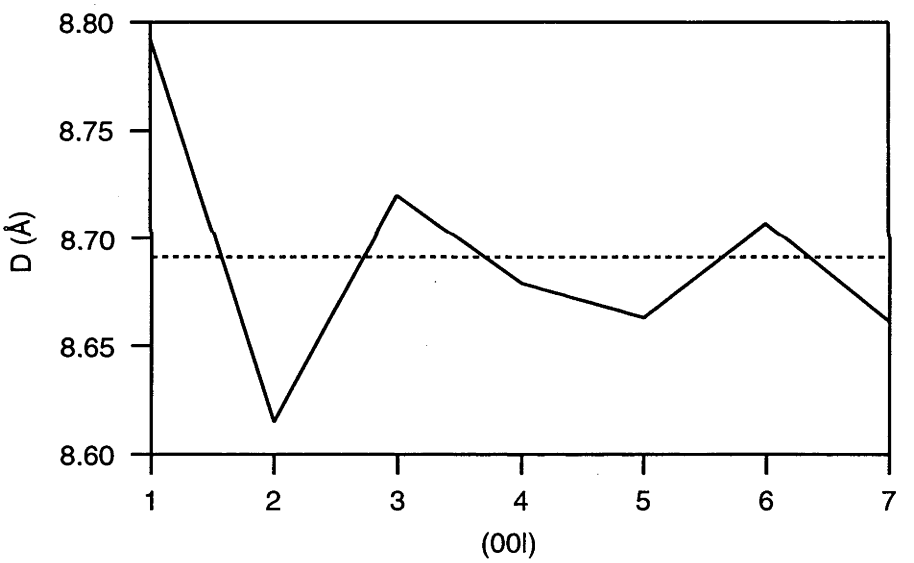

Figure 4.1.15: *c-axis d-spacing determined from each (00l) value of the KC_{25} pattern, plotted against the (00l) index. The average of 8.691 Å is shown as a dashed line.*

The c-axis simulation shown in Figure 4.1.14 uses the same values for N_3 and δ as the RbC_{25} simulation, though with a much smaller *c*-axis dimension; again as with the RbC_{25} simulation, there is a misfit in the simulated intensity for (001), and the data shows the shifts away from integer (00l) values that is characteristic of interstratification. Figure 4.1.15 shows this misfit of the KC_{25} *c*-axis peaks as a function of (00l), with a similar pattern of shifts as seen in the RbC_{25}; simulated interference functions using the

Hendricks-Teller formula were again made, and the peak shifts of the simulated peaks (in Figure 4.1.16) shows that the KC_{25} sample is also contaminated by ~10% stage 3 K-GIC.

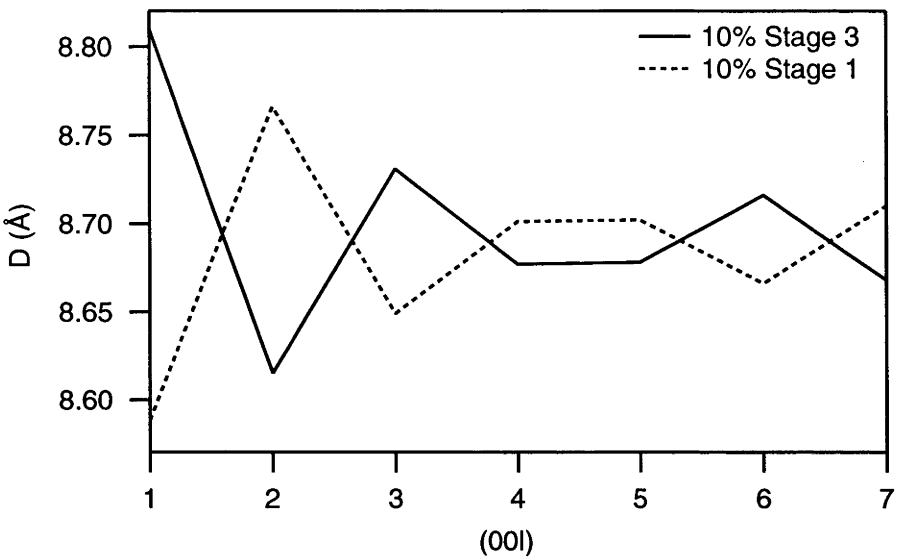

Figure 4.1.16: *the shifts in the (00l) D-spacing of two simulated interstratified structures, one of which is 90% stage 2 K-GIC and 10% stage 1, the second of which is 90% stage 2 and 10 % stage 3.*

4.1.3 Conclusion

The binary GIC RbC_{25} was found to adopt the same *ab*-plane structure that has been described in previous works, a $\sqrt{43}x\sqrt{43}$ hexagonal superlattice of the graphite layer; from the *c*-axis pattern it was determined that approximately 10% of the sample consisted of a stage 3 GIC. Unsurprisingly the *ab*-plane pattern of KC_{25} could not be indexed, since it is probably incommensurate, but the *c*-axis data found that this sample too was approximately 10% stage 3.

References

1. G.R.S. Naylor and J.W. White, *Structure of Second Stage Graphite-Rubidium, $C_{24}Rb$.* Journal of the Chemical Society, Faraday Transactions, 1987. **83(11)**: p. 3447-3458.

2. S.C. Moss and R. Moret, *Structural Properties and Phase Transitions*, in *Graphite Intercalation Compounds I Structure and Dynamics*, H. Zabel and S.A. Solin, Editors. 1990, Springer-Verlag: Berlin. p. 5-58.

3. D.E. Nixon and G.S. Parry, *The expansion of the carbon-carbon bond length in potassium graphites.* Journal of Physics C, 1969. **2**: p. 1732-1741.

4. A.C. Larson and R.B. Von Dreele, LANSCE, MS-H805, Los Alamos National Laboratory, NM 87545, USA, .

5. M.J. Winokur and R. Clarke, *Low-temperature structural transition in KC_{24}.* Phys. Rev. B, 1986. **34**(7): p. 4948-4951.

4.2: Argon Physisorption by Rubidium Graphite Intercalation Compounds: The Structure of $RbAr_xC_{25}$ for $0<x<1.2$

Of all the ternary graphite intercalation compounds described in the initial studies, the alkali metal-argon GICs appear to have been the most neglected. A literature search found no further publications on either the Cs-Ar or the Rb-Ar compounds since the early gas absorption studies[1]. They found that the argon-rubidium-graphite system possesses the Type III or "all-or-none" isotherm, with no gas being absorbed until a critical pressure is reached, after which the reaction proceeds rapidly to saturation, achieving a final Ar/Rb ratio of 1.2. Here we will present powder diffraction data for the ternary intercalation compounds $RbAr_xC25$ for $0<x<1.2$ from oriented samples

4.2.1: Data

Figure 4.2.1 a) and b) shows the *ab*-plane diffraction patterns obtained from an oriented sample of stage-II rubidium-GIC that was cooled in stages from room temperature to 90 K while under an atmosphere of argon. The sample was prepared to a stoichiometry of RbC_{25}, and weighed 0.413 g, equivalent to 1.07×10^{-3} moles. The sample stick contained 4.5×10^{-3} moles of Ar, which provided a sufficient reservoir to reach the published saturation stoichiometry of $RbAr_{1.2}C_{25}$. However, these early experiments did not measure the pressure of the gas while it was being cooled, and so the uptake was not directly measured; the final saturation value is assumed to be at or near the published value. Each *ab*-plane scan took ~12 hours. *c*-axis scans were also taken after each *ab*-plane scan and are shown in Figure 4.2.2 (a) and (b).

Figures 4.2.3 and 4.2.4 show the *ab*-plane and *c*-axis oriented diffraction patterns for $RbAr_xC_{25}$, for $0.0 < x < \sim 1.2$. These are not all from the same sample: the patterns at $Ar_{1.2}$ are the same sample as the earlier patterns, while the patterns at Ar fillings of 0.0, 0.135 and 0.375 are all of a later sample used during the filling experiments. Attempts to dope the sample by increasing the pressure of argon gas over this (later) sample at a temperature of 90 K, failed to reach a stoichiometry of greater than $RbAr_{0.49}C_{25}$, at the maximum pressure (600 Torr) of Ar which could be attained by the gas handling line used: the patterns for all samples between $Ar_{0.375}$ and $Ar_{0.49}$ were the same, and only the former is shown here. However, cooling the sample slowly under the same pressure of Ar would produce the pattern shown in Figure 4.2.1, which from the *c*-axis data is clearly near the saturation value.

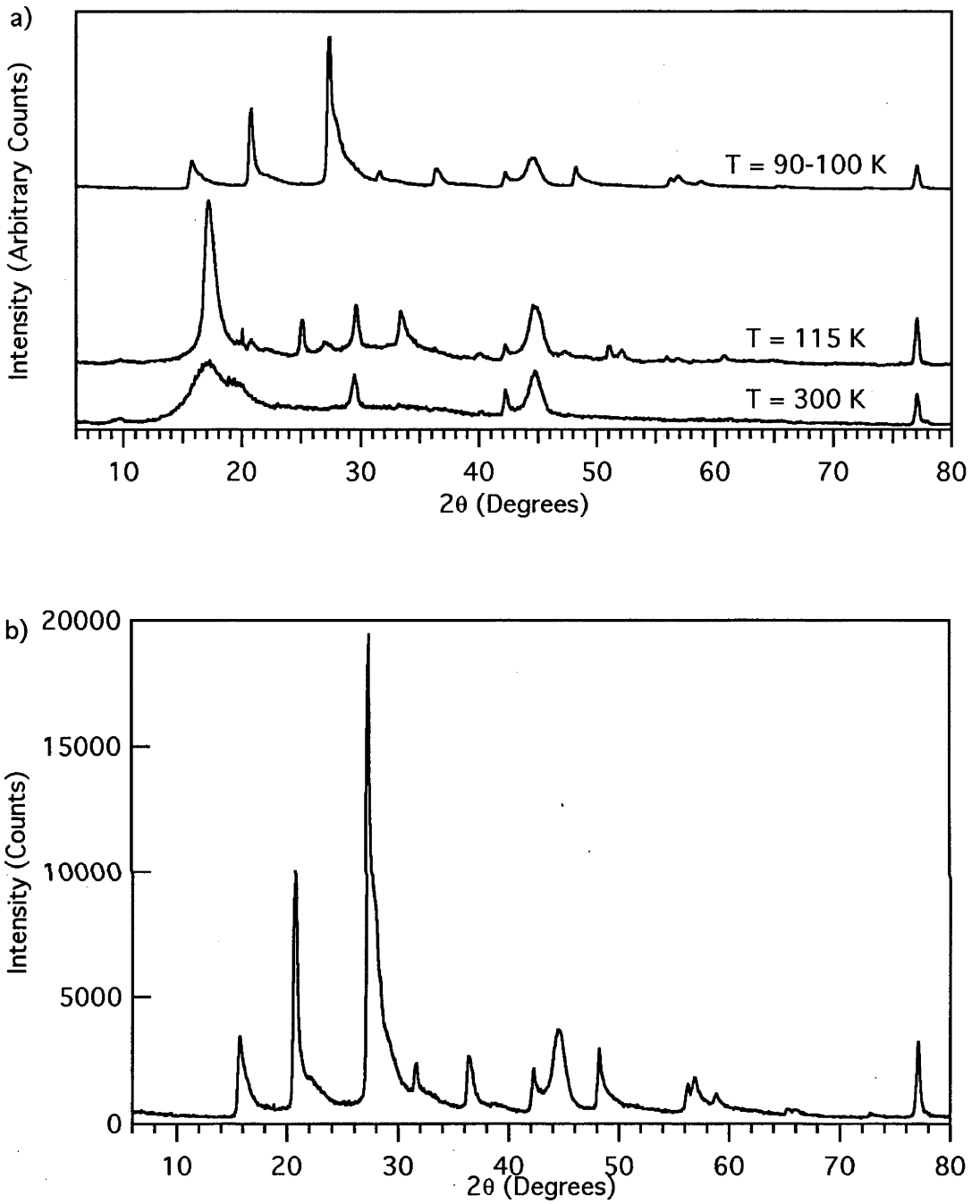

Figure 4.2.1: ***a)*** *A series of ab-plane-oriented XRD patterns, taken as a sample of* RbC_{25}*, under an atmosphere of Ar, was cooled from 300 K to 90 K. The patterns taken at 90 K and 100 K were identical, and are combined here to improve statistics. Note that the strongest peak in the Rb-Ar phase, at 27.4°, has appeared in the 115 K pattern.* ***b)*** *The combined 90 K + 100 K scans enlarged.*

This does not mirror reported results or our experience with Ar absorption on powdered RbC_{25}, but is similar to the reported absorption behaviour of N_2 on KC_{24}, where a ternary compound was obtained by slowly cooling a sample under nitrogen gas.

Though we conducted no further studies to determine the cause of this aberrant behaviour, it is possibly a result of the lower surface area of large pieces of "Papyex" graphite compared to fine powdered host.

4.2.2: Results

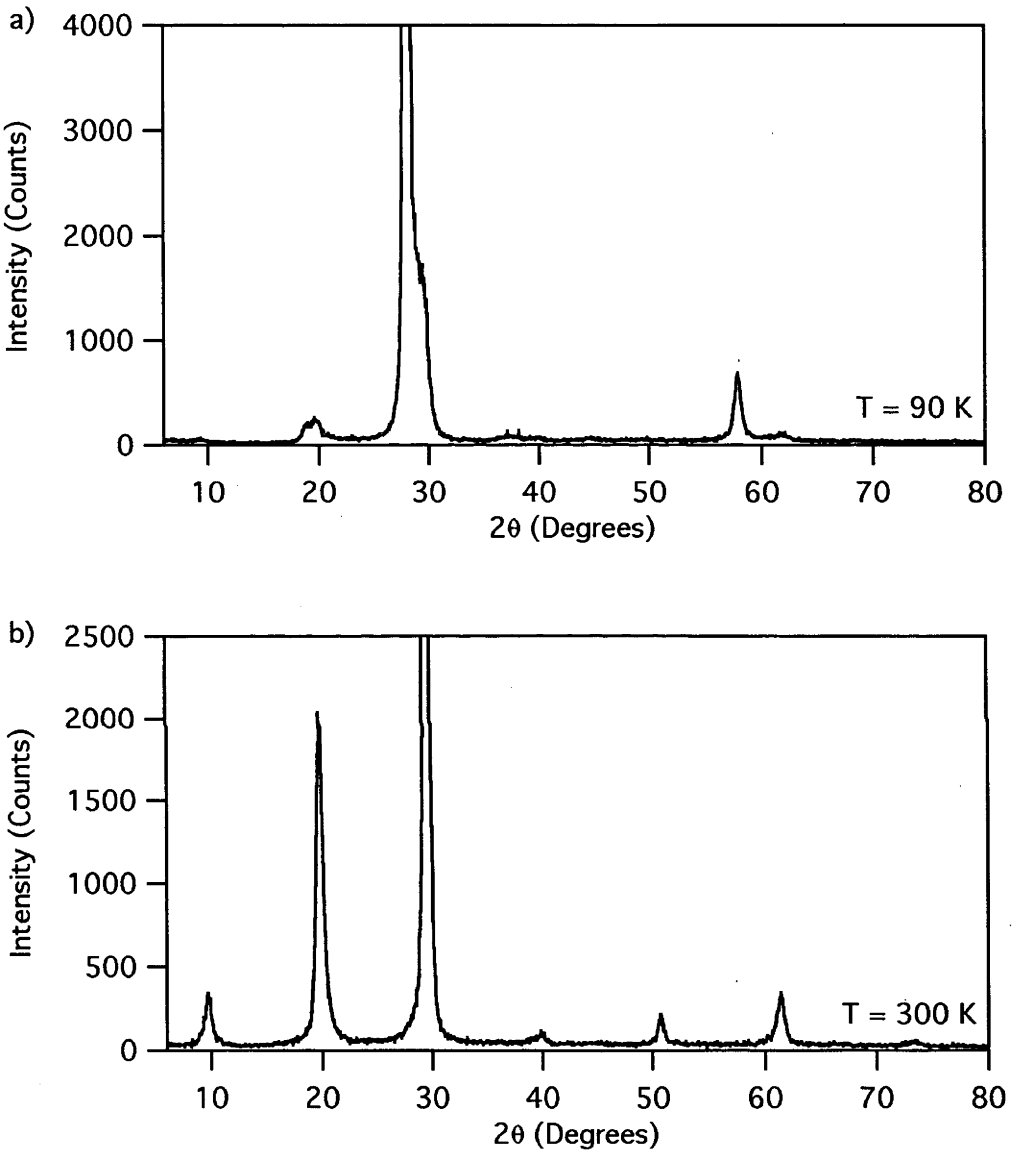

Figure 4.2.2: *c-axis oriented XRD patterns, taken as a sample of RbC_{25} was cooled from (b) 300 K to (a) 90 K, under an atmosphere of Ar. The strongest peak (indexed as (003)) is off scale in both patterns.*

Onset of Ar absorption occurred near 115 K. The strongest peak of the ternary pattern at 90 K appears in the 115 K pattern, which is otherwise identical to the diffraction pattern of RbC_{25} at that temperature. It is immediately apparent that the $RbAr_{1.2}C_{25}$ ternary at 90 K has a new in-plane crystal structure, while the narrower

lines and their closer approximation to the "perfect" turbostratic shape both indicate larger in-plane crystal domain sizes.

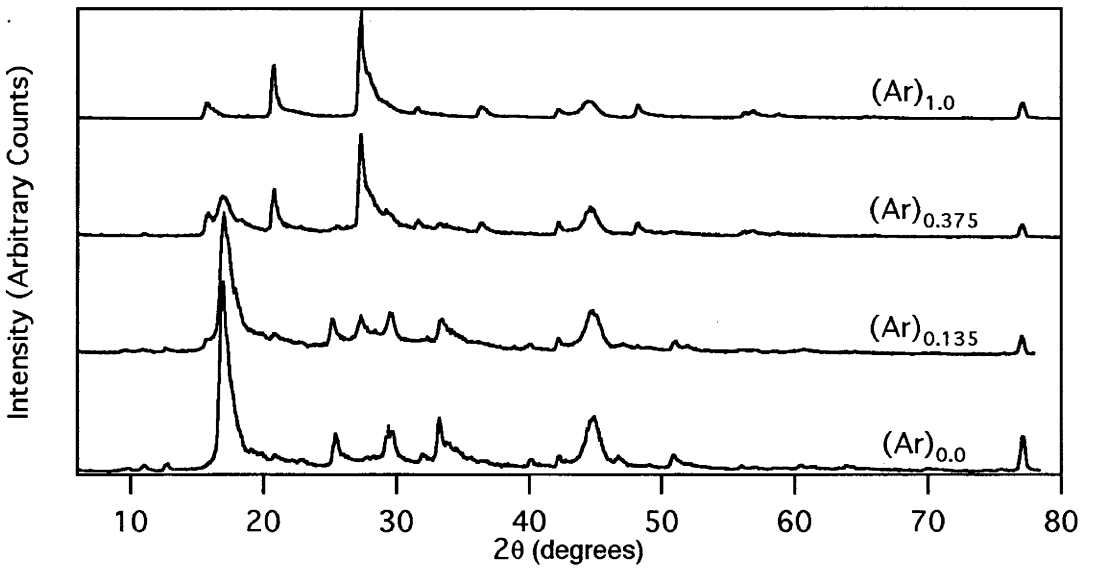

Figure 4.2.3: *the ab plane XRD patterns of $RbAr_xC_{25}$, for $0<x<1.2$, all acquired at 90 K; there is no sign of a transitional structure between the initial RbC_{25} pattern and the final ternary pattern.*

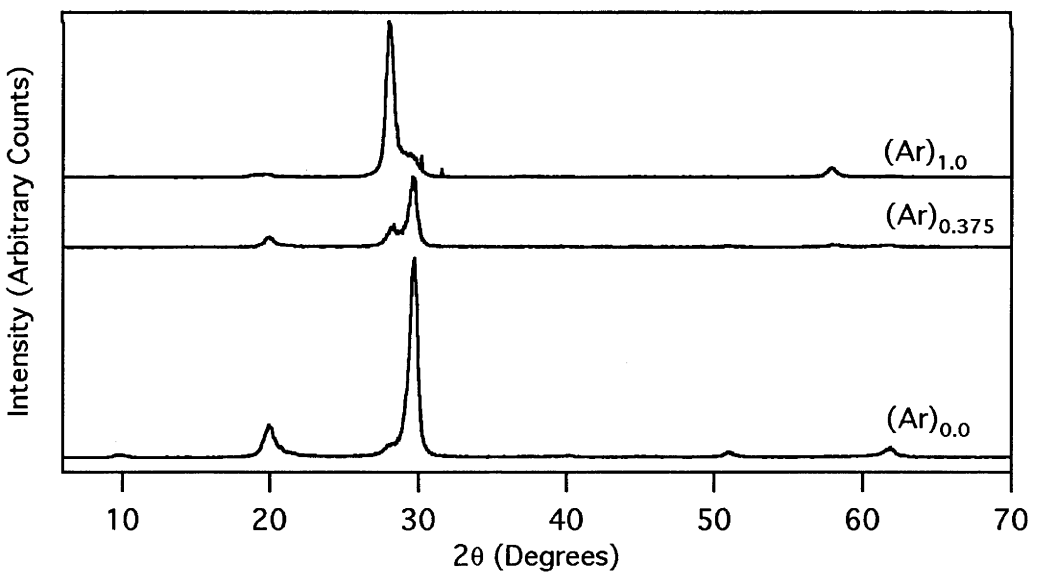

Figure 4.2.4: *$RbAr_xC_{25}$ c-axis diffraction patterns taken at 90-100 K for increasing Ar concentrations.*

In both sets of data, *ab*-plane and *c*-axis, the diffraction peaks of the ternary pattern simply replace those of the binary. The *c*-axis data shows that even at low argon fillings,

there are only two c-axis spacings present in the sample. From this it possible to conclude that there are no transitional phases between the initial binary and final ternary GICs phases.

Data				Phase A		Phase B	
2θ (Degrees)	Intensity (Counts)	I/Imax x100	D (Å)	l_a	D x l_a (Å)	l_b	D x l_b (Å)
18.94	180	1.586	4.685	2	9.371		
19.72	240	2.115	4.502			2	9.004
28.06	11348	100	3.180	3	9.540		
29.41	1724	15.192	3.037			3	9.111
57.88	692	6.098	1.593	6	9.559		
61.72	92	0.811	1.503			6	9.017

Table 4.2.1: *Indexing of the c-axis diffraction pattern for $RbAr_{1.2}C_{25}$ as a two phase system - Phase B has the same c-axis dimensions as stage-II RbC_{25}, while Phase A has an expanded cell dimension of ~9.55 Å.*

The final GIC phases were identified by complete indexing of the *ab*-plane data. Comparison with the diffraction pattern of the binary compound (the undoped trace in Figure 4.2.3), shows that either the ternary phase has a smaller unit cell than the $\sqrt{43}$x$\sqrt{43}$ structure of RbC_{25}, or there are a number of systematic absences. Table 4.2.1 shows the simplest two-dimensional indexing of the 90 K pattern, which we have found by an exhaustive process of generating all possible lattices. We find a primitive hexagonal lattice with unit cell dimension a equal to $\sqrt{28}$ x a_{gr}, the graphite cell dimension of 2.46 Å. This is one of the registered superstructures of a hexagonal lattice, and is shown in Figure 4.2.3. There are quite a number of absent reflections, including all the (3,k) reflections up to k=7, and additionally, there is systematic increase of a as the Miller index of a peak increases, with the higher angle peaks much closer to the correct positions for a $\sqrt{28}$x$\sqrt{28}$ structure: this may be a result of the turbostratic peak offset first noted by Warren[2], of the form $\Delta(\sin\theta)=0.16\lambda/L$, or it may be an offset error in the instrument alignment, most likely as a result of the sample position difficulties encountered with the experimental arrangement. The later pattern simulations will correct for both of these; inherently for the turbostratic offset, and by taking the value of a_{gr} from the graphite breakthrough peaks of the sample the second will appear in the simulated pattern.

Data			√28x√28 Cell			
2θ (Degrees)	Intensity (Counts)	D (Å)	h	k	a	$(a/a_{gr})^2$
15.76	1288	5.623	2	0	12.985	27.68
20.77	3655	4.277	2	1	13.065	28.02
27.34	7053	3.262	2	2	13.048	27.95
31.6	688	2.831	4	0	13.077	28.07
36.4	367	2.468	4	1	13.06	28.00
42.28	688	2.138	1	0	2.4682	1
44.56	1309	2.033				
48.22	1051	1.887	6	0	13.075	28.06
56.26	522	1.635	4	4	13.081	28.09
56.92	588	1.618	7	0	13.075	28.06
58.84	332	1.569	6	2	13.068	28.03
65.32	66	1.428	6	3	13.092	28.14
66.1	61	1.414	8	0	13.057	27.99
72.82	48	1.299	6	4	13.074	28.06
77.08	1232	1.237	1	1	2.4745	1.005

Table 4.2.2: *Simple indexing of the ab plane diffraction peaks from Figure 4.2.2 on a two-dimensional hexagonal cell with axes (√28x√28) x a_{gr}, the graphite in-plane dimension of 2.46Å. The peaks at 42.28° and 77.08° are indexed as the graphite (10) and (11) peaks, while the unassigned peak at 44.5° is the (101) breakthrough. The c-axis (003) breakthrough usually seen in these patterns is presumably hidden beneath the very strong turbostratic peak at 27.34°.*

The √28x√28 models all fail the basic test of producing absences of the major peaks; as none of the hexagonal plane groups have any systematic absences[3], this is perhaps unsurprising. As an alternative to the √28x√28 cell, the diffraction pattern may also be indexed by a two phase system consisting of 2x2 and √7x√7 hexagonal commensurate phases; this is shown in Table 4.2.3. This two phase indexing has the obvious advantage that there are no systematic absences.

The *c*-axis data, indexed in Table 4.2.1, show that there is a considerable expansion of the c-axis spacing - the strongest line at 29.50° (3.028 Å) in the undoped pattern moves to 28.03° (3.183 Å) in the 90 K sample, accompanied by a significant change in the structure factor for the sample. Most of the lines in the original pattern disappear, except for the (002), (003) and (006) lines. The in-plane data indicate that the intensity

remaining at ~29.5 Å (3.028 Å) arises from one of the phases in the two-phase ternary system with a similar c-axis spacing to RbC_{25}.

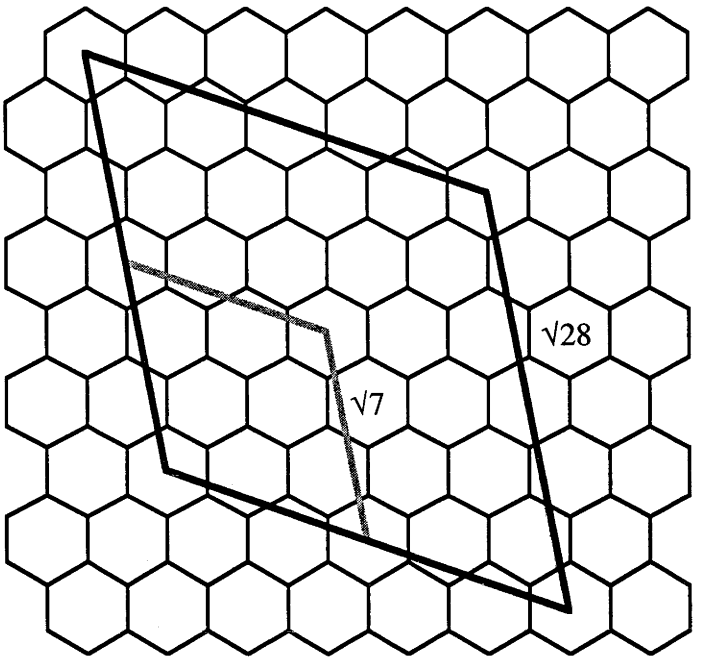

Figure 4.2.5: *the unit cells of the commensurate √7x√7 and √28x√28 hexagonal superlattices.*

4.2.3 *ab*-Plane Intensity Simulations of Ternary $RbAr_{1.2}C_{25}$ Structures.

Early intensity fits were performed with the Rietveld refinement suite "GSAS": this program cannot simulate turbostratically disordered compounds, but is adequate for testing whether the gross intensities of a model match the data[4]. Later simulations were undertaken using the whole pattern turbostratic simulation technique described in Chapter 2, which is much more computationally intensive.

Given that after the gas is removed from the ternary intercalate (by heating and/or pumping upon the sample) the sample reverts to the original structure, and further that there does not seem to be a change in the staging of the GIC, it may be concluded that the alkali-metal ions retain roughly the same in-plane density as in the binary compound, as a gross change in this density would require a change of stage number or for guest ions to be driven out of the host.

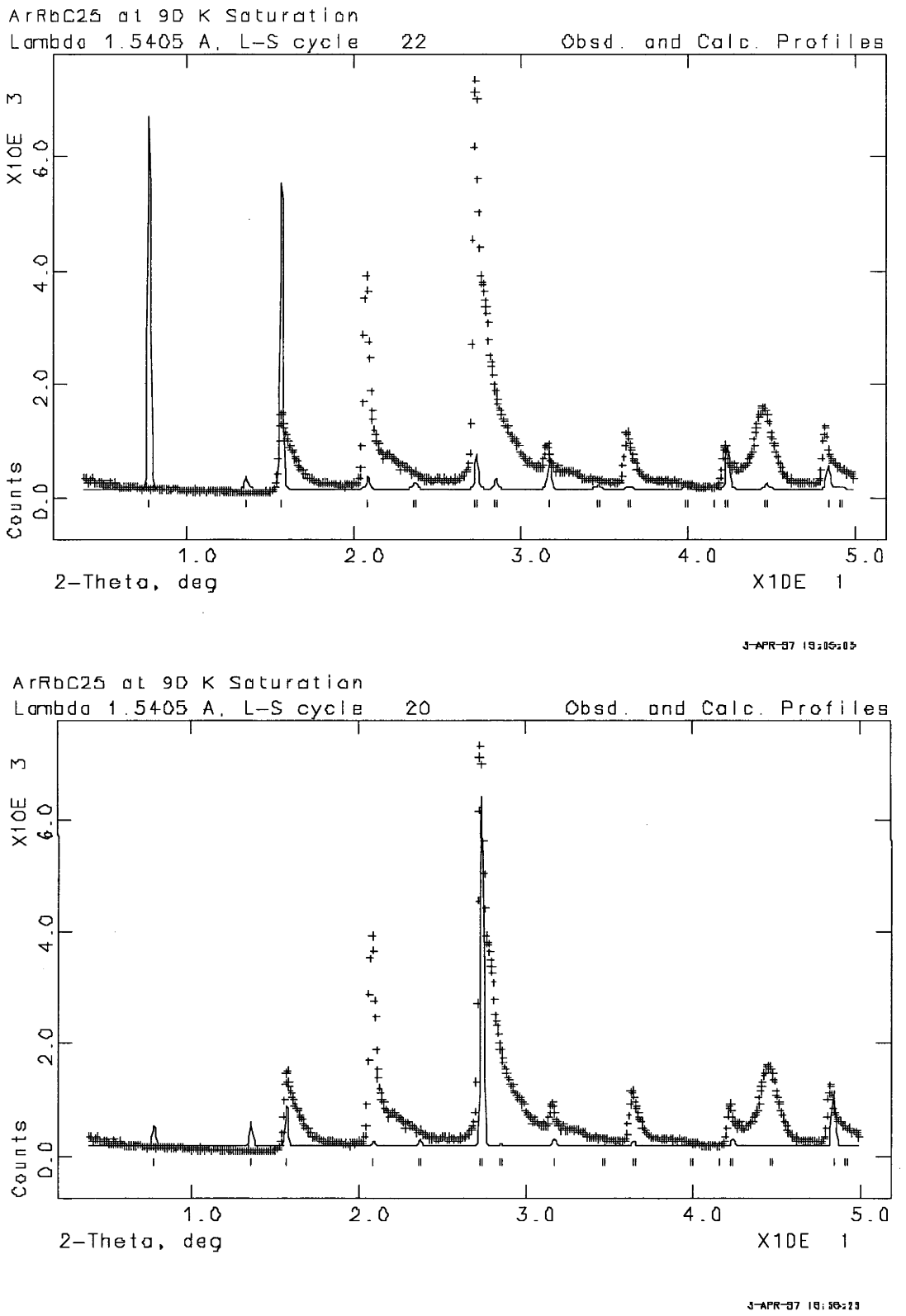

Figure 4.2.6: *Two single-phase Rietveld fit to the ab-plane oriented 90K* $RbAr_{1.2}C_{25}$ *pattern using a* $\sqrt{28}x\sqrt{28}$ *P6 unit cell. The upper phase has rubidium atoms at (0, 0) and (0.5, 0.5), and an argon atom at (0.0310, 0.1718), producing a stoichiometry of* $Ar_3Rb_2C_{56}$ *.The lower phase has rubidium atoms at (0, 0), (0.5,0.5) and (1/3, 2/3), and an argon atom at (1/6, 2/6), producing a stoichiometry of* $Ar_3Rb_3C_{56}$.

The $\sqrt{28}x\sqrt{28}$ cell is exactly double the $\sqrt{7}x\sqrt{7}$ hexagonal commensurate cell: since the binary GIC $\sqrt{43}x\sqrt{43}$ structure can be considered to be hexagonal $\sqrt{7}x\sqrt{7}$ domains separated by 2x2 domain walls, many of the $\sqrt{28}x\sqrt{28}$ model structures were designed with the Rb packing close to $\sqrt{7}x\sqrt{7}$. Two examples of the best fits to $\sqrt{28}x\sqrt{28}$ cells are shown in Figures 4.2.6. They are clearly unsatisfactory, further enhancing our belief in a two-phase final system.

Data			2x2 Cell				$\sqrt{7}x\sqrt{7}$ Cell			
2θ (Degrees)	Intensity (Counts)	D (Å)	h	k	a (Å)	$(a/a_{gr})^2$	h	k	a (Å)	$(a/a_{gr})^2$
15.76	1288	5.623					1	0	6.493	6.92
20.77	3655	4.277	0	1	4.938	4.003				
27.34	7053	3.262					1	1	6.524	6.986
31.60	688	2.831					2	0	6.538	7.018
36.40	367	2.468	1	1	4.936	4.000				
42.28	688	2.138	1	0	2.468	1	1	0	2.468	1
44.56	1309	2.033								
48.22	1051	1.887					3	0	6.537	7.015
56.26	522	1.635					2	2	6.54	7.022
56.92	588	1.618	2	1	4.942	4.009				
58.84	332	1.569					3	1	6.534	7.008
65.32	66	1.428	3	0	4.948	4.020				
66.10	61	1.414					4	0	6.529	6.997
72.82	48	1.299					3	2	6.537	7.014
77.08	1232	1.237	1	1	2.475	1.005	1	1	2.475	1.005
80.98	90	1.187	3	1	4.943	4.011				
84.04	226	1.152								

Table 4.2.3 *The diffraction peaks of the saturated $RbAr_{1.2}C_{25}$ ab-plane oriented pattern indexed as a two phase compound composed of $\sqrt{7}x\sqrt{7}$ and 2x2 commensurate structures. As before, the rows at 42.28° and 77.08° are indexed as the graphite (1,0) and (1,1) diffraction peaks, though they could also be assigned as peaks of either commensurate structure.*

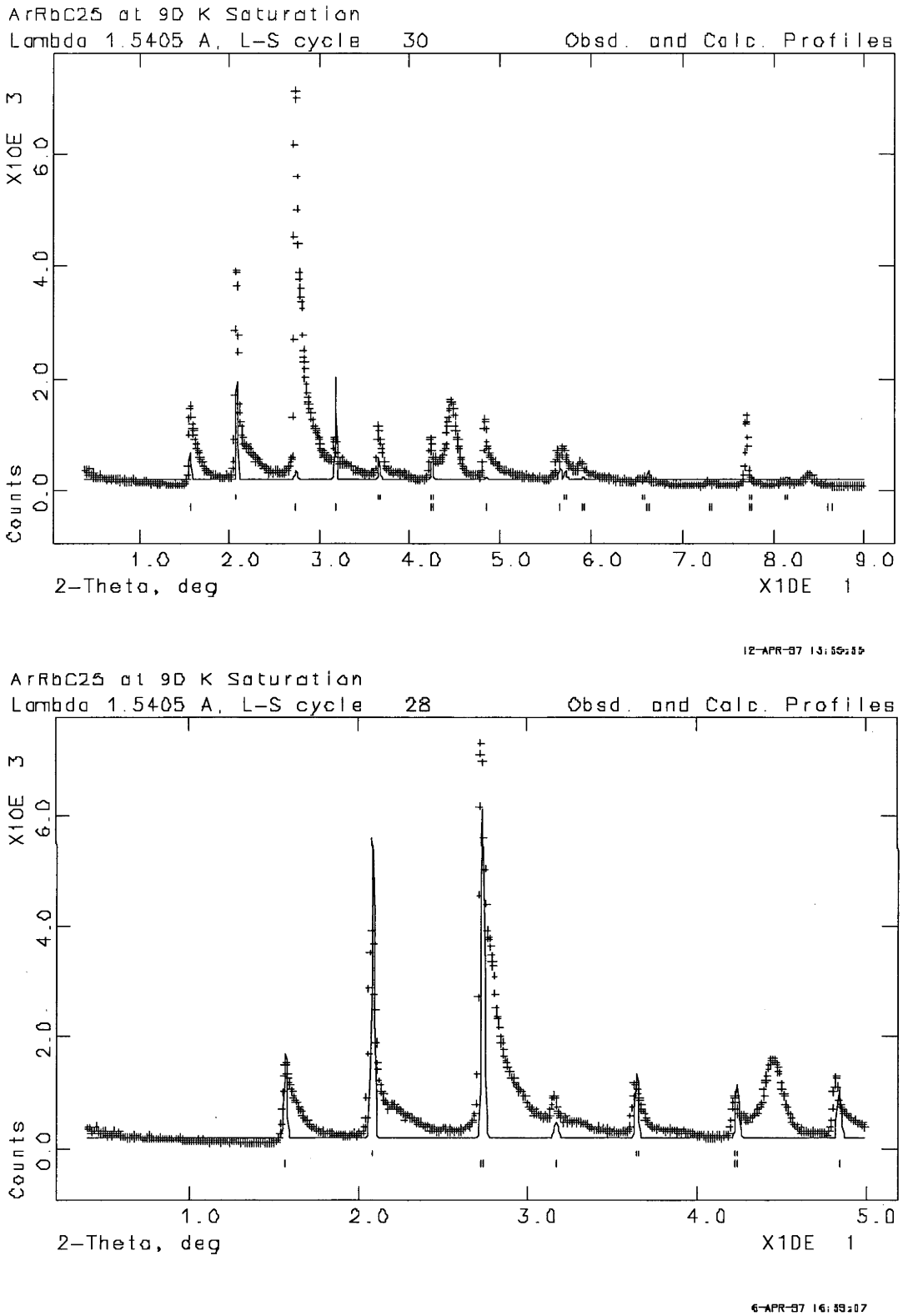

Figure 4.2.7: *Two two-phase Rietveld fits to the ab-plane oriented 90K* $RbAr_{1.2}C_{25}$ *pattern. In both patterns, Phase 1 has a 2x2 P6 unit cell with a rubidium atom at (0,0). In the upper diagram Phase 2 has a* $\sqrt{7}x\sqrt{7}$ *P6 unit cell with a rubidium atom at (0,0) and an argon atom at (0.5,0.5), while in the lower diagram the cell is identical except the argon atom is at (1/3,2/3).*

Two different GSAS intensity simulations of a two phase system are shown in Figure 4.2.7. Here it was assumed that the √7x√7 phase is the only phase containing argon atoms, while the 2x2 phase is a binary Rb-GIC, and that both phases have P6 in-plane symmetry. Only the Rb and Ar atoms are included in the model, as the graphene layers have no contributions to the *ab*-plane intensities below the graphite (10) peak at 42.12°, and only (*hk0*) reflections are included.

The only difference between the two simulations in Figure 4.2.7 is the position of the Ar atoms in the √7x√7 unit cell: in the upper diagram the argon atom is at the two fold axis at (1/2, 1/2), with a site multiplicity of 3; in the lower diagram the argon is at the three fold axis at (1/3, 2/3). Clearly the second structure provides a good fit to the gross intensities of the *ab*-plane data, so further calculations employing the whole-pattern-simulation method were undertaken based on the second structure, the two phases of which are shown in Figures 4.2.8 and 4.2.9.

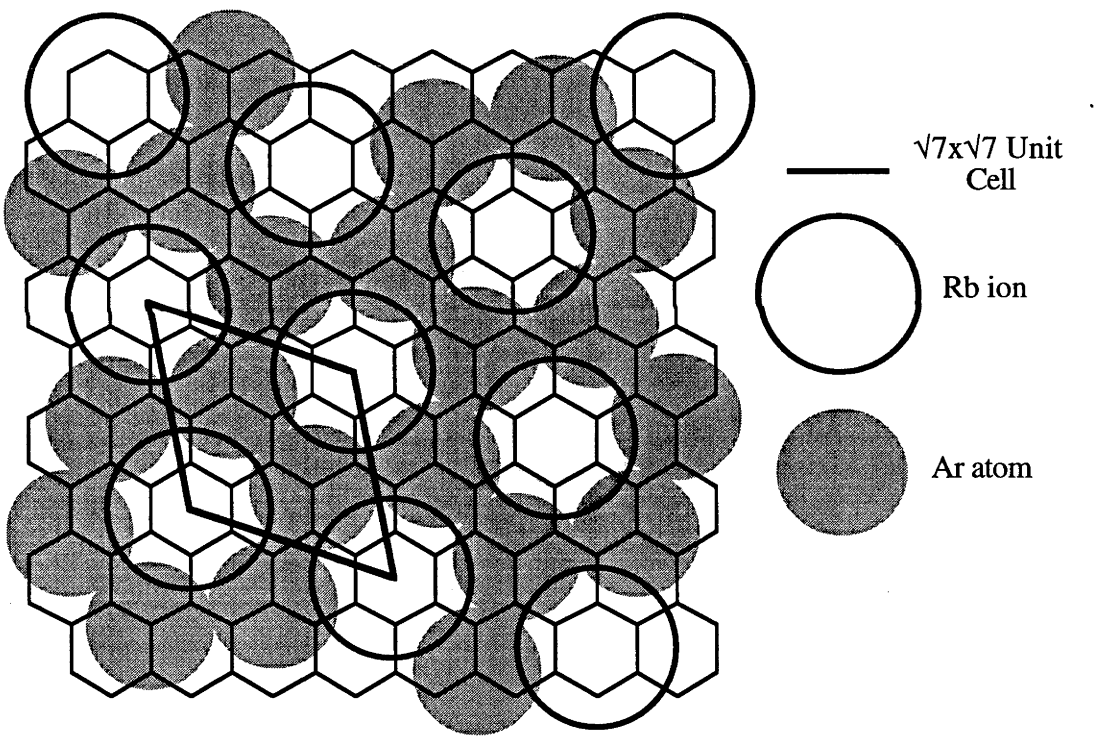

Figure 4.2.8: *ab-plane structure for the √7x√7 $RbAr_2C_{28}$ argon-rich phase used in the following simulations; the Van der Waals radii are used for atomic and ionic sizes. Though the graphene layer is shown, it's contributions are not included in the simulations.*

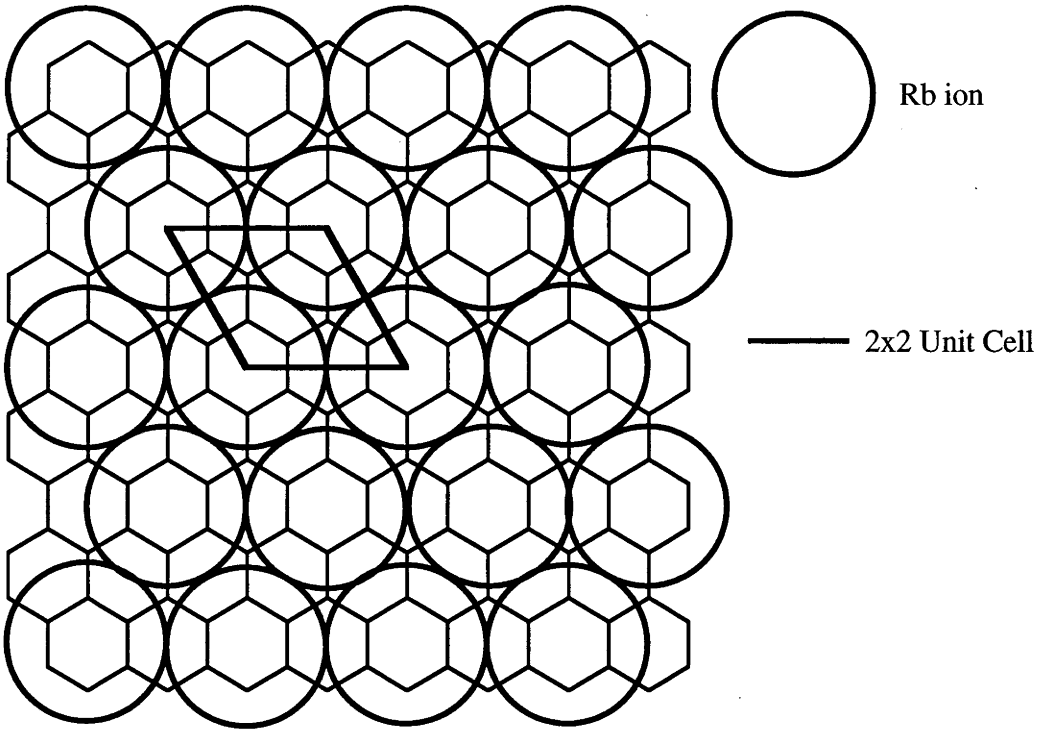

Figure 4.2.9: *ab-plane structure for the 2x2 RbC_{16} argon-poor phase used in the following simulations; the Van der Waals radii are used for the rubidium ions shown. Again, though the graphene layer is shown, it's contributions are not included in the simulations.*

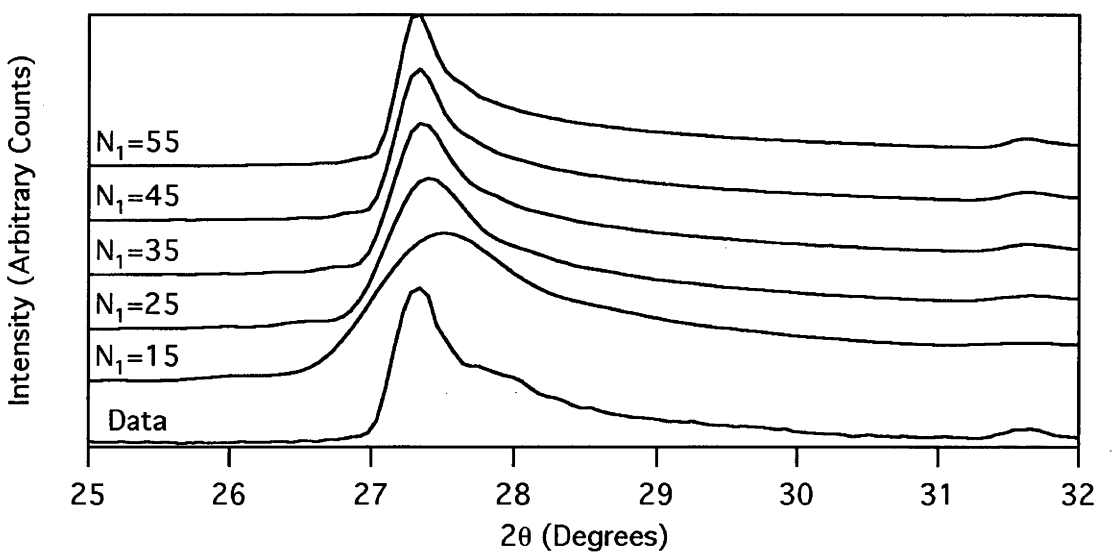

Figure 4.2.10: *Pattern simulations for the strongest √7x√7 peak, at 27.34°. The lowest trace is experimental data, taken at 90 K; the others are simulations of the ab-plane structure shown in Figure 4.2.9;, calculated over the range 25.00°-32.02° with a step size of 0.06°. The parameter N_1 shown is the size of the in-plane crystallites in number of unit cells (see Chapter 2). The other constants used in the calculations were a_{gr} (the graphite ab-plane unit cell dimension) = 2.475 Å; c=9.55 Å; λ = 1.54178 Å.*

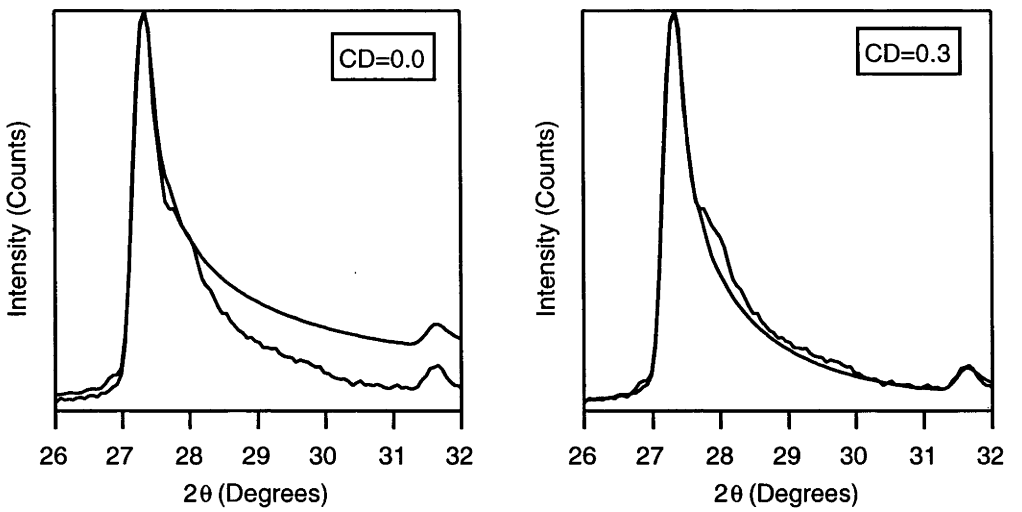

Figure 4.2.11: *The effect of the c-axis damping factor CD on the simulated turbostratic band shape of the $\sqrt{7}x\sqrt{7}$ $RbAr_2C_{28}$ structure. The best fit was found for CD=0.3, as shown. The pattern simulations both use N_1=45; a_{gr} = 2.475 Å; c=9.55 Å; λ = 1.54178 Å; the data was taken at 90 K.*

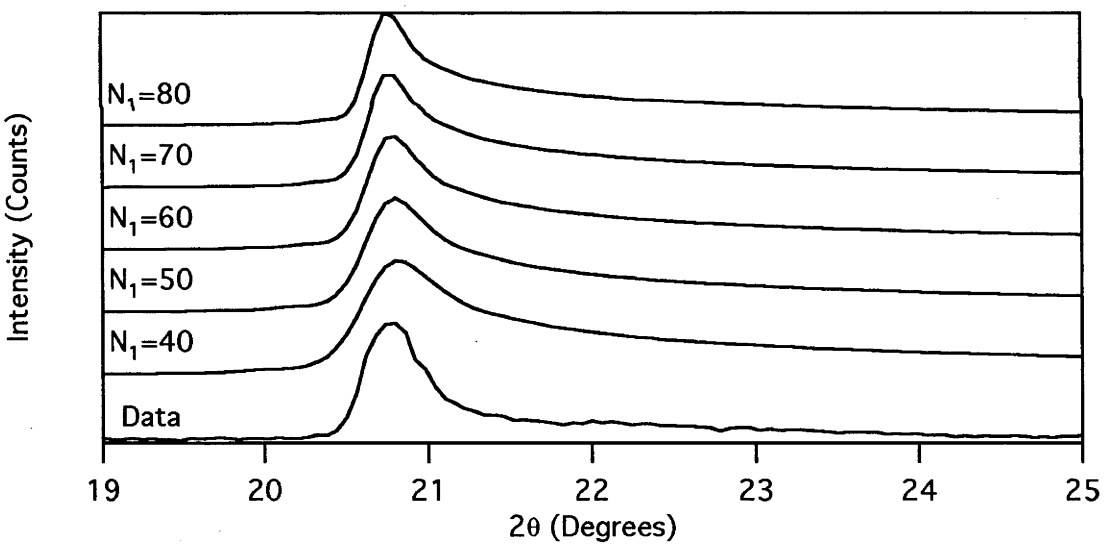

Figure 4.2.12: *Pattern simulations for the strongest 2x2 peak, at 20.77°. The lowest trace is experimental data, taken at 90 K; the others are simulations calculated over the range 19.00°-25.00° with a step size of 0.06°. The ab-plane crystal structure used for the simulations is shown in Figure 4.2.10; the value N_1 being the size of the in-plane crystallites (see Chapter 2). The other constants used in the calculations were a_{gr} = 2.478 Å; c=9.0 Å; λ = 1.54178 Å.*

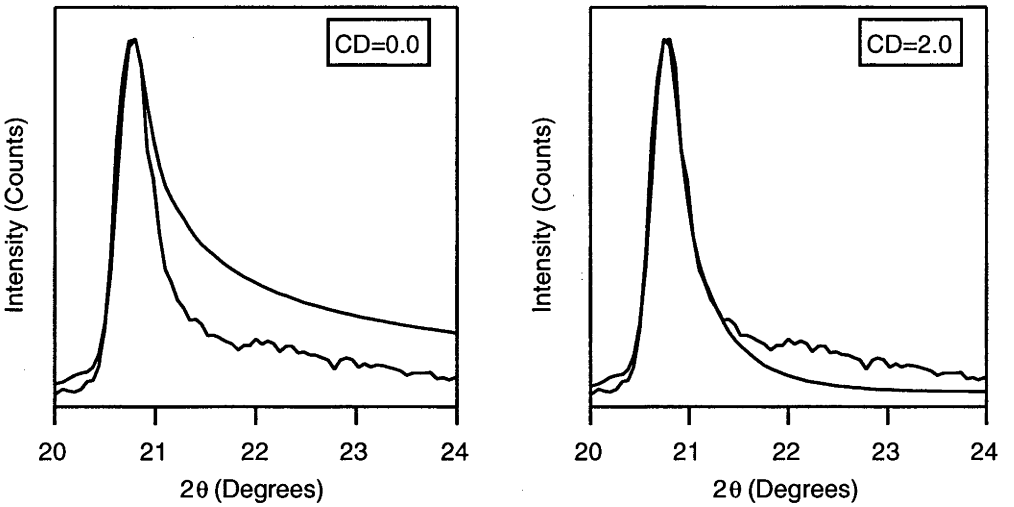

Figure 4.2.13: *The effect of the c-axis damping factor CD on the simulated turbostratic band shape of the (1,0) 2x2 peak, compared with data taken at 90K from a saturated sample. The pattern simulations both use* N_1*=60;* a_{gr} *= 2.478 Å; c=9.00 Å;* λ *= 1.54178 Å.*

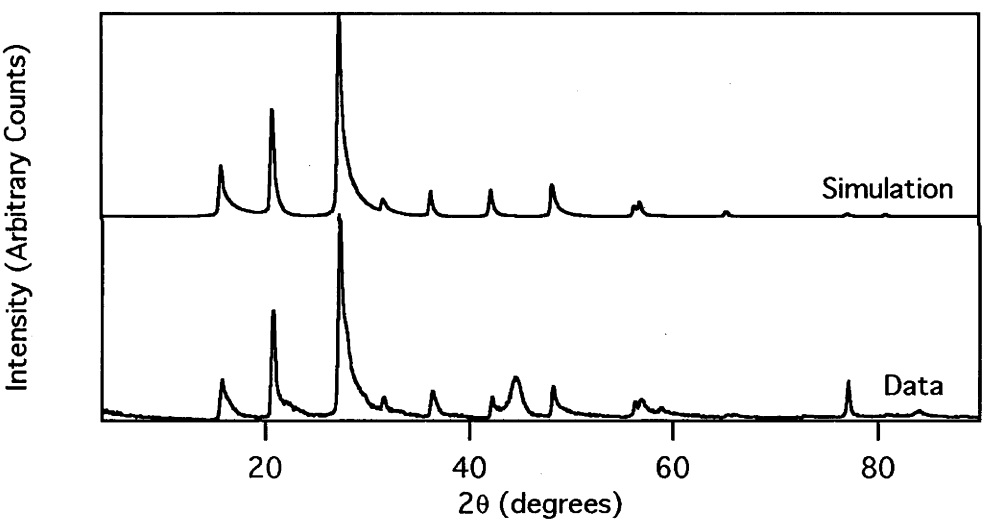

Figure 4.2.14: *The combined best simulations of the 2x2 and* $\sqrt{7}x\sqrt{7}$ *phases compared with the data from the saturated* $RbAr_{1.2}C_{25}$ *taken at 90K. A 4th order polynomial was fitted to the data and subtracted to remove background. The values used for the simulations are shown in Table 4.2.5.*

The final best simulation, shown in Figure 4.2.14, uses the following values:

	Phase A	Phase B
Symmetry	P6	P6
a	2	2.646 ($\sqrt{7}$)
a_{gr}	2.478 Å	2.475 Å
c	9.0 Å	9.55 Å
N_1=N_2	60	45
N_3	1	1
CD	2.0	0.3
Thermal factors	Rb=0.0	Rb=0.9 Ar=0 .7

***Table 4.2.4**: the parameters used for the simulations shown in Figure 4.2.14.*

Both simulations give very similar values for the graphite in-plane dimension; though they are considerably greater than the value of a_{gr} for pristine graphite (2.46Å), the value for a_{gr} in the binary RbC_{25} sample was 2.472Å, within experimental error of the values found here. The c-axis parameter is included for completeness, but it had little effect on the final simulations, since N_3, the number of unit cells along the c-axis in the simulated crystallite, is equal to 1 for both simulations. The *ab*-plane domains are very nearly the same size for both phases: 300 Å for the 2x2 phase and 290 Å for the $\sqrt{7}$x$\sqrt{7}$ phase. While thermal factors were needed for the $\sqrt{7}$x$\sqrt{7}$ simulation, none were used for the 2x2 simulation shown, as any thermal correction of significant value reduced the high order peaks entirely, and had no apparent effect on the quality of fit. CD, the c-axis damping factor, is a major difference between the parameters used for the two phase simulations. As described in Chapter 2, a correction for *c*-axis contributions to an oriented *ab*-plane sample is required, and these simulations use one of the form exp(-CDl^2); for a single oriented GIC sample with two phases, CD should have a similar value in the simulations of both phases. An alternative simulation of the 2x2 phase is shown in Figure 4.2.16, where a degree of *c*-axis ordering has been introduced, in the form of the parameter δ, the probability of defect-free stacking between any two layers of the 2x2 phase, as described in Chapter 2.

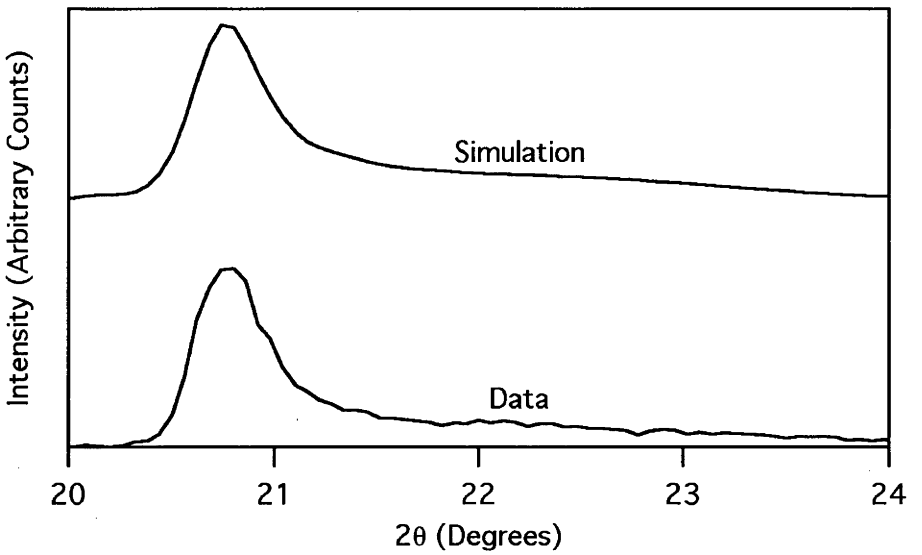

Figure 4.2.15: *A comparison of a simulated turbostratic band shape of the (1,0) 2x2 peak including a c-axis ordering parameter δ with data taken at 90K The parameters used in the simulation are N_1=50; N_3=5; δ=0.5; CD=0.5;a_{gr} = 2.478 Å; c=9.00 Å; λ = 1.54178 Å.*

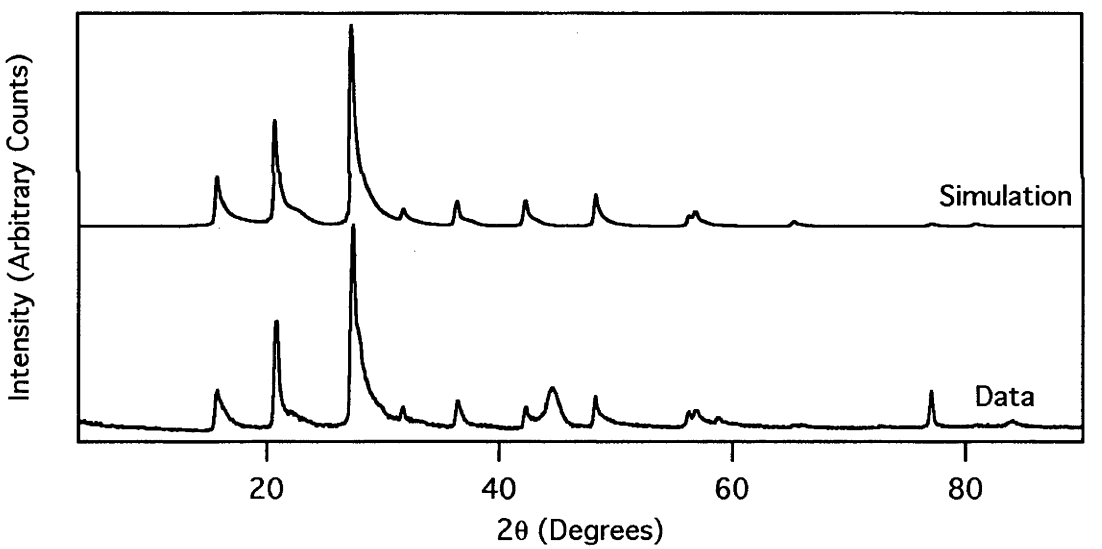

Figure 4.2.16: *The combined simulations of the c-axis-ordered 2x2 phase and the purely turbostratic √7x√7 phases compared with the data from the saturated $RbAr_{1.2}C_{25}$ taken at 90K. The 2x2 simulation uses the same parameters as used in Figure 4.2.16.*

The parameters use for the simulation shown in Figure 4.2.16 are shown in Table 4.2.5

	Phase A	Phase B
Symmetry	P6	P6
a	2	2.646 ($\sqrt{7}$)
a_{gr}	2.478 Å	2.475 Å
c	9.0 Å	9.55 Å
$N_1=N_2$	50	45
N_3	5	1
δ	0.5	0
CD	0.5	0.3
Thermal factors	Rb=0.0	Rb=0.9 Ar=0 .7

Table 4.2.5 *the parameters used for the simulations shown in Figures 4.2.16 and 4.2.17.*

While the simulation of the 2x2 phase shown in Figures 4.2.15 and 4.2.16 has a superior fit to the (10) peak, the fit to the other (and much less intense) peaks of the 2x2 pattern is not better than for the purely turbostratic simulation. Furthermore, a range of values for N_3 and δ can be used to give a similar peak shape to that shown in the figures above, once the c-axis damping factor is added, with the result that the parameters given in Table 4.2.5 can only be considered suggestive. Nonetheless, these simulations suggest, without necessarily proving, that there may be some c-axis ordering in the RbC_{16} 2x2 phase.

4.2.4 *c*-Axis Intensity Simulations of Ternary $RbAr_{1.2}C_{25}$ Structures

The *c*-axis simulations are computationally simpler than the *ab*-plane calculations, so that there was no need to use a quicker method such as Rietveld fits first.

A simple pattern calculation is shown in Figure 4.2.17, compared with the *c*-axis diffraction pattern for the sample cooled to 90 K under 600 Torr of argon, and the structure used for this calculation is shown in Figure 4.2.18. In this first simulation the stoichiometry used is $RbAr_{1.2}C_{25}$: this represents a single phase system - an interstitial solution - or a two phase system with both phases adopting the same *c*-axis structure.

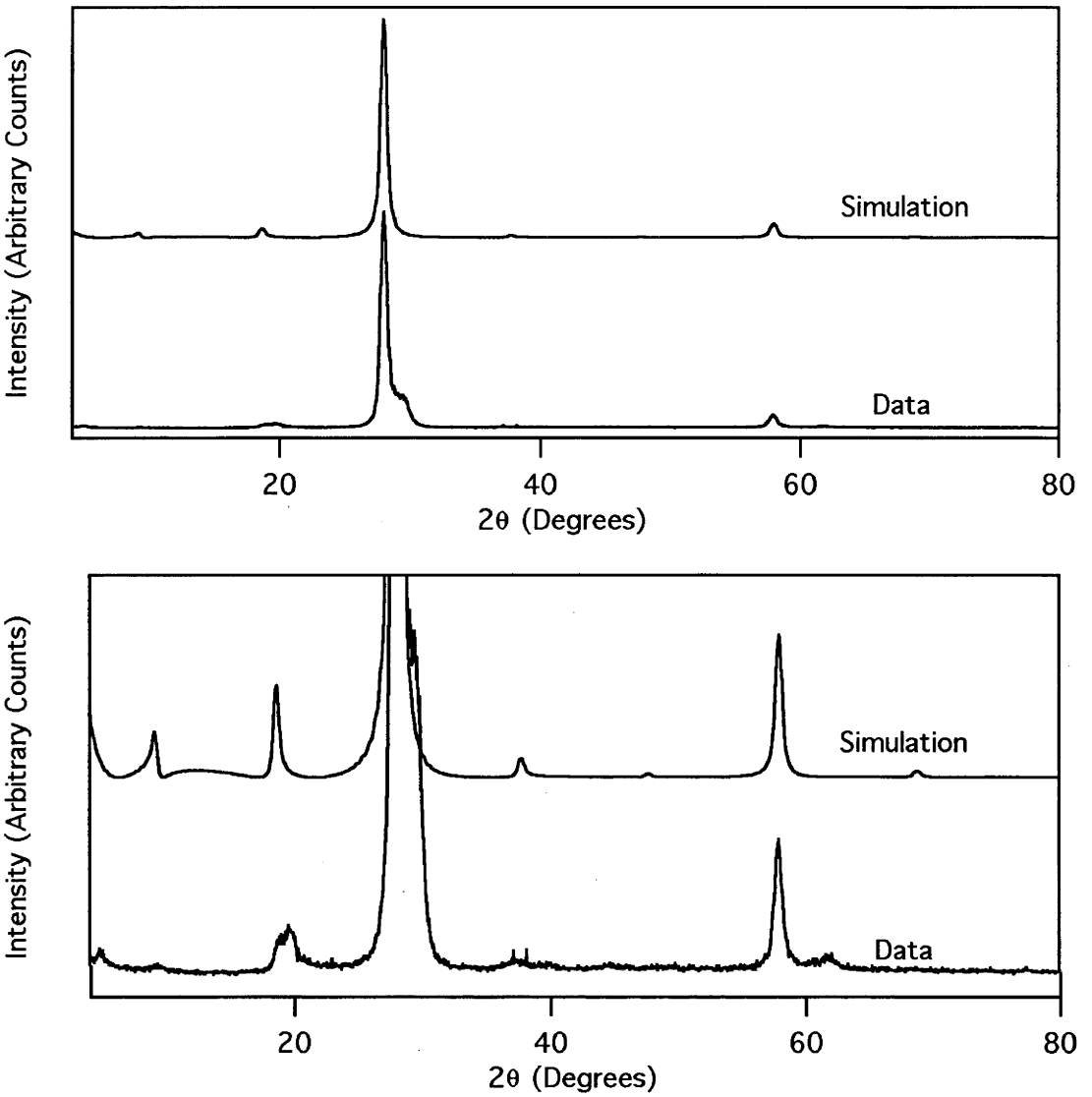

***Figure 4.2.17**: A comparison of c-axis data for $RbAr_{1.2}C_{25}$ and a simulated pattern calculated with the following parameters: c=9.55Å, N_3=20, δ=10, and an overall temperature factor α=0.2, with the ratio Ar/Rb=1.2. See Chapter 2 for a description of these parameters.*

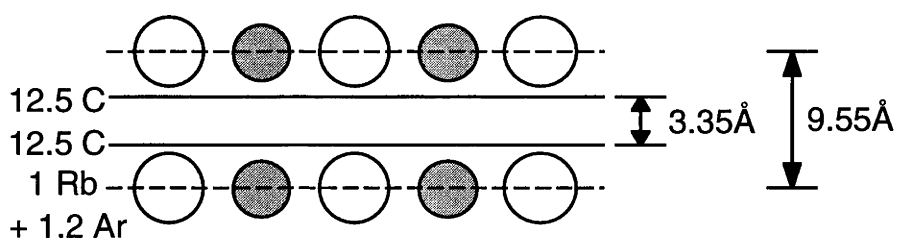

***Figure 4.2.18:** The c-axis structure used for the simulation shown in 4.2.18. Each Rb-Ar layer contains 1 Rb atom and 1.2 Ar atoms, and is separated from the next by two graphene layers which are 3.35 Å apart.*

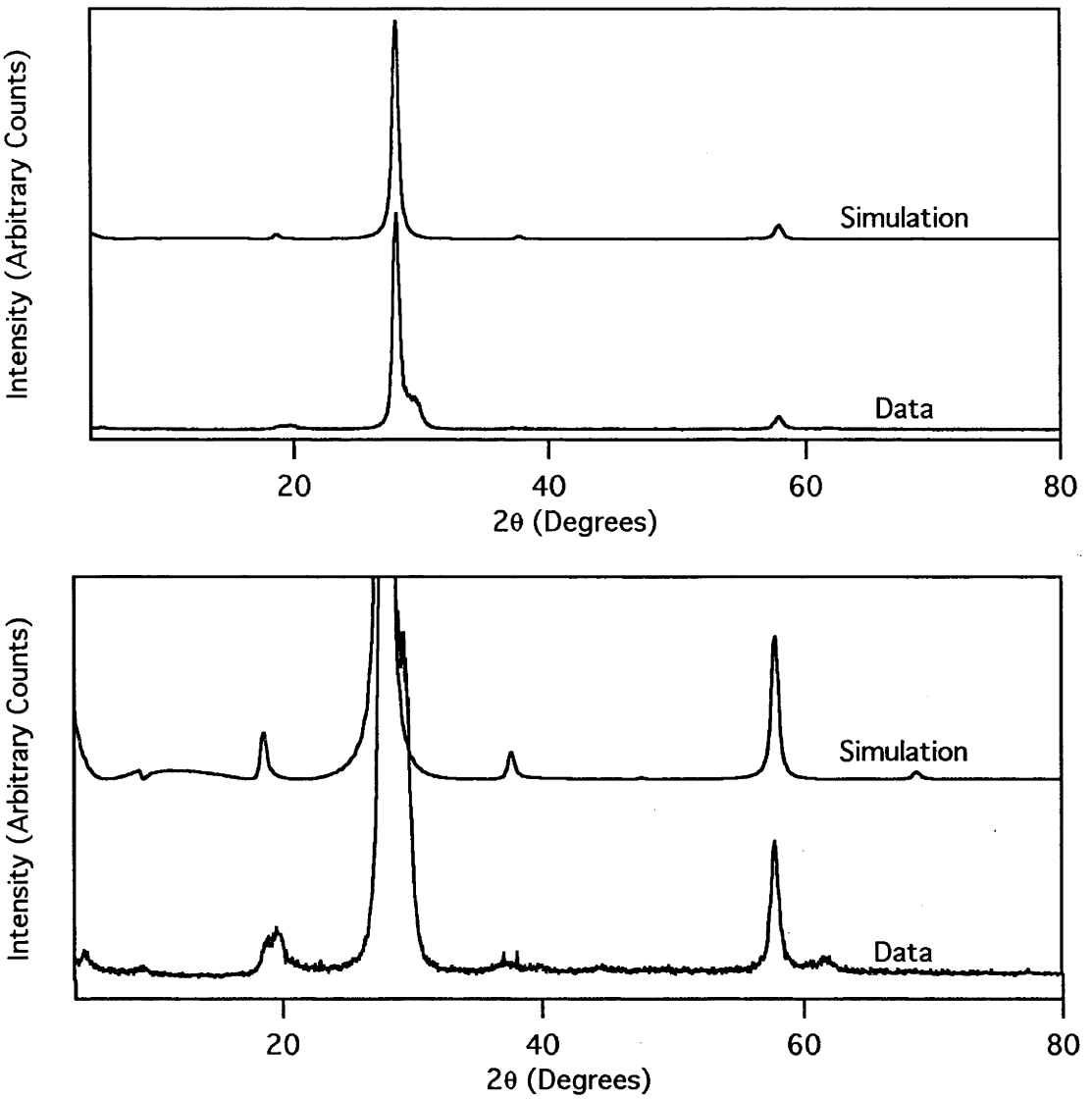

Figure 4.2.19: *A comparison of c-axis data for saturated $RbAr_{1.2}C_{25}$ and a simulated pattern calculated with the following parameters: c=9.55Å, N_3=20, δ=10, and an overall temperature factor α=0.2, with the ratio Ar/Rb=2.0. See Chapter 2 for a description of these parameters.*

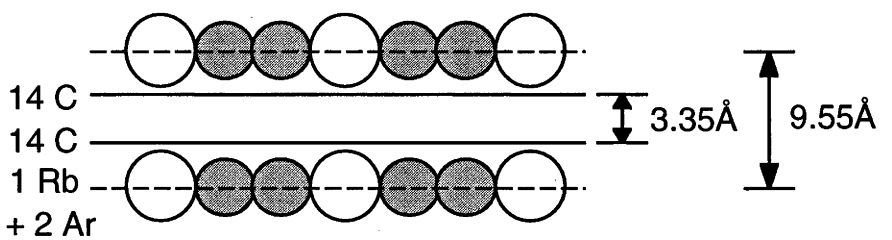

Figure 4.2.20: *c-axis structure used for the powder diffraction simulation shown in Figure 4.2.19. Each Rb-Ar layer contains a ratio of 1 Rb atom and 2 Ar atoms, and is separated from the next by two graphene layers which are 3.35 Å apart.*

A second model, shown in Figure 4.2.20, attempts to simulate the diffraction pattern from a sample with the same stoichiometry ($RbAr_{2.0}C_{28}$) as the $\sqrt{7}x\sqrt{7}$ structure, which is compared with the data in Figure 4.2.17. In both sets of simulations the (003) peaks of the simulations are normalised to the (003) maxima of the data. While both simulations are imperfect, the second gives a better intensity match for the (001) and (002) lines, as shown in Table 4.2.6. In both these c-axis simulations we have ignored the contribution of the phase with $c \approx 9.05$ Å. Thus, for example, the peak at $2\theta = 61.72$ is not present. Thus Table 4.2.6 lends support to the conclusion that one phase is argon-rich and one argon-poor compared to the average stoichiometry of $RbAr_{1.2}C_{25}$.

Diffraction Peak	Data	Simulation: $RbAr_{1.2}C_{25}$	Simulation: $RbAr_{2.0}C_{25}$
001	0.61	2.01	0.37
002	1.59	4.01	2.07
003	100.00	100.00	100.00
004	0.75	0.82	1.15
005	0.00	0.15	0.06
006	6.10	6.21	6.21
007	0.00	0.27	0.31

Table 4.2.6: *Comparison of simulated and real intensities of c-axis lines. They are taken from the simulated patterns shown in Figures 4.2.17 and 4.2.19.*

4.2.5 Conclusion

The *ab*-plane data are consistent with a model of a two phase system, wherein all the argon absorbed by the binary rubidium-GIC is taken up by an expanded phase with an increased *c*-axis cell dimension, and a reduced in-plane rubidium density compared with the binary GIC; the second phase contains no argon, and possesses the same *c*-axis spacing as the binary compound but with an increased in-plane rubidium density; the *c*-axis data, while not definitive, agree with the same model, and show that both phases have remained as stage-2 as far as can be determined. The saturated rubidium-argon-graphite system is thus a bi-intercalation compound of formula $RbC_{16} \bullet RbAr_2C_{28}$ (st. 2).

References

1. K. Watanabe, T. Kondow, M. Soma, T. Onishi, and K. Tamaru, *Molecular-sieve type sorption on alkali graphite intercalation compounds.* Proceedings of the Royal Society of London A, 1973. **333**: p. 51-67.

2. B.E. Warren, *X-Ray Diffraction in Random Layer Lattices.* Phys. Rev., 1941. **59**(9): p. 693-699.

3. T. Hahn, ed. *International Tables for Crystallography: Volume A Space Group Symmetry.* 1983, International Union for Crystallography.

4. A.C. Larson and R.B. Von Dreele, LANSCE, MS-H805, Los Alamos National Laboratory, NM 87545, USA.

4.3: Methane Absorption by Rubidium Graphite Intercalation Compounds: The Structure of $Rb(CH_4)_xC_{25}$

As with Ar sorption, the methane isotherm of absorption on RbC_{25} possesses the "type-III" shape[1], shown for the cesium-methane compound as Figure 1.14, with little gas absorbed until a critical pressure is reached, after which there is rapid progression to a saturated ternary, of composition $(CH_4)_{0.9}RbC_{25}$. Here we will present powder diffraction patterns from oriented samples of the ternary intercalation compound $Rb(CH_4)_{0.9}C_{25}$ at temperatures above the boiling point of methane at 111.65 K.

4.3.1: Data

Figure 4.3.1 shows the *ab*-plane diffraction pattern of an oriented sample of RbC_{25} as it was cooled in stages from 130 K to 90 K while under one atmosphere of CH_4. Attempts to increase the CH_4 concentration in the sample by increasing the pressure of methane gas over the sample at temperatures above 110 K failed to produce any significant absorption at the pressures of up to an atmosphere, which is the maximum the gas handling system could safely attain. Only cooling the sample slowly, while it was under the maximum pressure of methane we could attain, produced absorption approaching saturation. This high pressure over the sample was obtained by cooling the sample stick to 80 K (beneath the freezing point of CH_4 at 90.75 K), opening the stick to the methane-filled gas-handling line, freezing all the CH_4 in the system into the sample stick, then closing the stick and increasing the temperature. While it is possible that there was some absorption into the sample from condensed CH_4 while the sample was heated, liquid methane would be expected to move to the bottom of the specimen can rather than remain on the sample; at the higher temperatures where absorption was observed no liquid condensation of CH_4 on the sample should be expected, and the take-up seen would therefore be from the vapour phase rather than the liquid. The RbC_{25} sample was prepared to a stoichiometry of Rb:C = 1:25, and weighed 0.405 g, equivalent to 1.05×10^{-3} moles. The sample stick contained 2.95×10^{-3} moles of CH_4, sufficient to attain the published saturation stoichiometry of $(CH_4)_{0.9}RbC_{25}$. The scans at 120 K and 90 K are shown in more detail in Figures 4.3.2 and 4.3.3 respectively, while *c*-axis powder diffraction patterns of the (003) peak at 120, 130 and 145 K are shown in Figure 4.3.4, and of the complete c-axis pattern at 120 K in Figure 4.3.5.

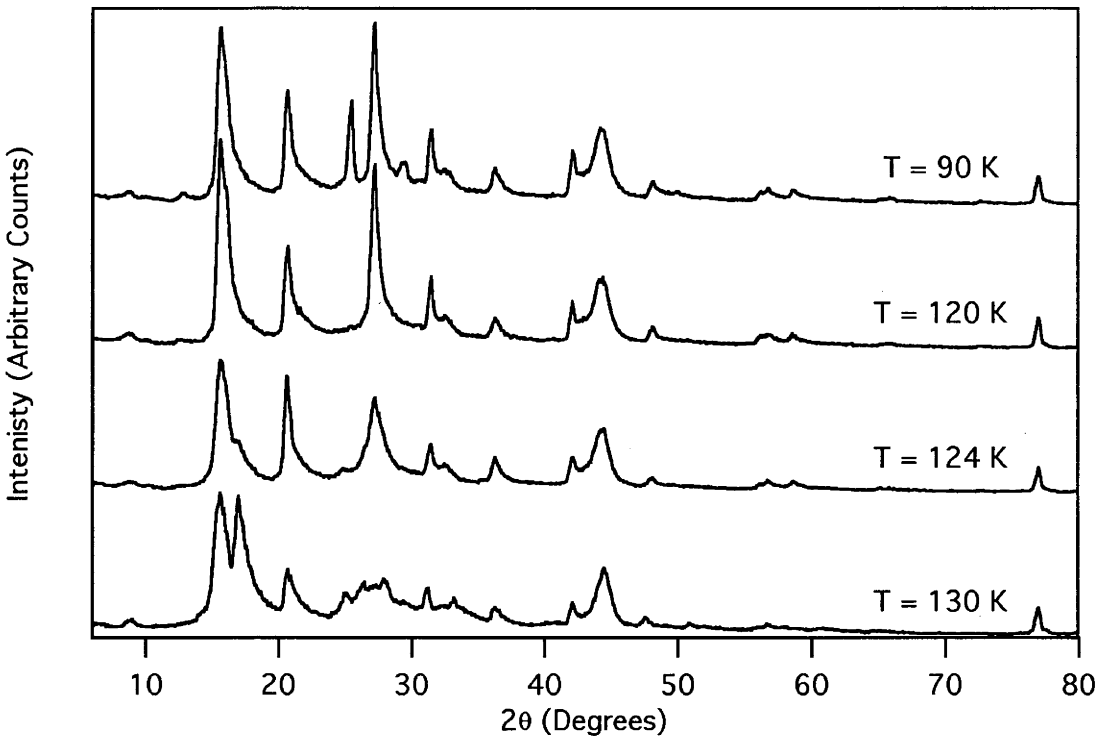

Figure 4.3.1: *ab-plane oriented XRD patterns of RbC_{25} sample cooled from 130 K to 90 K under an atmosphere of CH_4.*

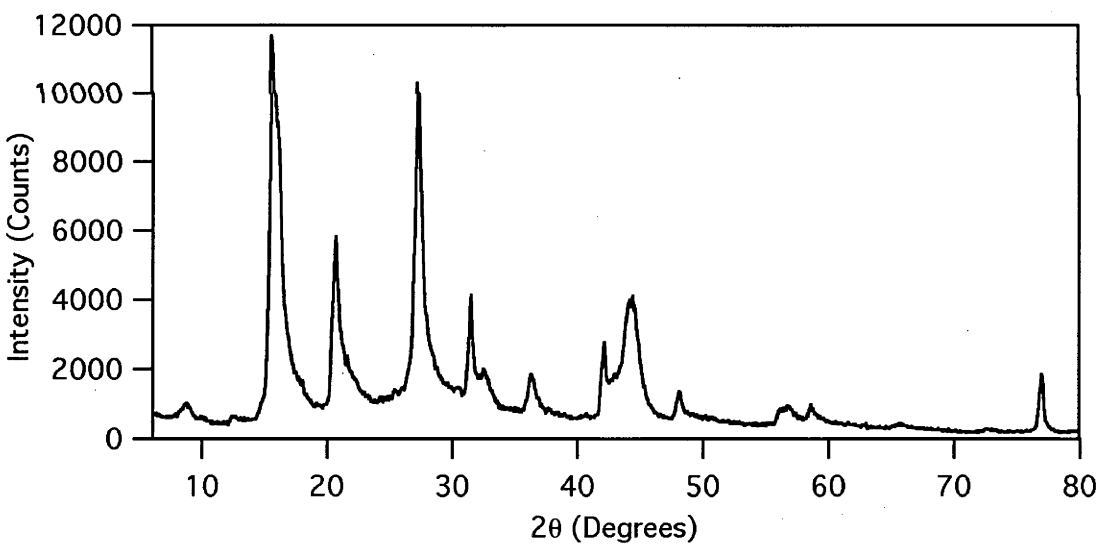

Figure 4.3.2: *An expanded graph of the ab-plane oriented XRD patterns of $(CH_4)_{\sim 0.9}RbC_{25}$ sample at 120 K.*

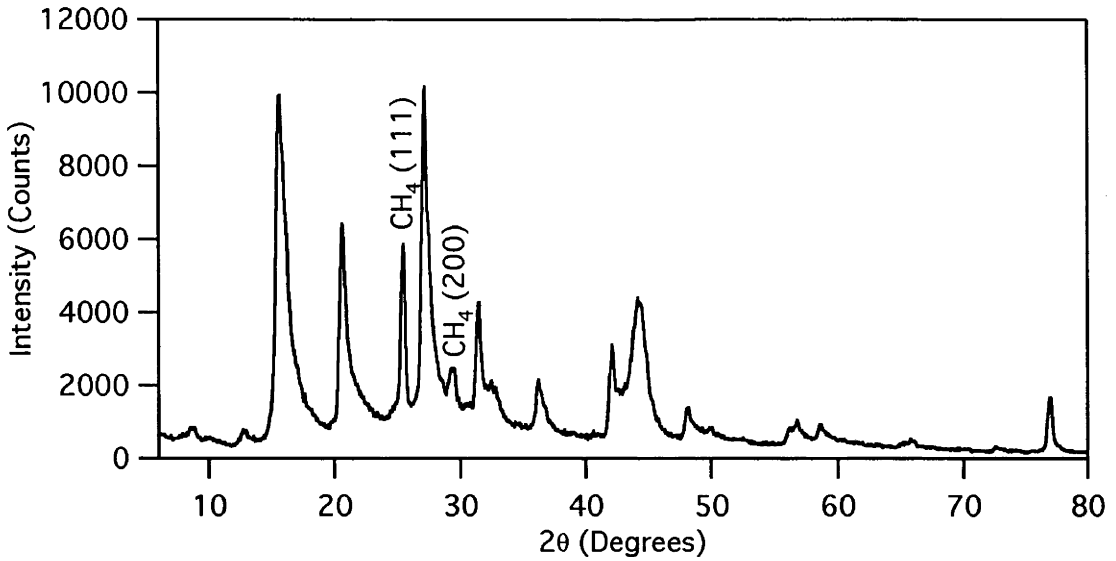

Figure 4.3.3: *ab-plane oriented XRD patterns of* $(CH_4)_{\sim 0.9}RbC_{25}$ *sample at 90 K; it is identical to the 120 K pattern except for the presence of two new peaks, indexed as the (111) and (200) lines of fcc solid methane, and are indicated as such on the pattern.*

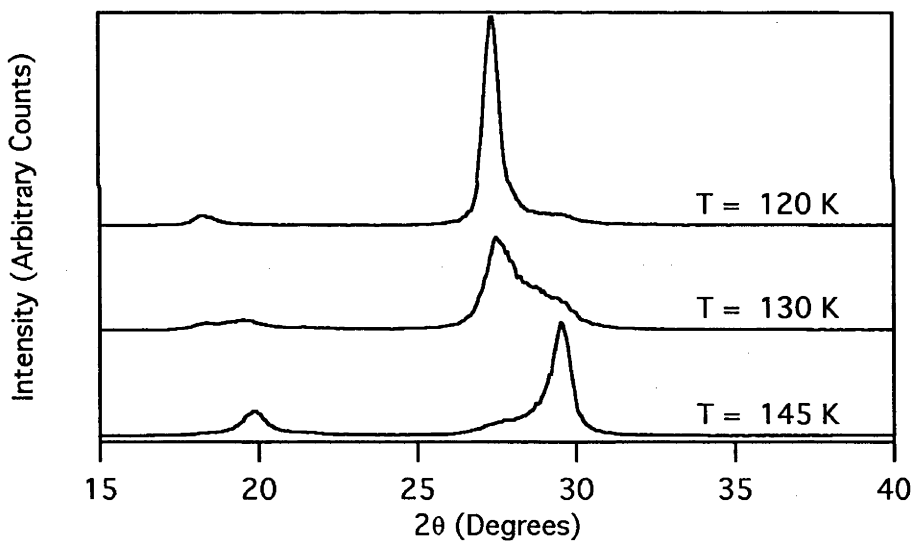

Figure 4.3.4: *c-axis oriented scans of* $(CH_4)_{\sim 0.9}RbC_{25}$ *at 120, 130 and 145 K, showing the (002) and (003) peaks.*

4.3.2: Results

The *c*-axis and the *ab*-plane data show that methane absorption begins between 145 K and 130 K. A significant portion of the sample retains the RbC_{25} *ab*-plane and *c*-axis patterns at 130 K, indicating a mixed binary-ternary system; at 120 K the sample appears to be single ternary compound; at 90 K two peaks associated with a new phase appear in

the *ab*-plane data, which can be assigned to the face-centred-cubic structure of solid methane. The *c*-axis data displays a rapid change from one spacing to another, without strong evidence of intermediate spacings.

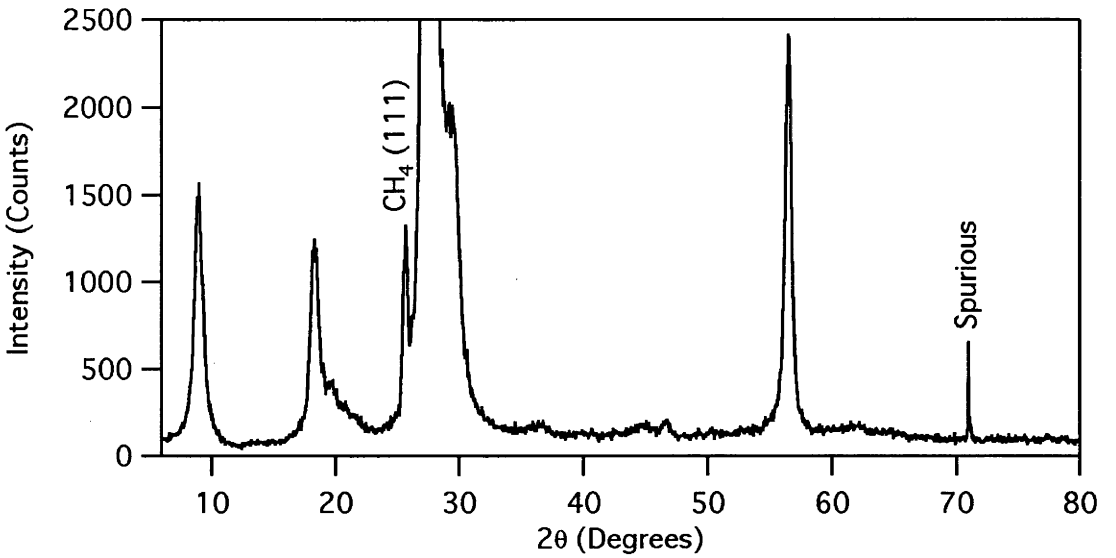

Figure 4.3.5: *c-axis oriented scans of $Rb(CH_4)_{\sim 0.9}C_{25}$ at 90 K. The strongest peak, indexed as (003), is set off scale to allow the smaller peaks to be visible. An anomalous peaks has appeared at 26.52° and is attributed to the fcc phase of solid CH_4. A sharp (but multiple-point) peak at 70.98° is not associated with either the ternary GIC phase(s) or with solid CH_4; it does not appear in other patterns and is thought to be spurious electronic noise.*

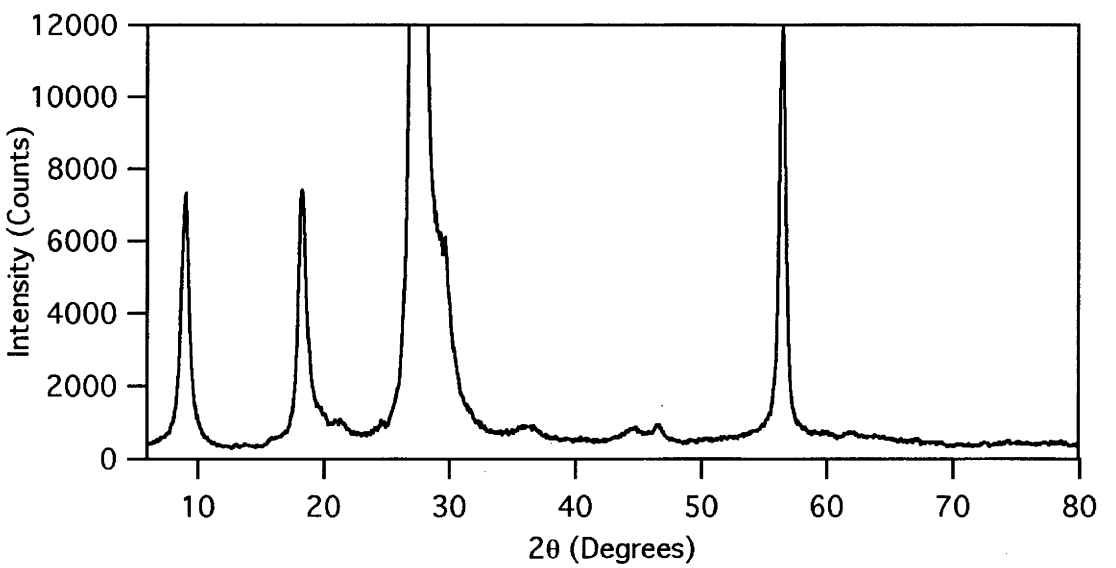

Figure 4.3.6: *c-axis oriented scans of $Rb(CH_4)_{\sim 0.9}C_{25}$ at 120 K. The strongest peak, indexed as (003), is set off scale to allow the smaller peaks to be visible.*

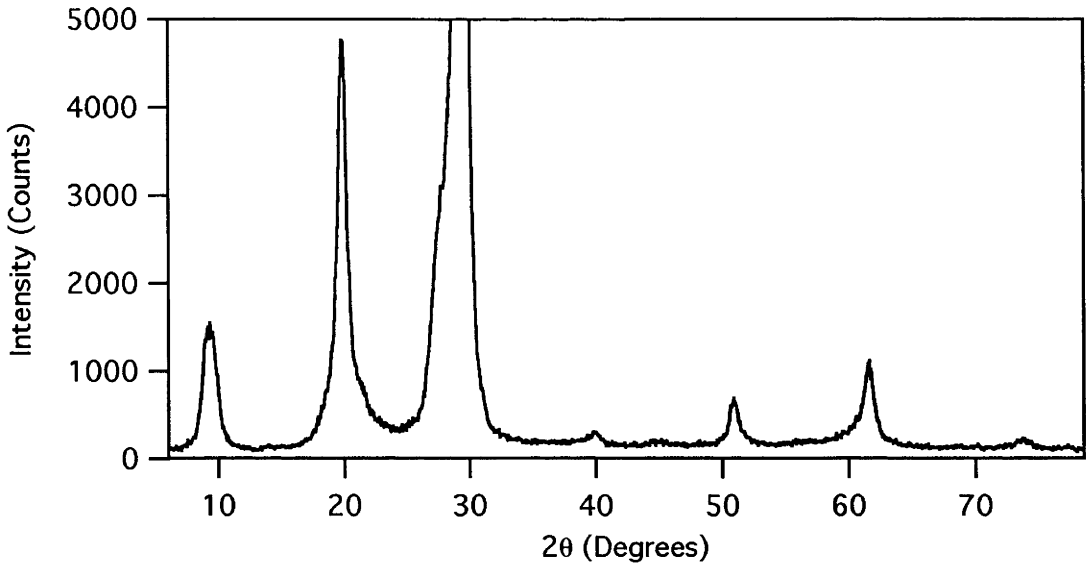

Figure 4.3.7: *c-axis oriented scans of RbC_{25} at 145 K. The strongest peak, indexed as (003), is set off scale to allow the smaller peaks to be visible. The intensities and peak positions have returned to the values for binary RbC_{25} at this temperature, with some remnant intensity at greater d-spacing.*

Data				Phase 1		Phase 2	
2θ (Degrees)	Intensity (Counts)	I/Imax x100	D (Å)	l_a	D x l_a (Å)	l_b	D x l_b (Å)
9.06	7316	6.346	9.753	1	9.752		
18.3	7418	6.434	4.844	2	9.688		
21.24	1045	0.906	4.178			2	8.359
27.39	115286	100	3.254	3	9.761		
29.7	6106	5.296	3.006			3	9.017
36.3	881	0.764	2.473	4	9.891		
44.76	816	0.708	2.023				
46.5	938	0.814	1.951	5	9.757		
56.52	11939	10.36	1.627	6	9.761		

Table 4.3.1: *An attempt to index the 120 K $Rb(CH_4)_{\sim 0.9}C_{25}$ c-axis diffraction pattern using the same two-phase approach used for the c-axis argon-rubidium pattern in Table 4.2.1. Unlike the rubidium-argon system, an unexpanded phase cannot be clearly indexed.*

Table 4.3.1 shows an attempt to index the peaks of the 120 K $(CH_4)_{\sim 0.9}RbC_{25}$ *c*-axis oriented diffraction pattern, applying the same two-phase approach used for the *c*-axis

$RbAr_{1.2}C_{25}$ diffraction patterns in Chapter 4.2. There the argon-rubidium *c*-axis pattern was determined to be the result of a phase with an expanded c-axis cell dimension, and a second phase with a much weaker pattern, with a repeat distance close to that of the unintercalated binary GIC. As can be seen from Table 4.3.1, the methane-rubidium *c*-axis patterns are less informative: while an expanded phase with a *c*-axis cell dimension of 9.77 Å can easily be indexed, no other c-axis repeat can be unambiguously determined from the data; though there are other peaks, they are insufficient in number and resolution to conclusively index any other single phase.

Tables 4.3.2 and 4.3.3 show the indexing of the *ab*-plane diffraction pattern at 90 K; the majority of the peaks can be indexed using the same $\sqrt{28}$x$\sqrt{28}$ cell that was initially applied to the saturated argon-rubidium-graphite patterns in Table 4.2.2; and can thus also fit the 2x2 and $\sqrt{7}$x$\sqrt{7}$ indexing. Two additional peaks that appear only on the 90 K pattern are indexed as the (111) and (200) lines of the high temperature phase of solid methane, which freezes at 90.75 K into a face-centred-cubic lattice with lattice constant 5.96 Å. This assignment is supported by shape of these peaks, which lack the turbostratic profile common to the rest of the pattern. Additionally, there appears to be a considerable 2θ zero-offset in the methane patterns; all of the diffraction lines associated with the Rb-CH_4 phase are approximately 0.1-0.2° lower than the corresponding peaks in the Rb-Ar compound (indexed in Table 4.2.2), while the peaks indexed as solid fcc methane also have a similar offset compared with the expected positions. This offset may be the result of a sample offset from the centre of the focussing circle, or of a misalignment in the diffractometer optics.

There are also two additional reflections at 12.78° and 32.52° that cannot be indexed as part of the 2x2 or $\sqrt{7}$x$\sqrt{7}$ phases, nor as peaks of frozen methane, especially since they are present in the 120 K pattern. There are several explanations that could account for their origin: there may be an additional *ab*-plane phase present; one of the phases may have a slight distortion away from a true hexagonal structure towards a monoclinic lattice; the peaks may be satellite peaks associated with an incommensurate modulation. Given that the hexagonal indexing is quite good and fits accurately (once the correction mentioned above is made) to the superlattices of the graphite grid, the most likely explanation is that there is an extra phase in the compound, but the two observed peaks do not provide sufficient data to index this phase.

Data			√28x√28 Cell				
2θ (Degrees)	Intensity (Counts)	D (Å)	h	k	l	a	$(a/a_{gr})^2$
8.82	843	10.025	0	0	1	10.025	(c)
12.78	701	6.9265	-	-		-	-
15.66	9934	5.6586	2	0		5.275	27.829
20.64	6418	4.3031	2	1		5.307	28.164
25.5	5875	3.493	1	1	1	6.05	(CH_4)
27.24	10172	3.2737	2	2		5.286	27.943
29.4	2378	3.0379	2	0	0	6.076	(CH_4)
31.5	4243	2.84	4	0		5.295	28.04
32.52	1990	2.7532	-	-		-	-
36.3	1838	2.4747	4	1		5.286	27.944
42.12	3127	2.1453	1	0		1	1
44.34	4275	2.0429	1	0	1	-	-
48.18	1401	1.8886	6	0		5.282	27.901
56.22	853	1.6361	4	4		5.284	27.919
56.76	1041	1.6218	7	0		5.292	28.005
58.68	934	1.5733	6	2		5.288	27.966
65.94	477	1.4166	8	0		5.282	27.904
72.66	310	1.3012	6	4		5.288	27.96
76.98	1672	1.2386	1	1		1	1

Table 4.2.2: *the 90 K ab-plane powder diffraction pattern of* $Rb(CH_4)_{\sim 0.9}C_{25}$ *indexed on a √28x√28 cell. The peaks marked* (CH_4) *and (c) are indexed as frozen methane and c-axis breakthroughs respectively. The peaks at 12.78° and 32.52° cannot be indexed as any of these phases.*

Data			2x2 Cell				√7x√7 Cell			
2θ (Degrees)	Intensity (Counts)	D (Å)	h	k	a (Å)	$(a/a_{gr})^2$	h	k	a (Å)	$(a/a_{gr})^2$
8.82	843	10.025								
12.78	701	6.927								
15.66	9934	5.659					1	0	2.638	6.957
20.64	6418	4.303	1	0	2.006	4.023				
25.5	5875	3.493					1	1	6.050	7.953
27.24	10172	3.274					1	1	2.643	6.986
29.4	2378	3.038								
31.5	4243	2.84					2	0	2.648	7.01
32.52	1990	2.753								
36.3	1838	2.475	1	1	1.998	3.992				
42.12	3127	2.145	1	0	1	1	1	0	1	1
44.34	4275	2.043								
48.18	1401	1.889					3	0	2.641	6.975
56.22	853	1.636					2	2	2.642	6.98
56.76	1041	1.622	2	1	2	4.001				
58.68	934	1.573					3	1	2.644	6.991
65.94	477	1.417					4	0	2.641	6.976
72.66	310	1.301					3	2	2.644	6.99
76.98	1672	1.239	1	1	1	1	1	1	1	1

Table 4.3.3: *the 90 K ab-plane powder diffraction pattern of* $Rb(CH_4)_{\sim 0.9}C_{25}$ *indexed on a 2x2 cell and a √7x√7 cell. The remaining peaks are indexed in Table 4.3.2.*

4.3.3 *ab*-Plane Intensity Simulations of Ternary $Rb(CH_4)_{0.9}C_{25}$ Structures.

As with the argon-rubidium-graphite system, initial *ab*-plane simulations of the methane-rubidium-GIC were undertaken using the Rietveld refinement package GSAS[2]; and again as with the $RbAr_{1.2}C_{25}$ system, no $\sqrt{28}x\sqrt{28}$ cell could produce an adequate match with the gross intensities of the experimental XRD pattern. A Rietveld refinement based on the same two phases used for the Rb-Ar ternary system again gives an excellent match to the gross positions and intensities of the 120 K *ab*-plane diffraction pattern, and is shown in Figure 4.2.8.

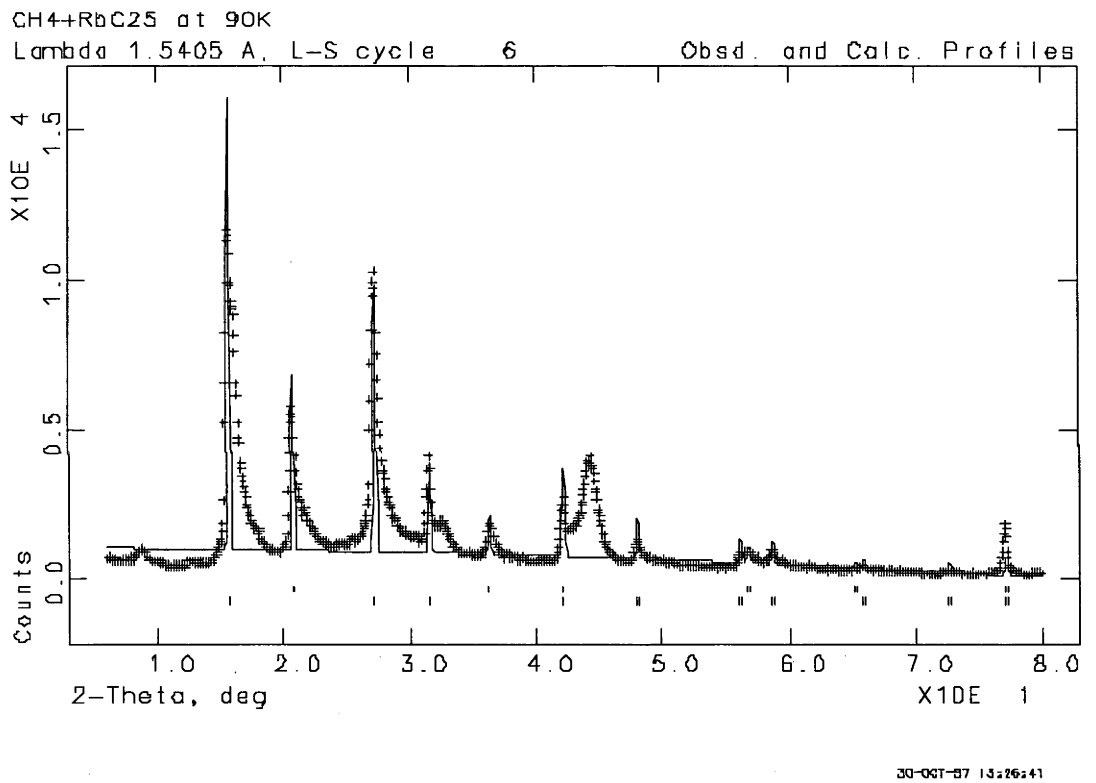

Figure 4.3.8: *A two-phase Rietveld fit to the ab-plane oriented 120K* CH_4RbC_{25} *pattern. Phase 1 has a 2x2 P6 unit cell with a rubidium atom at (0,0), while Phase 2 has a* $\sqrt{7}x\sqrt{7}$ *P6 unit cell with a rubidium atom at (0,0) and an carbon atom at (1/3,2/3), representing a methane molecule; the hydrogen atoms on the methane molecule are not included for simplicity and due to their lower x-ray structure factor.*

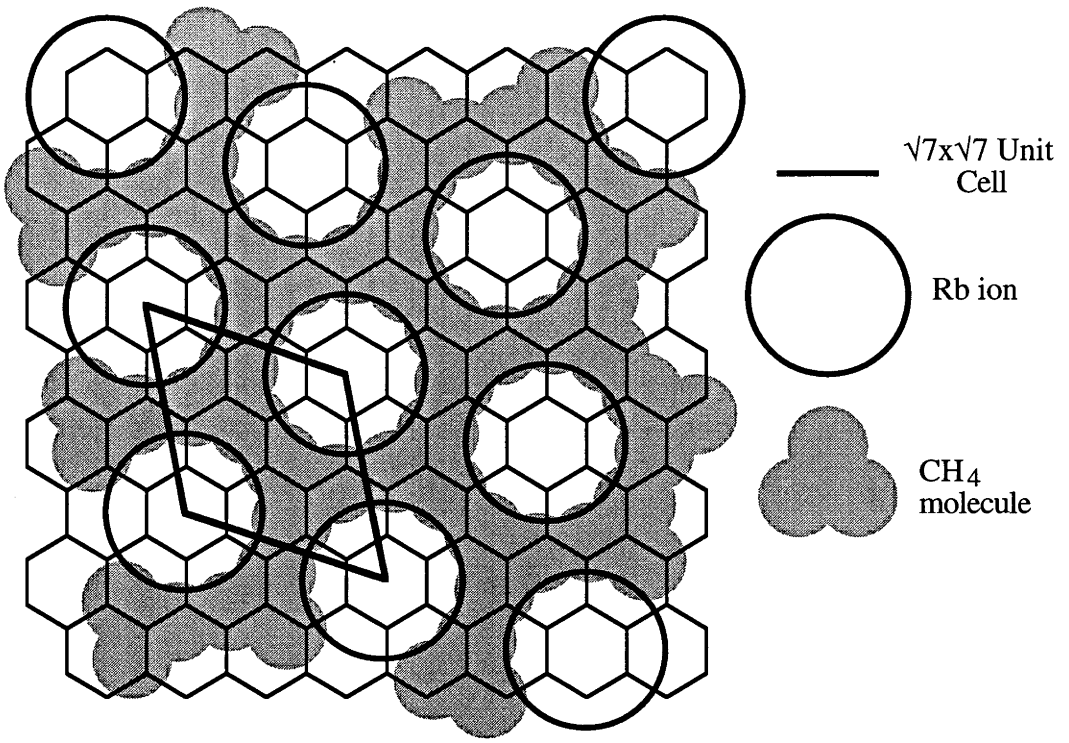

Figure 4.3.9: *ab-plane structure for the √7x√7 $(CH_4)_2RbC_{28}$ methane-rich phase used in the following simulations. As with the argon-rubidium simulations, the graphene layer is shown here but its contributions are not included. Van der Waals radii are used for the guest species.*

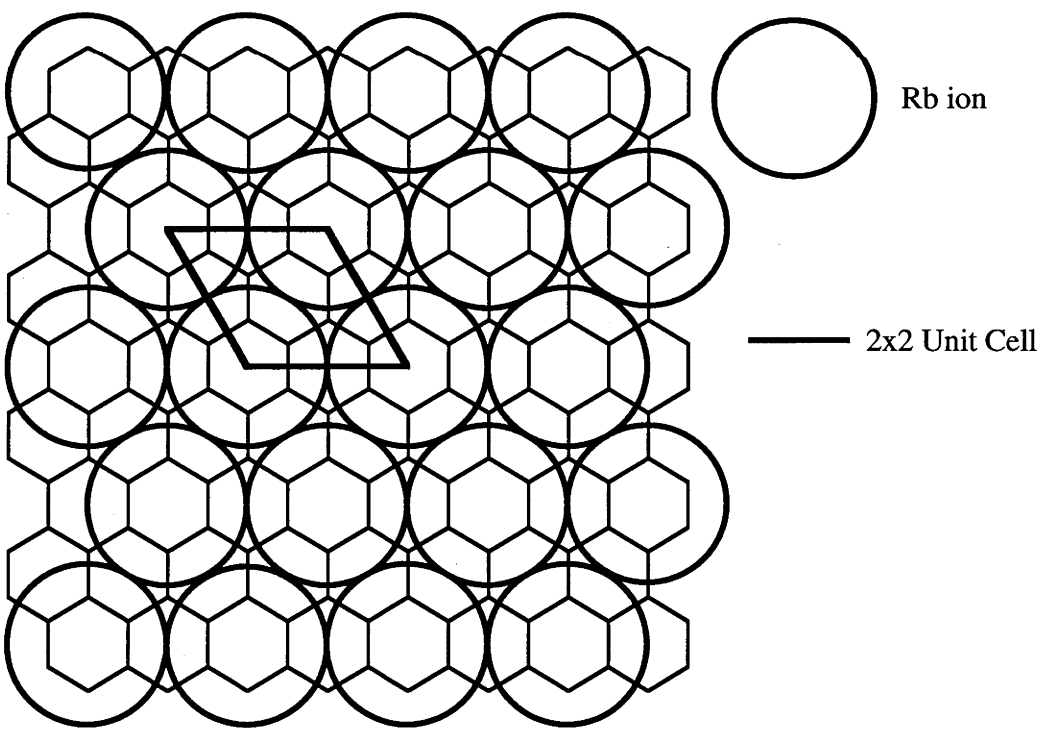

Figure 4.3.10: *The ab-plane structure for the 2x2 RbC_{16} methane-poor phase used in the following simulations. Van der Waals radii are used for the guest species.*

From the methane *ab*-plane indexing given in Table 4.3.3 and the Rietveld refinement shown in Figure 4.3.8, the conclusion may be drawn that the methane-rubidium-graphite system has phase separated in the same manner as the argon-rubidium-graphite system, that is into an methane-rubidium phase with an *ab*-plane unit cell dimension equal to $\sqrt{7}$ times the graphite unit cell dimension and a pure rubidium phase with an ab-plane unit cell dimension equal to twice the graphite cell dimension. Further simulations using the whole-pattern-simulation method described in Chapter 2 were undertaken, using in the *ab*-plane the structures shown in Figures 4.3.9 and 4.3.10. These have a stoichiometry of $Rb(CH_4)_2C_{28}$ for the $\sqrt{7}x\sqrt{7}$ phase and RbC_{16} for the 2x2. Example simulations are shown for the $\sqrt{7}x\sqrt{7}$ and 2x2 phases in Figures 4.3.11-4.3.14, with the full combined simulated pattern shown in Figure 4.3.15. In all these figures, the 2θ position of the data was shifted by +0.15° to correct for the zero position offset mentioned above.

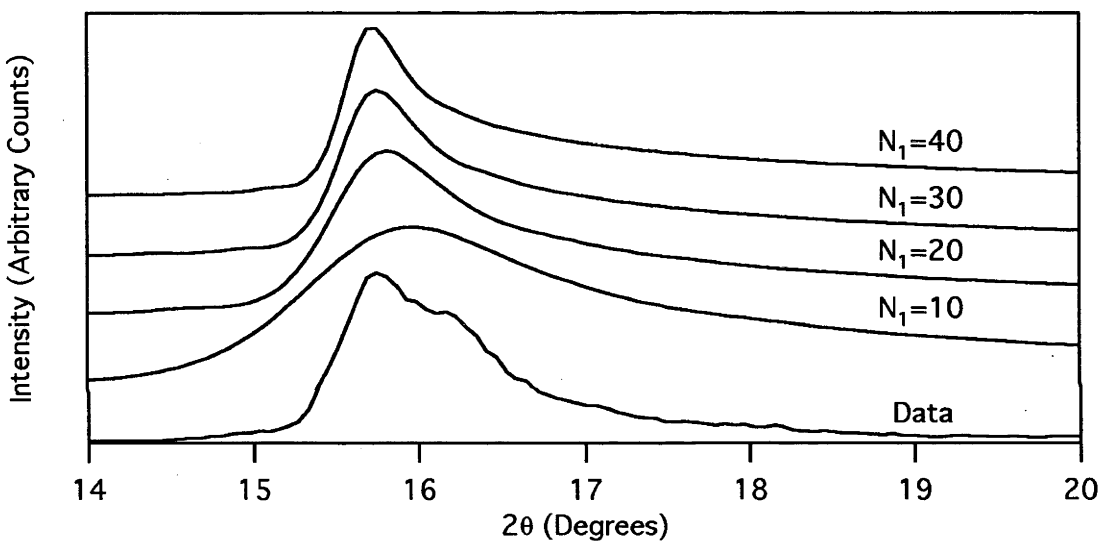

***Figure 4.3.11**: The strongest $RbCH_4C_{25}$ band assigned to the $\sqrt{7}x\sqrt{7}$ phase versus simulated $\sqrt{7}x\sqrt{7}$ phase (10) bands with ab-plane domain size $10<N_1<40$. The other parameters used in the simulation are $N_3=1$, $a_{gr}=2.475$, $c=9.75$, $\lambda=1.54178$, $CD=0.0$.*

The simulations of the $\sqrt{7}x\sqrt{7}$ phase do not include any contribution from the hydrogen atoms in the methane molecules: the methane molecule is treated as a single carbon atom at the (1/3, 2/3) site. This assumption was made to simplify the calculations, and was considered valid given the much lower scattering factor of hydrogen, and its faster fall-off with increasing 2θ, compared to the other atoms in the system, as shown in Figures 2.7 and 2.8.

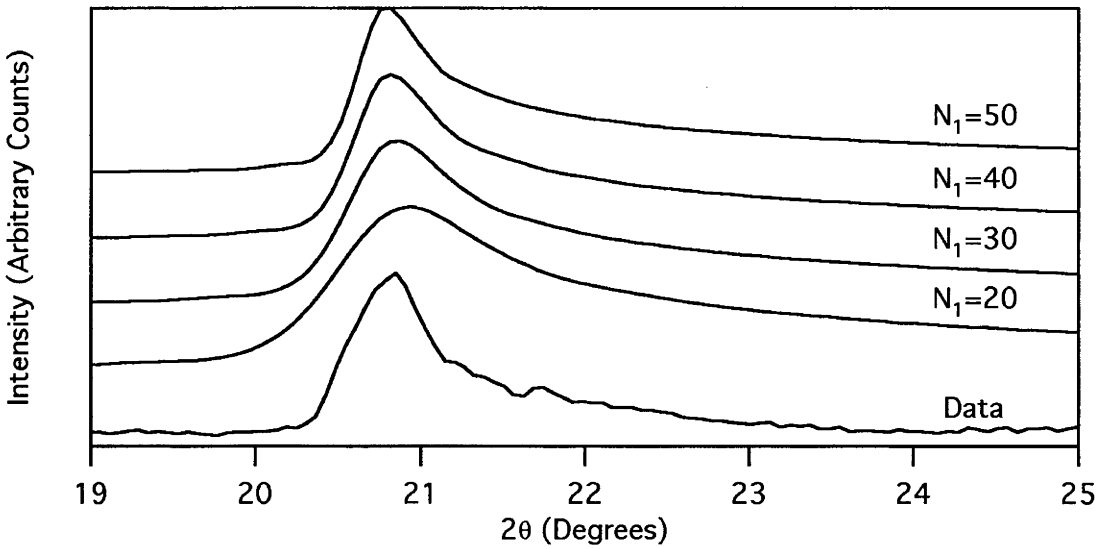

Figure 4.3.12: *The strongest $RbCH_4C_{25}$ band assigned to the 2x2 phase versus simulated 2x2 phase (10) bands with ab-plane domain size 20<N1<50. The other parameters used in the simulation are N3=1, a_{gr}=2.478, c=9.0, λ=1.54178, CD=0.0.*

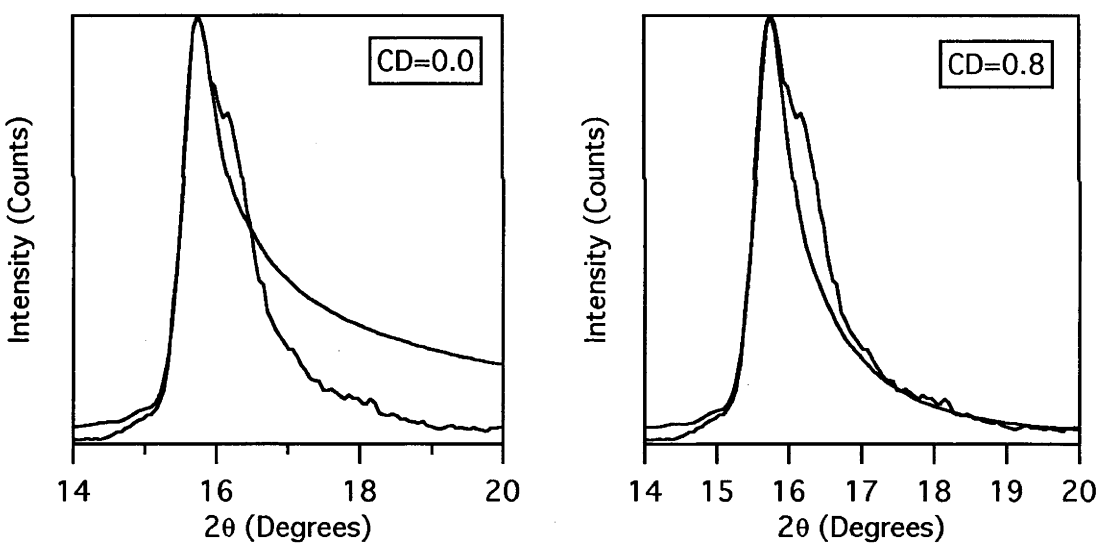

Figure 4.3.13: *The strongest $RbCH_4C_{25}$ band assigned to the √7x√7 phase is compared employing different values of the orientational parameter CD on a simulated profile based on N1=30, N3=1, a_{gr}=2.475, c=9.75, λ=1.54178.*

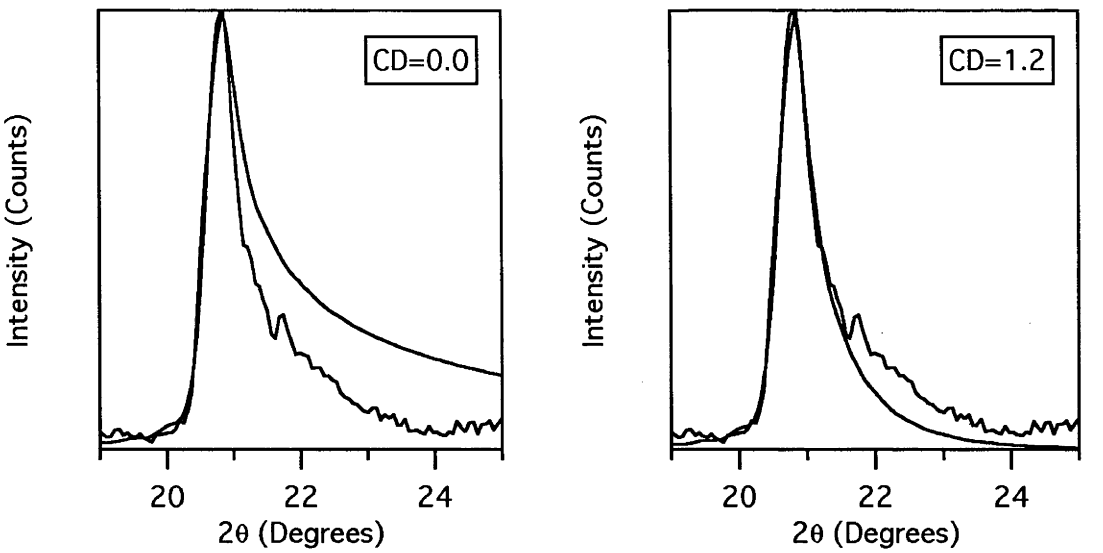

Figure 4.3.14: *The strongest $RbCH_4C_{25}$ band assigned to the 2x2 phase is compared with four simulations employing different values of the orientational parameter CD on a simulated profile based on N_1=30, N_3=1, a_{gr}=2.475, c=9.75, λ=1.54178.*

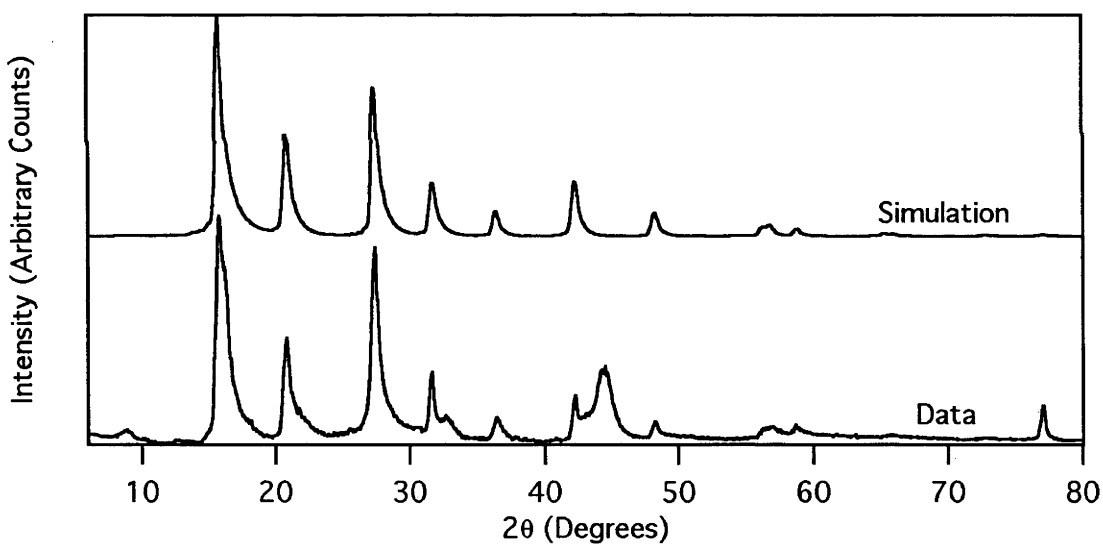

Figure 4.3.15: *the combined best simulations compared with data taken at 120 K. The parameters used for these simulations are shown in Table 4.3.4.*

The final best simulation, shown above in Figure 4.3.15, uses the following values:

	Phase A	Phase B
Symmetry	P6	P6
a	2	2.646 ($\sqrt{7}$)
a_{gr}	2.478 Å	2.475 Å
c	9.0 Å	9.75 Å
$N_1=N_2$	40	30
N_3	1	1
CD	1.2	0.8
Thermal factors	Rb=0.6	Rb=0.8 CH_4=0.8

***Table 4.3.4**: the parameters used for the simulations shown in Figure 4.3.15.*

The parameters used for the best $Rb(CH_4)_{0.9}C_{25}$ simulations have a number of similarities with those employed for the $Rb(Ar)_{1.2}C_{25}$ simulations. The values for a_{gr}, the graphite in-plane dimension, are the same for both compounds: 2.478 Å for the 2x2 phases, and 2.475 Å for the $\sqrt{7}$x$\sqrt{7}$ ternary phases. While the in-plane crystallite domains are considerably smaller for the methane-rubidium GIC than for the argon-rubidium GIC in terms of numbers of unit cells across (the values used in the calculations and thus shown above), the physical dimensions of the 2x2 and $\sqrt{7}$x$\sqrt{7}$ phases are the same within each system: 198 Å for the 2x2 and 196 Å for the $\sqrt{7}$x$\sqrt{7}$ Å in the methane system, compared with 297 Å for the 2x2 phase and 294 Å for the $\sqrt{7}$x$\sqrt{7}$ phase in the argon system.

Unlike the rubidium-argon GIC system, there is no sign of 3-dimensional ordering in the 2x2 phase; the orientational parameters CD for each phase produce a peak shape similar enough to the observed pattern that there is no need for any except purely turbostratic simulations, with N_3 equal to 1. The values of *c* used will therefore have little effect on the final calculations. This may be evidence indicating that the two phases in the rubidium-argon GIC have separated into separate *c*-axis as well as *ab*-plane domains, so that there is an interlayer interaction between adjacent 2x2 domains, while the rubidium-methane GIC is a randomly interstratified system. The nature of the interstratification of these systems will be discussed in Chapter 5.

There are three obvious flaws with the simulated pattern shown in Figure 4.3.15 when compared with the data: the intensity produced for the $\sqrt{7}$x$\sqrt{7}$ (11) band at 27.24° is a

good deal less than that expected, and there is a peak at 32.5° which is not simulated at all. Additionally, the simulated (20) peak of the $\sqrt{7}x\sqrt{7}$ phase does not match the observed peak shape. These differences are shown in Figure 4.3.16.

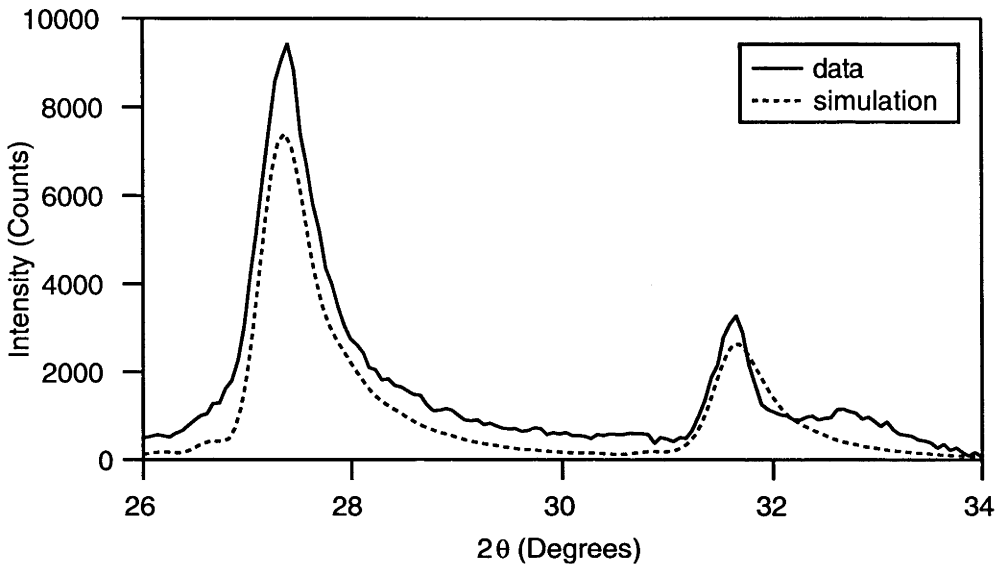

Figure 4.3.16: *the $\sqrt{7}x\sqrt{7}$ simulated pattern compared with $Rb(CH_4)_{0.9}C_{25}$ data taken at 120 K. The three major inaccuracies in the simulation are present in this diagram: an intensity misfit of the (11) peak, a shape misfit of the (20), and an unexplained peak at 32.5°. These may all result from contributions of the hydrogen atoms which are not included in the simulations.*

The (11) peak is at the same position that the *c*-axis (003) breakthrough would be expected; since the *c*-axis pattern isn't simulated at all in the *ab*-plane patterns this may be a source of some of the extra intensity. The misfit in shape of the (20) cannot be explained in the same manner; nor the peak at 35.5°. It is also possible that contributions from the hydrogen atoms, which are ignored in these simulations, are responsible for the extra intensity at (11), and if there is a high degree of orientational ordering in the methane molecule it may have an effect on the peak shape as well (see Chapter 2).

The simulations of the *c*-axis patterns, which are undertaken below, provide more information on the nature of the orientational structure of the methane molecules in this system. We will return to the *ab*-plane structure after the *c*-axis structure is described.

4.3.4 *c*-Axis Intensity Simulations of Ternary $Rb(CH_4)_{0.9}C_{25}$ Structures.

The *c*-axis simulations are computationally simpler than the *ab*-plane calculations, so that there was no need to use a quicker method such as Rietveld fits first. Unlike the first *ab*-plane simulations, the hydrogen contributions to the structure factor are needed to give a satisfactory fit and so are included.

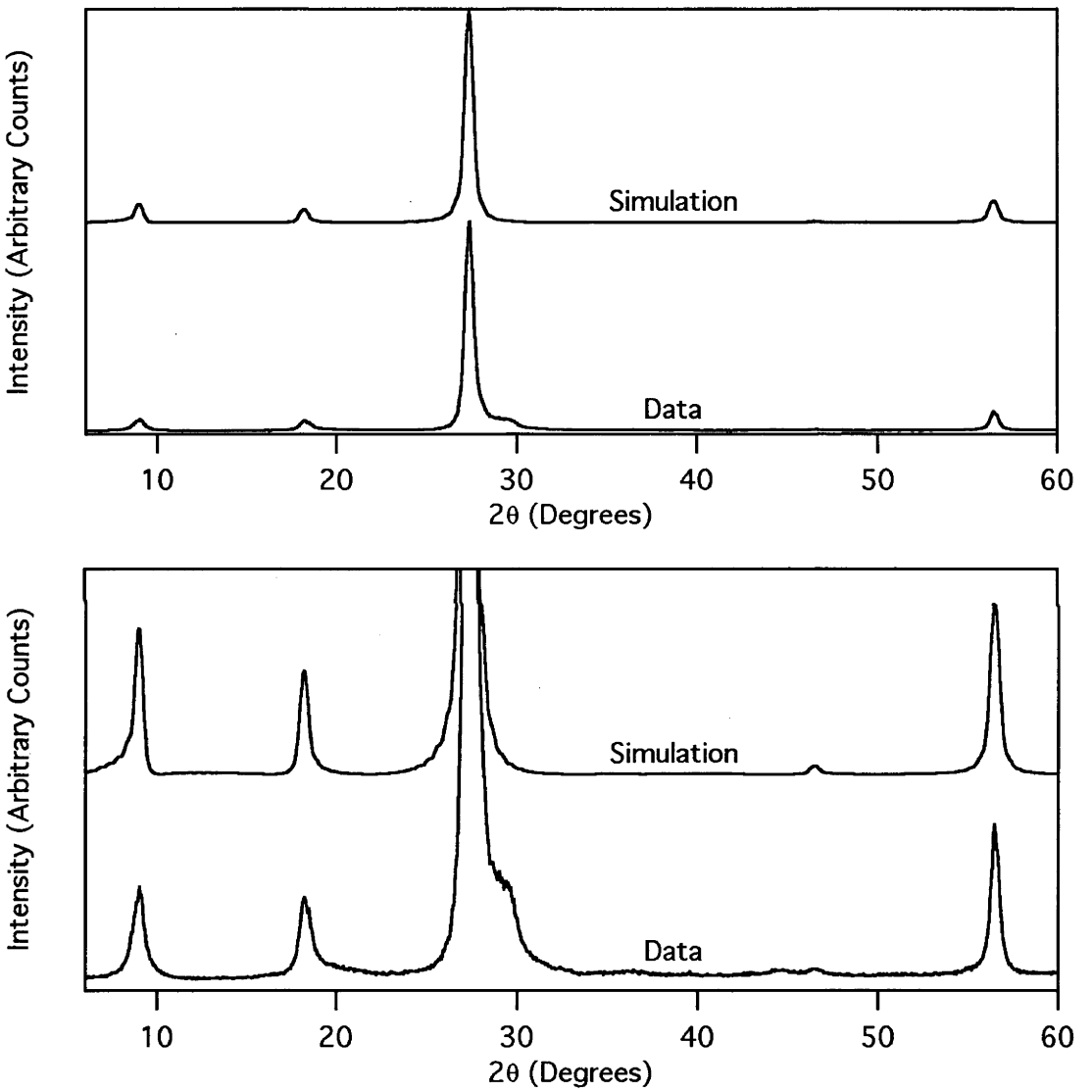

***Figure 4.3.17**: c-axis data taken at 120 K compared with simulated pattern for $Rb(CH_4)_{2.0}C_{28}$. The methane molecules are mass-centred on the mean rubidium position. The parameters used are N_3=18, Δ=12, C=9.77, λ=1.54178.*

Two pattern calculations are shown in Figures 4.3.17 and 4.3.19, compared with the *c*-axis diffraction pattern for the sample cooled to 120 K under an atmosphere of CH_4, while the structured used for these calculation are shown in Figures 4.3.18 and 4.3.20.

In both the pattern simulations the stoichiometry used is $Rb(CH_4)_{2.0}C_{28}$, representing the $\sqrt{7}x\sqrt{7}$ phase.

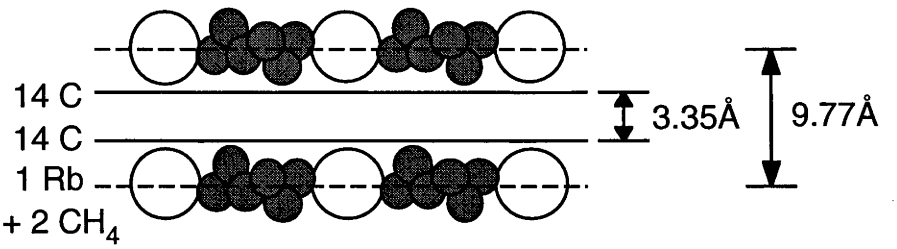

Figure 4.3.18: *The c-axis cell used for the simulations shown in Figure 4.3.17. Note the alternating CH_4 packing, with the methane molecules mass centred on the mean rubidium position. The atomic coordinates are in Table 4.3.5*

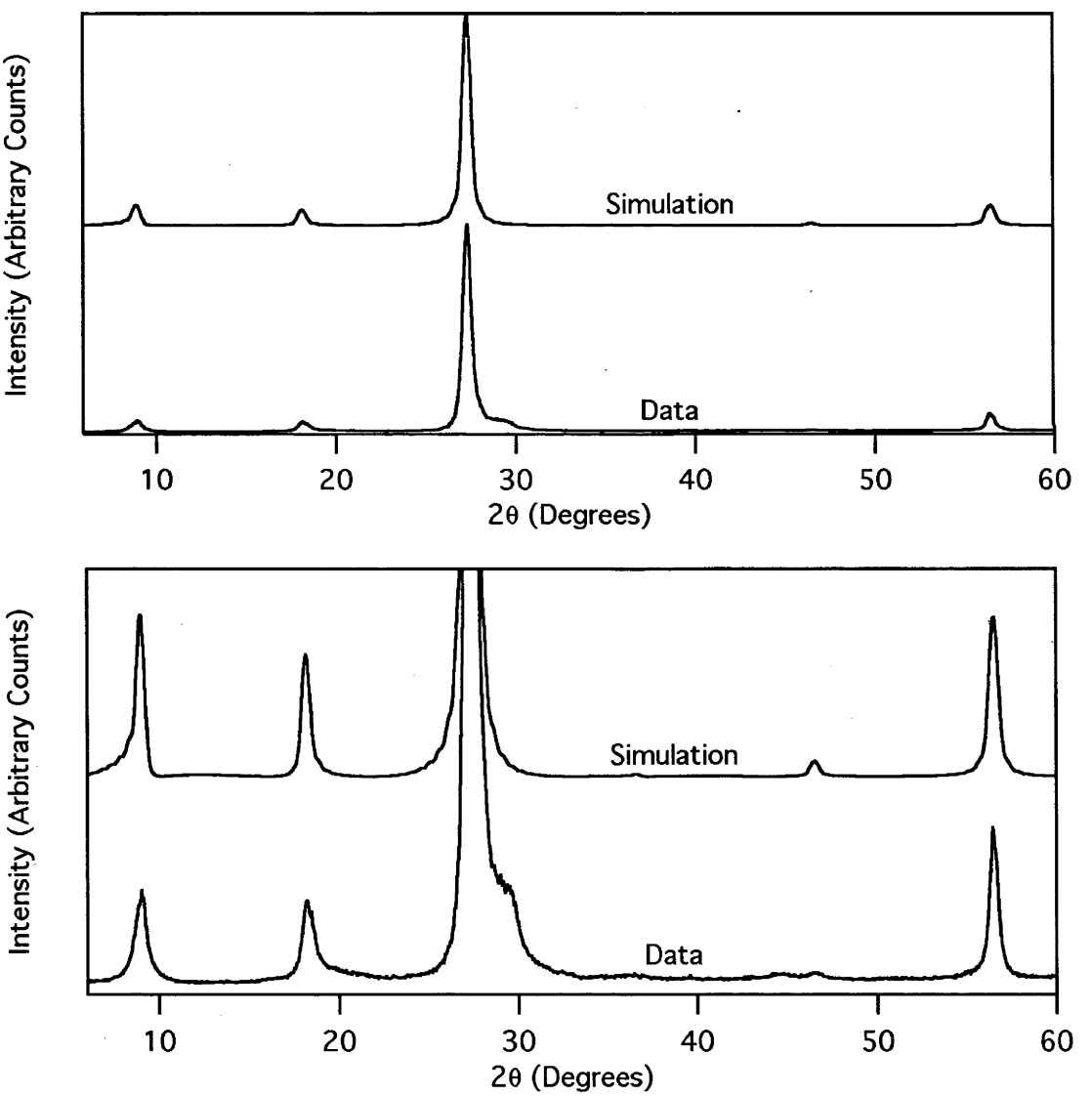

Figure 4.3.19: *C-axis data taken at 120 K compared with simulated pattern for $Rb(CH_4)_{2.0}C_{28}$. The methane molecules are geometrically-centred on the mean rubidium position. The parameters used are N_3=18, Δ=12, C=9.77, λ=1.54178.*

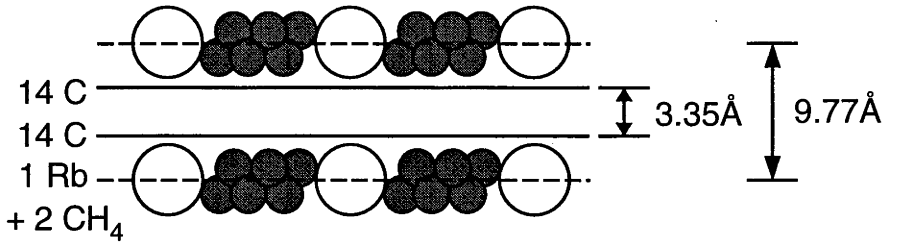

Figure 4.3.20: *The c-axis cell used for the simulations shown in Figure 4.3.19. Note the alternating CH_4 packing, with the methane molecules centred geometrically on the mean rubidium position. The atomic coordinates are in Table 4.3.5.*

	Carbon Atoms	Hydrogen Atoms
Mass Centred	2x0.0	1x0.122, 1x-0.122 3x0.038, 3x-0.038
Geometrically Centred	1x0.037, 1x-0.037	4x0.075, 4x-0.075

Table 4.3.5: *the c-axis fractional coordinates of the atoms of the CH_4 molecules in the two models - mass centred and geometrically centred - shown in Figures 4.3.18 and 4.3.20.*

In the *c*-axis simulations shown above, the primary differences between the pattern simulations is in the position of the methane molecules along the c-axis. In both sets of simulations the structure used has the methane molecules aligned so that a threefold axis of the tetrahedron is perpendicular to the neighbouring graphene layers, with 50% of the molecules in an "upright" orientation and the remainder in a "downwards" orientation. as shown in Figures 4.3.18 and 4.3.20. This orientation produced the best simulation intensities out of those tried. Two different models are shown in the simulations. In the mass-centred model, shown in Figures 4.3.17 and 4.3.18, the methane molecules are positioned so that the carbon atom is at the same c-axis position as the layers of rubidium atoms. In the geometrically-centred model, the CH_4 molecules are positioned so the hydrogen atoms are equidistant from the layer of alkali metal ions and from the upper and lower graphene layers. The atomic positions of the hydrogen and carbon atoms in the methane molecules are shown in Table 4.3.5 for both models.

Table 4.3.6 shows the peak intensities of several simulated *c*-axis patterns compared with the data taken at 120 K. The peak intensities are shown as a percentage of the strongest peak, which is the (003) reflection in all patterns. The mass-centred and geometrically centred models are shown, with the mass-centred model giving a slightly better fit to the low angle peaks, where the hydrogen contribution to the overall structure

factor is the greatest. Also listed are the same models with the contributions of the hydrogen atoms ignored: these are sufficiently worse that it is clear that the hydrogen contribution must be included.

Peak	Data (120 K)	Mass Centred with Hydrogen	Geometrically Centred with Hydrogen	Mass Centred with no Hydrogen	Geometrically Centred with no Hydrogen
001	5.683	8.771	9.409	14.98	14.95
002	5.063	6.139	6.959	8.447	8.447
003	100.0	100.0	100.0	100	100.0
005	0.792	0.508	0.803	0.529	0.529
006	9.386	10.36	9.707	10.65	10.65
$\Sigma\|y(o)-y(i)\|^2$		11.72	17.58	99.13	99.54

Table 4.3.6: *The c-axis peak intensities (as a percentage of the strongest peak) of data taken from the* $Rb(CH_4)C_{25}$ *compared with three simulations; the* $Rb(CH_4)_{2.0}C_{28}$ *simulation with mass-centred methane molecules shown in Figures 4.3.17 and 4.3.18, the* $Rb(CH_4)_{2.0}C_{28}$ *simulation with geometrically centred methane molecules shown in Figures 4.3.19 and 4.3.20, and with a mass-centred* $Rb(CH_4)_{2.0}C_{28}$ *simulation identical to the mass centred pattern but with no hydrogen atoms included in the structure factor.*

The c-axis simulations do not include any contribution from an RbC_{16} phase: as with the rubidium-argon simulations, they are either far less than that produced by the $Rb(CH_4)_2C_{28}$ structure, or they have the same *c*-axis spacing as the rubidium-methane phase and are thus hidden beneath the pattern produced by that phase. Again, as with the argon-rubidium-graphite system, the *c*-axis data and simulations do not lend positive support to the two-phase model of the methane-rubidium-graphite system, but neither do they disprove it.

4.3.5 *ab*-plane $Rb(CH_4)_{0.9}C_{25}$ Simulations with Hydrogen Contributions

Given that the structural models including contributions from hydrogen atoms provided the best approximation to the *c*-axis data, it is worthwhile to introduce these contributions to the *ab*-plane simulations in the hope of correcting the errors noted above.

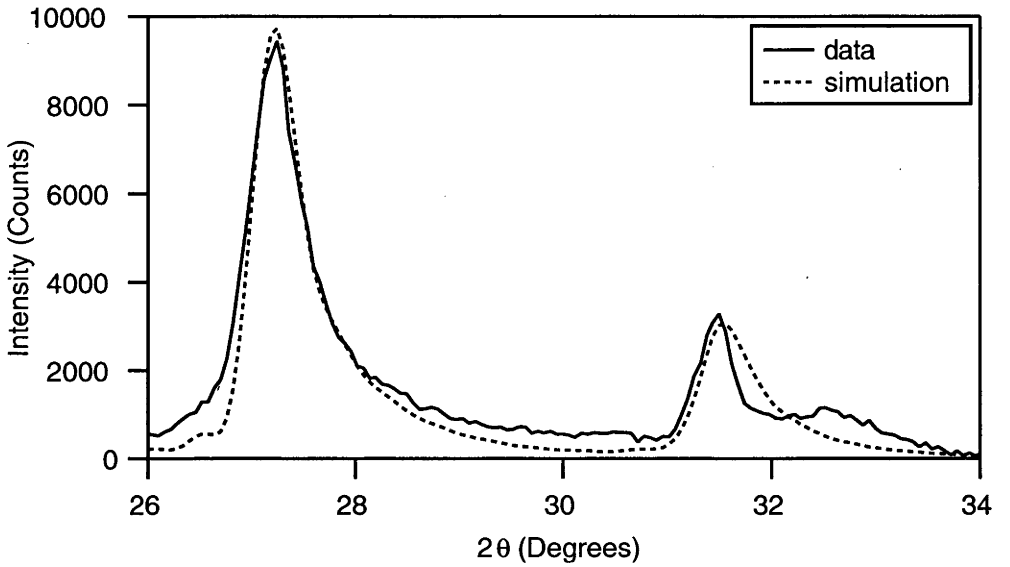

Figure 4.3.21: *The (11) and (20) reflections of the* $Rb(CH_4)_{0.9}C_{25}$ *ab-plane data taken at 120 K compared with the best simulation (including hydrogen contributions), while the intensity misfit of the (11) is corrected, the shape misfit of the (20) and the peak at 35.5° are still not simulated.*

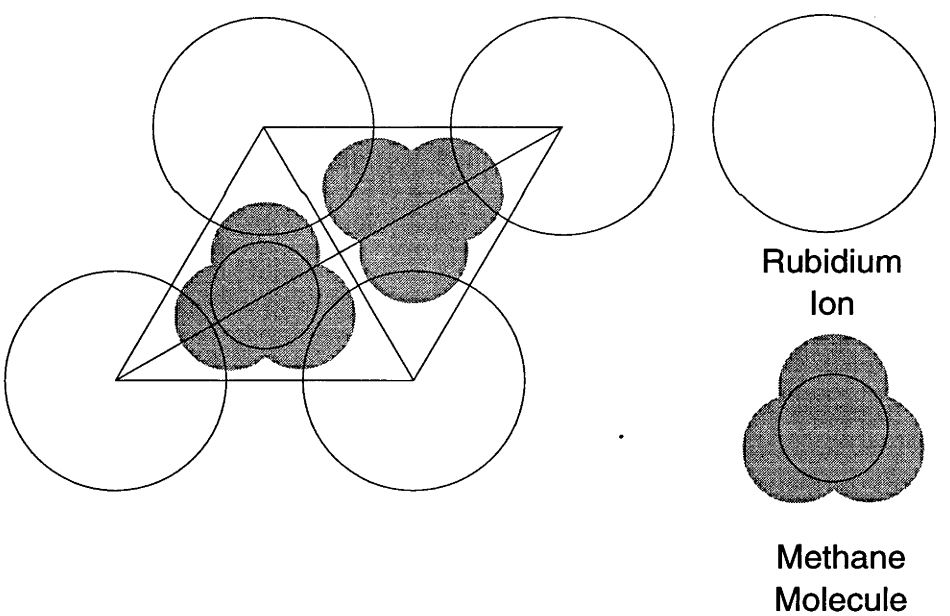

Figure 4.3.22: *the* $\sqrt{7}x\sqrt{7}$ *P6 ab-plane structure used for the simulation shown in Figure 4.3.21. The methane molecules are mass centred on the c-axis plane of the rubidium ions, and are in the orientation shown, with one hydrogen atom at the threefold site and the other three at (0.508,0.204) and its equivalent positions for each methane molecule.*

The best *ab*-plane $\sqrt{7}x\sqrt{7}$ simulation found employing the hydrogen contributions is shown in Figure 4.3.21. The structure placed the methane molecules at the threefold site

at (1/3,2/3), oriented in the manner shown in Figure 4.3.22. The CH_4 molecules are mass-centred on the rubidium ion plane along the c-axis of the simulated cell.

The simulated pattern in Figure 4.3.21 only displays the region of the misfit at 26°-34° in 2θ; a comparison with the same region shown in Figure 4.3.16 shows that the contributions of the hydrogen atoms have corrected the intensity misfit in the (11) band, but have not had any effect on the shape of the (20) reflection. The unusual peak shape of the (20), and its adjacency to the unindexed peak at ~35.5°, indicates that there is an inaccuracy in the simulated model. The evidence that the hydrogen atoms do make a significant intensity contribution at this angle in 2θ implies that there is an orientational arrangement of the methane molecules in the sample which is not reflected in the simulation. Efforts to improve this simulation were not successful.

4.3.6 Conclusion

As with the rubidium-argon system, the *ab*-plane data are best explained by a two phase model of the system, with the methane molecules all occupying the threefold site in ternary phase with $\sqrt{7}x\sqrt{7}$ *ab*-plane lattice and an expanded *c*-axis dimension, of stoichiometry $Rb(CH_4)_2C_{28}$. The remainder of the rubidium is in a compressed phase with a 2x2 in-plane lattice, though a separate *c*-axis pattern associated with this phase was not observed. Small remaining inaccuracies in the *ab*-plane simulated patterns could not be removed, and are thought to be the result of orientational ordering in the methane molecules which were not included in the model, but apart from these the model is adequate. The saturated rubidium-methane-graphite system is thus a bi-intercalation compound of formula $RbC_{16} \bullet Rb(CH_4)_2C_{28}$ (st. 2).

References

1. K. Watanabe, T. Kondow, M. Soma, T. Onishi, and K. Tamaru, *Molecular-sieve type sorption on alkali graphite intercalation compounds.* Proceedings of the Royal Society of London A, 1973. **333**: p. 51-67.

2. A.C. Larson and R.B. Von Dreele, LANSCE, MS-H805, Los Alamos National Laboratory, NM 87545, USA.

4.4: Nitrogen Absorption by Potassium Graphite Intercalation Compounds: The Structure of $K(N_2)_{\sim 0.7}C_{25}$

As with the other large molecules physisorbed to make the ternary GICs described in the initial studies[1], there had been few later publications on potassium-nitrogen-graphite system. However, nuclear resonance photon scattering experiments[2] on N_2 in KC_{25} showed that the N_2 molecule was lying parallel to the graphite planes in the sample. The original studies found that nitrogen would only be absorbed in KC_{25} by slowly cooling the sample in the presence of the gas - a behaviour we have seen in all the large molecule ternary GICs - and that the saturation stoichiometry was $K(N_2)_{\sim 0.7}C_{25}$. Here we will present powder diffraction patterns from oriented samples of the ternary intercalation compound $K(N_2)_{\sim 0.7}C_{25}$ over a range of temperatures.

4.4.1: Data

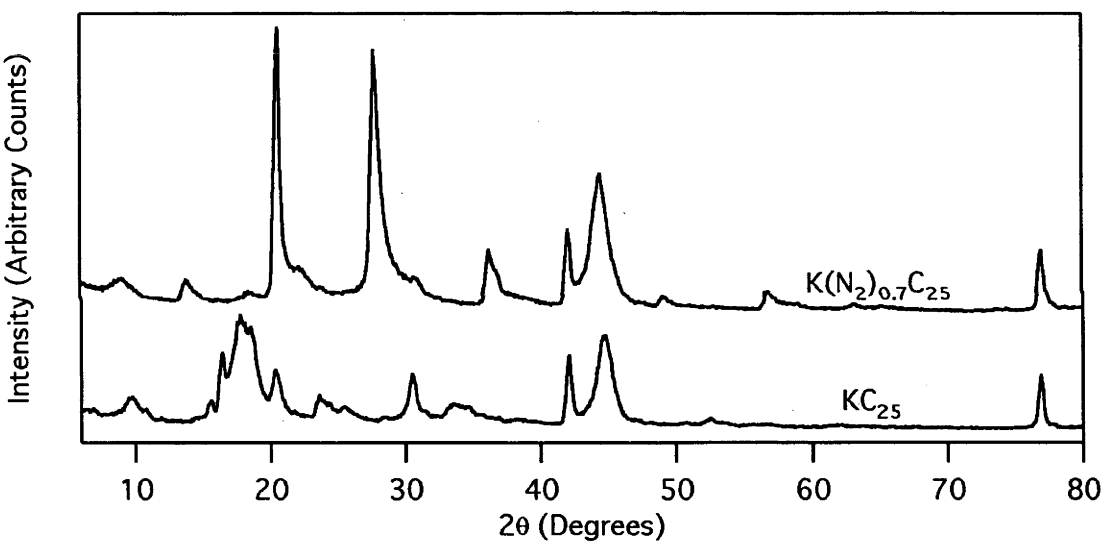

Figure 4.4.1: *ab-plane oriented x-ray powder diffraction patterns of the binary graphite intercalation compound KC_{25} and its physisorbed ternary GIC $K(N_2)_{0.7}C_{25}$, both taken at 90 K. There is no remnant of the binary pattern in the ternary structure.*

Figure 4.4.1 shows the *ab*-plane diffraction patterns obtained from an oriented sample of stage 2 potassium graphite intercalation compound that was cooled in stages from room temperature to 90 K while under an atmosphere of nitrogen. This pattern is compared with the diffraction pattern obtained from the binary GIC KC_{25} at the same temperature.

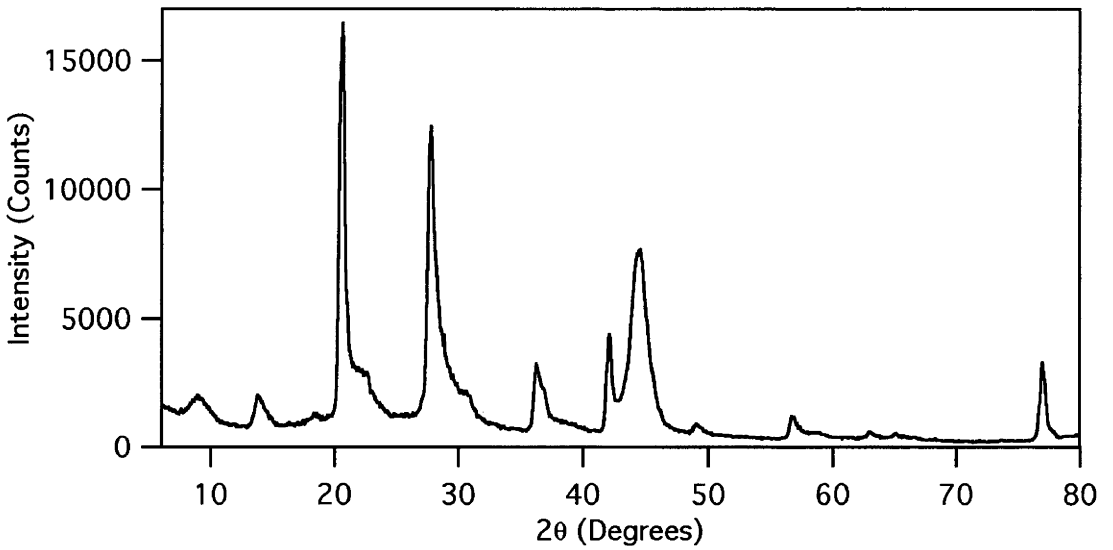

Figure 4.4.2: *ab-plane oriented x-ray powder diffraction pattern of* $K(N_2)_{0.7}C_{25}$ *at 130 K.*

Figure 4.4.2 shows the *ab*-plane XRD powder diffraction pattern from the ternary compound at 130 K. The sample was prepared to a ratio of K:25C, and weighed 0.479 g, equivalent to 1.41×10^{-3} moles of KC_{25}. The sample stick contained 560 Torr of nitrogen, equivalent to 3.09×10^{-3} moles of N_2, which provided a sufficient reservoir to reach the published saturation stoichiometry of $K(N_2)_{0.7}C_{25}$. Each *ab*-plane scan took ~12 hours. *c*-axis scans were taken also while the sample was being cooled and are shown in Figures 4.4.3 and 4.4.4.

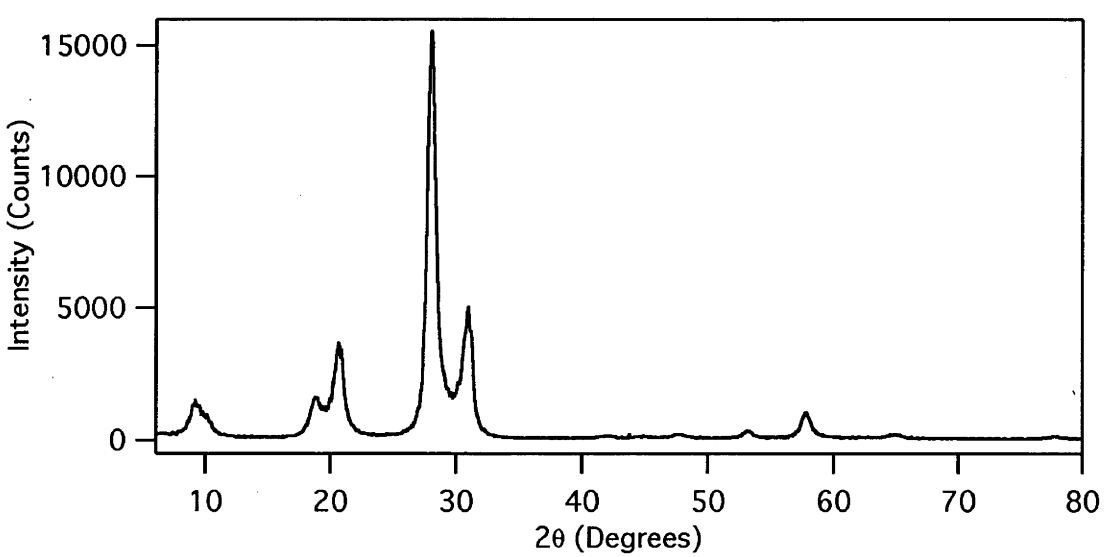

Figure 4.4.3: *c-axis oriented x-ray powder diffraction pattern of* $K(N_2)_{0.7}C_{25}$ *at 130 K.*

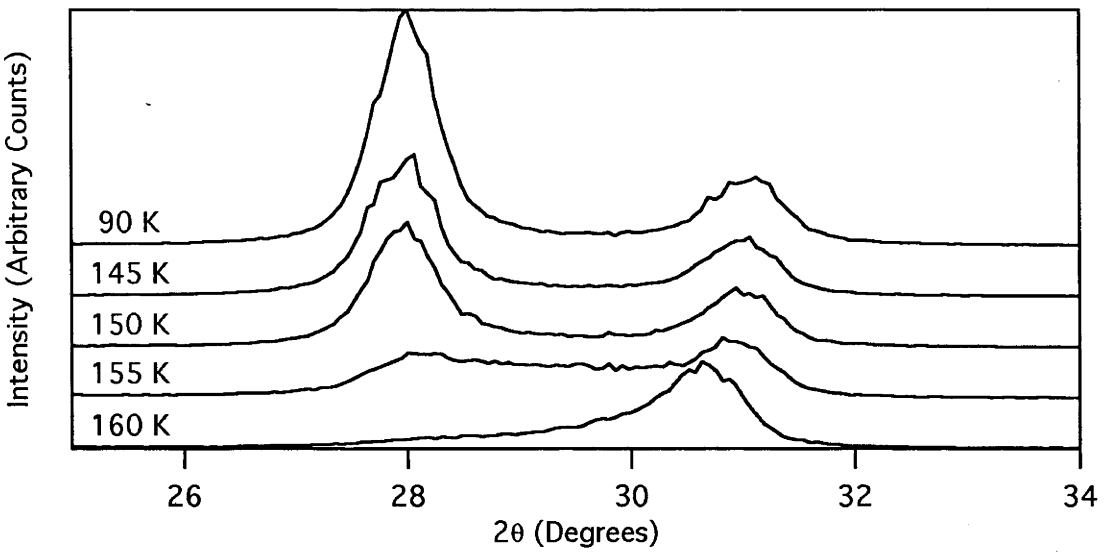

Figure 4.4.4: *c-axis x-ray powder diffraction patterns of* $K(N_2)_{0.7}C_{25}$ *as the sample is cooled from 160 K to 90K, showing the strongest peaks, indexed as the (003) peaks of a two phase system. Note that the original* KC_{25} *(003) peak does not appear in the final pattern.*

4.4.2: Symmetry and Unit Cell

Comparison of the two *ab*-plane XRD diffraction patterns shown in Figure 4.4.1 shows that the ternary sample has adopted a new in-plane crystal structure, with apparently little or no remnant structure of the binary compound. The ternary pattern shows peaks with the turbostratic band shape, and does not have the incommensurate satellite peaks of the KC_{25} binary. The *c*-axis patterns in Figures 4.4.3 and 4.4.4 show the saturated ternary is apparently a two phase system, and that the unmodified binary *c*-axis pattern does not appear in that of the saturated sample.

Table 4.4.1 contains an indexing of the 130 K c-axis oriented XRD pattern from the saturated ternary sample as a two phase system, with an expanded phase (presumably containing the adsorbed nitrogen molecules) having an average *c*-axis dimension of 9.55 Å, and a second phase with an average c-axis dimension of 8.61 Å. Unlike the argon-rubidium and methane-rubidium systems described earlier, the second phase can be very clearly distinguished from the c-axis pattern assigned to the expanded phase, and it also has a compressed c-axis dimension compared with the 8.69 Å dimension of binary KC_{25} GIC at the same temperature.

Data				Phase A		Phase B	
2θ (Degrees)	Intensity (Counts)	I/Imax x100	D (Å)	l_a	D x l_a (Å)	l_b	D x l_b (Å)
9.24	1355	8.71	9.571			1	9.571
10.08	959	6.17	8.775	1	8.775		
18.84	1629	10.5	4.710			2	9.420
20.7	3645	23.4	4.291	2	8.582		
28.02	15553	100	3.184			3	9.553
31.02	5034	32.4	2.883	3	8.649		
42	171	1.1	2.151	4	8.604		
44.82	148	0.95	2.022				
47.7	233	1.5	1.907			5	9.533
53.16	347	2.23	1.723	5	8.614		
57.78	1048	6.74	1.596			6	9.574
64.92	233	1.5	1.436	6	8.618		
77.82	133	0.86	1.227	7	8.591		

Table 4.4.1: *Indexing of the 130 K c-axis oriented XRD pattern of $K(N_2)_{0.7}C_{25}$ as a two phase system. Compared with KC_{25}, with a c-axis dimension D = 8.69 Å, there is an expanded phase with D = 9.55 Å and a compressed phase with D = 8.61 Å.*

The two phase indexing is obviously similar to the $\sqrt{7}x\sqrt{7}$ and 2x2 two phase system that was used to describe the Rb-Ar and Rb-CH_4 systems, in that there is an expanded phase and a compressed phase compared to the average ab-plane packing of the binary KC_{25} compound. There are two significant differences, however - obviously the expanded phase has potassium ions packed in a 3x3 unit cell as opposed to the $\sqrt{7}x\sqrt{7}$ P6 cell in the rubidium system. Less obviously, there are systematic absences in the 3x3 indexing, for example the (11) and (21) are absent, and this will have to be replicated by a successful structural model.

Data			6x6 cell				
2θ (Degrees)	Intensity (Counts)	D (Å)	h	k	l	a	$(a/a_{gr})^2$
8.88	2027	9.958	0	0	1	9.958	(c)
13.8	2011	6.417	2	0		14.819	35.786
18.36	1312	4.832	0	0	2	9.958	(c)
20.64	16451	4.303	3	0		14.907	36.211
22.56	2290	3.941				-	-
27.72	12452	3.218	4	0		14.864	36.002
36.24	3244	2.479	3	3		14.872	36.043
42.12	4384	2.145	1	0		2.477	1
44.52	7621	2.035	1	0	1	-	-
49.08	907	1.856	4	4		14.849	35.931
56.82	1106	1.62	6	3		14.85	35.937
62.94	591	1.477	6	4		14.865	36.007
65.1	534	1.433	9	0		14.89	36.13
76.98	3293	1.239	1	1		2.4772	1

Table 4.4.2: *Indexing of the 130 K ab-plane oriented XRD pattern of* $K(N_2)_{0.7}C_{25}$ *as a single phase 6x6 registered hexagonal superlattice of the graphite host. This model has a large number of absent reflections.*

The *ab*-plane data is indexed in Tables 4.4.2 and 4.4.3, as a 6x6 single phase compound and as a 3x3 and 2x2 two phase system respectively, all using the P6 hexagonal plane group. The 6x6 indexing suffers from a similar problem to the $\sqrt{28}$x$\sqrt{28}$ indexing of the argon-rubidium and methane-rubidium phases, in that it requires that there are a great number of systematically absent reflections in the data which must be simulated in any model. Again, as with the previous studies, no model based on a 6x6 unit cell could be constructed that would reproduce the observed intensities.

Data			2x2 Cell				3x3 Cell			
2θ (Degrees)	Intensity (Counts)	D (Å)	h	k	a (Å)	$(a/a_{gr})^2$	h	k	a (Å)	$(a/a_{gr})^2$
8.88	2027	9.958								
13.8	2011	6.417					1	0	7.410	8.947
18.36	1312	4.832								
20.64	16451	4.303	1	0	4.969	4.023				
22.56	2290	3.941								
27.72	12452	3.218					2	0	7.432	9.001
36.24	3244	2.479	1	1	4.958	4.005				
42.12	4384	2.145	1	0	2.477	1	1	0	2.477	1
44.52	7621	2.035								
49.08	907	1.856					2	2	7.424	8.983
56.82	1106	1.620	2	1	4.950	3.993				
62.94	591	1.477					3	2	7.432	9.002
65.1	534	1.433	3	0	4.963	4.014				
76.98	3293	1.239	1	1	2.477	1	1	1	2.477	1

Table 4.4.3: *Indexing of the 130 K ab-plane oriented XRD pattern of* $K(N_2)_{0.7}C_{25}$ *as a two phase system consisting of 2x2 and 3x3 registered hexagonal superlattices of the graphite host. The (11) and (21) peaks of the 3x3 lattice are notably absent.*

4.4.3 *ab*-Plane Rietveld Simulations of Ternary $K(N_2)_{0.7}C_{25}$ Structures.

In creating the models of the 3x3 structure, the location of the N_2 molecules within the unit cell is the primary variable that can be altered to produce different peak intensities.

Four models are shown in Figure 4.4.5, varying only in the position of the nitrogen molecules. The Rietveld refinement program GSAS[3] was used to calculate the peak intensities for these four different models, which are shown in Figures 4.4.6 - 4.4.9. The 2x2 phase is also included in these simulations. In the models, the nitrogen molecules are:

a) in a vertical orientation at the threefold axis at (1/3,2/3), the same location as the argon atoms and methane molecules in the $RbAr_{2.0}C_{25}$ and $Rb(CH_4)_{2.0}C_{25}$ $\sqrt{7}x\sqrt{7}$ phases described previously. This model has stoichiometry $K(N_2)_{2.0}C_{36}$;

b) in a horizontal orientation at the two-fold axis at (1/2,0), with the long axis of the N_2 molecule oriented towards the nearest K^+ ions. This model has stoichiometry $K(N_2)_{3.0}C_{36}$;

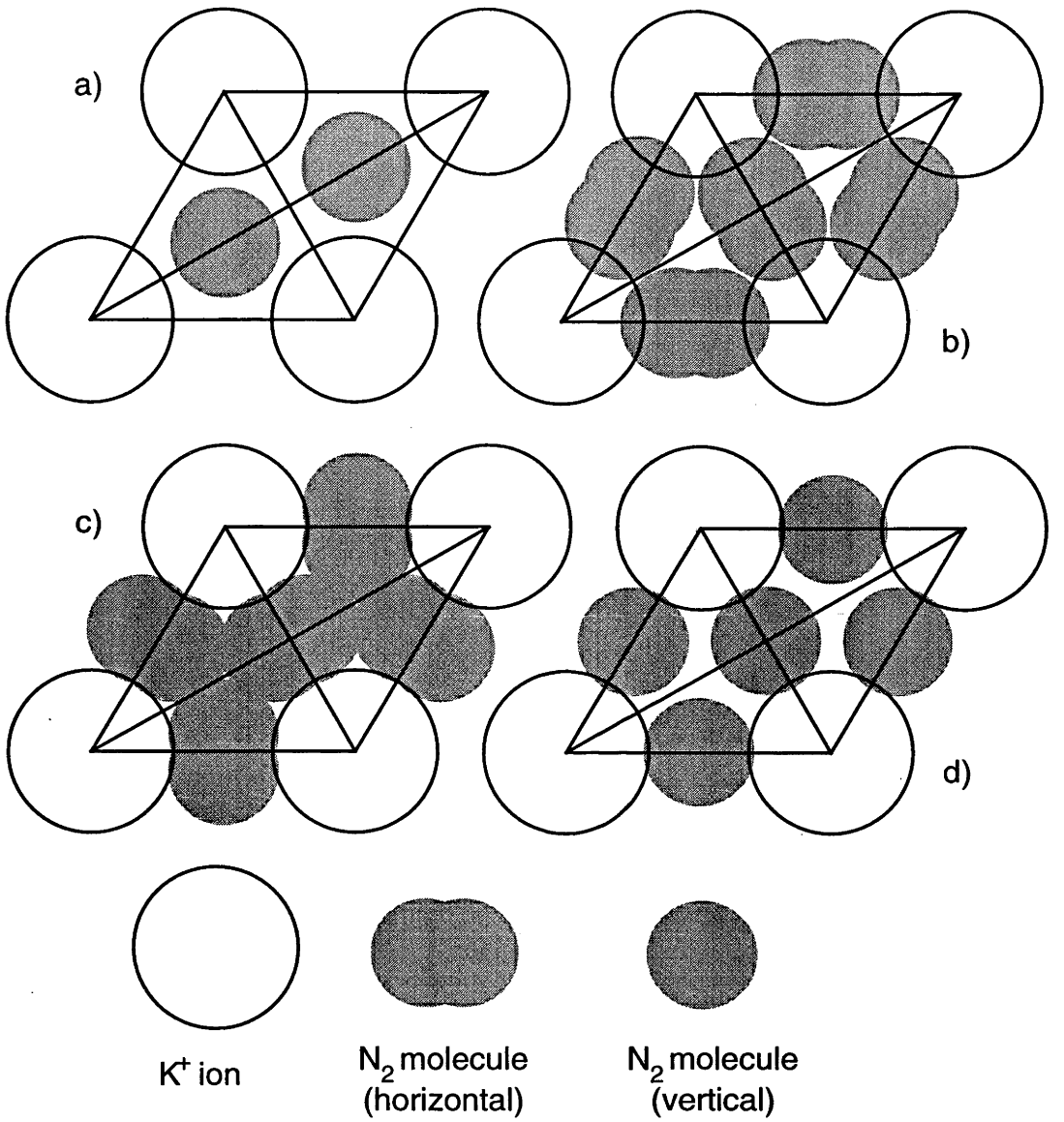

Figure 4.4.5: *Four ab-plane models of the 3x3 unit cell of the potassium-nitrogen-graphite phase, with the nitrogen molecule varying in position and orientation between the models. The models are described in more detail in the text.*

c) in a horizontal orientation at the two-fold axis at (1/2,0), with the long axis of the N_2 molecule oriented away from the nearest K^+ ions. This model has stoichiometry $K(N_2)_{3.0}C_{36}$;

d) in a vertical orientation at the two-fold axis at (1/2,0), with the long axis of the N_2 molecule oriented towards the graphene layers. This model has stoichiometry $K(N_2)_{3.0}C_{36}$.

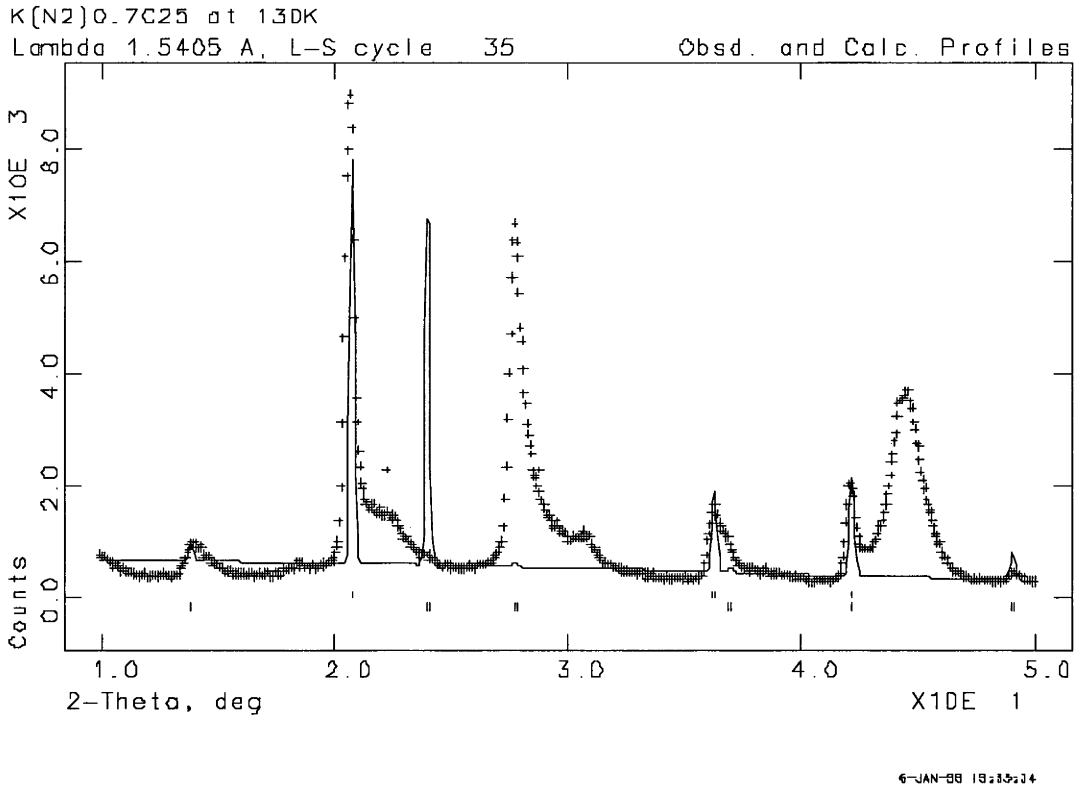

Figure 4.4.6: *GSAS Rietveld simulation of the 3x3 model a), described above.*

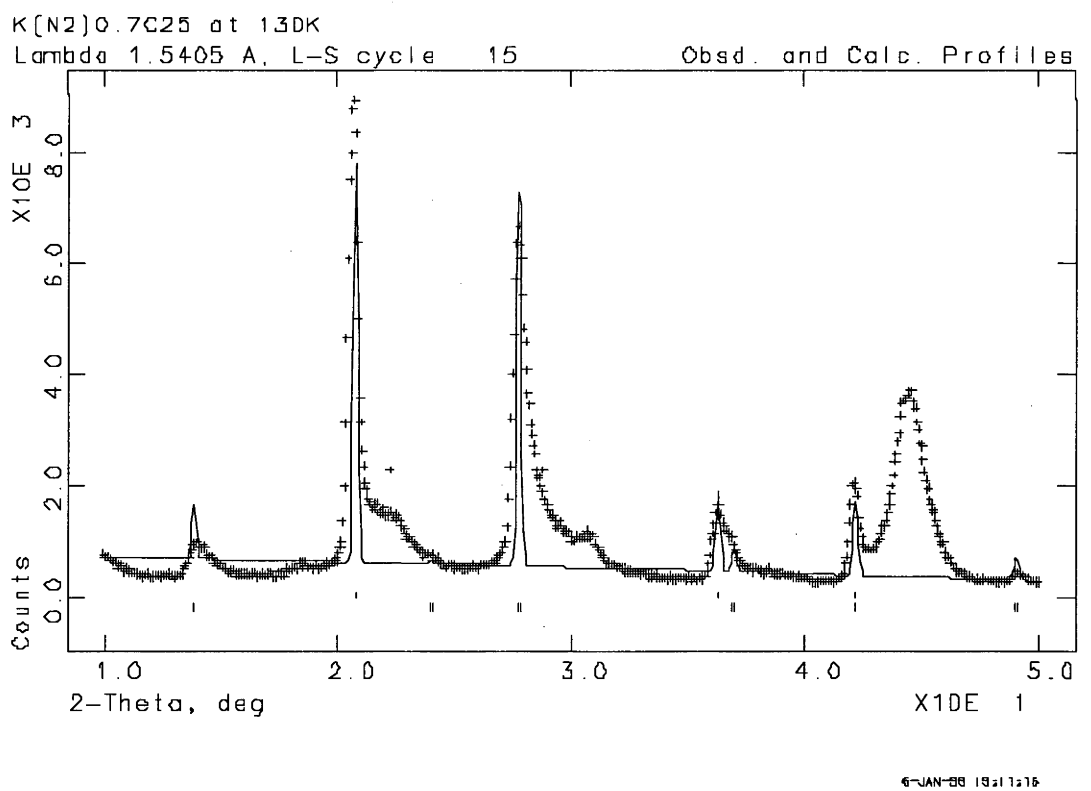

Figure 4.4.7: *GSAS Rietveld simulation of the 3x3 model b), described above.*

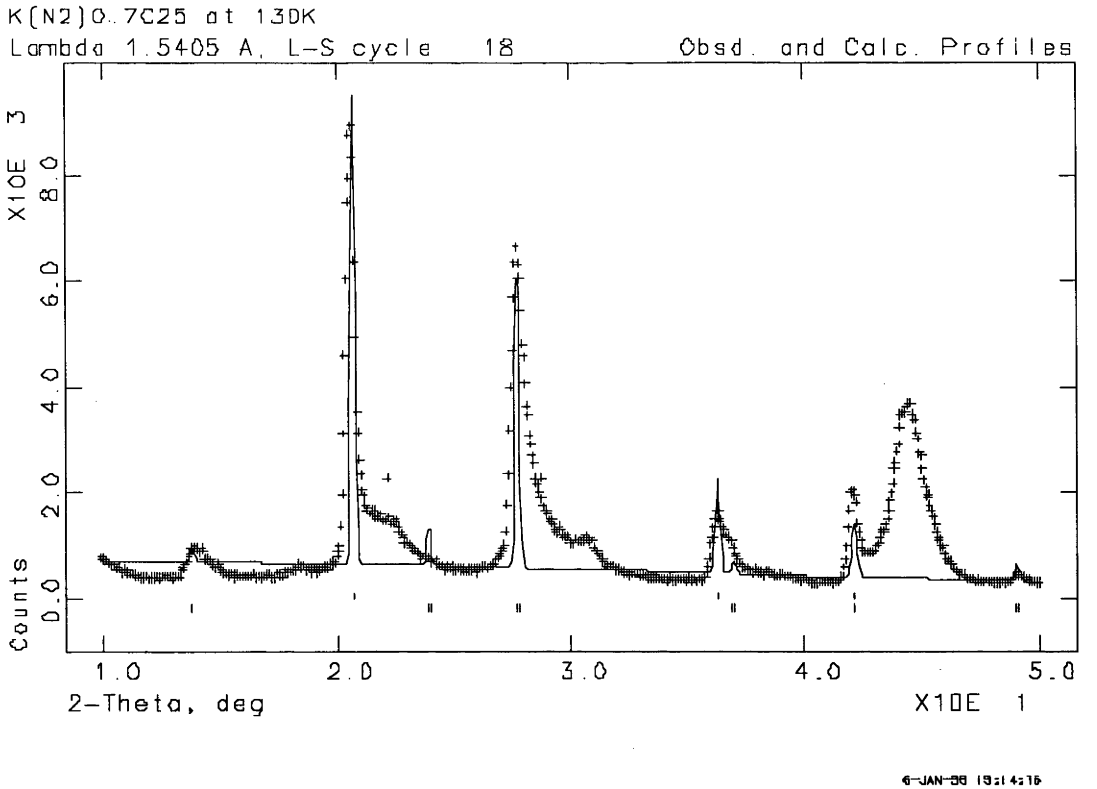

Figure 4.4.8: *GSAS Rietveld simulation of the 3x3 model c), described above.*

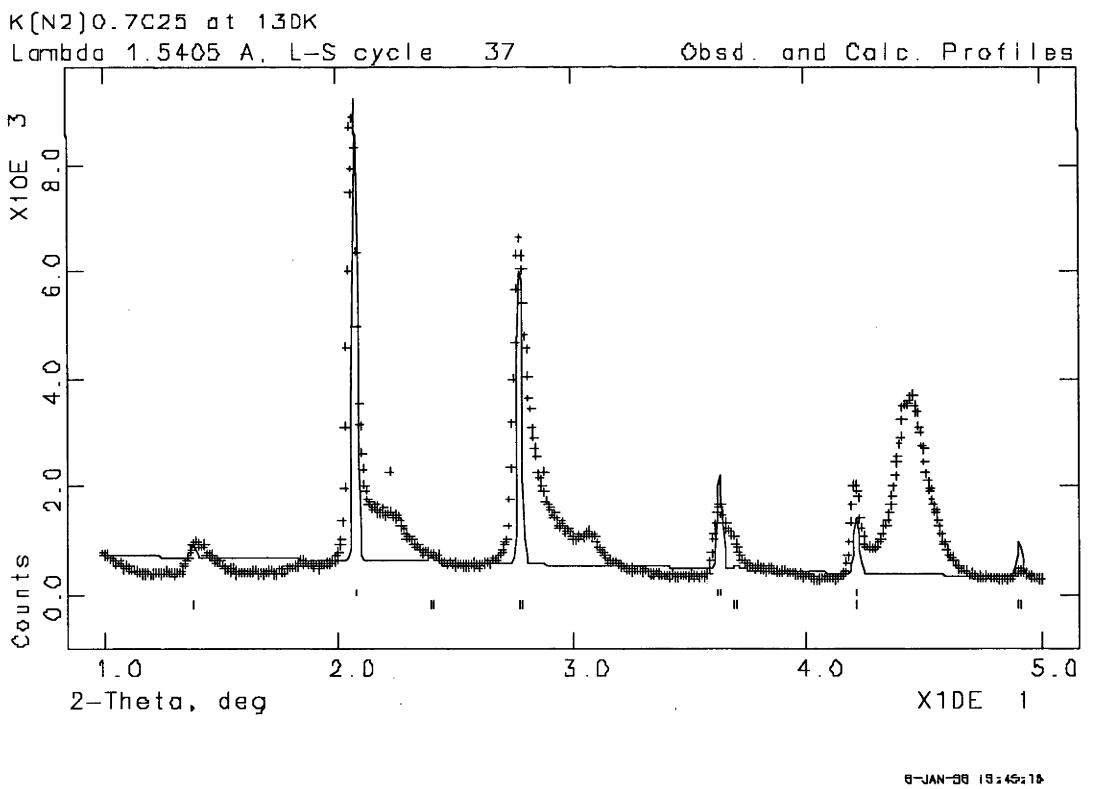

Figure 4.4.9: *GSAS Rietveld simulation of the 3x3 model d), described above.*

Looking at the four Rietveld fits, model a), with the N_2 molecule located at the (1/3,2/3) position, is obviously and unsurprisingly incorrect. model c) produces intensity at the (21) position of the 3x3 phase which is not observed in the data, while model d) produces far too little intensity at the (10) position. Of these models, only model b) reproduces the observed intensity with any accuracy, and so b) will be used in the later full-pattern simulations.

4.4.4 *ab*-Plane and *c*-axis Full-Pattern Simulations of Ternary $K(N_2)_{0.7}C_{25}$ Structures.

4.4.4.1 *ab*-plane Simulations

The structures shown in Figure 4.4.10 and 4.4.11 were used in these simulations for the expanded 3x3 phase and compressed 2x2 phase respectively.

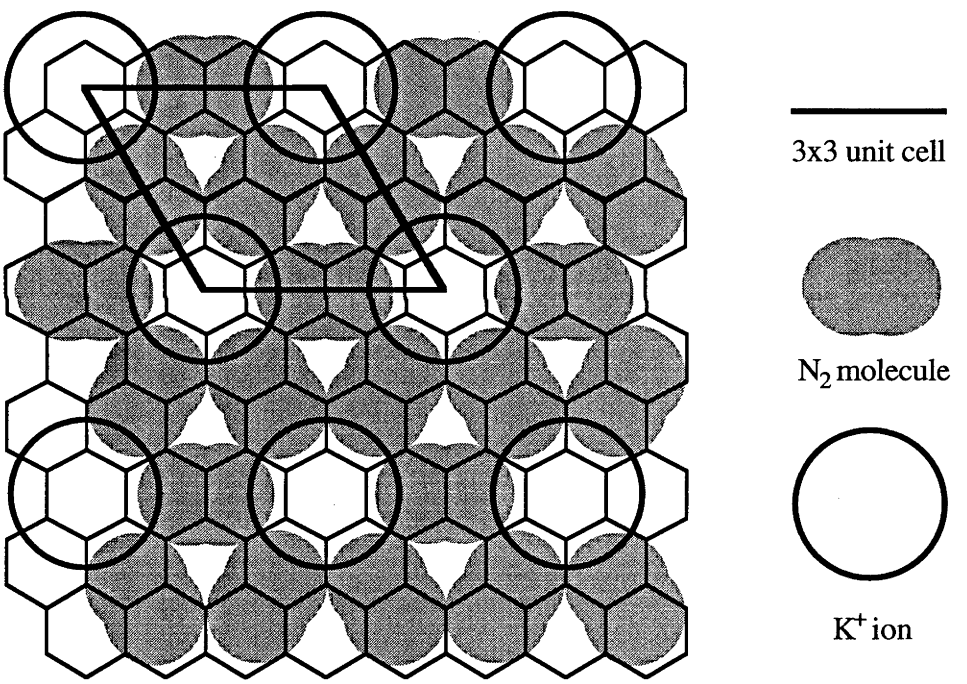

Figure 4.4.10: *ab-plane structure for the 3x3 $K(N_2)_3C_{36}$ nitrogen-rich phase used in the following simulations; the Van der Waals radii are used for atomic and ionic sizes. The N_2 molecule is centred on the twofold axis at (1/2,0), with the long axis of the molecule oriented towards the nearest K^+ ions. Though the graphene layer is shown, its contributions are not included in the simulations.*

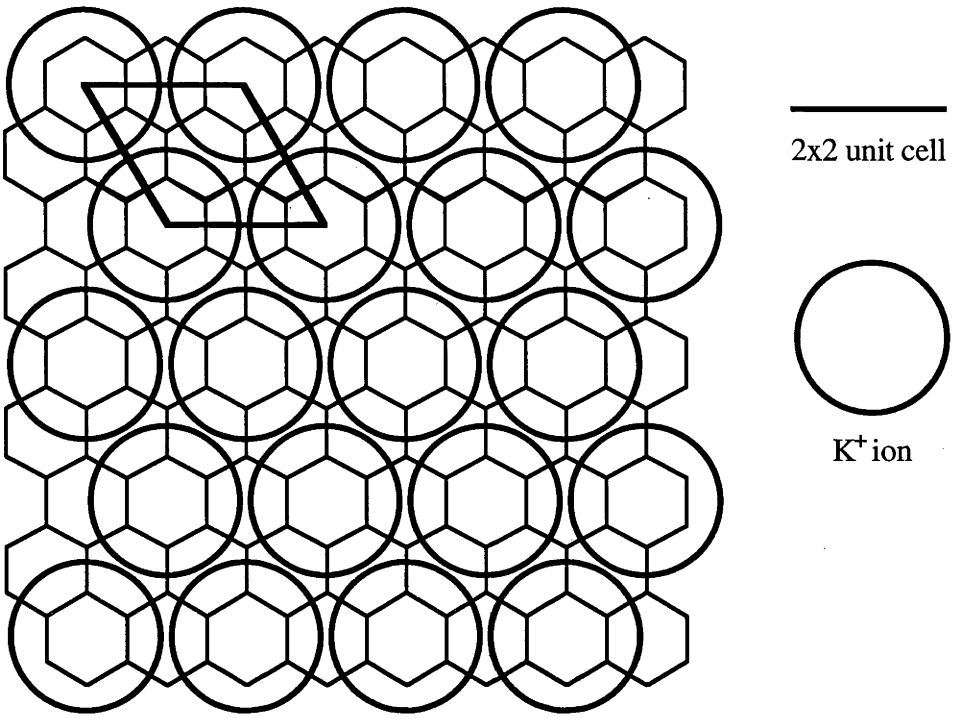

Figure 4.4.11: *ab-plane structure for the 2x2 KC_{16} nitrogen-poor phase used in the following simulations; the Van der Waals radii are used for atomic and ionic sizes. Though the graphene layer is shown, it's contributions are not included in the simulations.*

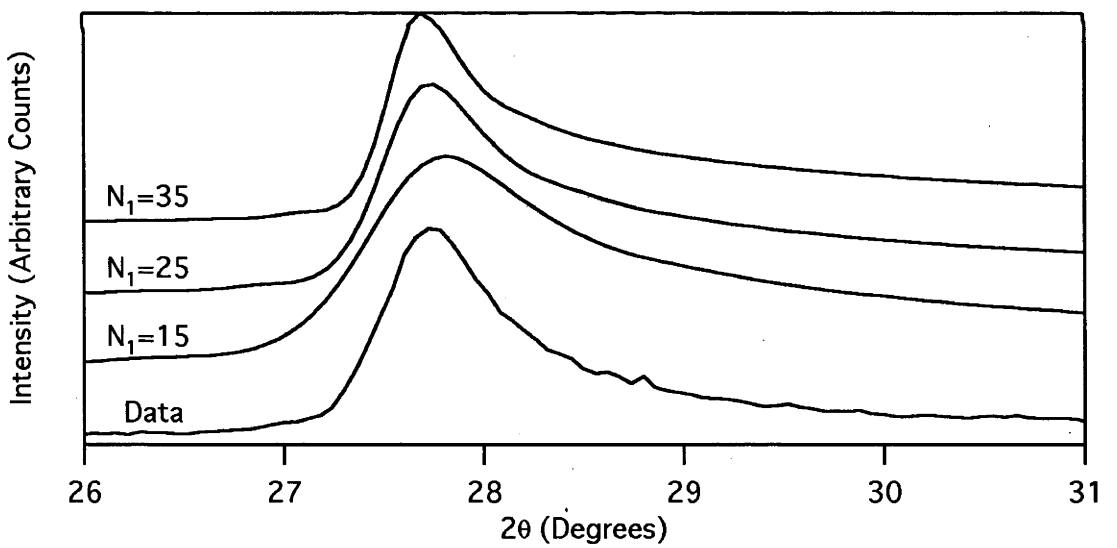

Figure 4.4.12: *Simulations of the (20) 3x3 turbostratic band, the most intense. The lowest trace is experimental data, taken at 130 K; the others are simulations of the $K(N_2)_{3.0}C_{25}$ ab-plane structure shown in Figure 4.4.10;, calculated over the range 25.02°-32.04° with a step size of 0.06°. N_1 is the size of the in-plane crystallites (see Chapter 2). The other constants were a_{gr} = 2.475 Å; c=9.55 Å; λ = 1.54178 Å. A 2θ correction of -0.15° was applied to the simulated patterns.*

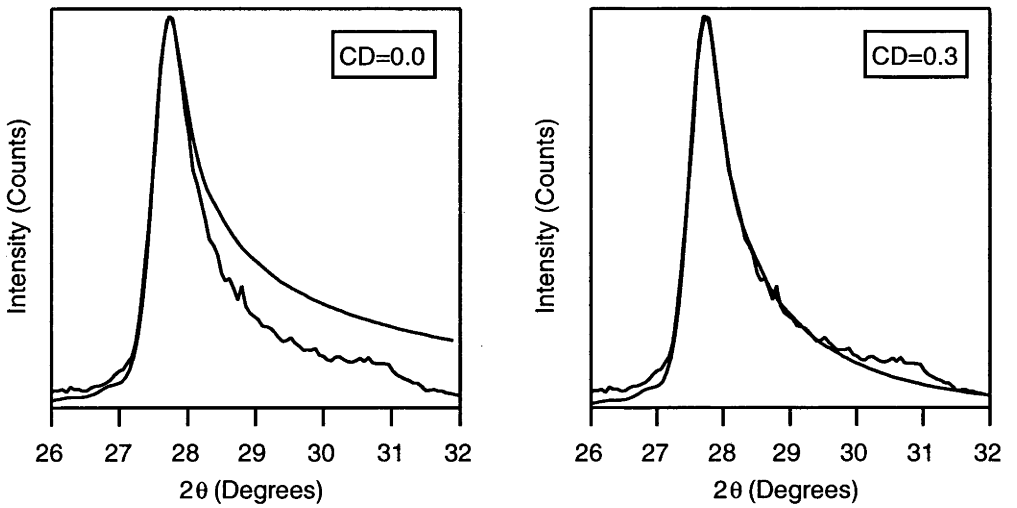

Figure 4.4.13: *The effect of the c-axis damping factor CD on the simulated turbostratic band shape of the 3x3 $K(N_2)_{3.0}C_{25}$ structure compared with data taken at 130 K. The pattern simulations all use N_1=40; a_{gr} = 2.475 Å; c=9.55 Å; λ = 1.54178 Å. A 2θ zero-point correction of -0.15° was applied to the simulated patterns.*

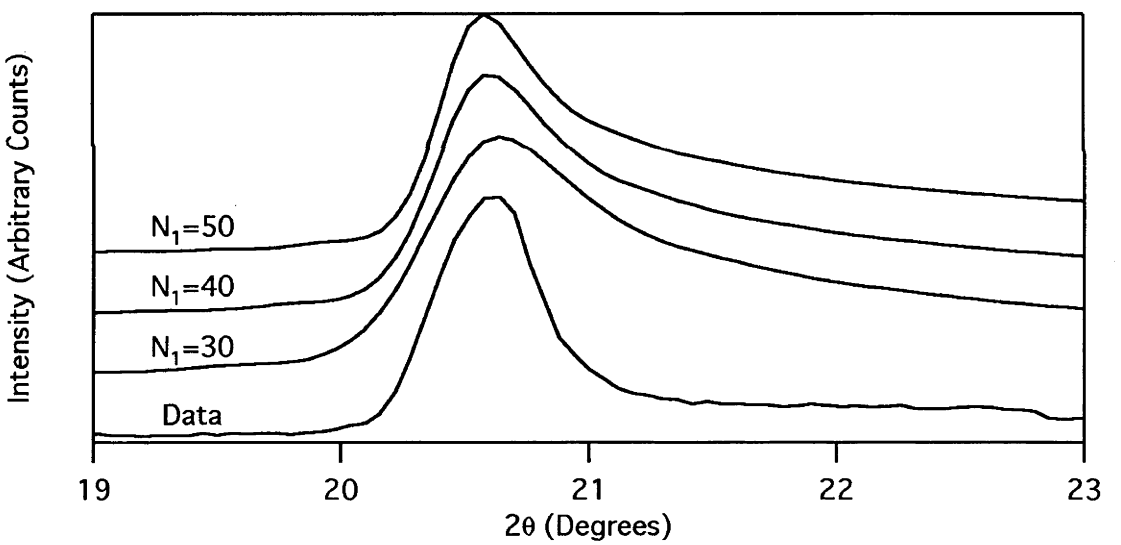

Figure 4.4.14: *Pattern simulations for the strongest 2x2 turbostratic band, the (10) peak at 20.64°. The lowest trace is experimental data, taken at 130 K; the others are simulations of the KC_{16} ab-plane crystal structure shown in Figure 4.4.11; calculated over the range 19.02°-25.02° with a step size of 0.06°. The other constants used in the calculations were a_{gr} = 2.475 Å; c=9.55 Å; λ = 1.54178 Å. A 2θ of -0.24° was applied to the simulated patterns.*

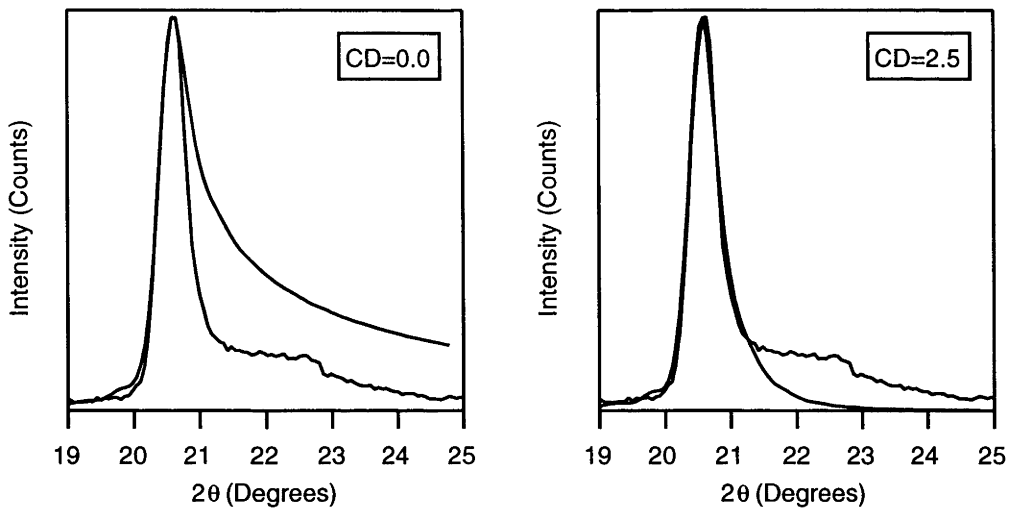

Figure 4.4.15: *The effect of the c-axis damping factor CD on the simulated turbostratic band shape of the 2x2 KC_{16} structure compared with data taken at 130 K. The pattern simulations all use N_1=40; N_3=1; a_{gr} = 2.475 Å; c=9.55 Å; λ = 1.54178 Å. A 2θ zero-point correction of -0.24° was applied to the simulated patterns.*

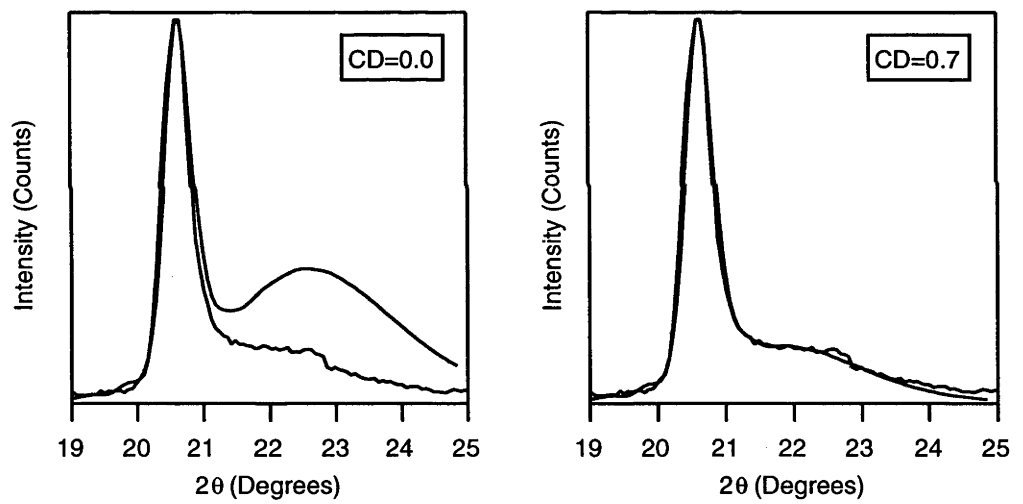

Figure 4.4.16: *The effect of the c-axis damping factor CD on the simulated turbostratic band shape of the 2x2 KC_{16} structure compared with data taken at 130 K. The pattern simulations all use N_1=40; N_3=2; δ=2.0; a_{gr} = 2.475 Å; c=9.55 Å; λ = 1.54178 Å. A 2θ zero-point correction of -0.18° was applied to the simulated patterns.*

Figure 4.4.14 shows an attempt to find the *c*-axis damping factor CD for the 2x2 phase that is consistent with a purely turbostratic structure, that is one with no interlayer interactions. The final value of CD is very much greater the value found for the 3x3 data. It also fails to account for the "shoulder" on the 2x2 (10) peak, which cannot be attributed

to a c-axis breakthrough. An alternative peak shape is simulated in Figure 4.4.15, where the assumption of a purely turbostratic interaction has been abandoned. This produces a much smaller value of CD, but one which is still considerably greater than that for the 3x3 simulations, and it also reproduces the "shoulder" seen on the data.

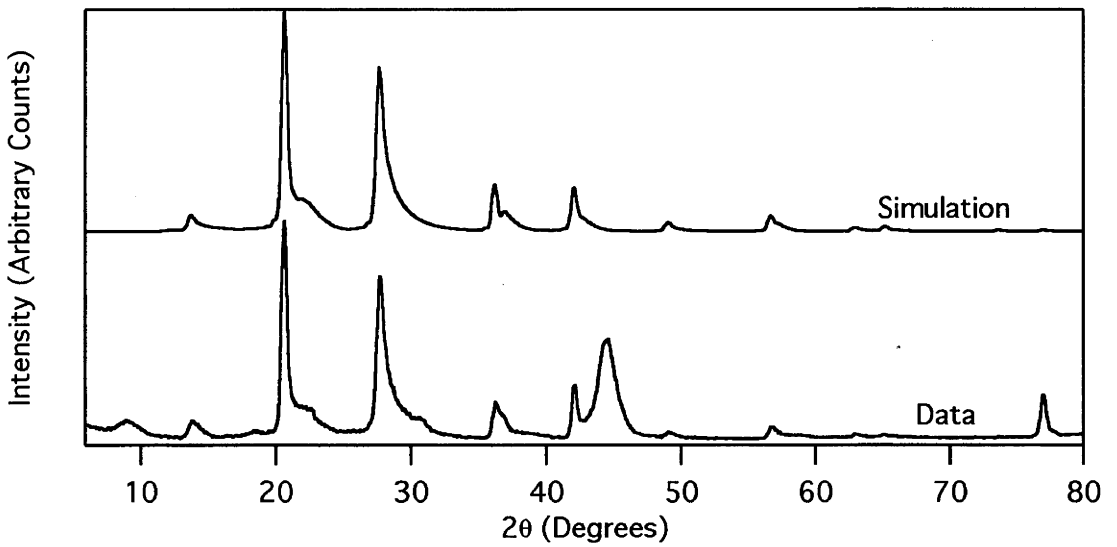

Figure 4.4.17: *The combined best 2x2 and 3x3 simulations compared with the* $K(N_2)_{0.7}C_{25}$ *data taken at 130 K. A 3rd order polynomial function was subtracted from the data in an attempt to remove the background. The parameters used in the simulations are shown in Table 4.4.4.*

The final best combined simulation, shown in Figure 4.4.17, employs the following parameters:

	Phase A	**Phase B**
Symmetry	P6	P6
a	2	3
a_{gr}	2.475 Å	2.475 Å
c	8.61 Å	9.55 Å
$N_1=N_2$	40	25
N_3	2	1
δ	2.0	0
CD	0.7	0.3
Thermal factors	Rb=0.5	Rb=0.7 K=0 .7
2θ zero	-0.18°	-0.18°

Table 4.4.4*: the parameters used for the simulations shown in Figure 4.4.17.*

Figure 4.4.17 shows a comparison of the best 2x2 and 3x3 simulations with data taken at 130 K, while Table 4.4.4 contains the factors used for the simulated patterns. Several peaks do not appear in the simulated pattern: the peaks at 8.88°, 18.36° and ~30.8° are attributed to c-axis breakthroughs, while the large peak at 44.92° and 76.98° are the graphite (101) and (11) bands seen in all the GIC diffraction patterns observed. The in-plane crystallite sizes are quite similar for both phases: 198 Å for the 2x2 phase vs 185 Å for the 3x3, and the values of a_{gr} and the 2θ shift employed in the final simulation are the same. N_3, the thickness of the simulated crystallites along the c-axis, is unitary for the 3x3 simulation but is not for the 2x2 phase, which was also found for the $RbAr_{1.2}C_{25}$ 2x2 phase. As with the simulation of the $RbAr_{1.2}C_{25}$ 2x2 phase, a range of values for N_3 and δ can be used to give a similar peak shape to that shown in the figures above, so that the parameters shown in table 4.4.4 cannot be considered definitive. The primary problems of the simulation in Figure 4.4.16 are that the value of CD is still significantly different for the two phases, and that the overlapping bands at 36.24° are more distinct in the simulation than in the data.

4.4.4.2 *c*-Axis Pattern Simulations

As with the samples in Chapter 4, the full pattern *c*-axis simulations are fast enough that there is no need for Rietveld simulations first.

Given that the *c*-axis patterns are clearly two phase, a separate structural model must be developed for each phase. Beginning with the assumption that the expanded phase contains the N_2, while the compressed phase is a binary potassium-graphite intercalation compound, two models for the minor phase present themselves: firstly, the minor phase may be remnant KC_{25}, with the same stoichiometry; secondly, it may be the 2x2 phase simulated in the *ab*-plane data, in which case the stoichiometry would be KC_{16}. Figure 4.4.18 shows a comparison of these two models with the data obtained at 130 K. From this it is clear that the intensities of the minor phase more closely match those of the 2x2 KC_{16} model. While the average *c*-axis spacing of the minor phase is 8.61 Å, there is a good deal of variation from this mean, for example the (002) peak position indicates a spacing of 8.58 Å while the (003) produces one of 8.65 Å, which may be a sign of an interstratified system; 8.65 Å is chosen for these simulations to position the simulated (003) peak, from which the simulation is normalised to the measured strong intensities, at the same position as the (003) peak in the data.

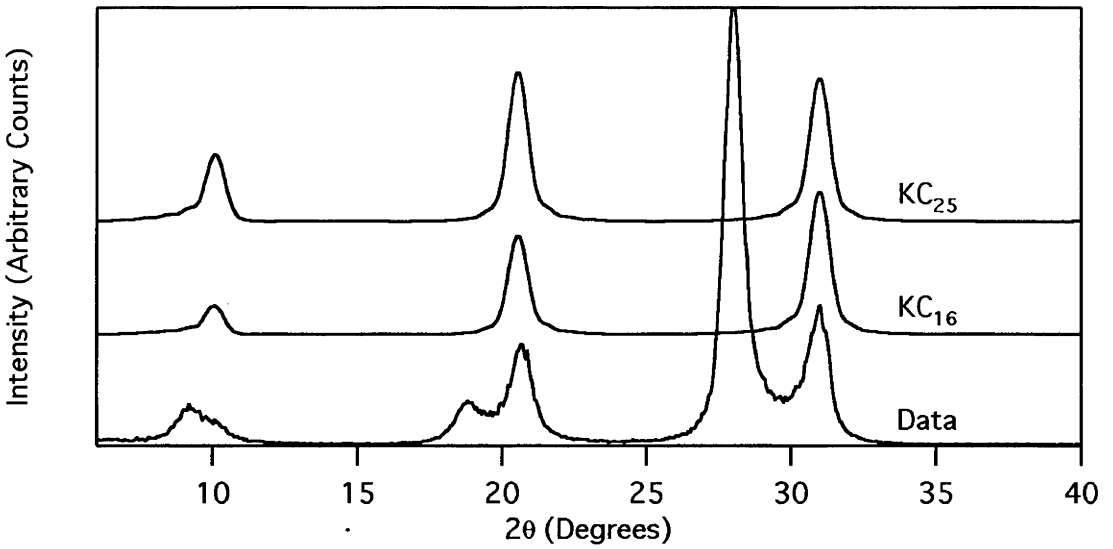

Figure 4.4.18: *c-axis simulations for KC_{16} and KC_{25} compared with data taken at 130 K. The parameters used for both simulations are D = 8.65 Å, N_3 = 14, δ = 10, λ = 1.54178 Å; only the K/C ratio is altered.*

Assuming that the expanded phase contains the nitrogen, and also that it is the 3x3 phase of the ab-plane data, two initial models present themselves, both with stoichiometry $K(N_2)_{3.0}C_{36}$: in the first model, the nitrogen molecules are centred on the plane of the K^+ ions, and are aligned horizontally in that plane; in the second, they are again centred on the plane but are aligned vertically. The two models are shown in Figures 4.4.20 and 4.4.21. The first of these models corresponds to the *ab*-plane models b) and c) above, while the third corresponds to the *ab*-plane model d); the ab-plane model a) is considered to be ruled out by the Rietveld intensity simulations. The intensities of the simulated patterns in Figure 4.4.19 indicate that the horizontal orientation for the N_2 gives a much closer simulation of the data than the vertically oriented nitrogen molecules. This confirms the results of the *ab*-plane simulations above.

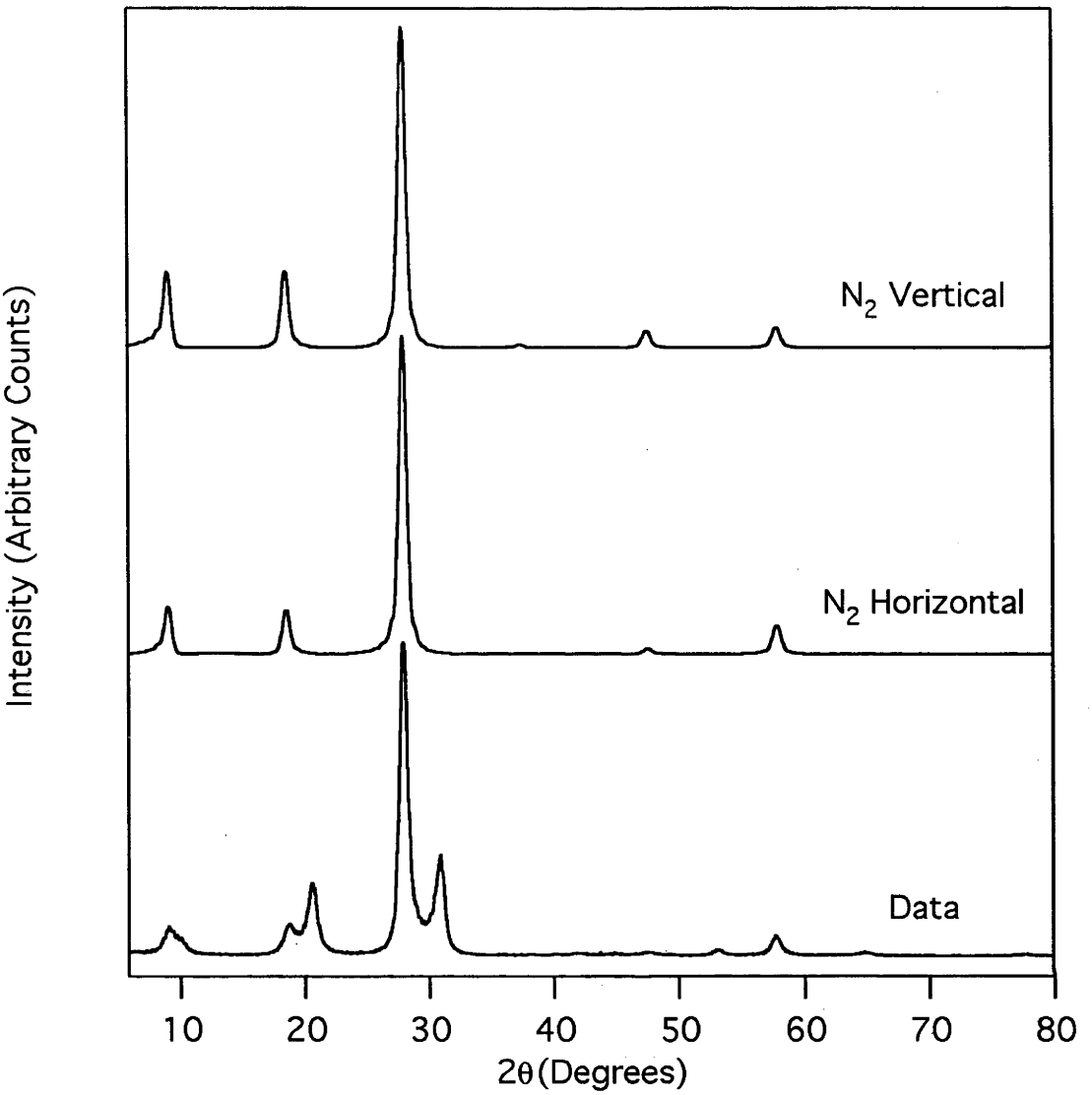

Figure 4.4.19: *c-axis oriented XRD data taken at 130 K compared with horizontal N_2 and vertical N_2 c-axis simulations for $K(N_2)_{3.0}C_{36}$. The parameters used for both simulations are D = 9.55 Å, N_3 = 14, δ = 10, λ = 1.54178 Å. The structures used are shown in Figures 4.4.20 and 4.4.21.*

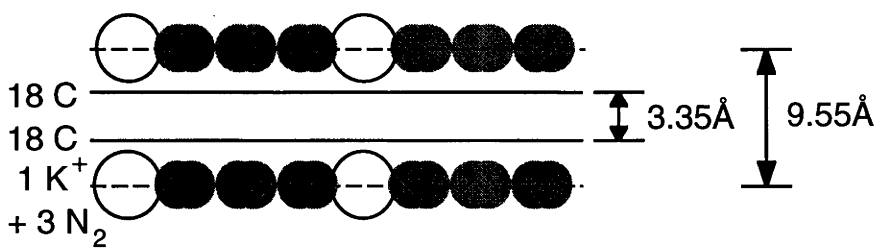

Figure 4.4.20: *c-axis structure used for the horizontal powder diffraction simulation shown in Figure 4.4.19. Each K^+-N_2 layer contains a ratio of 1 K^+ ion to 3 N_2 molecules, and is separated from the next by two graphene layers which are 3.35 Å apart. The N_2 molecules are aligned horizontally in the K^+ plane.*

The combined KC_{16} and $K(N_2)_{3.0}C_{36}$ *c*-axis simulated patterns are compared with the data taken at 130 K in Figure 4.4.21 below. This produces a good fit to the peak intensities and positions, but combined simulation has three areas where it fails to reproduce observed features in the data:

i) the low angle intensities from the $K(N_2)_{3.0}C_{36}$ (001) and (002) peaks are considerably greater than the observed intensities;

ii) there is a greater overlap between the main peaks produced by the two phases in the data than in the simulated patterns;

iii) There is a variation away from the average c-axis dimension for both phases in several of the data peaks, especially the (002) peaks, while positions of the simulated peaks are exact. This is the characteristic sign of an interstratified system, and appears to have been carried over from the KC_{25} binary, which was found to be interstratified. This will be discussed in more detail in Chapter 5.

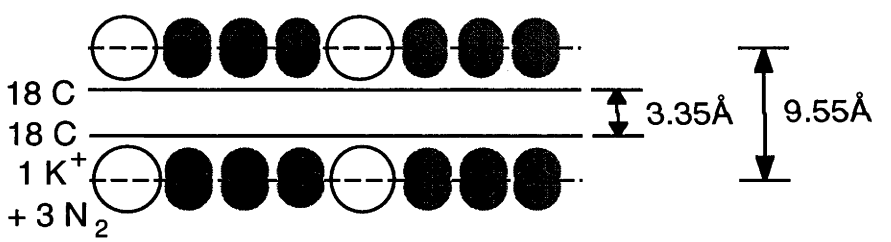

Figure 4.4.21: *c-axis structure used for the vertical powder diffraction simulation shown in Figure 4.4.19. Each K^+-N_2 layer contains a ratio of 1 K^+ ion to 3 N_2 molecules, and is separated from the next by two graphene layers which are 3.35 Å apart. The N_2 molecules are aligned vertically along the c-axis but are mass centred in the K^+ plane.*

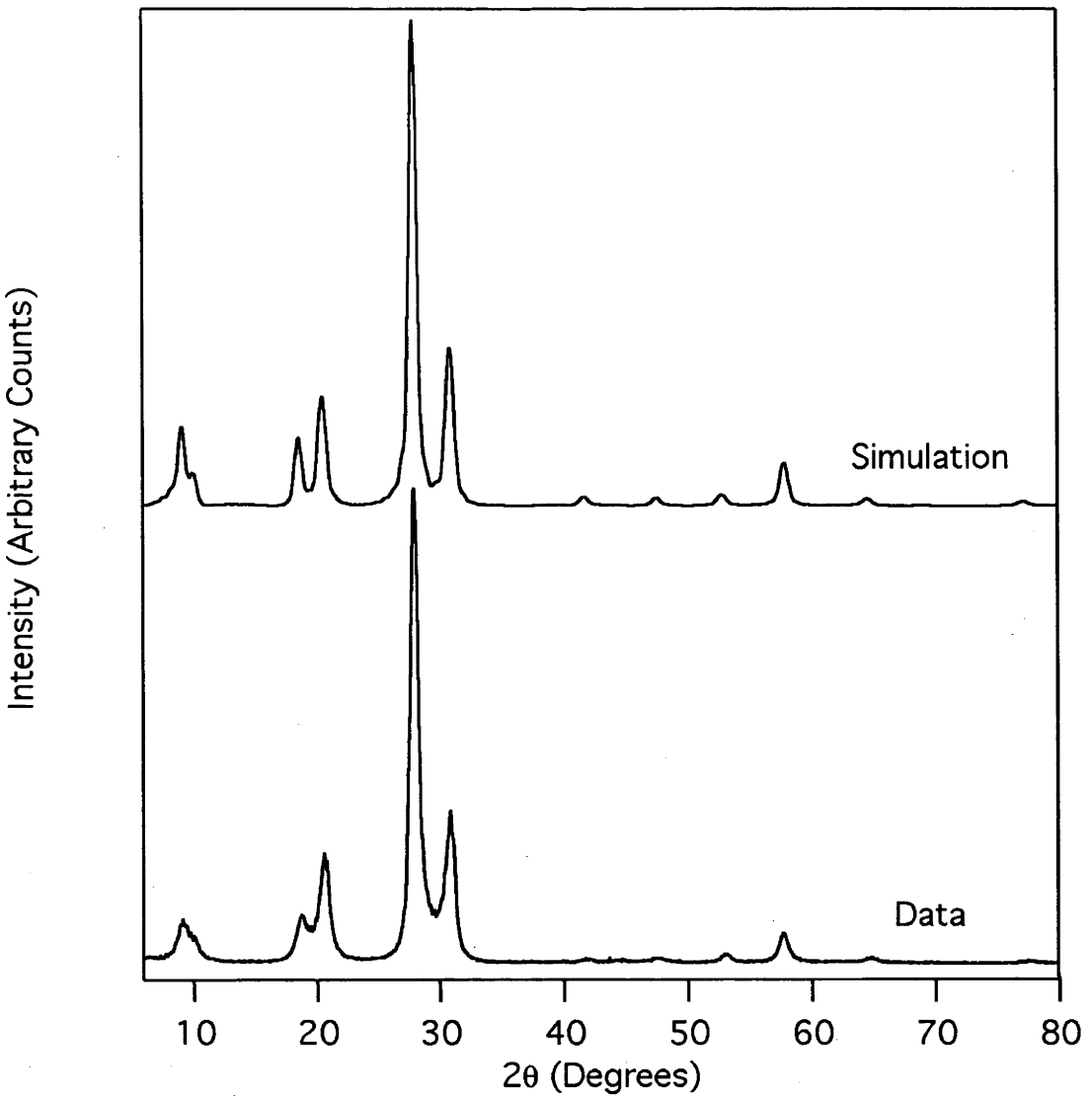

Figure 4.4.21: *c-axis data taken at 130 K from a $K(N_2)_{0.7}C_{25}$ sample compared to the combined KC_{16} and $K(N_2)_{3.0}C_{36}$ simulations. The parameters used for the KC_{16} phase simulations are D = 8.65 Å, N_3 = 14, δ = 10, λ = 1.54178 Å, and for the $K(N_2)_{3.0}C_{36}$ simulations are D = 9.55 Å, N_3 = 14, δ = 10, λ = 1.54178 Å, with horizontally aligned N_2 molecules.*

4.4.5 Conclusion

While there are some small discrepancies between the simulations and the data, the best simulations of both the *ab*-plane and *c*-axis data are consistent with a model of a two-phase system, with all of the nitrogen contained in an expanded phase possessing an expanded *ab*-plane and *c*-axis unit cell dimension, of stoichiometry $K(N_2)_{3.0}C_{36}$, while the remnant potassium is contained in a compressed phase, with a compressed *ab*-plane

and *c*-axis unit cell, of stoichiometry KC_{16}. Both phases have remained stage 2 graphite intercalation compounds. The saturated potassium-nitrogen-graphite system is thus a bi-intercalation compound of formula KC_{16}• $K(N_2)_{3.0}C_{36}$ (st. 2).

References

1. K. Watanabe, T. Kondow, M. Soma, T. Onishi, and K. Tamaru, *Molecular-sieve type sorption on alkali graphite intercalation compounds.* Proceedings of the Royal Society of London A, 1973. **333**: p. 51-67.

2. R. Moreh, S. Melloul, and H. Zabel, *Orientation of molecularly intercalated N_2 in C_{24} K.* Physical Review B, 1993. **47 (16)**: p. 10754-10759.

3. A.C. Larson and R.B. Von Dreele, LANSCE, MS-H805, Los Alamos National Laboratory, NM 87545, USA.

4.5: Nitrogen Absorption by Rubidium Graphite Intercalation Compounds: The Structure of $Rb(N_2)_{1.0}C_{25}$

Little further research had been done on the physisorbed nitrogen ternary graphite intercalates RbC_{25} or KC_{24} since the pioneering studies[1], apart from nuclear resonance photon scattering experiments on N_2 in RbC_{24} which showed that the N_2 molecule was lying parallel to the graphite planes[2, 3]. The original studies found that nitrogen adopted the "Type II" sorption isotherm, an intermediate case between the "Type I" classical Langmuir isotherm and the "Type III" isotherm adopted by the $RbAr_{1.2}C_{25}$ and $Rb(CH_4)_{0.9}C_{25}$ systems, and that the saturation stoichiometry was $Rb(N_2)_{1.0}C_{25}$. The Type II isotherm was associated with an intermediate expansion of the host galleries on intercalation. Here we will present powder diffraction patterns from oriented samples of the ternary intercalation compound $Rb(N_2)_{1.0}C_{25}$ at over a range of temperatures.

4.5.1 Data

Figures 4.5.1, 4.5.2 and 4.5.3 show the *ab*-plane oriented diffraction pattern obtained from a sample of RbC_{25} as it was slowly cooled under an atmosphere of nitrogen. The sample mass was 0.413 grams, equivalent to 1.07×10^{-3} moles of RbC_{25}. As with the other large molecule physisorbed ternaries studied, it was more difficult to achieve the published saturation stoichiometries with large solid samples produced from pyrolytic graphite than it was with powdered samples. Figure 4.5.4 shows the c-axis oriented patterns from the same samples.

4.5.2 Results

Physisorption of the nitrogen gas begins at a somewhat higher temperature, between 200 K and 180 K, than it does in the potassium-nitrogen system. As the temperature is lowered to 160 K in the sample of $Rb(N_2)_xC_{25}$ a new phase or phases replace the XRD pattern of binary RbC_{25}. By 120 K a number of small peaks appear, suggesting either a new weak phase or as satellite peaks of one of the original phases. The patterns at 90 K and 120 K are identical and are combined in Figure 4.5.1 to improve counting statistics, while expanded views of the 160 K pattern and 90-120 K combined patterns are shown in Figure 4.5.2 and 4.5.3. It is clear from these diagrams that the reflection at 20.92° has a narrower peak profile than the others in the pattern, and appears to be the product of a different crystal structure, a conclusion made more likely by the observed behaviour of phase separation in the other ternary GICs studied previously.

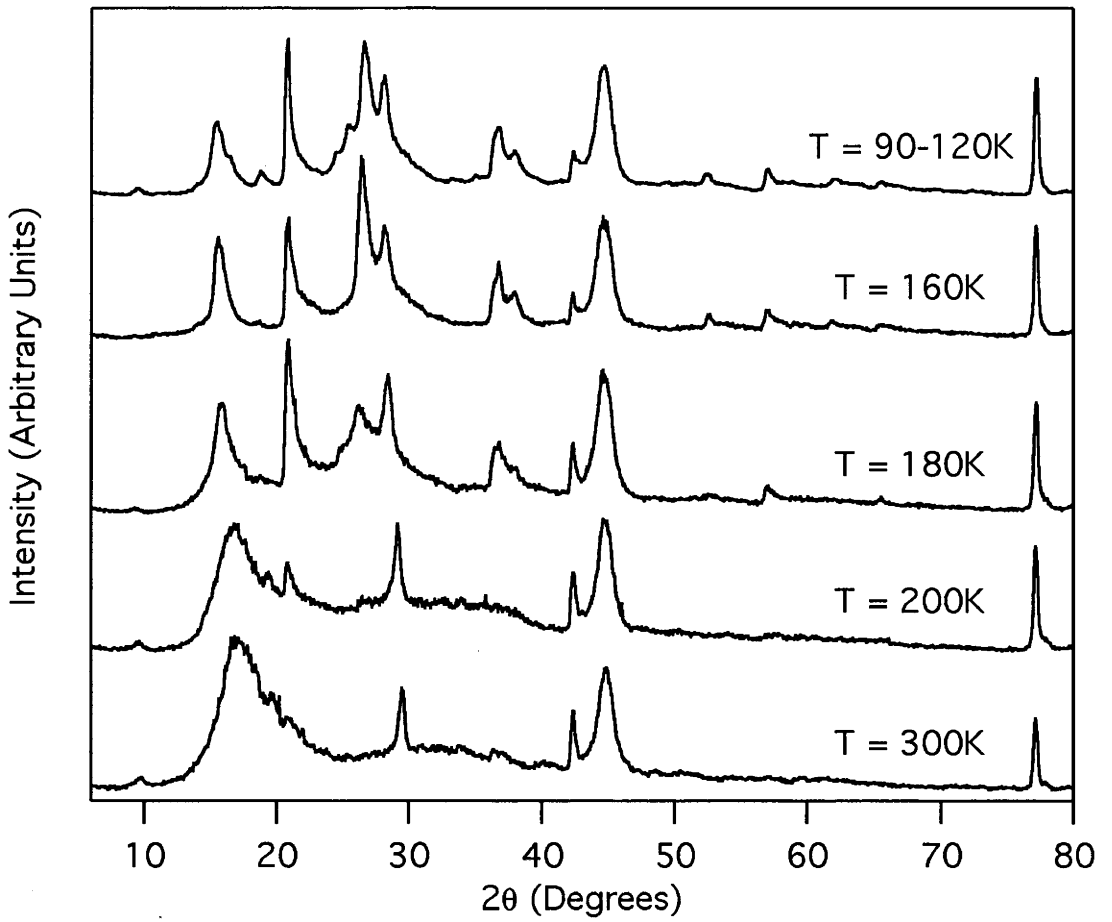

Figure 4.5.1: *ab-plane oriented XRD patterns of an RbC_{25} sample cooled from 300 K to 90 K under an atmosphere of N_2.*

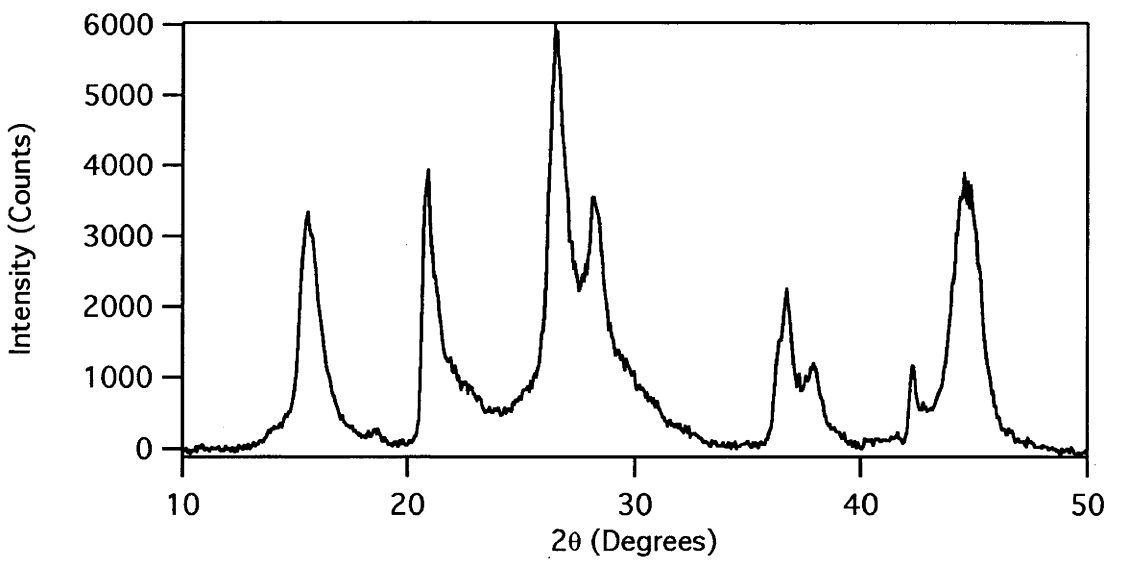

Figure 4.5.2: *the ab-plane oriented diffraction pattern from the $Rb(N_2)C_{25}$ sample at 160 K. A fourth order polynomial background has been subtracted from the data.*

In the expanded views of the 160 K and 90-120 K patterns it is very clear that new peaks have appeared in these patterns after cooling. This is associated with a considerable drop in the relative intensity (compared to the graphite (10) and (101) peaks at 42.28° and 44.68°) of all the peaks of the pattern except the peak at 20.92°, which as has already been noted appears to belong to another phase. This implies that the new peaks are associated with only one of the phases, but does not determine whether they are the satellite peaks produced by a modulation of an existing phase or an entirely new structure.

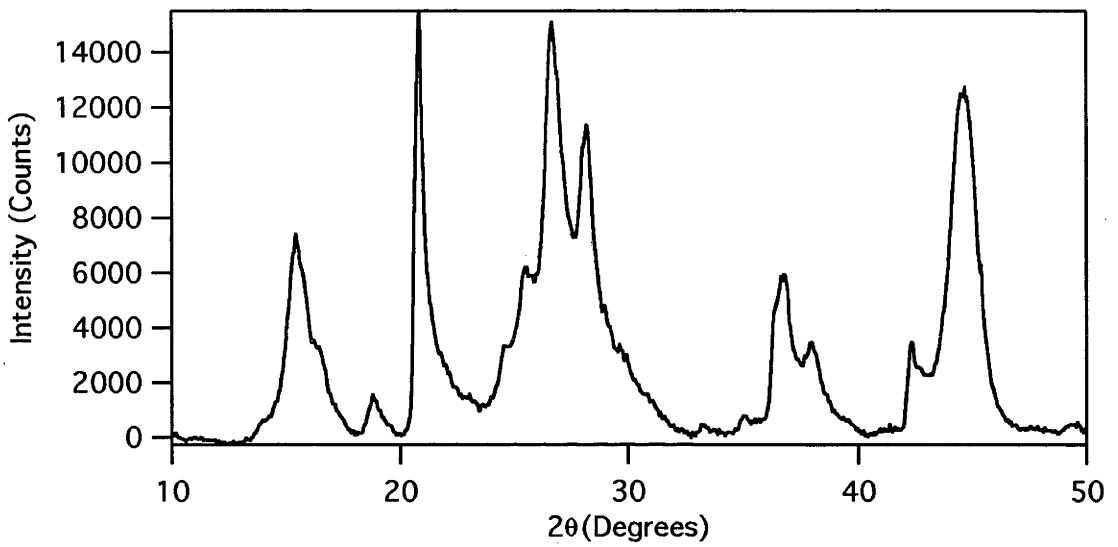

Figure 4.5.3: *the combined ab-plane oriented diffraction patterns from the* $Rb(N_2)C_{25}$ *sample at 90-120 K. A fifth order polynomial background has been subtracted from the data.*

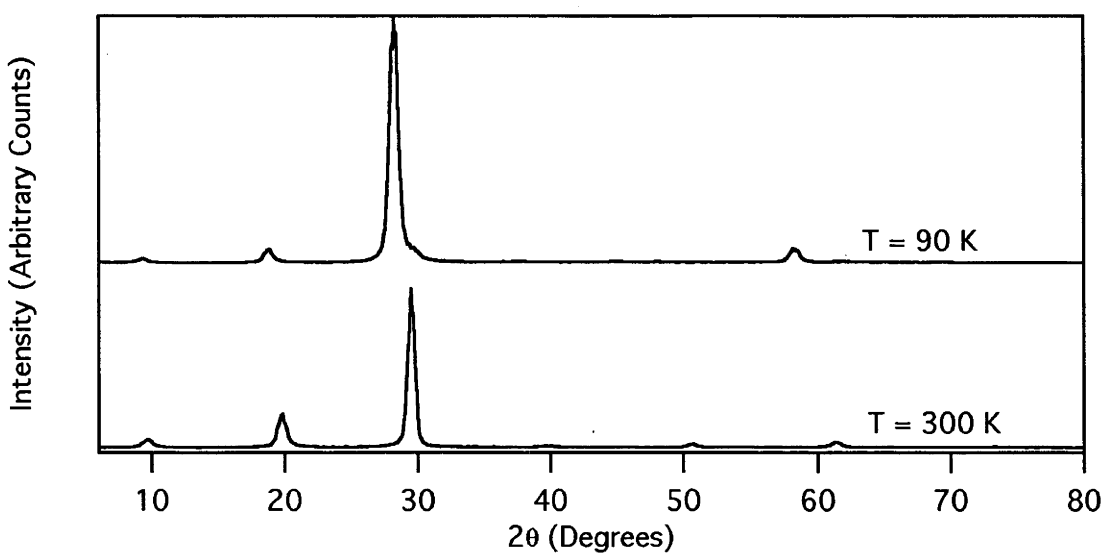

Figure 4.5.4: *c-axis oriented diffraction patterns of* $Rb(N_2)_{1.0}C_{25}$ *at 90 K and* RbC_{25} *at 300 K.*

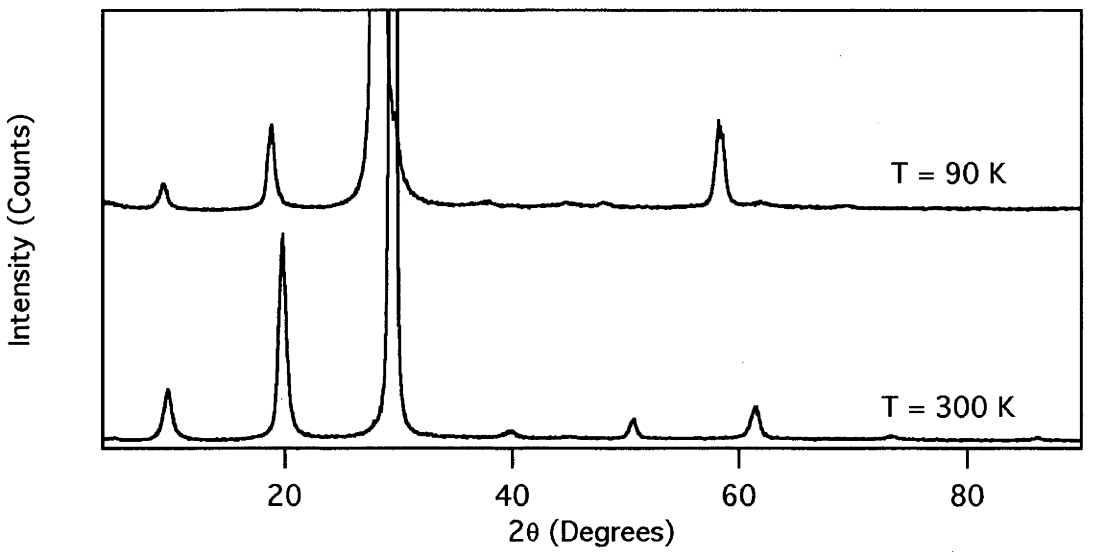

Figure 4.5.5: *expanded c-axis oriented diffraction patterns of* $Rb(N_2)_{1.0}C_{25}$ *at 90 K and* RbC_{25} *at 300 K.*

The *c*-axis data also shows similar behaviour to the other large-molecule ternary GICs; upon absorption the *c*-axis expands to a single new spacing, with no sign of an intermediate or second phase. The 90 K saturated *c*-axis oriented pattern is indexed in Table 4.5.1, showing the usual range of d-spacings seen in these patterns, and producing a final d-spacing of 9.468 Å. There is also a significant decrease in the intensity of all the peaks relative to the strongest (003) reflection upon absorption, which again is behaviour seen in the other large molecule ternaries.

Data				Cell	
2θ (Degrees)	Intensity (Counts)	I/Imax x100	D (Å)	l	D x l (Å)
9.34	980	1.95	9.168	1	9.468
18.82	3031	6.03	4.715	2	9.430
28.24	50251	100	3.160	3	9.480
58.30	2757	5.48	1.582	6	9.496

Table 4.5.1: *a simple indexing of the c-axis oriented 90 K* $Rb(N_2)C_{25}$ *pattern, showing an average D-spacing of 9.468 Å, with considerable deviation from the average. No measurable peaks of a second phase could be seen.*

2θ (Degrees)	Intensity (Counts)	D (Å)
14.08	398	6.290
15.58	3336	5.687
18.58	270	4.775
20.92	3922	4.246
26.56	5903	3.356
28.18	3552	3.167
36.76	2246	2.445
37.96	1204	2.370
42.28	1161	2.138
44.68	3460	2.028
52.66	437	1.738
57.04	623	1.615
61.84	399	1.500
65.5	313	1.425
77.2	3962	1.236
80.98	278	1.187
84.1	738	1.151

Table 4.5.2: *The peaks of the ab-plane oriented 160 K $Rb(N_2)C_{25}$ pattern. No obvious indexing of the entire pattern could be found, but the peak at 20.92° appears similar to the strongest peak of the 2x2 phase seen in the other large-molecule ternary GICs.*

Table 4.5.2 contains the *ab*-plane oriented diffraction data from the sample at 160 K, chosen because the addition of the many extra low intensity peaks of the 90-120 K pattern would complicate any attempts at indexing. This does not particularly help, because a clear indexing of the entire pattern has been elusive with the exception of one prominent peak. Comparing the data with the patterns of the argon-rubidium-graphite and methane-rubidium-graphite systems (Figure 4.5.6) shows that the peak at 20.92° seems to possess the same position and shape as the (10) peak of the 2x2 pattern found in these systems.

Attempts to index the remainder of the pattern, manually or through employing a computerised search, by a registered superlattice of graphite or an incommensurate lattice, have all failed. The available lattices would have to either have small unit cells or a great number of absent reflections, and the problem is rendered more difficult by the small number of easily distinguishable peaks. These are quite wide, implying the maximum

intensity of the peaks are shifted away from the actual d-spacing, a feature of the diffraction patterns produced by turbostratic structures with a small domain size.

4.5.3 *ab*-plane simulations of the 2x2 RbC_{16} phase

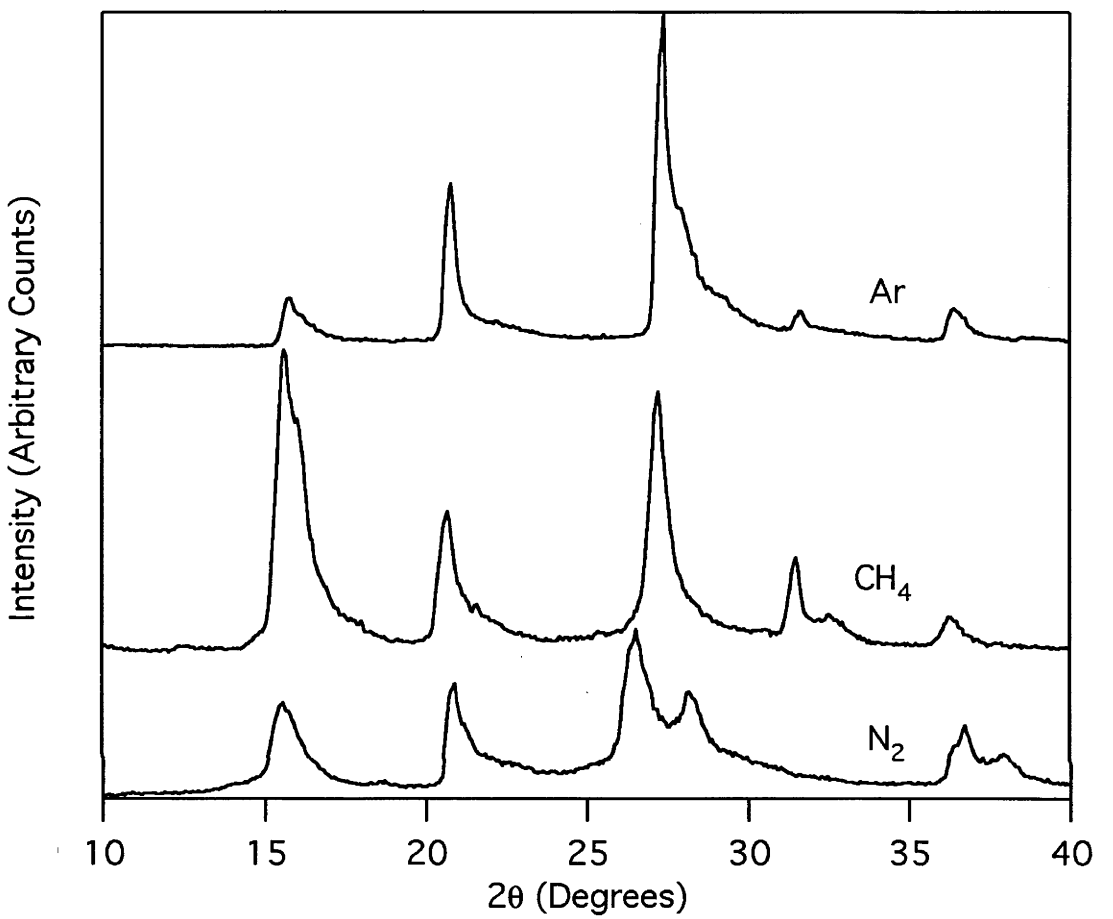

Figure 4.5.6: *the ab-plane oriented diffraction patterns from the three saturated large-molecule rubidium-gas-graphite compounds studied in this work:* $RbAr_{1.2}C_{25}$, $Rb(CH_4)_{0.9}C_{25}$ *and* $Rb(N_2)_{1.0}C_{25}$. *The peak at ~20.9° appears in all three patterns.*

While there is no indexable structure to be found for most of the pattern, it would appear from Figure 4.5.6 that the compound has behaved the same way as the other large-molecule ternaries in that it has phase separated into an expanded phase containing the nitrogen molecules and a compressed phase which remains a binary GIC; and furthermore that this compressed phase has adopted the same hexagonal P6 2x2 graphite superlattice also found in the previous studies. Given this assumption, the 2x2 structure could be simulated and then subtracted from the data to show a remnant pattern that would be produced only by the unknown ternary compound.

Figures 4.5.7 shows a comparison between a simulated 2x2 P6 *ab*-plane pattern and the data at around 20° and 37°, where the (10) and (11) of the 2x2 structure appear. there is a good fit to the peak at 20.92°, while the (11) appears to correspond to a shoulder on the peak at 36.76°. As with the *ab*-plane simulations in previous sections, only the contribution from the alkali ions is shown; there is no graphite contribution.

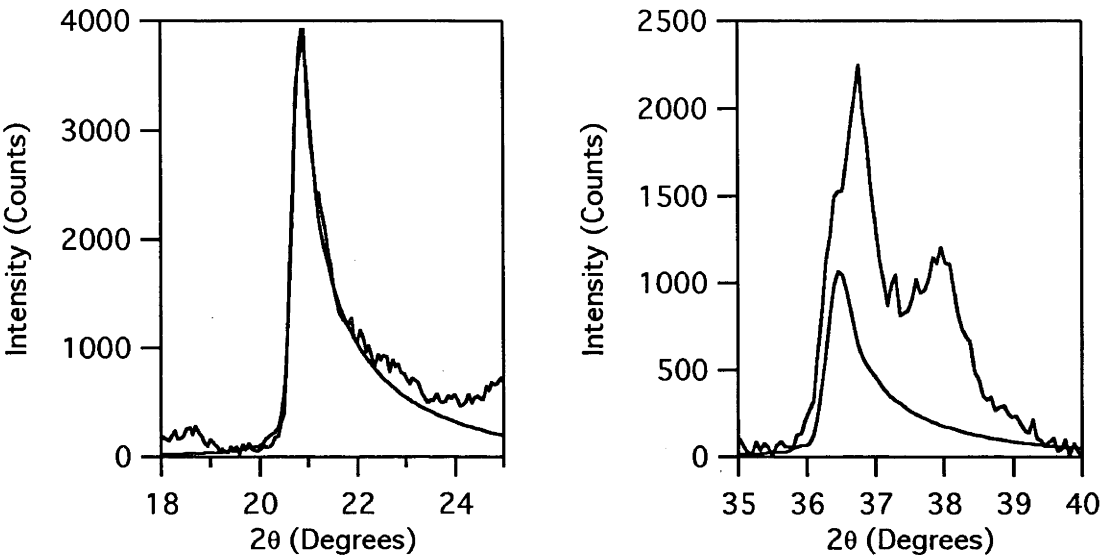

Figure 4.5.7: *the ab-oriented diffraction pattern compared with the (10) and (11) peaks of a simulated 2x2 RbC_{16} structure, with parameters N_1=50, a_{gr}=2.47 Å, λ=1.54178 Å and CD=0.3.*

The best fit to the peak at 20.92° is a 2x2 RbC_{16} *ab*-plane structure with in-plane crystallite size N_1=50, graphite axis a_{gr}=2.47 Å, λ=1.54178 Å and *c*-axis damping factor CD=0.3. Subtracting this simulated 2x2 pattern from the data (Figure 4.5.8) shows a remnant difference pattern that should correspond to the nitrogen-rubidium-graphite ternary phase. Again, this remnant difference pattern could not be indexed.

No simulations of the *c*-axis data were made: there are too many variables for it to be useful. In the previous studies, the stoichiometry of the phases in each system, binary and ternary, was determined by the goodness of the fits of the simulated patterns to the ab-plane oriented diffraction pattern. Except for the $K(N_2)_{0.7}C_{25}$ system, the *c*-axis data showed weak or no sign of a second phase, so the c-axis simulations used the stoichiometry of the ternary phase set by the $\sqrt{7}x\sqrt{7}$ structure, which for the rubidium-argon and rubidium-methane systems were $Rb(Ar)_2C_{28}$ and $Rb(CH_4)_2C_{28}$. Since no equivalent *ab*-plane structure could be found here, a *c*-axis simulation would be required to fit an unknown Rb:C ratio, an equally unknown Rb:N_2 ratio - as well as the other parameters used in the previous fits - to the intensity of the 4 strong peaks of the saturated c-axis diffraction patterns.

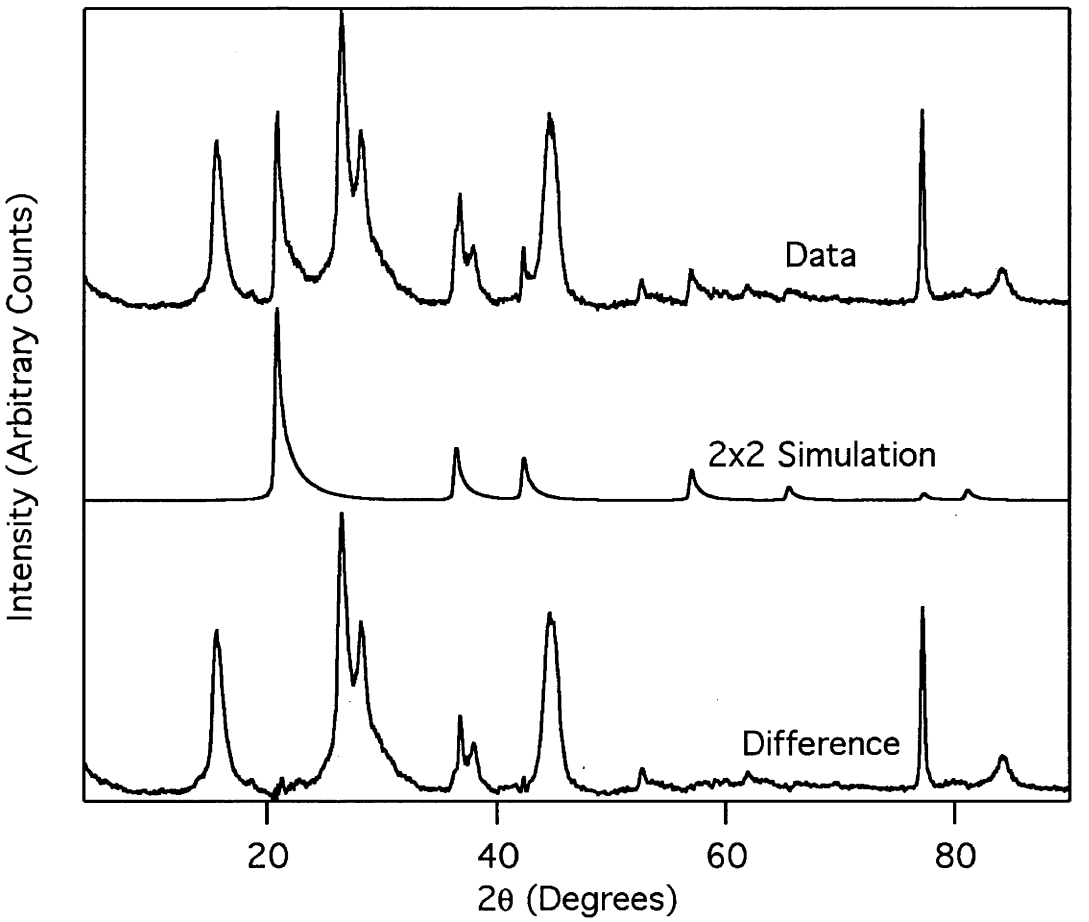

Figure 4.5.8: *the 160 ab-plane* $Rb(N_2)_{1.0}C_{25}$ *diffraction pattern with a 4th order polynomial background removed, the complete 2x2 simulated pattern shown in Figure 4.5.7, and the difference pattern produced by subtracting the simulated pattern from the data.*

4.5.4 Conclusion

The *ab*-plane diffraction pattern of rubidium-nitrogen-graphite ternary GIC could not be entirely indexed with a single or two phase model, however the 2x2 RbC_{16} phase seen in the previously studied $RbAr_{1.2}C_{25}$ and $Rb(CH_4)_{0.9}C_{25}$ compounds does appear in the pattern. This implies that the $Rb(N_2)_xC_{25}$ system undergoes similar behaviour to the other large molecule ternary, phase separating into a compressed binary GIC and an expanded ternary GIC that contains all of the physisorbed gas. It is this ternary phase, which may be incommensurate with the graphite lattice, that could not be indexed. As a result quantitative *ab*-plane and *c*-axis simulations could not be undertaken.

References

1. K. Watanabe, T. Kondow, M. Soma, T. Onishi, and K. Tamaru, *Molecular-sieve type sorption on alkali graphite intercalation compounds.* Proceedings of the Royal Society of London A, 1973. **333**: p. 51-67.

2. R. Moreh, H. Pinto, Y. Finkelstein, and F. Beguin, *Tilt of N_2 Molecules Physintercalated into $C_{24}K$ and $C_{24}Rb$.* Journal of Physics and Chemistry of Solids, 1996. **57**(6-8): p. 909-913.

3. R. Moreh, S. Melloul, and H. Zabel, *Orientation of molecularly intercalated N_2 in C_{24} K.* Physical Review B, 1993. **47 (16)**: p. 10754-10759.

4.6 Hydrogen and Deuterium Absorption by Rubidium Graphite Intercalation Compounds: Studies of $Rb(H_2)_xC_{25}$ and $Rb(D_2)_xC_{25}$.

The hydrogen and deuterium alkali-metal ternary graphite intercalation compounds have attracted the most interest[1-13]. Unlike the large molecule ternary GICs also discovered in the initial studies there was the potential for industrial applications in hydrogen storage and isotopic refinement. The discoverers[14] categorised the $Rb(H_2)_xC_{25}$ and $Rb(D_2)_xC_{25}$ isotherms as "Type I" - the classic Langmuir isotherm and shown in Figure 1.13 - and found that they achieved identical saturation stoichiometries: $Rb(H_2)_{2.05}C_{25}$ and $Rb(D_2)_{2.05}C_{25}$.

4.6.1 Hydrogen Absorption by RbC_{25}

4.6.1.1 Data

As with the previous physisorbed systems, there was difficulty in the present experiments in reaching the published saturation stoichiometry with either hydrogen or deuterium by the standard method of increasing the pressure over the sample at a fixed temperature. Here the sample was exposed to a particular pressure of gas, the drop of pressure in the calibrated volume was measured over a period of time, and when a desired stoichiometry was achieved the sample stick was closed off and *ab*-plane- and *c*-axis-oriented diffraction experiments undertaken. By this method the maximum stoichiometry attained was $Rb(H_2)_{1.86}C_{25}$ The sample weighed 0.413 grams, equivalent to 1.07×10^{-3} moles, assuming an Rb:C ratio of 1:25. Figure 4.6.1 shows the ab-plane oriented diffraction patterns taken of a $Rb(H_2)_xC_{25}$ sample as the hydrogen stoichiometry x was varied from 0.31 to 1.86, while Figure 4.6.3 shows c-axis oriented patterns from the same series.

4.6.1.2 $Rb(H_2)_xC_{25}$ *ab*-plane Results

The *ab*-plane structures display a sequence of behaviour upon gas absorption different to that of the large-molecule ternaries: the ab-plane data displayed in Figure 4.6.1 show that a sudden structural phase change occurs between the stoichiometries of $Rb(H_2)_{0.87}C_{25}$ and $Rb(H_2)_{1.10}C_{25}$.

At the lowest hydrogen filling shown ($(H_2)_{0.31}$) the *ab*-plane structure is identical to the $\sqrt{43}x\sqrt{43}$ structure of binary RbC_{25}. As the filling increases to $(H_2)_{0.61}$ and $(H_2)_{0.87}$, the $\sqrt{43}$ structure disappears: by $(H_2)_{0.87}$ the strongest $\sqrt{43}x\sqrt{43}$ peak has broadened

considerably but remains, at 16.98°/5.217Å; the remainder of the √43x√43 peaks have either vanished or become much weaker. This suggests a simple insertion of the hydrogen molecule at random into the existing rubidium-ion lattice which has its in-plane coherence length degraded by the process. Between a filling of $(H_2)_{0.87}$ and $(H_2)_{1.10}$, a transition occurs to a more crystalline system: two strong satellite peaks with different profile shapes appear, bracketing what appears to be the same main peak near 17° seen at lower fillings, with extra sharp but weak higher order reflections from what seems to be the same structure. As the filling increases beyond $(H_2)_{1.10}$, the new peaks steadily decrease in intensity as more hydrogen is absorbed, to a minimum at the saturation value of x=1.86.

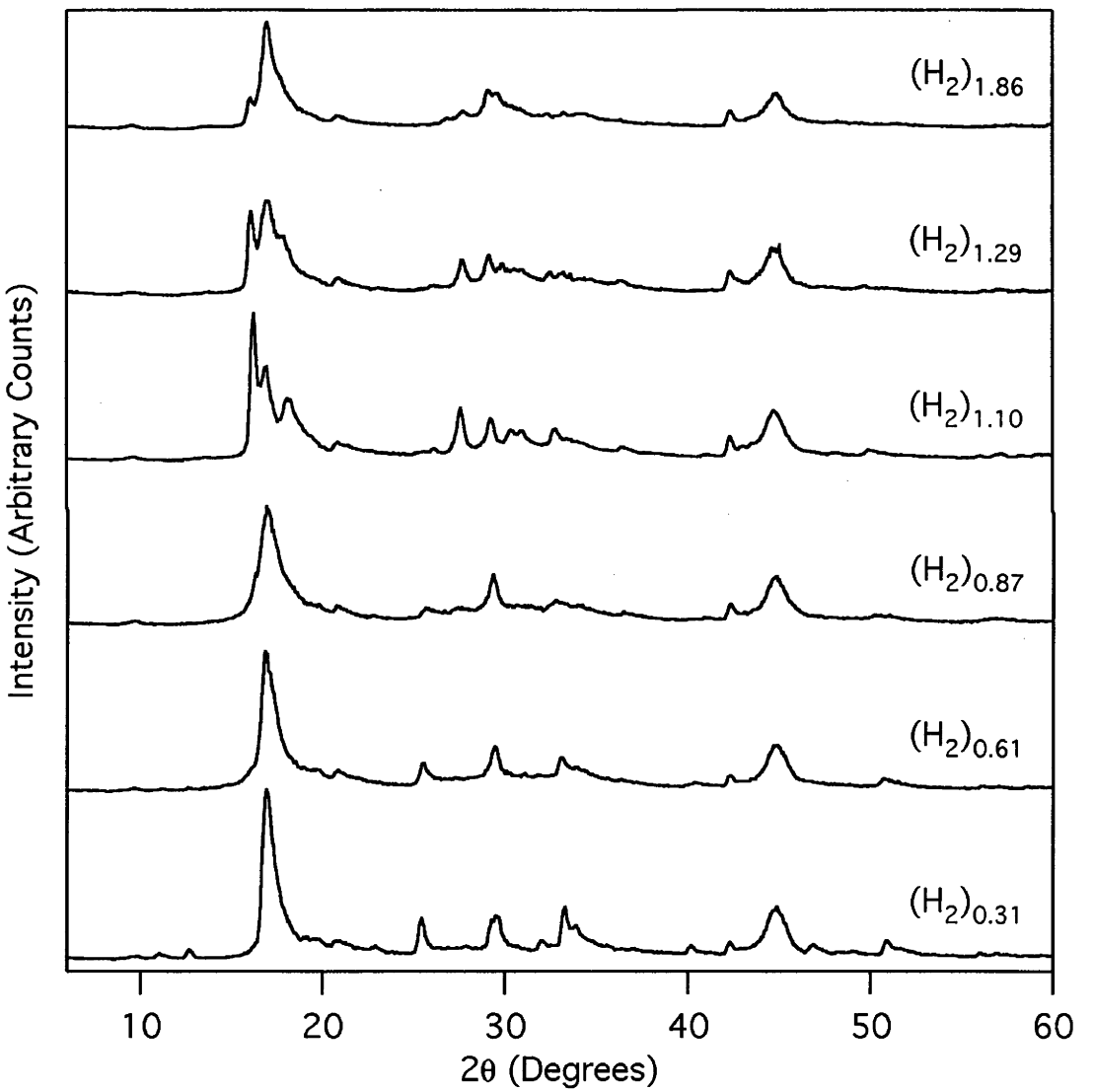

Figure 4.6.1: *A series of ab-plane oriented diffraction patterns of* $Rb(H_2)_xC_{25}$ *taken at 90 K, for* $0.31 < x < 1.86$.

Figure 4.6.2 shows a plot of two *ab*-plane oriented diffraction patterns of a $Rb(H_2)_{1.15}C_{25}$ sample at 90 K and 100 K respectively, indicating that the new structure

that appears at the $Rb(H_2)_{1.15}C_{25}$ stoichiometry disappears between these two temperatures, though hydrogen sorption begins at a much higher temperature.

2θ	Intensity	D-spacing
9.66	528	9.156
16.98	10005	5.222
19.62	1845	4.524
20.88	1738	4.254
25.68	1616	3.469
27.48	1573	3.246
29.34	4340	3.044
32.76	2202	2.734
34.08	1783	2.631
36.48	1307	2.463
42.3	1891	2.137
44.76	4138	2.025
50.28	1027	1.815
56.94	712	1.617
60.42	763	1.532
77.16	3048	1.236
80.58	656	1.192
84.54	1828	1.146

Table 4.6.1: *The primary reflections of the ab-plane oriented XRD pattern of* $Rb(H_2)_{0.87}C_{25}$ *at 90 K.*

The major peaks from the $Rb(H_2)_{0.87}C_{25}$ and $Rb(H_2)_{1.10}C_{25}$ patterns are listed in Tables 4.6.1 and 4.6.2 respectively. Neither of these tables include an indexing scheme because no unit cell could be found. Several models were tried:

i) The registered hexagonal and oblique two-dimensional superlattices of graphite with cell dimensions up to 12 x a_{gr} were checked but no small cells indexed the patterns. While some of the larger cells produced the observed reflections a great many absent reflections were also required to reproduce the entire observed patterns.

ii) a computerised search of the incommensurate single phase two-dimensional oblique lattices - only computationally possible because the search was limited to two-dimensions - up to a cell dimension of 18 Å was attempted. Again, while some very large unit cells produced the observed peaks they also produced many unobserved ones.

2θ	Intensity	D-spacing
9.54	727	9.27
13.62	700	6.501
16.26	18024	5.451
16.98	11085	5.222
18.12	6623	4.896
20.88	2342	4.254
26.16	1611	3.406
27.6	6309	3.232
29.22	5050	3.056
30.36	3866	2.944
30.9	3592	2.894
32.7	3742	2.738
36.48	1821	2.463
41.04	992	2.199
42.3	2879	2.137
43.02	1760	2.102
44.7	5636	2.027
48	1181	1.895
49.92	1464	1.827
50.34	1411	1.813
56.04	804	1.641
57.18	1094	1.611
58.38	895	1.581
59.28	1006	1.559
62.1	1022	1.495
77.1	3540	1.237
80.52	589	1.193
84.54	884	1.146

Table 4.6.2: *The primary reflections of the ab-plane oriented XRD pattern of* $Rb(H_2)_{1.10}C_{25}$ *at 90 K.*

iii) Assuming that the hydrogen system phase separated, a two phase system was tried as a model. The possibility of phase separation receives some support from the data, as there appear to be two different profile shapes in the satellite peaks that appear at $(H_2)_{1.10}$. Again, none of the smaller commensurate or incommensurate systems, oblique

or hexagonal, reproduced the observed peaks, and all of the larger cells produced unobserved reflections that could not be removed with realistic structural models.

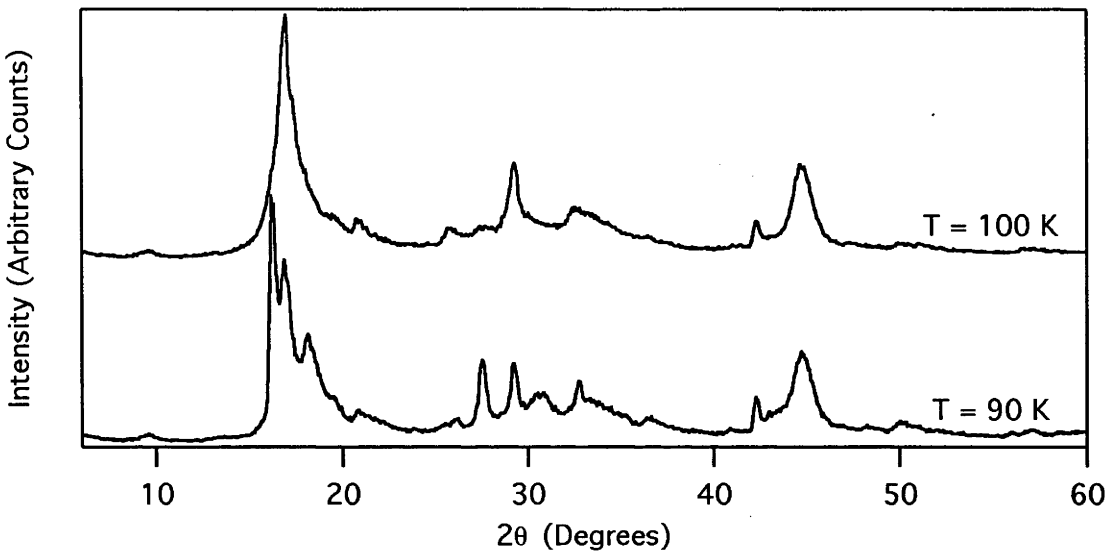

Figure 4.6.2: *Two ab-plane oriented diffraction patterns of* $Rb(H_2)_{1.15}C_{25}$ *taken at 90 K and 100 K; the new phase(s) disappear between these two temperatures, though hydrogen is still retained by the GIC.*

Given the failure of these structural models to even index the pattern produced by the $Rb(H_2)_{1.10}C_{25}$ sample, let alone to produce a structural model, and by extension the patterns with higher hydrogen fillings, it is an obvious conclusion that the actual structure is more complex.

However, it is possible to make a less quantitative description of the diffraction data from the $(H_2)_{1.10}$ pattern than an indexed structure. The peak shape around $2\theta=17°$ is not inconsistent with (a) a significant drop of intensity in the residual peak at $2\theta=17°$ seen at lower fillings, (b) the construction of a two dimensional expanded, incommensurate layer lattice, with a primary reflection at $2\theta=16.26°/d=5.45Å$, and (c) the construction of a two dimensional compressed, incommensurate layer lattice, with a primary reflection at $2\theta=18.2°/d=4.89Å$. If this model is correct, the hydrogen doping causes a disproportionation of the alkali-metal lattice. At higher fillings the crowding is such that minimum volume is once again achieved by uniform packing through a structure close to the $\sqrt{43}x\sqrt{43}$ lattice of RbC_{25}, and the multiphase system appearing around $x=1.16$ is slowly eliminated.

It is possible that the disproportionation of the AM ion lattice is a result of some hydrogen atoms adopting an orientation parallel to the graphene players, and the others perpendicular. Alternatively, it may be a result of a simultaneous separation into an

expanded hydrogen rich ternary GIC and a compressed AM-GIC binary, which would be similar to the behaviour seen previously in the large-molecule ternary GICs. These models cannot be distinguished by the x-ray diffraction data presented here; however in Chapter 5 an attempt will be made to reconcile these data with previously published studies of hydrogen tunnelling in the same system.

4.6.1.3 $Rb(H_2)_xC_{25}$ *c*-axis Results

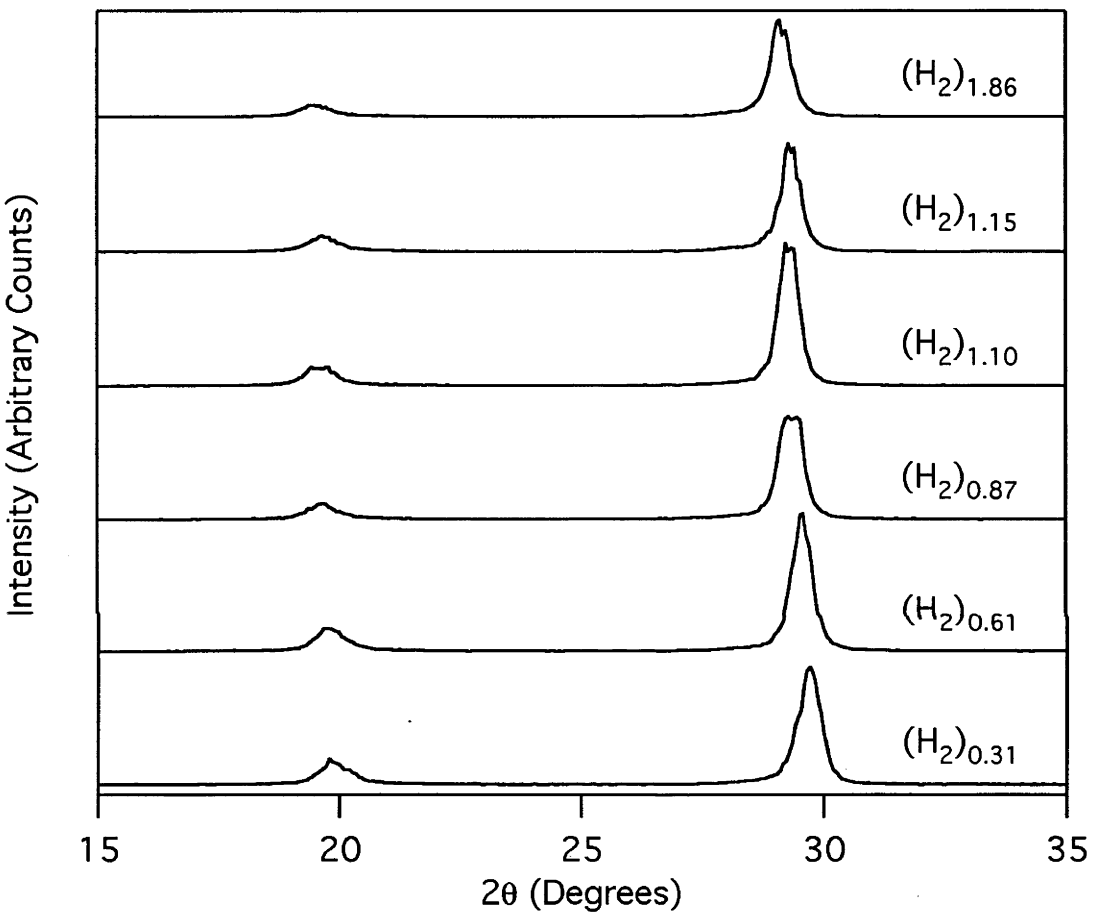

Figure 4.6.3: *A series of c-axis oriented diffraction patterns of* $Rb(H_2)_xC_{25}$ *taken at 90 K, for* $0.31 < x < 1.86$.

The c-axis data shown in Figure 4.6.2 indicates that the c-axis dimension shows a steady expansion with hydrogen filling, rather than the jump to a new c-axis spacing that was seen with the large-molecule systems; though the (003) peak at $(H_2)_{0.87}$ has an unusual profile shape that may indicate a two phase system, the full width at half maximum of the (003) peaks remains relatively steady through the series.

While it was possible to produce the same *c*-axis simulations for the hydrogen data as were made for the large-molecule ternary GICs, that has not been done here, primarily

because for these samples they have little descriptive value. The contribution of the hydrogen atoms to the diffraction pattern was so small that the simulations were effectively of RbC_{25} compounds with varying c-axis dimensions. Instead, the d-spacing, standard deviations of d-spacing from each calculated pattern and the full width at half maximum of the (003) peaks (determined from a gaussian peak fit) from each pattern are tabulated in Table 4.6.3 and displayed in Figure 4.6.4.

$Rb(H_2)_xC_{25}$	D-spacing (Å)	Standard Deviation (Å)	(003) FWHM (Degrees)
0.31	8.98	0.02	0.563
0.61	9.05	0.02	0.512
0.87	9.11	0.05	0.623
1.10	9.11	0.02	0.504
1.15	9.13	0.03	0.480
1.86	9.17	0.03	0.497

Table 4.6.3: *The c-axis d-spacing, standard deviation thereof and full width at half maximum of the (003) peaks of the c-axis oriented* $Rb(H_2)_xC_{25}$ *diffraction patterns shown in Figure 4.6.3.*

Figure 4.6.4 shows two different fits to the *c*-axis d-spacing vs filling data. A logarithmic fit to all the data points shows an approach to a limit dimension of 9.17 Å at the highest stoichiometry, but it is in error at the lower end: the *c*-axis dimension of binary RbC_{25} is the same as that of the $Rb(H_2)_{0.31}C_{25}$ pattern. The line fit removes the first point as an outlier and fits a straight line to the rest of the data. This (within error) produces the straight line expansion expected by Vegard's Law[15]; this is a very similar fit to that seen in the $Rb(H_2)_xC_{25}$ system, described below.

In summary, the *c*-axis data shows a steady but non-linear expansion of the c-axis dimension of the $Rb(H_2)_xC_{25}$ sample with increasing x, approaching a maximum of 9.17 Å, but provides little useful information as to the nature of the *ab*-plane structure or structures.

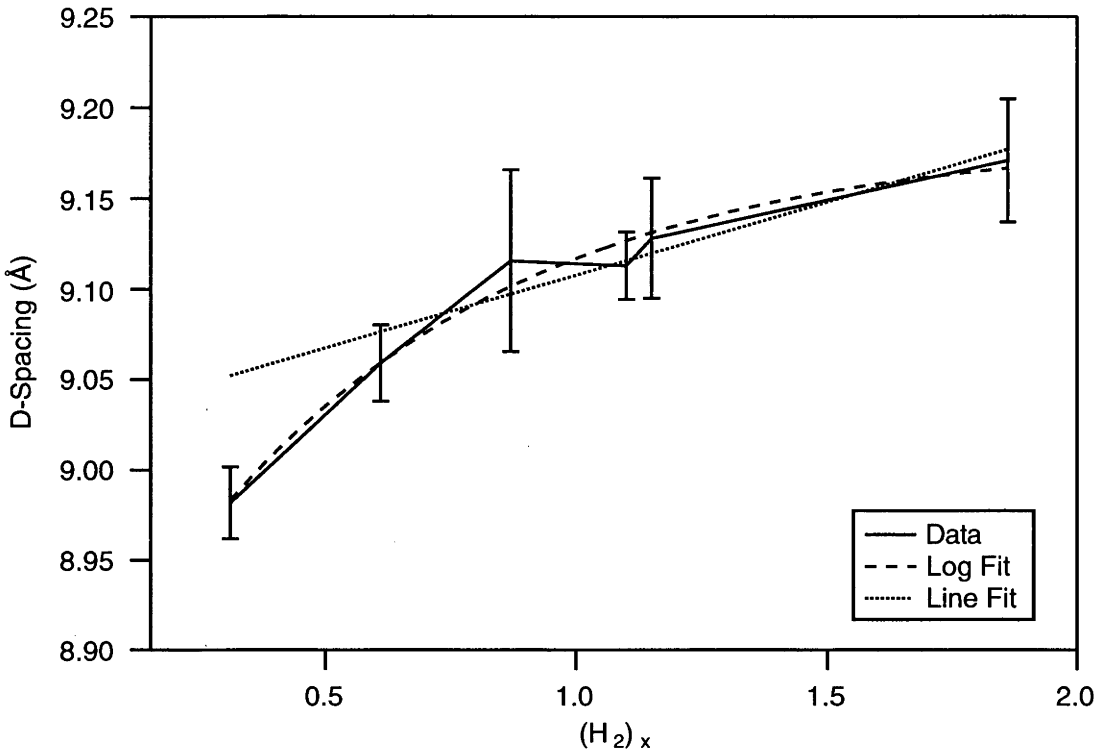

Figure 4.6.4: *a plot of average c-axis d-spacing vs. hydrogen filling for the c-axis series shown in Figure 4.6.3, with two different fits to the data. The curve labelled "Log Fit" is a curve of the form* $V_1+V_2exp(-V_3x)$ *fitted to the data, where* V_1 = *9.1835,* V_2 = *-0.32877 and* V_3 = *1.5955. The "Line Fit" is a straight line of the form* $D = 9.0274+0.08043(H_2)_x$*: this fit does not include the point at* $(H_2)_{0.31}$*, which is assumed to be an outlier. The error bars on the D-spacing values are the standard deviations of the calculated D-spacing of each pattern.*

4.6.2 Deuterium Absorption by RbC_{25}

4.6.2.1 Data

The sorption behaviour of the rubidium-deuterium-graphite system was the same as that described for the hydrogen system above - increasing uptake with steadily increasing pressure. The sample weighed 0.406 grams, equivalent to 1.05×10^{-3} moles of RbC_{25}. Figure 4.6.5 shows the ab-plane oriented diffraction patterns for the $Rb(D_2)_xC_{25}$ system for x=0.0, 0.98, 1.18 and 1.73, while Figure 4.6.7 shows the c-axis oriented patterns for the same fillings.

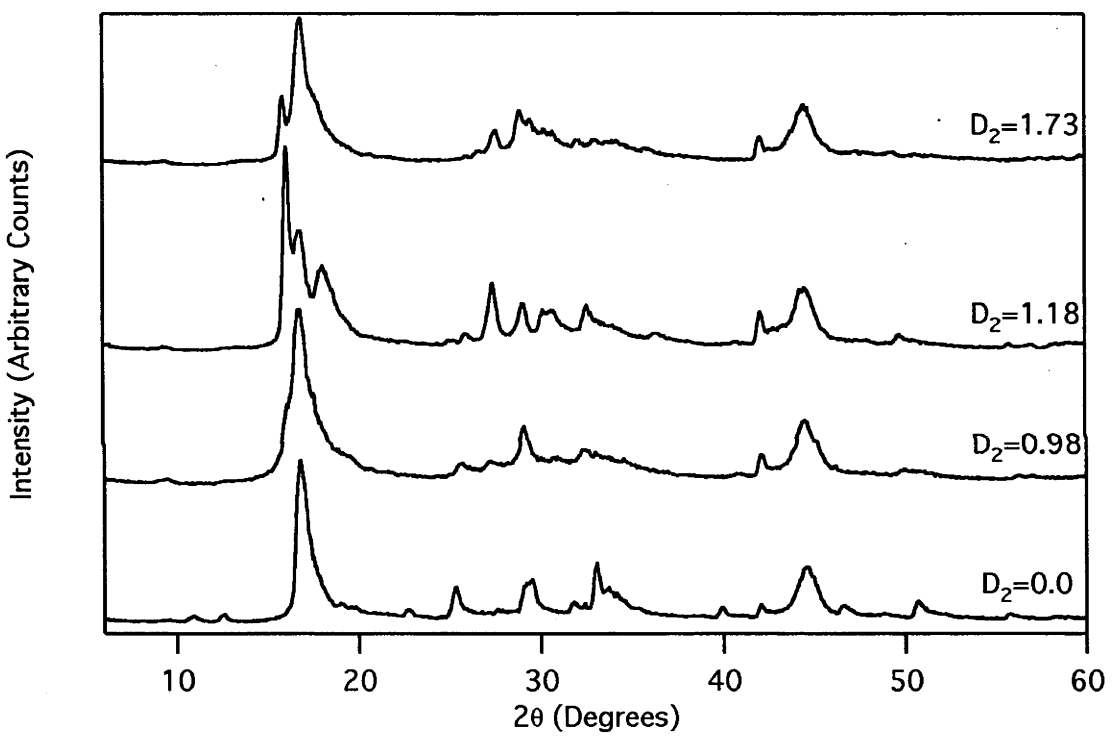

Figure 4.6.5: *A second series of ab-plane oriented diffraction patterns of $Rb(D_2)_xC_{25}$ taken at 90 K, for $0.0 < x < 1.73$.*

4.6.2.2 *ab*-plane $Rb(D_2)_xC_{25}$ Results

As with the hydrogen compounds the rubidium-deuterium-graphite diffraction patterns show a steady elimination of the $\sqrt{43}x\sqrt{43}$ structure of the binary RbC_{25} GIC, followed by a transition to a new structural phase or phases at a stoichiometry of $Rb(D_2)_{1.2}C_{25}$, after which the peaks associated with the new phases steadily diminish in intensity with increasing deuterium filling. The only major difference between the hydrogen and deuterium systems is that the phase transition to begins at a slightly higher filling in the

deuterium system: between $Rb(D_2)_{0.98}C_{25}$ and $Rb(D_2)_{1.18}C_{25}$, compared with $Rb(H_2)_{0.87}C_{25}$ and $Rb(H_2)_{1.0}C_{25}$, respectively. However, this may indicate an error in the method by which gas uptake was measured, affected as it is by the small sample size and large dead-space volumes of the experimental arrangement - as a result, it is possible that the transition actually occurs at the same filling.

2θ	Intensity	D-spacing
6.24	767	14.16
9.42	561	9.388
13.44	534	6.588
16.08	15271	5.512
16.80	9044	5.277
18.06	6523	4.912
25.14	1025	3.542
25.86	1568	3.445
27.42	5267	3.253
29.04	3786	3.075
30.18	3286	2.961
30.66	3321	2.916
32.58	3646	2.748
36.48	1544	2.463
40.74	928	2.215
42.12	3142	2.145
44.52	4947	2.035
49.74	1486	1.833
55.80	841	1.647
57.00	724	1.616
58.38	870	1.581
62.04	800	1.496
72.54	441	1.303
74.34	414	1.276
76.86	3082	1.240
77.70	557	1.229

Table 4.6.4: *The primary reflections of the ab-plane oriented XRD pattern of* $Rb(D_2)_{1.2}C_{25}$ *at 90 K.*

Table 4.6.4 (above) shows the diffraction angle, intensity and D-spacing for the $Rb(D_2)_{1.18}C_{25}$ pattern shown in Figure 4.6.5. These values are very similar to those

found for the $Rb(H_2)_{1.18}C_{25}$ pattern, and again could not be indexed using the methods employed for the hydrogen patterns.

Figure 4.6.5 shows the diffraction patterns from the *ab*-plane oriented patterns of $Rb(D_2)_{1.18}C_{25}$ at 90 K and 100 K, demonstrating that as with the hydrogen system the ordered structure is destroyed by this increase in temperature. Additionally the difference pattern found by subtracting the 100 K pattern from the 90 K pattern is included, on the assumption that the 90 K pattern consists of a structure similar to the 100 K pattern with the peaks associated with the new structure(s) superimposed upon it.

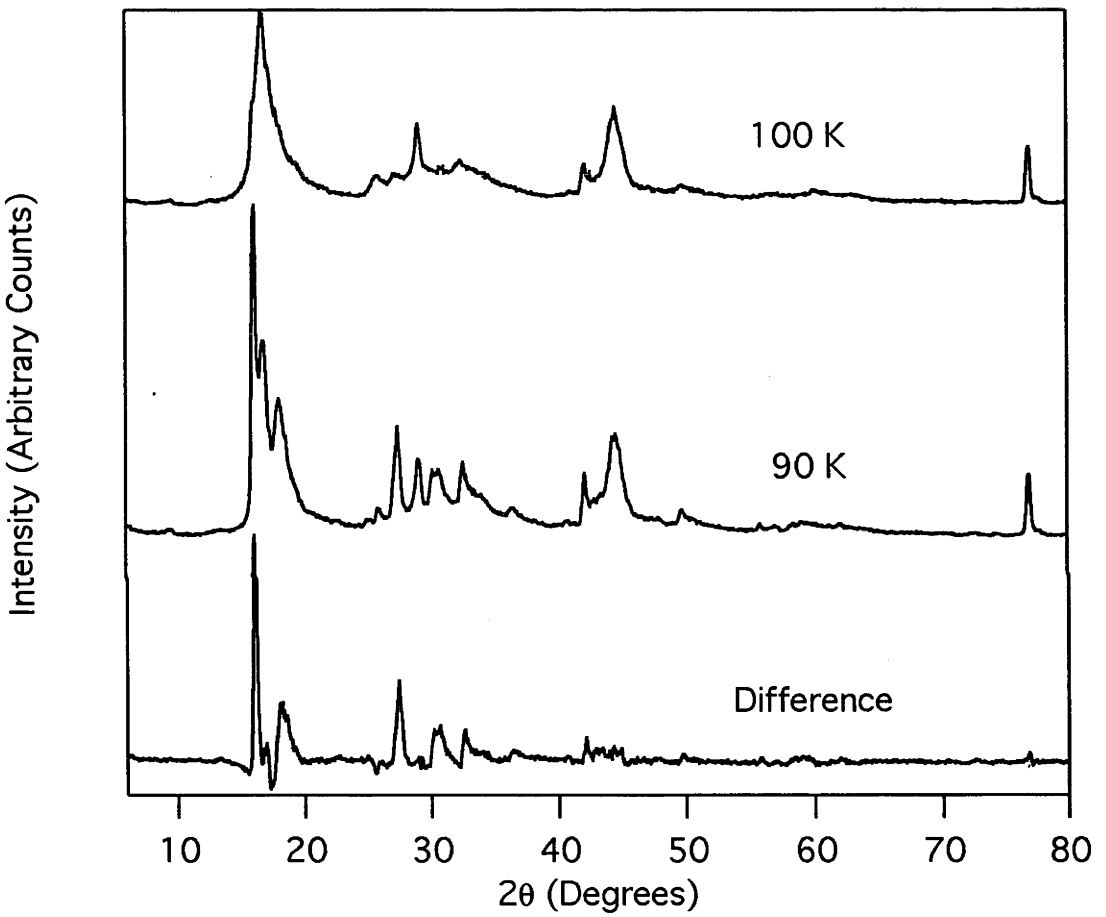

Figure 4.6.5: *the ab-plane oriented diffraction patterns of* $Rb(D_2)_{1.18}C_{25}$ *at 90 K and 100 K, and the difference pattern.*

In the difference pattern it appears that there are two different peak profiles involved - peaks at 16.08° and 27.42° having a narrow peak with little sign of a turbostratic shape, while wider peaks with a pronounced asymmetric peaks are found at 18.06° and 30.18°. If this indicates that there are two different phases producing these structures, it explains the difficulty in indexing the pattern: there are only two to three clearly resolved peaks for each phase, which is insufficient to unambiguously index a structure which is not an easily recognisable superlattice of graphite.

4.6.2.3 *c*-axis $Rb(D_2)C_{25}$ Results

The c-axis oriented diffraction patterns from the $Rb(D_2)_xC_{25}$ system for x=0.0, 0.98, 1.18 and 1.73 are shown in Figure 4.6.6, showing the same continuous expansion of the *c*-axis dimension with gas adsorption that was seen in the hydrogen system. Simulations of these c-axis patterns are not shown for the same reasons as for the hydrogen system: the simulations patterns are effectively that of RbC_{25} with an expanded c-axis.

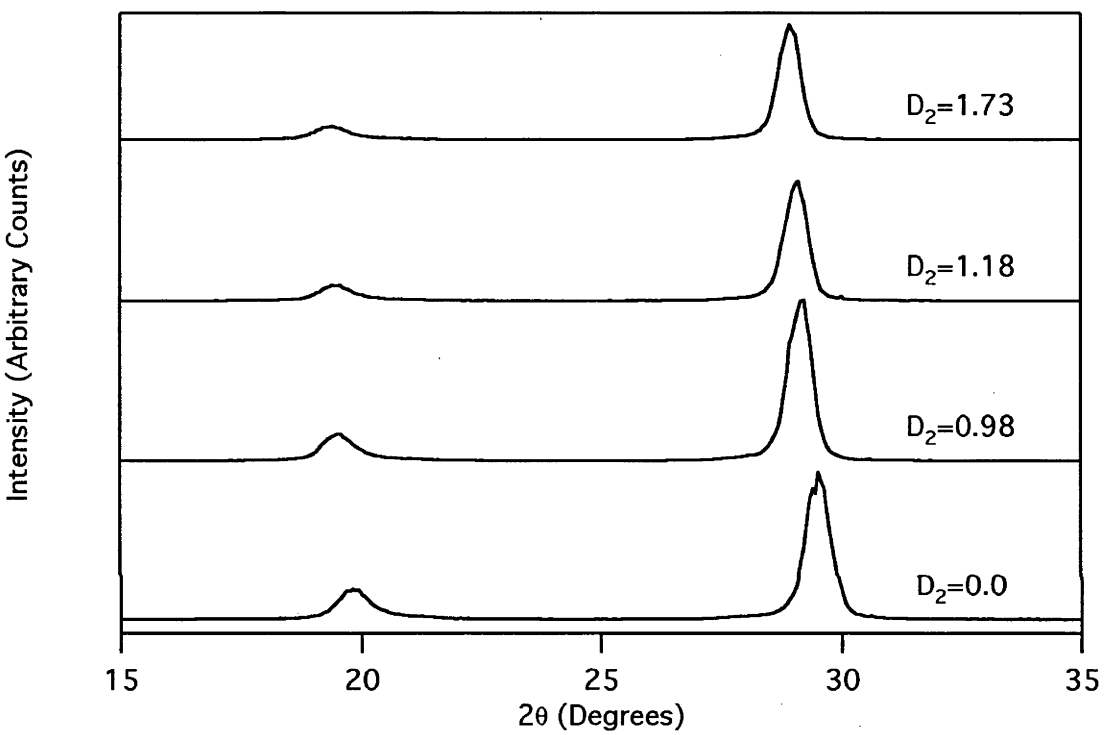

Figure 4.6.6: *A series of c-axis oriented diffraction patterns of $Rb(D_2)_xC_{25}$ taken at 90 K, for 0.0 < x < 1.78.*

Figure 4.6.7 shows a plot of c-axis spacing versus deuterium stoichiometry, as well as a curve fit. One notable difference from the hydrogen data an obvious linear expansion in *c*-axis dimension with deuterium filling, without the logarithmic form seen in the hydrogen data. The d-spacing of the $Rb(H_2)_{0.31}C_{25}$ pattern, removed to allow a Vegard's Law fit to the hydrogen data in Figure 4.6.4, would appear to be in error. The deuterium data are summarised in Table 4.6.5, which indicate that the d-spacings are all approximately 0.05 Å larger than those found for hydrogen, with somewhat larger standard deviations.

$Rb(D_2)_xC_{25}$	D-spacing (Å)	Standard Deviation (Å)	(003) FWHM (Degrees)
0.0	9.04	0.07	0.62
0.98	9.15	0.05	0.60
1.18	9.18	0.06	0.52
1.73	9.23	0.07	0.55

Table 4.6.5: *The c-axis d-spacing, standard deviation thereof and full width at half maximum of the (003) peaks of the c-axis oriented $Rb(D_2)_xC_{25}$ diffraction patterns shown in Figure 4.6.6.*

Figure 4.6.7 shows these tabulated data as well as a linear fit, as opposed to the exponential curve found to fit the hydrogen data, here approaching a maximum value of 9.23 Å

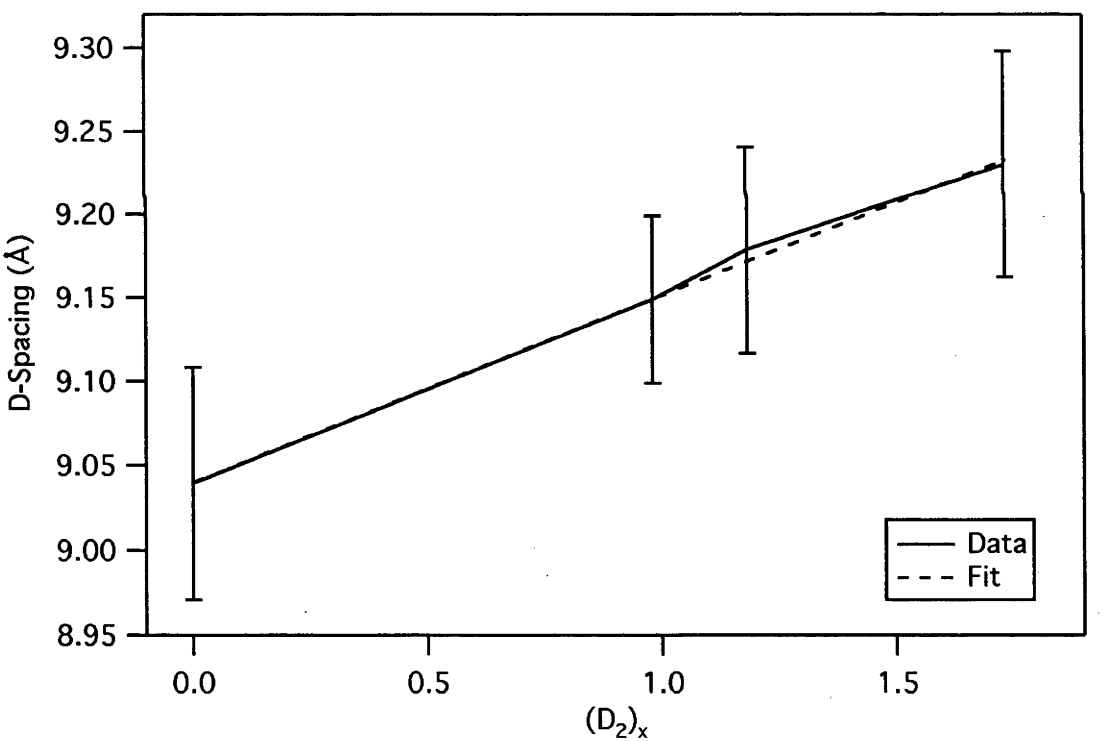

Figure 4.6.7: *a plot of average c-axis d-spacing vs. deuterium filling for the c-axis series shown in Figure 4.6.6, with a line fitted to the data, D-Spacing = 9.04 + 0.11 x $(D_2)_x$. The error bars on the D-spacing values are the standard deviations of the calculated D-spacing of each pattern.*

In summary, the deuterium c-axis data shows a linear expansion of the c-axis with filling, and sheds little light on the *ab*-plane structures.

4.6.3 Conclusion

The $Rb(H_2)_xC_{25}$ and $Rb(D_2)_xC_{25}$ systems show very similar behaviour in both the ab-plane and c-axis oriented diffraction patterns: in the ab-plane structure, the $\sqrt{43}x\sqrt{43}$ structure of the binary RbC_{25} GIC is steadily eliminated with increasing gas sorption, until there is a phase change between a filling of 1.0 and 1.1, where a group of unindexable reflections appear. These reflections steadily diminish in intensity as sorption continues, to reach a minimum at saturation. The *c*-axis data shows an expansion of the interplanar spacing with adsorption, without any clear signs of an anomaly around a filling of 1.0.

References

1. T. Enoki, S. Miyajima, M. Sano, and H. Inokuchi, *Hydrogen-alkali-metal-graphite ternary intercalation compounds.* Journal of Materials Research, 1990. **5**(2): p. 435-465.

2. K. Ichimura and E. Takamura, *Hydrogen in alkali-metal-graphite intercalation compounds.* Synthetic Metals, 1991. **40**: p. 355-368.

3. P. Lagrange, A. Metrot, and A. Herold, *Physisorption de l'hydrogene sur le compose KC_{24}.* Comptes Rendus de l'Academie des Sciences Paris, Serie C, 1972. **275**: p. 765-767.

4. P. Lagrange and A. Herold, *Physisorption de l'hydrogene par les produits d'insertion du potassium dans les carbones imparfaitement organises.* Comptes Rendus de l'Academie des Sciences Paris, Serie C, 1975. **281**: p. 381-384.

5. P. Lagrange, M.-H. Portmann, and A. Herold, *Physisorption selective du protium et du deuterium par le compose d'insertion KC_{24}.* Comptes Rendus de l'Academie des Sciences Paris, Serie C, 1976. **283**: p. 511-514.

6. T. Terai and Y. Takahashi, *Sorption of hydrogen isotopes on potassium-carbon intercalation compounds at low temperatures.* Synthetic Metals, 1983. **7**: p. 49-55.

7. T. Terai and Y. Takahashi, *Sorption behaviour of hydrogen gas and tritiated hydrogen gas on potassium-carbon intercalation compounds.* Carbon, 1984. **22**(1): p. 91-95.

8. T. Terai and Y. Takahashi, *Storage and isotope separation of hydrogen by alkali metal-graphite intercalation compounds.* Material Science Forum, 1992. **91-93**: p. 839-848.

9. W.J. Stead, P. Meechan, and J.W. White, *Librations of Hydrogen in Stage II Caesium Graphite $C_{24}CS$.* Journal of the Chemical Society, Faraday Transactions, 1988. **84**(10): p. 1655-1688.

10. W.J. Stead, I.P. Jackson, J. McCaffrey, and J.W. White, *Tunnelling of Hydrogen in Alkali-metal-Graphite Intercalation Compounds - A systematic study of $C_{24}Rb(H_2)_x$ and its Structural Consequences.* Journal of the Chemical Society, Faraday Transactions, 1988. **84(10)**: p. 1669-1682.

11. K. Watanabe, T. Kondow, T. Onishi, and K. Tamaru, *Sorption of Molecular Hydrogen by Potassium Graphite.* Nature Physical Science, 1971. **233**: p. 160-161.

12. K. Watanabe, T. Kondow, T. Onishi, and K. Tamaru, *Molecular-Sieve Type Sorption on Alkali Graphites.* Chemistry Letters, 1972: p. 477-478.

13. H. Zabel, J.J. Rush, and A. Magerl, *Elastic Neutron Scattering on $C_{24}Rb(D_2)_x$ in the Dilute Concentration Regime.* Synthetic Metals, 1983. **7**: p. 251-255.

14. K. Watanabe, T. Kondow, M. Soma, T. Onishi, and K. Tamaru, *Molecular-sieve type sorption on alkali graphite intercalation compounds.* Proceedings of the Royal Society of London A, 1973. **333**: p. 51-67.

15. L. Vegard, *The constitution of mixed crystals and the space occupied by crystals.* Z. Physik, 1921. **5**: p. 17-26.

4.7 Hydrogen and Deuterium Absorption by Potassium Graphite Intercalation Compounds: Studies of $K(H_2)_xC_{25}$ and $K(D_2)_xC_{25}$.

The original studies found that there was a significant difference in the sorption behaviour of the potassium-hydrogen-graphite and potassium-deuterium-graphite systems, the D_2 being absorbed at a much lower pressure than the H_2, but with both gases reaching the same saturation stoichiometry of x=2.1[(1)]. These compounds have been the most popular as targets of later research of any of those described in the original study[(2-11)], presumably due to the possible applications.

4.7.1 Hydrogen Absorption by KC_{25}

4.7.1.1 Data

The $K(H_2)_xC_{25}$ and $K(D_2)_xC_{25}$ samples used could not be brought to the published saturation values of x=2.1; instead, in both the systems the maximum stoichiometry was ~0.7 at H_2 and D_2 at pressures of up to 500 τ, several times the pressure needed in the previous studies. As in the $RbAr_xC25$ system, where similar behaviour was observed, contrary to published results, this is possibly a result of the lower surface area of large pieces of "Papyex" graphite compared to fine powdered host that were used in previous studies. Several *ab*-plane oriented diffraction patterns from the $K(H_2)_xC_{25}$ system are shown in Figure 4.7.1 and in greater detail in Figure 4.6.2, while the c-axis oriented patterns from the sample samples are shown in Figure 4.7.4. The sample mass was 0.480 grams, equivalent to $1.41x10^{-3}$ moles as prepared to a stoichiometry of KC_{25}.

4.7.1.2 *ab*-plane Results

While the sample could be not made to attain the published saturation stoichiometry, the *ab*-plane data shows behaviour similar to that found in the $Rb(H_2)_xC_{25}$ system, where gas physisorption was found to destroy the structure of the binary GIC and replace it with a simpler diffraction pattern (at $(H_2)_{0.51}$). While greater concentrations (at $(H_2)_{0.69}$) produced a new diffraction pattern superimposed on the simpler pattern. Figures 4.7.2 and 4.7.3 shows the 6-46° region of these patterns, where the new peaks appear in the $(H_2)_{0.69}$ pattern, but the new diffraction peaks are so weak that no unit cell can be found. It is also unclear whether the new peaks are the result of one or more new ab-plane structures or whether they are the result of incommensurate modulations of the simpler pattern at $(H_2)_{0.51}$.

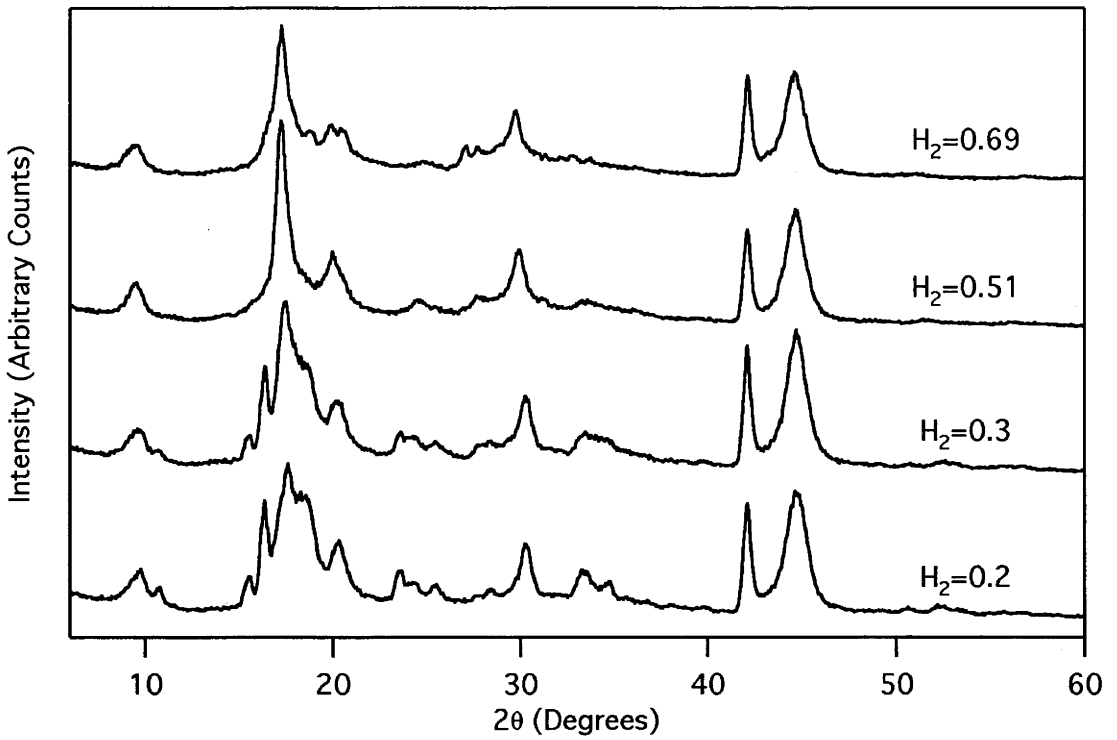

Figure 4.7.1: *the ab-plane oriented x-ray diffraction patterns produced by a sample of* $K(H_2)_xC_{25}$ *at x=0.2, 0.3, 0.51 and 0.69. The patterns at x=0.2 and x=0.3 are very similar to the binary* KC_{25} *patterns.*

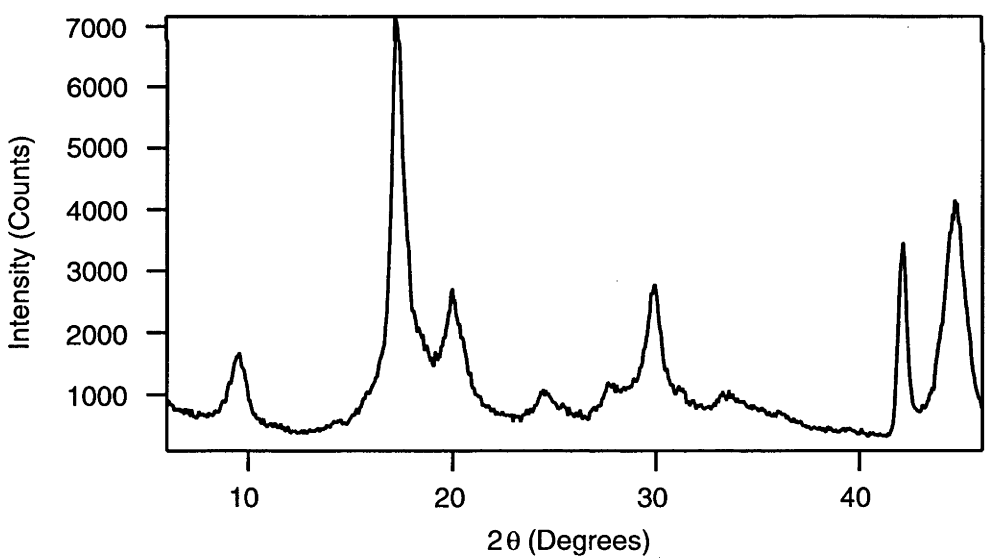

Figure 4.7.2: *a plot of the ab-plane oriented x-ray diffraction patterns produced by a sample of* $K(H_2)_{0.51}C_{25}$ *over the 2θ range 6°-46°.*

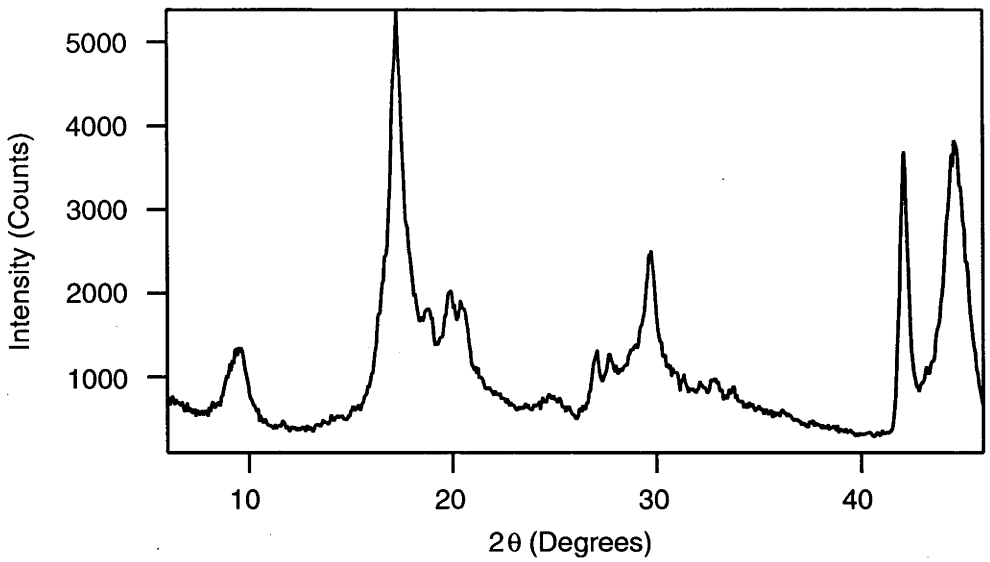

Figure 4.7.3: *a plot of the ab-plane oriented x-ray diffraction patterns produced by a sample of* $K(H_2)_{0.69}C_{25}$ *over the 2θ range 6°-46°.*

2θ (Degrees)	Intensity (Counts)	D-spacing (Å)	Comments
9.54	1674	9.270	*c* - (001)
17.22	7162	5.149	
20.04	2476	4.431	*c* - (002)
24.54	977	3.627	
27.66	1204	3.225	
29.94	2782	2.984	*c* - (003)
31.26	1068	2.861	
33.30	1053	2.690	
42.12	3800	2.145	gr - (10)
44.70	3947	2.027	gr - (101)
51.42	390	1.777	
56.16	302	1.638	
61.50	266	1.508	
76.92	2588	1.239	gr - (11)
77.70	403	1.229	

Table 4.7.1: *the peaks of the ab-plane oriented* $K(H_2)_{0.51}C_{25}$ *diffraction pattern shown in Figures 4.7.1 and 4.7.2. The c-axis breakthroughs and graphite peaks are indicated in the comments column.*

2q (Degrees)	Intensity (Counts)	D-spacing (Å)	Comments
9.48	1354	9.329	c - (001)
17.28	5383	5.132	
18.84	1810	4.710	
19.92	2033	4.457	c - (002)
20.52	1811	4.328	
24.96	800	3.567	
27.06	1277	3.295	
27.72	1268	3.218	
29.72	2512	3.006	c - (003)
32.22	904	2.778	
32.82	978	2.729	
33.72	882	2.658	
42.12	3696	2.145	gr - (10)
44.58	3824	2.032	gr - (101)
51	330	1.791	
56.82	280	1.620	
76.98	2166	1.239	gr - (11)
77.64	391	1.230	

Table 4.7.2: *the peaks of the ab-plane oriented* $K(H_2)_{0.69}C_{25}$ *diffraction pattern shown in Figures 4.7.1 and 4.7.3. The c-axis breakthroughs and graphite peaks are indicated in the comments sections.*

The simpler pattern is equally difficult to index, given that there is only one strong peak (at 17.22°) that is not either a *c*-axis breakthrough or a product of the graphite *ab*-plane pattern. There is a broad weak peak at 27.66° at a 1:$\sqrt{2}$ relationship to the 17.22° peak but beyond this little useful information. The *ab*-plane data point to a very complicated in-plane structure for this system and the need for very high diffraction resolution and careful stoichiometry control in future work. Here we treat only the most obvious effects.

4.7.1.3 *c*-axis Results

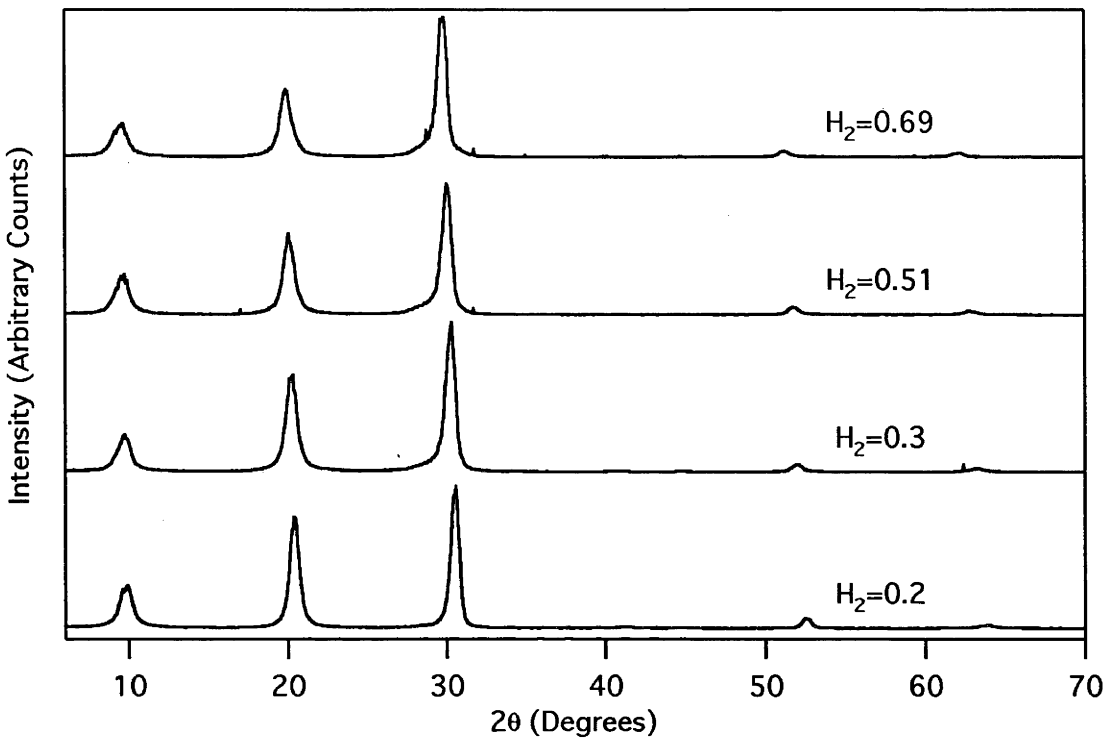

Figure 4.7.4: *the c-axis oriented x-ray diffraction patterns produced by a sample of $K(H_2)_xC_{25}$ at x=0.2, 0.3, 0.51 and 0.69. There is a steady expansion of c-axis spacing with hydrogen filling.*

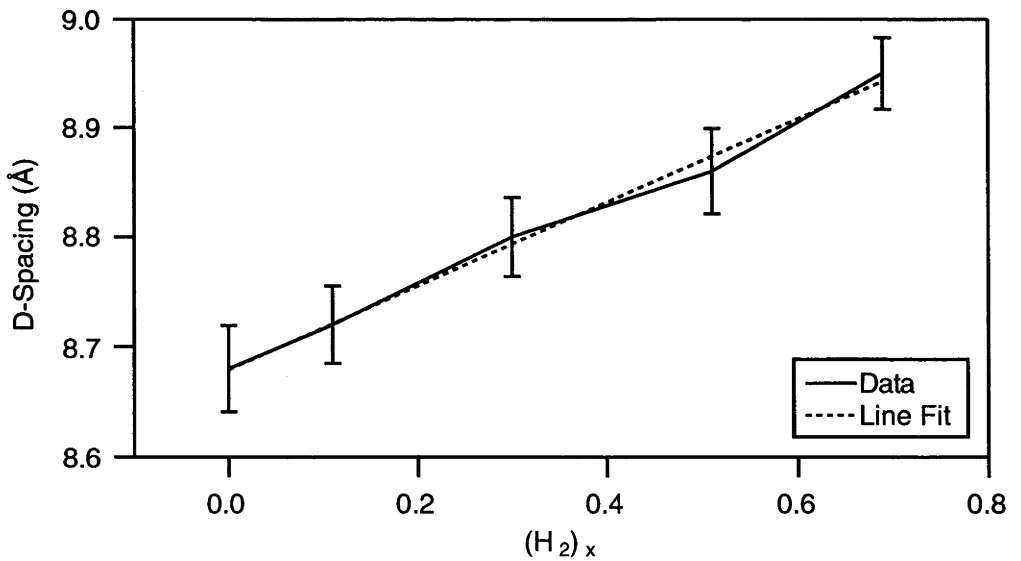

Figure 4.7.5: *the $K(H_2)_xC_{25}$ c-axis D-spacing found from the patterns in Figure 4.7.4 plotted against hydrogen filling x, showing a linear expansion with increasing hydrogen stoichiometry. A line of the form D=8.68+0.38x is fitted to the data. The error bars are determined from the standard deviation around the average c-axis d-spacing found from each peak in the pattern.*

The *c*-axis data (Figure 4.7.4) show no interesting features beyond an expansion of the interlayer distance with increasing filling, which follows Vegard's Law[12]. This is illustrated in Figure 4.7.5 and Table 4.7.3. The same linear approach to a maximum lattice spacing that was seen in the $Rb(H_2)_xC_{25}$ and $Rb(D_2)_xC_{25}$ *c*-axis patterns is seen here at the highest filling levels achieved.

$K(H_2)_xC_{25}$	D-spacing (Å)	Standard Deviation (Å)	(003) FWHM (Degrees)
0.11	8.72	0.04	0.66
0.3	8.80	0.04	0.78
0.51	8.86	0.04	0.75
0.69	8.95	0.03	0.77

Table 4.7.3: *The d-spacing and standard deviation of the c-axis oriented $K(H_2)_xC_{25}$ diffraction patterns shown in Figure 4.7.3 and as well as the full width at half maximum (in degrees) of the (003) peaks.*

4.7.2 Deuterium Absorption by KC_{25}

4.7.2.1 Data

The combined *ab*-plane diffraction patterns from the $K(D_2)_xC_{25}$ system is shown in Figure 4.7.6, for $0.14 < x < 0.68$, while the *c*-axis oriented data for the same stoichiometries are shown in Figure 4.7.8. The same sample of KC_{25} was used for both hydrogen and deuterium, and as with the hydrogen a stoichiometry greater than ~0.7 could not be achieved; unlike the hydrogen the potassium-deuterium-graphite system reached this limit at a much lower pressure over the sample.

4.7.2.2 *ab*-plane Results

Comparing Figure 4.7.1 and 4.75 it is clear that there is an overall similarity of behaviour in the hydrogen and deuterium systems. The KC_{25} binary structure is slowly eliminated as D_2 concentration increases, but by $(D_2)_{0.59}$ a new structure has appeared, with many low intensity peaks at low angles; by $(D_2)_{0.68}$ this new structure has diminished in intensity, while the peak at 17.38° has almost doubled in intensity. The low angle (6-36°) regions of these two patterns are shown in detail in Figure 4.7.6 and the peaks are listed in Tables 4.7.4 and 4.7.5

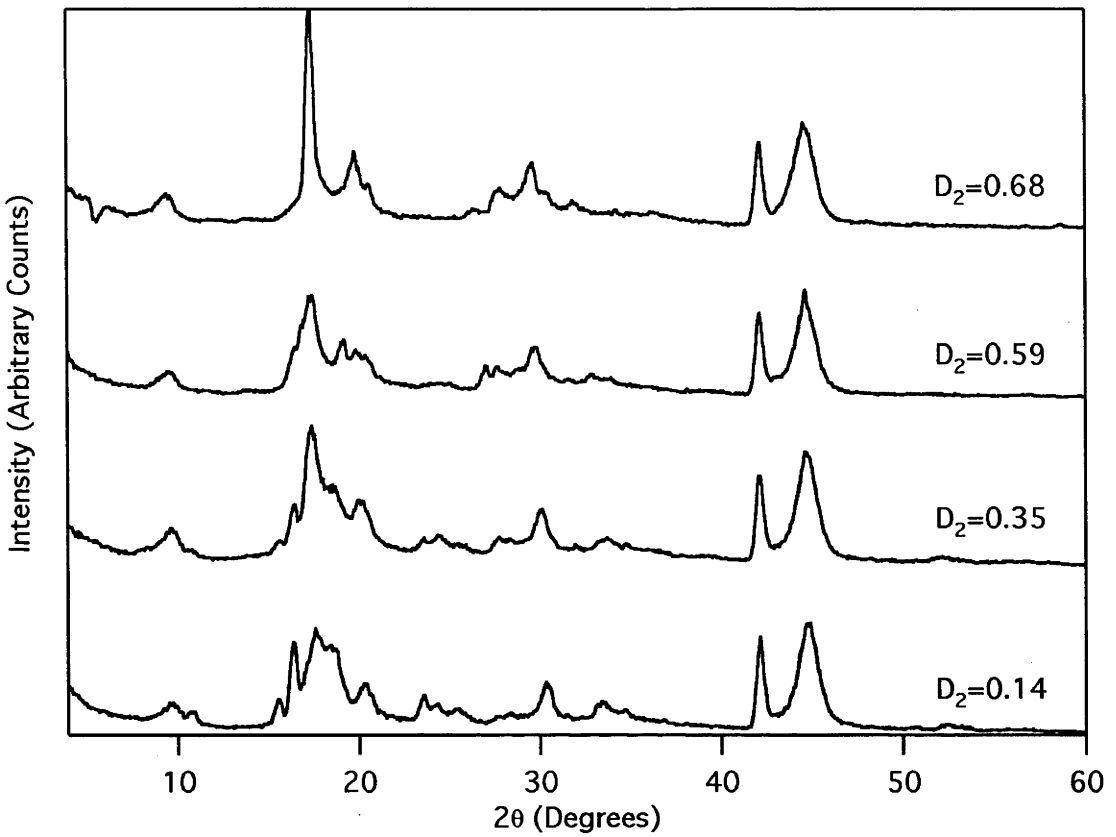

Figure 4.7.6: *the ab-plane oriented x-ray diffraction patterns produced by a sample of* $K(D_2)_xC_{25}$ *at x=0.14, 0.35, 0.59 and 0.68.*

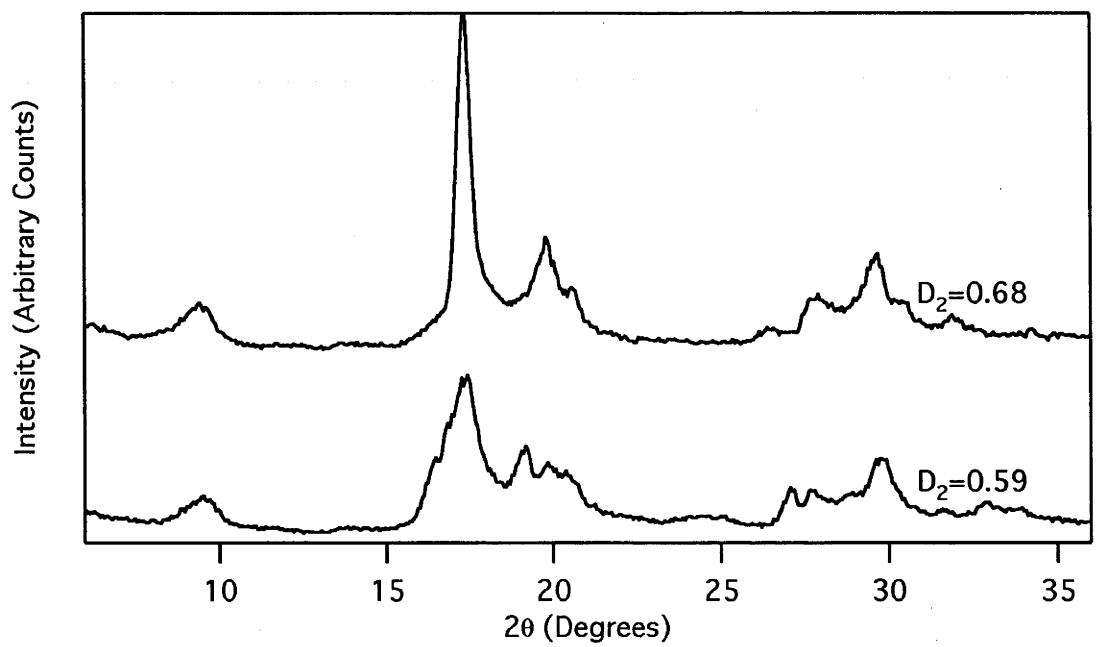

Figure 4.7.7: *the ab-plane oriented x-ray diffraction patterns produced by a sample of* $K(D_2)_xC_{25}$ *at x=0.59 and 0.68. A new pattern appears at* $K(D_2)_{0.59}C_{25}$ *pattern but alters significantly by* $K(H_2)_{0.68}C_{25}$.

2θ (Degrees)	Intensity (Counts)	D-spacing (Å)	Comments
9.52	1111	9.29	c - (001)
13.84	431	6.398	
17.44	3794	5.085	
19.18	2210	4.627	
19.84	1851	4.475	c - (002)
20.38	1663	4.357	
24.46	653	3.639	
27.1	1202	3.29	
27.7	1224	3.22	
28.84	1147	3.096	
29.8	1935	2.998	c - (003)
31.66	773	2.826	
32.92	963	2.721	
33.88	815	2.646	
42.1	3140	2.146	gr - (10)
44.62	3979	2.031	gr - (101)
56.92	265	1.618	
76.9	2021	1.24	gr - (11)
77.8	289	1.228	

Table 4.7.4: *the peaks of the ab-plane oriented* $K(H_2)_{0.59}C_{25}$ *diffraction pattern shown in Figures 4.7.5 and 4.7.6. The c-axis breakthroughs and graphite peaks are indicated in the comments column.*

The *ab*-plane data for the $K(D_2)_xC_{25}$ system have the same problem as those for the hydrogen system: the peaks of the new structures are very weak, and do not provide enough information to index a unit cell. The weak peaks of the new structures are not at the same 2θ position in the 0.59 and 0.68 patterns, implying that the weak structures are reorganising even at very small changes in stoichiometry. Apart from these qualitative observations, there is little useful data in the *ab*-plane results.

2θ (Degrees)	Intensity (Counts)	D-spacing (Å)	Comments
9.46	1335	9.349	c - (001)
13.66	512	6.482	
17.32	7933	5.12	
19.78	2878	4.488	c - (002)
20.56	1750	4.32	
26.5	799	3.363	
27.82	1495	3.207	
29.68	1495	3.01	c - (003)
30.34	1396	2.946	
31.9	1141	2.805	
36.28	744	2.476	
42.1	3197	2.146	gr - (10)
44.5	3914	2.036	gr - (101)
58.66	308	1.574	
60.46	294	1.531	
63.1	271	1.473	
76.96	2118	1.239	gr - (11)
77.8	432	1.228	

Table 4.7.5: *the peaks of the ab-plane oriented* $K(H_2)_{0.68}C_{25}$ *diffraction pattern shown in Figures 4.7.5 and 4.7.6. The c-axis breakthroughs and graphite peaks are indicated in the comments column.*

4.7.2.3 c-axis results

The $K(D_2)_xC_{25}$ *c*-axis data are shown in Figure 4.7.8 below. Reduced in Figure 4.7.9 and Table 4.7.6, they report a similar case to the hydrogen: a steady, linear expansion of the interlayer spacing of the GIC with the increase in deuterium filling.

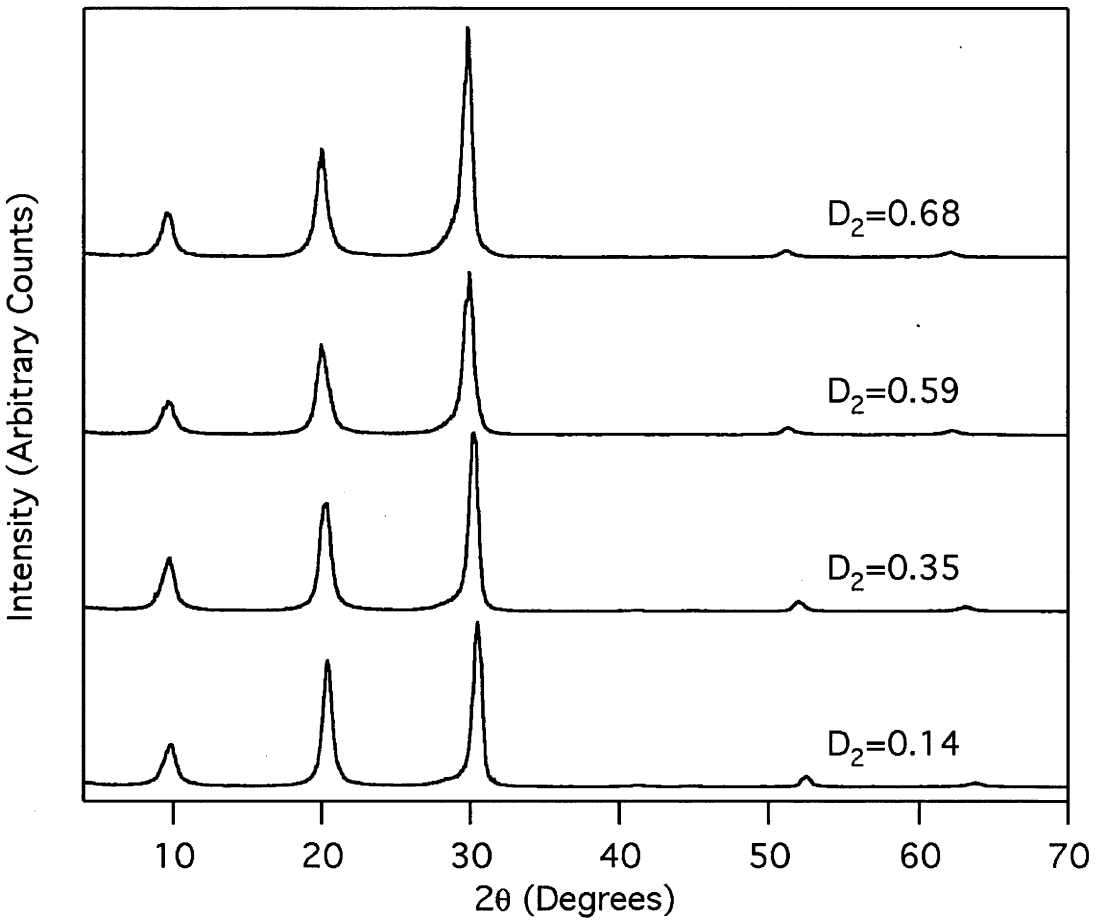

Figure 4.7.8: *the c-axis oriented x-ray diffraction patterns produced by a sample of $K(D_2)_xC_{25}$ at x=0.14, 0.35, 0.59 and 0.68. As with the hydrogen absorption, there is a steady expansion of c-axis spacing with deuterium filling.*

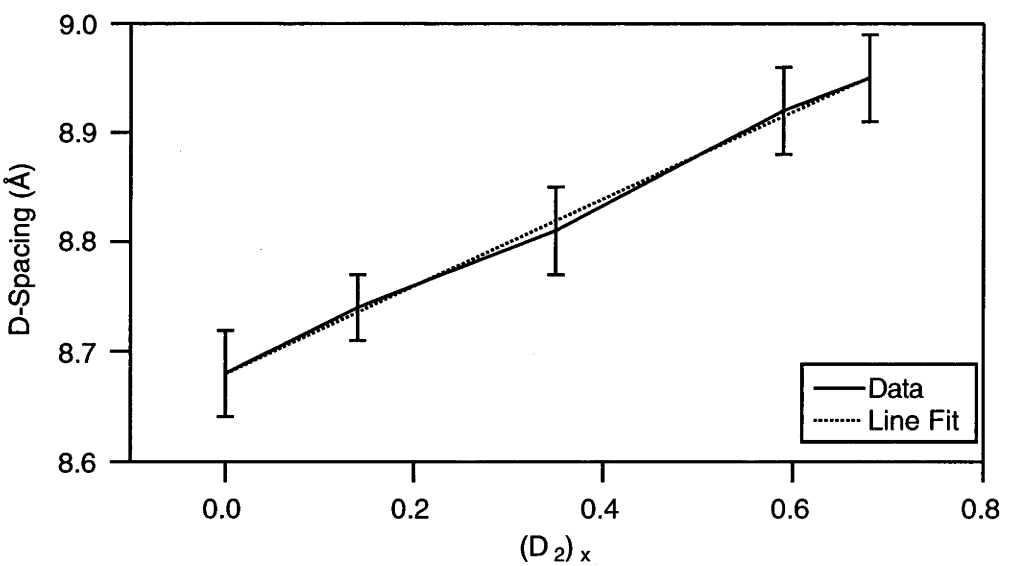

Figure 4.7.9: *a plot of the c-axis d-spacing determined from the $K(D_2)_xC_{25}$ c-axis data in Figure 4.7.8 versus the deuterium filling x, showing a linear expansion with filling. A line of the form D=8.68+0.40x is fitted to the data.*

$K(D_2)_xC_{25}$	D-spacing (Å)	Standard Deviation (Å)	(003) FWHM (Degrees)
0.14	8.74	0.03	0.74
0.35	8.81	0.04	0.77
0.59	8.92	0.04	0.85
0.68	8.95	0.04	0.77

Table 4.7.6: *The d-spacing and standard deviation of the c-axis oriented $K(D_2)_xC_{25}$ diffraction patterns shown in Figure 4.7.8 and as well as the full width at half maximum (in degrees) of the (003) peaks.*

4.7.3 Conclusion

Both the $K(H_2)_xC_{25}$ or $K(D_2)_xC_{25}$ ternary graphite intercalation compounds could only reach a maximum stoichiometry of x=~0.7, much less than the published saturation value of x=2.1. While the is evidence of a new ab-plane structure at this maximum, neither system provided diffraction data that could produce an indexed *ab*-plane unit cell in the regime studied; the c-axis data in both cases showed a linear expansion in interlayer spacing as x increased.

References

1. K. Watanabe, T. Kondow, M. Soma, T. Onishi, and K. Tamaru, *Molecular-sieve type sorption on alkali graphite intercalation compounds.* Proceedings of the Royal Society of London A, 1973. **333**: p. 51-67.

2. K. Ichimura and E. Takamura, *Hydrogen in alkali-metal-graphite intercalation compounds.* Synthetic Metals, 1991. **40**: p. 355-368.

3. N. Akuzawa, K. Katano, Y. Ohmura, T. Konishi, T. Amemiya, T. Terai, and Y. Takahashi, *Application of Alkali Metal-Graphite Intercalation Compounds to Cryosorption Material for Hydrogen Isotopes.* Tanso, 1988. **133**: p. 100-104.

4. N. Akuzawa, T. Sakamoto, H. Fujimoto, T. Kasuu, and Y. Takahashi, *Hydrogen physisorption by potassium-graphite intercalation compounds prepared from mesocarbon microbeads.* Synthetic Metals, 1995. **73**: p. 41-44.

5. T. Enoki, S. Miyajima, M. Sano, and H. Inokuchi, *Hydrogen-alkali-metal-graphite ternary intercalation compounds.* Journal of Materials Research, 1990. **5**(2): p. 435-465.

6. P. Lagrange, A. Metrot, and A. Herold, *Physisorption de l'hydrogene sur le compose KC_{24}.* Comptes Rendus de l'Academie des Sciences Paris, Serie C, 1972. **275**: p. 765-767.

7. P. Lagrange and A. Herold, *Physisorption de l'hydrogene par les produits d'insertion du potassium dans les carbones imparfaitement organises.* Comptes Rendus de l'Academie des Sciences Paris, Serie C, 1975. **281**: p. 381-384.

8. P. Lagrange, M.-H. Portmann, and A. Herold, *Physisorption selective du protium et du deuterium par le compose d'insertion KC_{24}.* Comptes Rendus de l'Academie des Sciences Paris, Serie C, 1976. **283**: p. 511-514.

9. T. Terai and Y. Takahashi, *Sorption of hydrogen isotopes on potassium-carbon intercalation compounds at low temperatures.* Synthetic Metals, 1983. **7**: p. 49-55.

10. T. Terai and Y. Takahashi, *Sorption behaviour of hydrogen gas and tritiated hydrogen gas on potassium-carbon intercalation compounds.* Carbon, 1984. **22**(1): p. 91-95.

11. T. Terai and Y. Takahashi, *Storage and isotope separation of hydrogen by alkali metal-graphite intercalation compounds.* Material Science Forum, 1992. **91-93**: p. 839-848.

12. L. Vegard, *The constitution of mixed crystals and the space occupied by crystals.* Z. Physik, 1921. **5**: p. 17-26.

Chapter 5: Discussion

5.1 Introduction

The work described in this thesis shows the response of the two-dimensional alkali ion lattice of binary GICs to sorption of molecules of different size, polarity and shape. Molecular dynamics simulations and neutron inelastic scattering studies of second and higher stage alkali-metal GICs show that the ionic lattice at room temperature is a highly modulated liquid[1]. The diffraction patterns at these temperatures show a liquid-like structure with a strong six-fold modulation as result of the graphite lattice.

The response of the ionic lattice to molecular absorption is differentiation into separate phases for all molecules examined except the hydrogen and deuterium at low concentration. We broadly classify the response of the ternary compounds into the categories of (a) formation of a solid solution and (b) disproportionation. The first behaviour is seen only in the rubidium-hydrogen and -deuterium systems for $x<1.0$; in all other systems, and in hydrogen and deuterium above $x=1.0$, the system phase separates. It is quite surprising that at temperatures as low as 90 K the two dimensional alkali metal lattice is reconstructed by argon or even by the higher concentrations of hydrogen. This temperature is well below the in-plane ordering phase transition (at 228 K for CsC_{24}, 165 K for RbC_{24} and 125 K for KC_{24})[1]. Here the ionic lattice might be expected to be rigid - both on the grounds of its commensurability and the indications of the strong temperature dependence in the ionic diffusion coefficient from molecular dynamics. The reconstruction observed here suggests that specific interactions between the adsorbed molecules and the ionic environment are strong. There have been simulations of these interaction potentials only for methane in CsC_{28} and a typical potential for a $\sqrt{7}x\sqrt{7}$ cesium lattice is shown in Figure 5.1[2]. The potential shows favoured sites for the molecular adsorption. Given the space available the probability is that only one site between the ions is occupied, which then suggests a high likelihood of positional disorder at elevated temperatures.

Another general point revealed by the present studies is that whereas for some adsorbed molecules - such as $Rb(H_2)_{<1.0}C_{25}$ - random filling of the alkali ionic lattice seems a proper description, in others such as $Rb(Ar)_{1.2}C_{25}$ there is a disproportionation of the two dimensional structure into separate phases. In the ensuing discussion we summarise the structural responses found by x-ray diffraction and look at the site structure for $Rb(H_2)_xC_{25}$ with the even finer focus provided by the molecular tunnelling spectra produced by inelastic neutron scattering experiments.

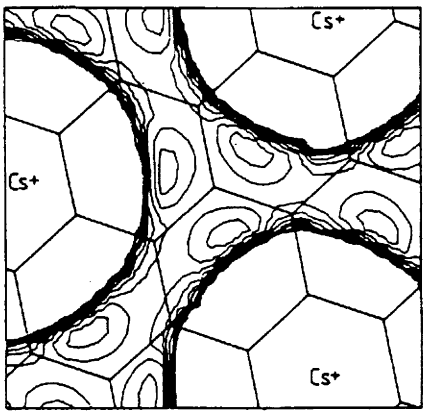

Figure 5.1: a contour map (1 kJ mol^{-1} intervals) of the rotationally minimised potential energy of a methane molecule in a √7x√7 lattice of cesium ions. Reproduced from Trouw and White[2].

5.2 Varieties of Response

As a first step for this work it was necessary to ensure that the structure of the binary materials matched that reported and so the diffraction patterns for RbC_{25} and KC_{25} were studied. The observed *ab*-plane patterns were consistent with previous studies[1, 3, 4]. However it was found that the (00*l*) diffraction peaks of both compounds showed the shift away from the average d-spacing characteristic of an interstratified structure[5, 6]. Analysis showed that both were approximately 10% stage 3 GIC, an effect also noted in the *c*-axis data collected from all the ternary derivatives of these compounds.

5.2.1 Disproportionation Response

Absorption of argon lead to the immediate appearance of a new diffraction pattern for all stoichiometries of $RbAr_xC_{25}$. There was no sign of an intermediate phase between the √43x√43 structure of RbC_{25} and the final diffraction pattern produced by the saturated ternary. A two-phase structural model composed of a 2x2 P6 cell with stoichiometry RbC_{16} and a √7x√7 P6 cell with stoichiometry $RbAr_2C_{28}$ produced a very good fit to the *ab*-plane diffraction pattern, with the Ar atoms occupying the threefold axis at (1/3, 2/3) in the hexagonal cell. The *c*-axis data were more equivocal, with a very strong expanded phase and a much weaker second phase with the same *c*-axis spacing as the binary GIC.

As with rubidium-argon-graphite, no intermediate phase was observed between the RbC_{25} structure and that of the saturated ternary of $Rb(CH_4)_xC_{25}$. The *ab*-plane patterns beneath 120 K were indexed using the same 2x2 and √7x√7 two phase model

employed for the rubidium-argon-graphite system. This produced a good fit to the data, predicting stoichiometries of RbC_{16} and $Rb(CH_4)_2C_{28}$ respectively. The methane molecule occupies the (1/3, 2/3) position in the $\sqrt{7}x\sqrt{7}$ cell, but the orientation of the molecule could not be determined by the *ab*-plane data. The *c*-axis data were indexed and modelled as a single expanded phase, with no evidence of a second phase.

Again, with $K(N_2)_xC_{25}$ no intermediate phases were seen, the diffraction pattern of the saturated ternary compound directly replacing that of the binary GIC. The *ab*-plane data at 90 K was fitted to a two phase system consisting of a 2x2 P6 cell of stoichiometry KC_{16} and 3x3 P6 cell of stoichiometry $K(N_2)_{1.0}C_{36}$. It was found that the nitrogen molecules occupy the twofold site at (0,1/2) in the 3x3 lattice, with the long axis of the molecule oriented towards the nearest K^+ ions and parallel to the graphene layers. The *c*-axis data showed two clearly distinguishable phases, both stage-2, one with an expanded *c*-axis dimension and the other with a compressed spacing compared to the binary GIC.

$Rb(N_2)_xC_{25}$ behaved in a similar manner to the other large molecule ternary GICs, with no intermediate phases between the binary and saturated ternary compound being observed. A structural phase transition took place as the ternary compound was cooled from 160 K to 120 K, with the weak reflections of a possibly incommensurate structure appearing at the lower temperature. The *ab*-plane data at 160 K could not be completely indexed on any commensurate cell, but the 2x2 P6 phase observed in all the previous systems was present, with the same stoichiometry of RbC_{16}. The remaining reflections could not be indexed, due to the small number of observable peaks. The *c*-axis data showed only a single expanded phase.

5.2.2 Solid Solutions and Disproportionation Response

This type of response was exhibited by both the rubidium-hydrogen and deuterium hydrogen GICs. Upon absorption, the *ab*-plane structure of RbC_{25} was slowly eliminated as filling increased, producing a diffraction pattern similar to the high temperature liquid-like phase of RbC_{25}. The response at these fillings was thus that of a solid solution formation. At approximately $Rb(H_2)_{1.0}C_{25}$, a rapid phase transition took place, with the appearance of several new diffraction peaks, which were attributed to the appearance of two new phases of lower than hexagonal symmetry; as filling increased to saturation at $(H_2)_{1.8}$, these new peaks steadily reduced in intensity, accompanied by an increase in intensity of the liquid-like primary diffraction peak. The *c*-axis data of both compounds showed a steady expansion of the lattice with filling, and with no evidence of multiple *c*-axis phases.

The potassium GICs $K(H_2)_xC_{25}$ and $K(D_2)_xC_{25}$ behaved in a similar manner: absorption replaced the *ab*-plane structure of the binary with a less well ordered structure, and again there was some sign of phase transitions at the higher fillings, but the new peaks were sufficiently weak that no quantitative results could be found. The *c*-axis data again showed steady expansion of a single phase system.

	K	Rb	Radius (Å)
Ar	-	P6 2x2 & $\sqrt{7}$x$\sqrt{7}$	1.91
CH_4	-	P6 2x2 & $\sqrt{7}$x$\sqrt{7}$	2.0
N_2	P6 2x2 & 3x3	P6 2x2 & unknown	1.5
H_2/D_2	interstitial soln.	interstitial soln & phase trans at x~1.0	1.2

Table 5.1: *the proposed structures of the ternary compounds found in these studies, compared with the effective spherical van der Waals radius of the physisorbed species*[7]*. The "large-molecule" ternaries, based on argon, methane or nitrogen, behave in a different manner to those composed of hydrogen or deuterium.*

The structural models proposed can be divided into at least two groups. In the first group, comprising the rubidium-argon, rubidium-methane, rubidium-nitrogen and potassium-nitrogen ternary GICs, absorption of the ternary gas is accompanied by immediate separation of the compound into two phases, an expanded phase containing all the ternary guest and a compressed binary phase. In the second group, comprising the hydrogen and deuterium ternary GICs of both alkali metals, absorption at first appears to produce an interstitial solution, which has the effect of breaking up the structure of the alkali metal ionic lattice into a less-ordered or even a liquid-like structure. In the rubidium-hydrogen-GICs, a transition to a more ordered structure takes place near a stoichiometry of $Rb(H_2)_{1.0}C_{25}$, but the behaviour of the potassium-hydrogen-GIC systems could not be determined. These models are summarised in Table 5.1.

One can make an alternative classification with three separate groups of structural models. This would keep that same two observed groups described above but would separate the potassium-nitrogen-graphite system from the other large-molecule ternary GICs, to be considered to be exhibiting a third type of behaviour. This is based on the observed separation of the *c*-axis structures into two separate large-scale phases upon absorption in the $K(N_2)_{0.7}C_{25}$ system, at the same time as the *ab*-plane structure

separates into the 2x2 and 3x3 phases. Thus the observed behaviour could be delineated as:

a) *ab*-plane and *c*-axis disproportionation, only observed in the $K(N_2)_{0.7}C_{25}$ system;

b) *ab*-plane disproportionation without c-axis phase separation, seen in all the large molecule ternary GICs ;

c) interstitial solid solution followed by a phase transition at higher filling, seen in the hydrogen and deuterium ternary GICs.

Which is the correct classification is a matter for further work: the nature of the *c*-axis structure of the rubidium-argon and rubidium-methane GICs is unclear, and this will be described in more detail below.

It is apparent that the phase change is driven by the availability of space within the ionic lattice for the new molecules. The response may be compared to the "universal curve" of Mori et al[8], described in Chapter 1, where the observed ionic lattices of the binary alkali-metal GICs are seen to fall on a curve connecting the 2x2 and $\sqrt{7}x\sqrt{7}$ superlattices, with the larger ions adopting a lattice nearer to the $\sqrt{7}x\sqrt{7}$ phase. For the larger molecules, the immediate response is to disproportionate to the two extremes (or beyond for the potassium-nitrogen ternary GIC) of the universal curve, at 2x2 and $\sqrt{7}x\sqrt{7}$. For the hydrogen and deuterium ternaries, the first response seems to be a movement along the curve at low fillings, until the compound separates into incommensurate phases that lie near the curve; as filling continues, the bulk compound returns to a position on the universal curve.

5.3: $Rb(Ar)_xC_{25}$, $Rb(CH_4)_xC_{25}$, $K(N_2)_xC_{25}$, $Rb(N_2)C_{25}$: The "Large Molecule" Ternary GICs:

The first three of these compounds are those whose entire *ab*-plane structures could be determined from the data and completely modelled with the techniques used. The Rb-N_2 GIC clearly behaves in a related manner, though the structure of the expanded phase could not be fully determined. We can make several observations from these structures

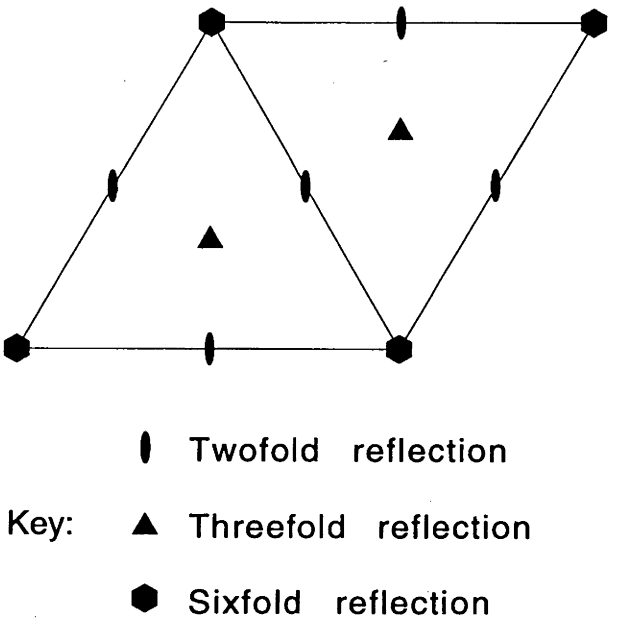

Figure 5.2: *the symmetry of the reflection points of a P6 plane cell. In the rubidium-argon and rubidium-methane GICs, the ternary guests are occupying the threefold site in the √7x√7 cell; in potassium-nitrogen the molecule occupies the twofold site of a 3x3 cell.*

The site occupied by the physisorbed guest appears to be determined as much by the electric moments of the molecule adsorbed as by available space. For argon and methane, which have no inherent dipole or quadrupole moments, the site is the threefold reflection point at (1/3, 2/3), while the nitrogen molecule, which has no dipole moment but does possess a quadrupole moment[9] of -4.67×10^{-40} Cm^2, occupies the twofold site at (1/2, 0), with the long axis of the molecule oriented towards the nearby rubidium ion. This would appear to be a result of the crystal field at each site: the argon and methane, with no quadrupole moment, occupy the site with the highest symmetry, while the nitrogen molecule, which possesses a quadrupole moment adopts a site with a quadrupole crystal field, between two potassium ions. The structural simulations found that the nitrogen molecule was parallel to the graphene layers, though a small deviation in angle (<30°) would be unlikely to be discovered by this technique.

	$RbAr_xC_{25}$	$Rb(CH_4)_xC_{25}$	$K(N_2)_xC_{25}$
Expanded Phase	294 Å	196 Å	186 Å
2x2 Phase	297 Å	198 Å	198 Å

Table 5.2: *The ab-plane crystal domain sizes determined from the profile fits described in Chapter 4.2-4.5 for the two phases present in each of the ternary compounds shown.*

The calculated in-plane domain size of the *ab*-plane crystallites, shown in Table 5.2, is effectively identical for each of the two phases present in the all three of the ternary GICs. However, the $K(N_2)_xC_{25}$ compound is differentiated from the others in that the c-axis data shows very clearly the appearance of a second separate compressed phase; evidence for such a phase is weak for $RbAr_xC_{25}$ and non-existent for $Rb(CH_4)_xC_{25}$. For the rubidium-nitrogen compound the size of the *ab*-plane crystallite of the expanded phase could not be found, but from observed peak widths it would appear to be considerably smaller than the 2x2 phase seen in the same patterns. The potassium-nitrogen compound also shows clear evidence of 3D ordering in the profile shape produced by its 2x2 phase; an alternate fit to the $RbAr_xC_{25}$ 2x2 phase system may be showing some 3D ordering - and as a result a smaller in-plane crystallite size - as well.

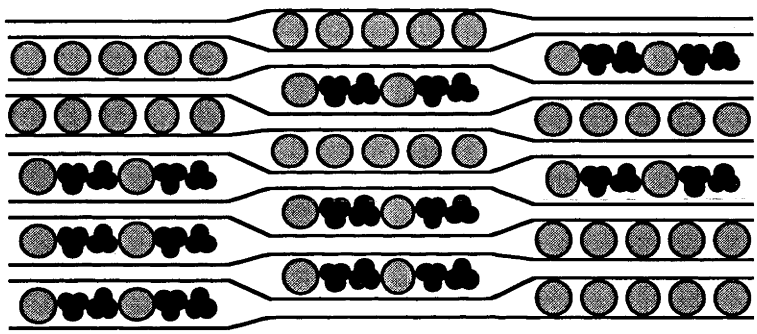

Figure 5.3: *a possible c-axis structure of $Rb(CH_4)_{0.9}C_{25}$: a random interstratification of the 2x2 P6 RbC_{16} phase and the $\sqrt{7}x\sqrt{7}$ P6 $Rb(CH_4)_2C_{28}$ phase.*

A possible explanation for the similarity in the domain sizes is that though the compounds have separated into two phases the structure is composed of the "pleated-layers" described by Daumas and Herold (see Chapter 1). This effect of this is shown in Figure 5.3: the curvature of the graphene layers at borders of each domain restricts the maximum size of any *ab*-plane crystallites, even though the each layer may be occupied by a different phase.

5.3.1 Interstratification

The peak shapes described above are evidence showing the nature of the c-axis stacking of the two different phases varies between the compounds. The potassium system has ordered into completely separate phases in both the *c*-axis and *ab*-planes. For the rubidium-methane compound the situation is unclear. It is possible that it consists of a randomly interstratified compound, as shown in Figure 5.3,. The lack of a strongly identifiable *c*-axis phase corresponding to the RbC_{16} 2x2 phase in the argon

and methane systems is one of the two major problems with the two-phase model for these compounds; a possible explanation invokes the contamination of the original stage 2 RbC_{25} samples by stage 3 GIC.

That a lamellar compound is formed by the interstratification of two different layer structures is indicated when the (00*l*) peaks are found at non-integral values of *l*[5]. This behaviour was observed in the diffraction patterns produced by the binary compounds RbC_{25} and KC_{25}, as described in section 4.1, and attributed to the presence of approximately 10% of the compound as a stage 3 intercalate. The presence of interstratification in the original compounds makes it hard to detect if there is a further interstratification of the $\sqrt{7}x\sqrt{7}$ and 2x2 domains in the ternary compounds derived from them, and it is very difficult to model the diffraction pattern of a system of more than two interstratified layers[5]. An additional problem with the argon *c*-axis data (section 4.2) is that there are only three observed peaks for each two phases identified. However, the $Rb(CH_4)_{0.9}C_{25}$ compound produced a *c*-axis pattern (section 4.3) with six observed peaks, while the two phases of the $K(N_2)_{0.7}C_{25}$ *c*-axis pattern produced five identifiable peaks for the expanded phase and seven for the compressed.

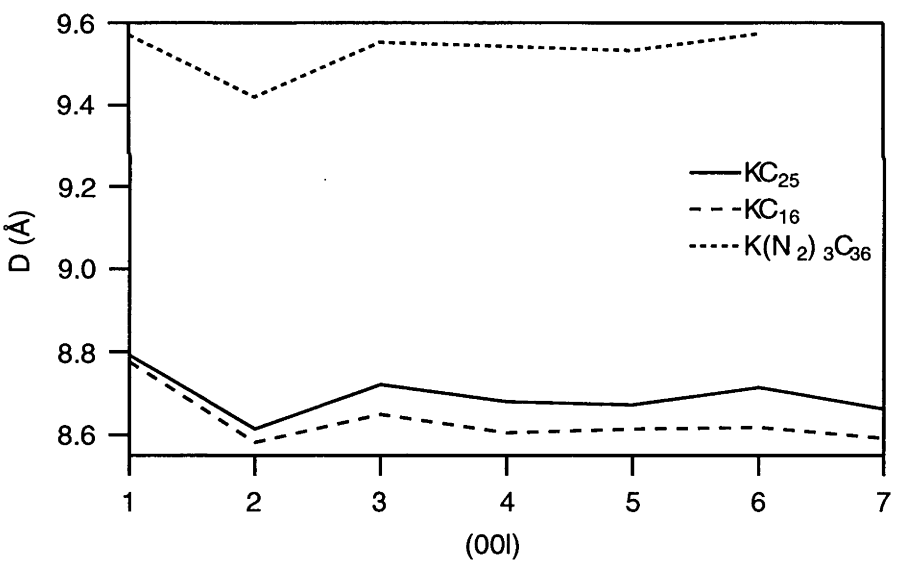

Figure 5.4: *the d-spacing calculated from the (00l) peaks in the KC_{25} c-axis pattern and the two phases of its nitrogen ternary. The shifts away from the average d are similar for all three series.*

The *c*-axis d-spacing calculated from each of the (00l) peaks in these patterns are shown in Figures 5.4 and 5.5. There is no significant change in the direction or magnitude of the shifts. For the potassium compound, this is not surprising, since the final product consists of two separated bulk phases, and they would each be expected to carry the effect of the stage 3 interstratification into their derived diffraction patterns.

With the methane, where only one c-axis spacing is visible, then if there is new interstratification of the compressed and the expanded phases, the effect is masked by the effect of the stage 3 contamination. The difference in spacing between a stage 2 and stage 3 intercalate is 3.35 Å, and as such is much larger that the ~0.8 Å difference in c-axis spacing expected between the ternary and binary phases of the $Rb(CH_4)_{0.9}C_{25}$ compound. The effect of the original 10% stage 3 interstratification, if preserved into the ternary compounds, would thus be expected to be greater in the *c*-axis diffraction patterns than that of the two phases of the final product.

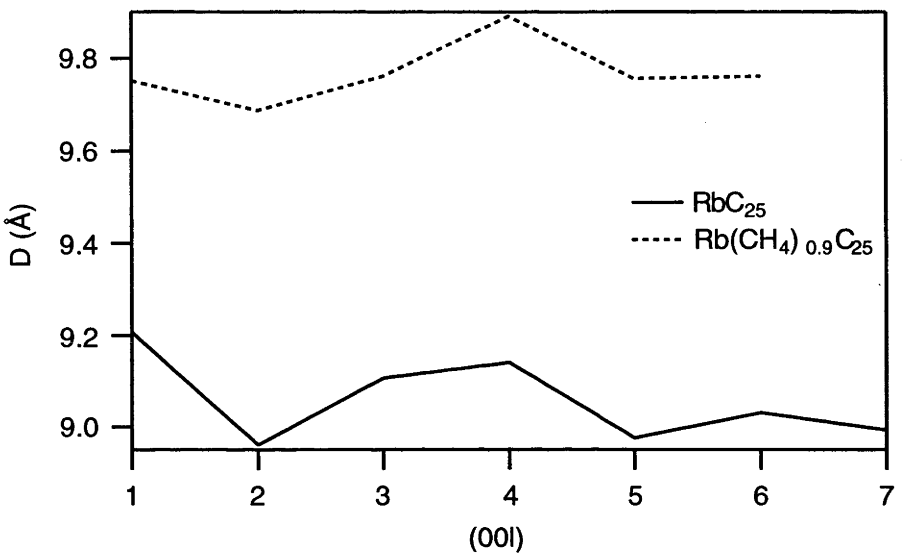

***Figure 5.5** the d-spacing calculated from the (00l) series of RbC_{25} and $Rb(CH_4)_{0.9}C_{25}$. The peak shifts away from the average in the ternary compound are not significantly different in direction or magnitude from those of the binary GIC.*

5.3.2 Stoichiometry and Structure

The second major problem with the two phase model for these compounds concerns the stoichiometry of the reaction. For the rubidium-argon compound the reaction may be described as:

$$x(Ar) + RbC_{25} \rightarrow y[Rb(Ar)_2C_{28}] + (1-y)[RbC_{16}]$$

The problem is that the disproportionation of RbC_{25} into RbC_{28} (the $\sqrt{7}x\sqrt{7}$ phase) and RbC_{16} (the 2x2 phase) sets the value of y = 0.75 in order to keep the ratio of Rb:C as 1:25. Given this value of y, this should set x = 2y = 1.5, but the measured value of x from gas uptake is 1.2. The same argument applies to the rubidium-methane-graphite system, which also separates into $Rb(CH_4)_2C_{28}$ and RbC_{16} phases; the measured value

of x from gas uptake is 1.0. In the case of the potassium-nitrogen system, the reaction is:

$$x(N2) + KC_{25} \rightarrow y[K(N_2)_3C_{36}] + (1-y)[KC_{16}]$$

Here the K:C ratio of 1:25 requires that y = 0.45, which would set x = 3y = 1.35. The measured uptake of nitrogen is ~0.7. The stoichiometry of the rubidium-nitrogen *ab*-plane expanded phase is unknown, along with its structure, but if the nitrogen molecules in the rubidium system are occupying the same position between rubidium ions as it does in the potassium 3x3 lattice, then the Rb:N_2 ratio would be between 1:2 and 1:3 for any *ab*-plane unit cell, depending on whether a nitrogen molecule is occupying the (1/2,1/2) site.

This misfit between the measured gas uptake and the stoichiometry of the observed structures implies that the structural model is incomplete. One possibility is that the absorbed gas is not filling all of the available sites in the expanded $\sqrt{7}x\sqrt{7}$ or 3x3 lattice, but is forming an interstitial lattice gas with random occupancy of the vacancies, with an 80% site occupancy in the rubidium-argon, 60% in the rubidium-methane, 50% in the potassium-nitrogen, and an unknown but probably similar value in the rubidium-nitrogen ternary GICs. Another explanation is that a large proportion of the *ab*-plane structure of the sample remains in a disordered state after absorption, with insufficient order to produce a crystalline diffraction pattern. Neither of these explanations are entirely satisfying: the intensities of the simulated *ab*-plane diffraction produced good matches with the observed intensities when a 100% site occupancy was assumed; a disordered ab-plane structure would be assumed to produce a large liquid-like diffraction peak at ~17°, as it does in the RbC_{25} and KC_{25} intercalates above the ordering transitions, and these peaks are not observed.

While these problems remain unsolved, the two-phase model for the rubidium-argon, rubidium-methane and potassium-nitrogen system accurately reproduces the intensities and positions of the observed diffraction peaks, and is the only model we have which does so.

5.4: The Hydrogen and Deuterium Ternary GICs

These two compounds exhibited behaviour radically different from that of the "large-molecule" ternary GICs, with the *ab*-plane diffraction patterns showing a steady elimination of the binary ionic lattice and then a very rapid transition to a new phase at an H_2:Rb ratio near 1.0, a phase that is slowly eliminated as the hydrogen doping is

increased. While the structures of the new phase or phases could not be determined from the diffraction data, a qualitative analysis implied the presence of two new phases, neither of which are commensurate with the graphite lattice.

The solid solution observed for $(H_2)_{<1.0}$ may be compared to the substitutional alkali-metal ternary GICs formed by a mixture of two heavy alkali metal ions in the interlayer galleries, as described in Chapter 1. The hydrogen molecules occupy random interstitial sites in the alkali lattice, as reported from neutron studies of oriented samples of rubidium-deuterium-graphite for low concentrations of deuterium[10]. Previous studies of hydrogen absorption in this system have assumed that the absorption of the hydrogen takes place without any alteration of the *ab*-plane lattice, with the H_2 molecules entering available sites within an assumed $\sqrt{7}x\sqrt{7}$ or $\sqrt{43}x\sqrt{43}$ superlattice[10, 11]. Clearly this assumption is invalid; the hydrogen molecules are randomly occupying sites in a lattice which is reconstructed by this action. If the behaviour seen in the other physisorbed molecules is repeated with the hydrogen system, the sites that are occupied would be determined by the native electric moments of the H_2 molecule. The quadrupole moments are reported as being $2.17x10^{-40}$ Cm^2 for H_2 and $2.14x10^{-40}$ Cm^2 for D_2, as compared with the $-4.67x10^{-40}$ Cm^2 for nitrogen. The charge distributions are shown in Figure 5.6

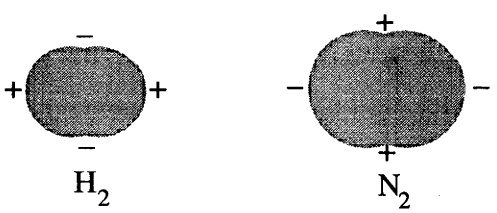

Figure 5.6: *the signs of the quadrupole moments for the hydrogen and nitrogen molecules.*

Given that the quadrupole moment of the hydrogen molecule is the opposite sign to that of nitrogen, if it is occupying the same site at (1/2,0) one might expect it to adopt the opposite orientation, with the axis of the molecule perpendicular to the line connecting the ionic centres. If however it is occupying the threefold site, the orientation would be vertical or random. These two options are shown as A and B in Figure 5.7, for a hexagonal cell of rubidium ions with a cell dimension of 6 Å, which is the average spacing in the liquid like structure of the ions observed before the phase transition near $(H_2)_{1.0}$.

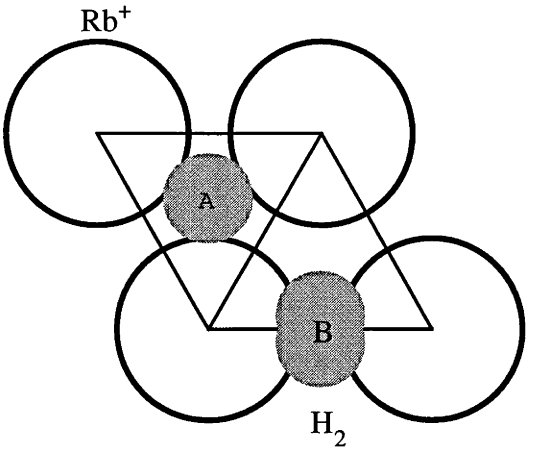

Figure 5.7: *two sites available to the hydrogen molecule in a hexagonal rubidium ionic lattice, A) the threefold site occupied by argon and methane in* $RbAr_2C_{28}$ *and* $Rb(CH_4)_2C_{28}$*, B) the twofold site occupied by nitrogen in* $K(N_2)_3C_{36}$*. The evidence from neutron scattering studies is that the threefold site is occupied by* H_2 *at low fillings.*

While from the quadrupole moment one might expect the hydrogen to adopt the twofold site, neutron scattering studies of aligned samples of $Rb(D_2)_xC_{24}$ for low values of x show that the molecule appears to be occupying the threefold site. Unfortunately the x-ray data presented here cannot determine the position of the hydrogen molecules due to its low scattering factor. It will be noted that the phase transition took place near $(H_2)_{1.0}$; below this stoichiometry the hydrogen molecule can decorate the lattice without needing to fill adjacent sites. As a result there can be at most one molecule per unit cell of rubidium. Thus it is a reasonable assumption that whichever site the H_2 is occupying the phase change is driven by the occupation of adjacent sites, with the phase transition resulting in a new hydrogen as well as rubidium packing.

The qualitative analysis of the hydrogen-rubidium XRD data (section 4.6), came to the conclusion that the system separated into two new phases near x=1.0, primarily on the grounds that two entirely different peak profiles were observed in the new diffraction pattern. It could not rule out that only a single phase is responsible for the diffraction peaks. A test of this analysis can be attempted using previously published[12] inelastic neutron scattering data from the same compounds. This technique measures the hindered rotational tunnelling of the hydrogen molecule, and is a very sensitive probe of the immediate environment of the absorbed hydrogen molecule. It complements the diffraction data, which measures the crystal structure over a large scale, and thus only detects the structures with a significant crystal size, while

inelastic neutron scattering probes short range structure. It is thus possible that the inelastic tunnelling spectra may show a tunnelling peak that does not appear to be associated with a crystal structure, if the absorption site which produces the tunnelling data is not part of a crystalline lattice.

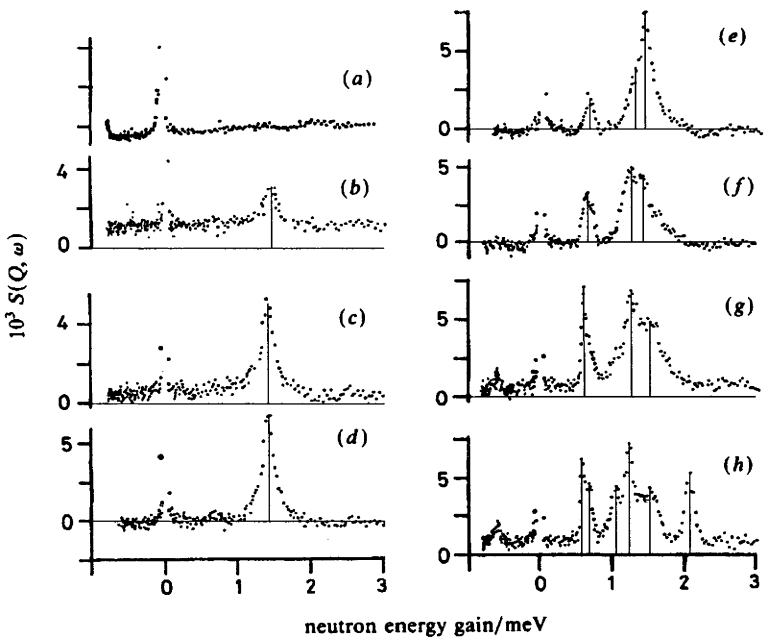

Figure 5.8: *a new interpretation of the peak positions and intensities from the hydrogen tunnelling in RbC_{25} data published by Stead et al. The stoichiometries are: a) RbC_{25}, b) $Rb(H_2)_{0.3}C_{25}$, c) $Rb(H_2)_{0.59}C_{25}$, d) $Rb(H_2)_{0.89}C_{25}$, e) $Rb(H_2)_{1.19}C_{25}$, f) $Rb(H_2)_{1.48}C_{25}$, g) $Rb(H_2)_{1.78}C_{25}$, h) $Rb(H_2)_{2.00}C_{25}$ Two new peaks appear in the tunnelling data at the same stoichiometry that new reflections appear in the diffraction data.*

The tunnelling data from Stead et al[12] are shown in Figure 5.8, with a new interpretation of the peak positions: a single tunnelling peak at ~1.45 meV appears on absorption and remains throughout the experiment; two more peaks at ~0.7 meV and ~1.3 meV appear between $(H_2)_{0.89}$ and $(H_2)_{1.19}$ and also endure; and at saturation three more peaks appear. These results are tabulated in Table 5.3 and plotted graphically in Figure 5.9.

$(H_2)_x$	Tunnelling Energy (meV)	Intensity ($x10^3$ n/s)	$(H_2)_x$	Tunnelling Energy (meV)	Intensity ($x10^3$ n/s)
0.30	1.49	3.10		0.62	7.21
0.59	1.43	5.08	1.78	1.27	6.96
0.89	1.43	6.90		1.53	4.88
	0.72	1.85		0.58	6.15
1.19	1.35	3.79		0.69	4.55
	1.48	7.34	2.00	1.05	4.39
	0.68	3.23		1.24	7.17
1.48	1.29	4.96		1.52	4.34
	1.44	4.43		2.08	5.29

Table 5.3: *the peak positions and intensities for the new interpretation of the hydrogen tunnelling data shown in Figure 5.5.*

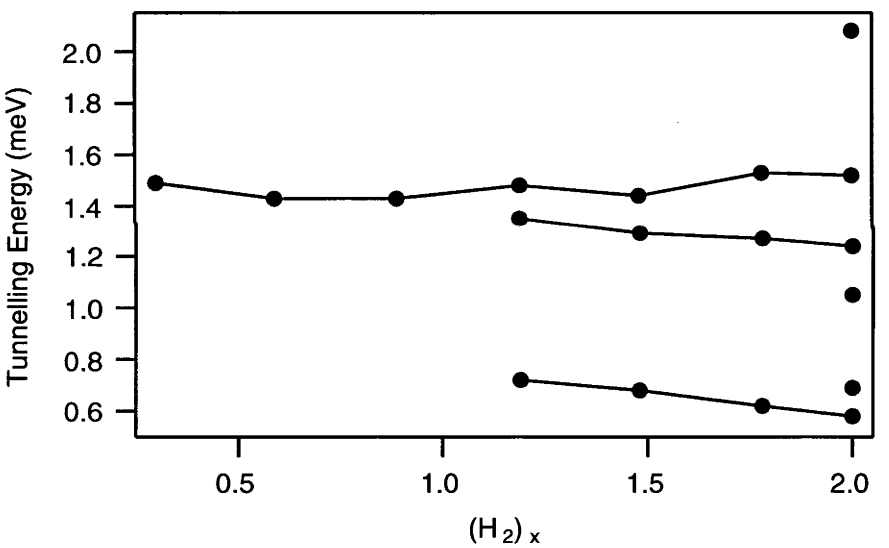

Figure 5.9: *the new interpretation of the hydrogen tunnelling data from Figure 5.8 and Table 5.3.*

The tunnelling data show that at the start of sorption there is a single strong peak at ~1.45 meV that grows in intensity as hydrogen stoichiometry is increased up to x=0.89. Comparing this with *ab*-plane diffraction data in Figure 4.6.1, the growth of this single tunnelling peak is associated with a steady disruption of the $\sqrt{43}x\sqrt{43}$ lattice of RbC_{25}, without the appearance of a new crystal structure to replace it. Stead et al[12] explained this peak as the hydrogen molecules occupying sites in the $\sqrt{7}x\sqrt{7}$ hexagons that form part of the $\sqrt{43}x\sqrt{43}$ structure, but the x-ray data presented in Figure 4.6.1 suggest that

the hydrogen is not occupying sites in the existing structure, but is reconstituting the ionic lattice as it is absorbed, to produce a disordered solid solution with little long range order. A peak near 1.45 meV is present in all the tunnelling spectra, and this site can be associated with the broad diffraction peak at ~17° that is present in all of the diffraction patterns.

At a stoichiometry of $Rb(H_2)_{1.19}C_{25}$, the tunnelling data show the appearance of new structure; this is the same stoichiometry where the new diffraction peaks appear in the x-ray data, and thus the new tunnelling sites are associated with this new crystal structure. Here the tunnelling data are interpreted as including two new peaks, one at 0.7 meV and another at 1.30 meV, overlapping the peak observed at lower fillings. The two new peaks appear to gain intensity at the expense of the peak at 1.45 meV as the stoichiometry increases to x=1.78, which is near the highest filling achieved with x-ray experiments, x=1.86; this behaviour is in contrast to that of the x-ray intensities, where the maximum intensity of the new peaks is reached at x=1.10, when they first appear, and then decreases to the gain of the peak at ~17° as hydrogen filling increases. This would indicate that the long-range order of the new structures formed at $(H_2)_{1.1}$ is being broken up by the absorption of more hydrogen molecules while the short range site symmetry remains the same. The tunnelling data at x=2.0 shows the sudden appearance of three new peaks; the x-ray experiments could not reach this stoichiometry.

In section 4.6, the new diffraction peaks that appeared at $(H_2)_{1.1}$ were assigned to two separate phases, one expanded and the other compressed with respect to the solid solution. The tunnelling data do not contradict this assignment: the two new sites are both at a lower energy that the peak at 1.45 meV, showing that there is a greater hindrance to the tunnelling in the new sites compared to the site in the solid solution; which in turn implies that there is less space available in the new sites, if only by a very small amount. If the hydrogen molecules are only occupying the threefold site in the available phases then there are two identical sites per unit cell in any plane group, and the two new tunnelling peaks would each be associated with a different phase. If some are occupying the twofold site, then a monoclinic cell could provide up to three sites with different local symmetry per cell. Thus the tunnelling data cannot show how many new phases are providing the new sites at x=1.0; it cannot determine whether they are part of one or two new phases. It is also possible that the new sites at 0.7 and 1.3 meV are different sites in a single monoclinic phase, while there is a second compressed phase that does not contain any hydrogen.

5.5 Further Work

While this study has elucidated the structural behaviour of some of the ternary intercalates discovered by Watanabe et al, many lacunae in our knowledge remain.

Most obviously, the ternary compounds based on the stage 2 cesium-graphite binary have not been investigated here at all, primarily because of the very high x-ray absorption of cesium. Transmission mode experiments, which are needed to study the *ab*-plane structure, require samples much thinner than those produced from the methods used here. Thinner samples of the order of 0.2 mm thick should allow x-ray studies of these compounds, as would synchrotron sources. Of particular interest for a structural study is the cesium-nitrogen-graphite system; the original studies found that this possessed the Type I isotherm, of the typical Langmuir shape - it is the only system apart from the hydrogen and deuterium compounds which was observed to have this isotherm. The rubidium-hydrogen system possessed the most complex behaviour of any of the compounds studied here, and whether similar behaviour would be seen in the cesium-nitrogen-graphite compound is an open question. The cesium-methane-graphite compound has been reported from *c*-axis neutron studies to pass through a two-phase system at an intermediate methane filling to a final single-phase compound at saturation: the *ab*-plane structure of this single phase is unknown[13]. Tunnelling spectra of the cesium-hydrogen and deuterium systems have already been published[14, 15], showing much more complex behaviour than that produced by the rubidium-hydrogen GIC; x-ray studies of the *ab*-plane structure would determine whether this complex behaviour is seen in the alkali ion lattice as well.

With the rubidium-hydrogen GICs, the behaviour of the observed structures with temperature was little studied in this work, but enough to determine that a very rapid phase transition takes place at 100 K. Further studies at lower temperatures, using the same samples and techniques used here, may find other phase transitions. Experiments with a much finer measurement of gas uptake would be able to determine the exact stoichiometry where the phase transition takes place. With this compound single crystal studies may be profitable at lower hydrogen fillings, but the phase transitions observed at higher fillings may cause a crystal to separate into different domains, and the immediate disproportionation seen in the other ternary compounds would probably destroy a single crystal. The same technique of using aligned samples may be applied to single wavelength neutron diffraction experiments, which would be vastly more sensitive to the position of the hydrogen molecules than XRD, but would require larger samples. The tunnelling data may have to be re-evaluated in more detail than above with regard to the available sites observed by the structural studies. The potassium-

hydrogen and potassium-deuterium systems appeared very complex, and *ab*-plane diffraction experiments at a synchrotron source with a more precise control of stoichiometry may provide better data.

The rubidium-argon, rubidium-methane and potassium-nitrogen GICs produced the *ab*-plane diffraction data which were most amenable to analysis, but the *c*-axis data were disturbed by the presence of a higher stage contaminant. *c*-axis studies on samples with a pure stage 2 structure should be able to determine how the two *ab*-plane phases observed in these compounds are interstratifying, and whether it is an entirely random interstratification, or an ordered structure and hence a form of fractional staging.

5.6 Conclusion

Contrary to the assumptions made in previous studies[10, 12], the physisorption of gases led to a significant alteration of the *ab*-plane structure of the alkali metal ionic lattices of RbC_{25} and KC_{25}, with the most common effect being a separation of the lattice in the *ab*-plane into an expanded and compressed phase, sometimes with a simultaneous separation in the *c* direction. The technique of using x-ray diffraction of oriented samples to investigate the *ab*-plane structure was found to be most useful for the larger physisorbed species, which could make a large contribution to the x-ray structure factor.

References

1. S.C. Moss and R. Moret, *Structural Properties and Phase Transitions*, in *Graphite Intercalation Compounds I Structure and Dynamics*, H. Zabel and S.A. Solin, Editors. 1990, Springer-Verlag: Berlin. p. 5-58.

2. F.R. Trouw and J.W. White, *Dynamics of Intercalated Molecules, Part 1-Sorption Potentials and Structure of $CsC_{24}(CH_4)$.* Journal of the Chemical Society, Faraday Transactions 2, 1988. **84**: p. 791-812.

3. G.R.S. Naylor and J.W. White, *Structure of Second Stage Graphite-Rubidium, C24Rb.* Journal of the Chemical Society, Faraday Transactions, 1987. **83(11)**: p. 3447-3458.

4. F. Rousseaux, R. Moret, D. Guerard, and P. Langrange, *X-ray study of the liquid and solid phases of the alkali metals in KC_{24}- and RbC_{24}-intercalated graphite single crystals.* Phys. Rev. B., 1990. **42**(1): p. 725-742.

5. R.C. Reynolds, *Interstratified Clay Minerals*, in *Crystal Structures of Clay Minerals and their X-Ray Identification*, G.W. Brindley and G. Brown, Editors. 1980, Mineralogical Society: London. p. 249-304.

6. S. Hendricks and E. Teller, *X-Ray Interference in Partially Ordered Layer Lattices.* Journal of Chemical Physics, 1942. **10**(3): p. 147-167.

7. K. Watanabe, T. Kondow, M. Soma, T. Onishi, and K. Tamaru, *Molecular-sieve type sorption on alkali graphite intercalation compounds.* Proceedings of the Royal Society of London A, 1973. **333**: p. 51-67.

8. M. Mori, S.C. Moss, Y.M. Jan, and H. Zabel, *Mass- and charge-density modulation of graphite in potassium-graphite intercalates.* Physical Review B, 1982. **25**(2): p. 1287-1296.

9. A.D. Buckingham, *Electric Moments of Molecules*, in *Physical Chemistry: An Advanced Treatise*, D. Henderson, Editor. 1970, Academic Press: New York. p. 349-386.

10. H. Zabel, J.J. Rush, and A. Magerl, *Elastic Neutron Scattering on $C_{24}Rb(D_2)_x$ in the Dilute Concentration Regime.* Synthetic Metals, 1983. **7**: p. 251-255.

11. J.P. Beaufils, T. Crowley, T. Rayment, R.K. Thomas, and J.W. White, *Tunnelling of hydrogen in alkali metal intercalation compounds I: $C_{25}Rb(H2)x$ and $C_{24}Cs(H_2)_x$.* Molecular Physics, 1981. **44**: p. 1257-1269.

12. W.J. Stead, I.P. Jackson, J. McCaffrey, and J.W. White, *Tunnelling of Hydrogen in Alkali-Metal-Graphite Intercalation Compounds - A Systematic Study of $C_{24}Rb(H_2)_x$ and its Structural Consequences.* Journal of the Chemical Society, Faraday Transactions, 1988. **84(10)**: p. 1669-1682.

13. H. Pilliere, J.L. Soubeyroux, and F. Beguin, *Influence of Critical Temperature on the Phases Formed During the Intercalation of Methane into CsC_{24}.* Phase Transitions, 1993. **46**: p. 27-39.

14. W.J. Stead, P. Meechan, and J.W. White, *Librations of Hydrogen in Stage II Caesium Graphite $C_{24}CS$.* Journal of the Chemical Society, Faraday Transactions, 1988. **84**(10): p. 1655-1688.

15. P.R. Hirst, J.W. White, Z.A. Bowden, L.M. Needham, and A.D. Taylor, *High-energy neutron inelastic scattering from H2 in $C_{28}Cs(H_2)_{1.52}$.* Chemical Physics Letters, 1988. **147**(2,3): p. 228-230.